

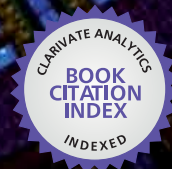


IntechOpen

# Fourier Transforms

## High-tech Application and Current Trends

*Edited by Goran S. Nikolic,  
Milorad D. Cakic and Dragan J. Cvetkovic*



WEB OF SCIENCE™



---

# **FOURIER TRANSFORMS - HIGH-TECH APPLICATION AND CURRENT TRENDS**

---

Edited by **Goran S. Nikolić, Milorad D. Cakić**  
and **Dragan J. Cvetković**

## Fourier Transforms - High-tech Application and Current Trends

<http://dx.doi.org/10.5772/62751>

Edited by Goran S. Nikolic, Milorad D. Cakic and Dragan J. Cvetkovic

### Contributors

Carlos Martin Orallo, Ignacio Carugati, Emmanuel Hernández, Miguel Angel Hernández López, Hugo Jorge Cortina Marrero, Edwin Román Hernández, Victor Iván Moreno Oliva, José Rafael Dorrego Portela, Yew Keong Choong, Alex Pappachen James, Maria Grazia Bridelli, Rozita Teymourzadeh, Irina Dolguntseva, Marco Q. Pisani, Massimo E. Zucco, Tiziana Cavaleri, Anca Armășelu, Mihály Dobróka, Hajnalka Szegedi, Péter Vass, Goran S. Nikolic, Milorad Cakic, Slobodan Glišić, Dragan J. Cvetkovic, Žarko Mitić, Dragana Marković-Nikolić

### © The Editor(s) and the Author(s) 2017

The moral rights of the and the author(s) have been asserted.

All rights to the book as a whole are reserved by INTECH. The book as a whole (compilation) cannot be reproduced, distributed or used for commercial or non-commercial purposes without INTECH's written permission.

Enquiries concerning the use of the book should be directed to INTECH rights and permissions department ([permissions@intechopen.com](mailto:permissions@intechopen.com)).

Violations are liable to prosecution under the governing Copyright Law.



Individual chapters of this publication are distributed under the terms of the Creative Commons Attribution 3.0 Unported License which permits commercial use, distribution and reproduction of the individual chapters, provided the original author(s) and source publication are appropriately acknowledged. If so indicated, certain images may not be included under the Creative Commons license. In such cases users will need to obtain permission from the license holder to reproduce the material. More details and guidelines concerning content reuse and adaptation can be found at <http://www.intechopen.com/copyright-policy.html>.

### Notice

Statements and opinions expressed in the chapters are those of the individual contributors and not necessarily those of the editors or publisher. No responsibility is accepted for the accuracy of information contained in the published chapters. The publisher assumes no responsibility for any damage or injury to persons or property arising out of the use of any materials, instructions, methods or ideas contained in the book.

First published in Croatia, 2017 by INTECH d.o.o.

eBook (PDF) Published by IN TECH d.o.o.

Place and year of publication of eBook (PDF): Rijeka, 2019.

IntechOpen is the global imprint of IN TECH d.o.o.

Printed in Croatia

Legal deposit, Croatia: National and University Library in Zagreb

Additional hard and PDF copies can be obtained from [orders@intechopen.com](mailto:orders@intechopen.com)

Fourier Transforms - High-tech Application and Current Trends

Edited by Goran S. Nikolic, Milorad D. Cakic and Dragan J. Cvetkovic

p. cm.

Print ISBN 978-953-51-2893-9

Online ISBN 978-953-51-2894-6

eBook (PDF) ISBN 978-953-51-4114-3

# We are IntechOpen, the world's leading publisher of Open Access books Built by scientists, for scientists

**3,750+**

Open access books available

**115,000+**

International authors and editors

**119M+**

Downloads

**151**

Countries delivered to

Our authors are among the  
**Top 1%**

most cited scientists

**12.2%**

Contributors from top 500 universities



**WEB OF SCIENCE™**

Selection of our books indexed in the Book Citation Index  
in Web of Science™ Core Collection (BKCI)

Interested in publishing with us?  
Contact [book.department@intechopen.com](mailto:book.department@intechopen.com)

Numbers displayed above are based on latest data collected.  
For more information visit [www.intechopen.com](http://www.intechopen.com)





# Meet the editors

Prof. Goran S. Nikolić was born in Knez Selo (Niš, Serbia) on 1 November 1966. He received his PhD degree in Chemical Engineering (2001) from the University of Niš. Currently, he is working as a full professor at the same university, on pharmaceutical-cosmetic engineering group of subjects at the Faculty of Technology in Leskovac. His research activities are development of pharmaceutical products and quality control of drugs. His competences are experience in project management and managing of academic institution at different levels. He is a member of several national projects in the technological development area and member of numerous TEMPUS Joint European projects of sustainable technologies, environmental application, and management courses. He has authored more than 300 scientific papers, numerous technological solutions for pharmaceutical industry, national monographies, international patents, university textbooks, and invitation lecturers. He is the editor of two international monographs on FTIR spectroscopy (InTech Open).

Prof. Milorad D. Cakić was born on 26 May 1951 in Leskovac, Serbia. He finished his studies at the Faculty of Chemistry in Skopje (Macedonia) in 1975. He completed his master studies in the field of molecular spectroscopy in 1978. His PhD thesis was defended at the same university in 1984. He was elected in 1985 as assistant professor at the University of Niš, Faculty of Technology in Leskovac, where he works today as a full professor. His main scientific interest is structure-spectral correlation investigations by different spectroscopic and chromatographic methods. He had published a number of articles in the field of synthesis and characterization of compounds with proven or potential pharmaceutical activity. He was an editor of many scientific publications and reviewer in a number of journals. His competences are experience in project management and managing of academic institution at different levels (dean, vice dean, head of the department, head of the laboratory, member of the senate, and deputy president of the Expert Board for Natural Sciences and Mathematics). Prof. Cakić is a member of the Board for the Accreditation of Scientific-Research Organizations of the Republic of Serbia.

Prof. Dragan J. Cvetković was born on 26 June 1977 in Leskovac. He finished elementary and high school in Lebane, and then he completed his studies at the Faculty of Technology in Leskovac in the year 2002. He finished his PhD thesis in the year 2012 at the Faculty of Technology in Leskovac. Dragan Cvetković participated in the realization of numerous projects funded by the Ministry of Science, Republic of Serbia. He was engaged on the project "Folding and Stability of Phycobilisome Proteins" at the Institute of Biology and Technology of Saclay, France. He also participated in realization of the project entitled "Contribution of Chemical Quenching of Singlet Oxygen to Pro- and Antioxidant Activity of Carotenoids," funded by the Polish Ministry of Science. He was elected as a teaching assistant in the year 2008 on Physical Chemistry, Colloid Chemistry, and Instrumental Analysis, but in the year 2012, he was elected as an assistant professor on physicochemical group of subjects at the Faculty of Technology in Leskovac.



---

# Contents

---

## Preface XI

- Section 1 Fourier Transform - The Most Powerful Analytical Tool for High-Tech Application 1**
- Chapter 1 **Inversion-Based Fourier Transform as a New Tool for Noise Rejection 3**  
Mihály Dobróka, Hajnalka Szegedi and Péter Vass
- Chapter 2 **Single Bin Sliding Discrete Fourier Transform 25**  
Carlos Martin Orallo and Ignacio Carugati
- Chapter 3 **Fourier Analysis for Harmonic Signals in Electrical Power Systems 43**  
Emmanuel Hernández Mayoral, Miguel Angel Hernández López, Edwin Román Hernández, Hugo Jorge Cortina Marrero, José Rafael Dorrego Portela and Victor Ivan Moreno Oliva
- Chapter 4 **High Resolution Single-Chip Radix II FFT Processor for High-Tech Application 67**  
Rozita Teymourzadeh
- Chapter 5 **Memristor Threshold Logic FFT Circuits 95**  
Alex Pappachen James
- Chapter 6 **Application of Fourier Series Expansion to Electrical Power Conversion 119**  
Irina Dolguntseva

- Section 2 New Spectral Application of the Fourier Transforms 147**
- Chapter 7 **Study of Green Nanoparticles and Biocomplexes Based on Exopolysaccharide by Modern Fourier Transform Spectroscopy 149**  
Goran S. Nikolić, Milorad D. Cakić, Slobodan Glišić, Dragan J. Cvetković, Žarko J. Mitić and Dragana Z. Marković
- Chapter 8 **Fourier Transform Infrared and Two-Dimensional Correlation Spectroscopy for Substance Analysis 175**  
Yew-Keong Choong
- Chapter 9 **Fourier Transform Infrared Spectroscopy in the Study of Hydrated Biological Macromolecules 191**  
Maria Grazia Bridelli
- Chapter 10 **Fourier Transform Hyperspectral Imaging for Cultural Heritage 215**  
Massimo Zucco, Marco Pisani and Tiziana Cavaleri
- Chapter 11 **New Spectral Applications of the Fourier Transforms in Medicine, Biological and Biomedical Fields 235**  
Anca Armășelu

---

## Preface

---

*By the turn of the millennium a technology known as virtual reality will be in widespread use. It will allow you to enter computer generated artificial worlds as unlimited as the imagination itself. Its creators foresee millions of positive uses, while others fear it as a new form of mind control...*

**- Lawnmower Man and Brett Leonard**

As of the onset of the twenty-first century, products considered high technology are often those that incorporate advanced computer electronics. High tech is a technology that involves the production or use of advanced or sophisticated devices. Because the high-tech sector of the economy develops or uses the most advanced technology known, it is often seen as having the most potential for future growth. This perception has led to high investment in high-tech sectors of the economy. But all this would not have been possible without the ongoing development of science and certain of its disciplines as the powerful analytical tools. One of them is Fourier analysis. The prevalent subject of Fourier analysis encompasses a vast spectrum of mathematics with parts that may appear quite different at first glance. In Fourier analysis, the term *Fourier transform* often refers to the process that decomposes a given function into the harmonic domain. This process results in another function that describes what frequencies are in the original function. Meanwhile, the transformation is often given a more specific name depending upon the domain and other properties of the function being transformed.

Fourier transform represents one of the oldest and most powerful analytical tools in many fields like applied mathematics, physical sciences, and engineering. Because of the Fourier transform which helps to describe the physical mechanism of collecting and reconstructing data, it also becomes a priceless image-processing instrument in other areas which are related to biomedicine, pharmaceuticals, biotechnology, bioinformatics, computer engineering, electrical and electronic engineering, information technology, artificial intelligence, nanotechnology, nuclear physics, photonics, robotics, and semiconductors. The development of Fourier transform techniques pushed the utilization of the spectroscopic methods dramatically. So, Fourier transform methods have long been proved to be extremely useful in all fields of science and technology, like telecommunications, audio technology, radio astronomy, seismology, aerospace, automotive, especially spectroscopy crystallography, medical image processing, and signal analysis techniques. Particularly, Fourier transform spectroscopy has become an innovative, powerful, and extra sensitive method to study biologically important systems, varying from simple molecules to highly complex samples like living cells and tissues. These enhanced spectroscopic methods in their modern form represent an

important area of research with various applications in diverse fields of science and industry.

Therefore, the main purpose of this book is to provide a modern review about the recent advances in Fourier transforms in high-tech and spectral application. In this sense, the book is organized into two sections. Section 1 presents Fourier transform as a new tool for high-tech application in electrical, electronic, and computer engineering. This section provides application of the single-bin sliding discrete Fourier transform, inversion-based Fourier transform as a new tool for noise rejection, application of Fourier series expansion to electrical power conversion, Fourier analysis for harmonic signals in electrical power systems, high-resolution single-chip radix II FFT processor for high-tech application, and memristor threshold logic FFT circuits. Section 2 deals with numerous Fourier transform spectroscopic techniques with a wide range of biological, biomedical, biotechnological, pharmaceutical, and nanotechnological applications. In this section, recent advances in Fourier transform spectral application in different fields, by virtue of various techniques such as two-dimensional correlation spectroscopy, visible spectroscopy, infrared-attenuated total reflectance, infrared photoacoustic spectroscopy, infrared imaging spectroscopy, ion cyclotron resonance mass spectrometry, etc., are presented.

This edition represents a reference review for Fourier transform methods as they are applied in signal processing and spectroscopy. More exactly, the book concerns an overview of the current status and of the recent achievements in Fourier transform spectroscopy and some selected new applications of Fourier analysis in the high-tech fields, with the emphasis on the own work done by the author of this book. The confluence of Fourier transform methods with high tech opens new opportunities for the detection and handling of the atoms and molecules using nanodevices, with potential for a large variety of scientific and technological applications.

In addition, the reference list included in each chapter contains both historical and extensive analysis which works together with the articles that describe several key breakthroughs in the mentioned areas of interest.

**Prof. Goran S. Nikolić**

**Prof. Milorad D. Cakić**

**Prof. Dragan J. Cvetković**

University of Niš, Faculty of Technology  
Leskovac, Serbia

---

# Fourier Transform - The Most Powerful Analytical Tool for High-Tech Application

---



---

# Inversion-Based Fourier Transform as a New Tool for Noise Rejection

---

Mihály Dobróka, Hajnalka Szegedi and Péter Vass

Additional information is available at the end of the chapter

<http://dx.doi.org/10.5772/66338>

---

## Abstract

In this study, a new inversion method is presented for performing two-dimensional (2D) Fourier transform. The discretization of the continuous Fourier spectra is given by a series expansion with the scaled Hermite functions as square-integrable set of basis functions. The expansion coefficients are determined by solving an overdetermined inverse problem. In order to define a quick algorithm in calculating the Jacobian matrix of the problem, the special feature that the Hermite functions are eigenfunctions of the Fourier transformation is used. In the field of inverse problem theory, there are numerous procedures for noise rejection, so if the Fourier transformation is formulated as an inverse problem, these tools can be used to reduce the noise sensitivity. It was demonstrated in many case studies that the use of Cauchy-Steiner weights could increase the noise rejection capability of geophysical inversion methods. Following this idea, the two-dimensional Fourier transform is formulated as an iteratively reweighted least squares (IRLS) problem using Cauchy-Steiner weights. The new procedure is numerically tested using synthetic data.

**Keywords:** noise rejection in Fourier transformation, series expansion-based inversion, robust Fourier transformation, Hermite functions, reduction to pole

---

## 1. Introduction

In signal processing, the frequency spectrum of the time domain signals plays a very important role. In order to change over from the time domain to the frequency domain, the Fourier transform is applied most frequently. In the case of equidistantly sampled discrete time domain data sets, the so-called discrete Fourier transform (DFT) algorithm is used to

---

determine the discrete frequency spectrum. In the numerically very efficient Fast Fourier Transform algorithm (FFT), the spectrum is determined by solving a complete set of inhomogeneous linear algebraic set of equations.

The measured data set always contains noise, which is linearly projected into the frequency domain during Fourier transformation, so the traditional FT algorithms are sensitive to noise, most significantly to non-Gaussian one. On the other hand, it is well-known that in the framework of inverse problem theory there are a collection of methods with excellent noise rejection capability. For this reason, it was proposed to handle the 1D Fourier Transform as an overdetermined inverse problem [1].

In inverse problem theory, it is known that the simple least squares (LSQ) method gives optimal solution in case of Gaussian data noises while it is very sensitive for outliers. To reduce the effect of outlying data various (robust) inversion methods have been developed. The least absolute deviation (LAD) is one of the most frequently applied robust inversion method, which can be numerically realized by linear programming or by using the so-called iteratively reweighted least squares (IRLS) procedure [2]. In this case, the  $L_1$  norm of the deviation between the observed and predicted data is minimized. The IRLS procedure which iteratively recalculates the so-called Cauchy weights results in a very efficient robust inversion method [3]. In applying Cauchy inversion, the scale parameter of the Cauchy weights should be *a priori* known. This problem is solved in the framework of the most frequent value (MFV) method (developed by Steiner [4, 5]), where the scale parameter is derived from the data set. The weights given by the MFV method have been extensively used in various IRLS inversion problems. A successful application in joint inversion of seismic and geoelectric data was published by Dobróka et al. [6]. Szűcs et al. [7] reported a considerable improvement due to the use of Steiner's weights in the interpretation of borehole geophysical data. The Cauchy weights improved by Steiner's MFV method (the so-called Cauchy-Steiner weights) were successfully applied in robust tomography algorithms by Dobróka and Szegedi [8].

In previous papers by Szegedi and Dobróka [9], the 1D Fourier transformation was handled as robust inverse problem using IRLS algorithm with Cauchy-Steiner weights. It was shown that the noise sensitivity of the continuous Fourier transform (and its discrete variants DFT and FFT) was appropriately reduced by using robust inversion. Following a fruitful inversion strategy developed at the Geophysical Department of the University of Miskolc we used series expansion as a discretization tool. Series expansion-based inversion methods were successfully used in the interpretation of borehole geophysical data [10, 11] and also in processing induced polarization data [12]. In this study, we further develop the previously published inversion-based 1D Fourier transform algorithm by extending it to 2D cases.

## 2. Theoretical background for 1D algorithm

The Fourier transform and its inverse allow establishing a connection between the time and frequency domain. For the one-dimensional case the Fourier transform is defined as

$$U(\omega) = \frac{1}{\sqrt{2\pi}} \int_{-\infty}^{\infty} u(t) e^{-j\omega t} dt, \quad (1)$$

where  $t$  denotes the time,  $\omega$  is the angular frequency and  $j$  is the imaginary unit,  $U(\omega)$  is the Fourier transform of a real-valued time function  $u(t)$ . Thus, the Fourier transform provides the frequency domain representation of a phenomenon investigated by the measurement of some quantity in the time domain. By means of the inverse Fourier transform

$$u(t) = \frac{1}{\sqrt{2\pi}} \int_{-\infty}^{\infty} U(\omega) e^{j\omega t} d\omega, \quad (2)$$

we can return from the frequency domain to the time domain.

A next step in formulating the Fourier transform as an inverse problem is the discretization of the frequency spectrum  $U(\omega)$ . In order to satisfy this requirement, let us assume that  $U(\omega)$  is approximated with sufficient accuracy by using a finite series expansion

$$U(\omega) = \sum_{i=1}^M B_i \Psi_i(\omega), \quad (3)$$

where the parameter  $B_i$  is a complex valued expansion coefficient and  $\Psi_i$  is a member of an accordingly chosen set of real valued basis functions.

Using the terminology of (discrete) inverse problem theory, the theoretical values of time domain data (forward problem) can be given by the inverse Fourier transform

$$u_k^{theor} = u_k^{theor} = \frac{1}{\sqrt{2\pi}} \int_{-\infty}^{\infty} U(\omega) e^{j\omega t_k} d\omega, \quad (4)$$

where  $t_k$  is the  $k$ th sampling time. Inserting the expression given in Eq. (3) one finds that

$$u_k^{theor} \cong \frac{1}{\sqrt{2\pi}} \int_{-\infty}^{\infty} \left( \sum_{i=1}^M B_i \Psi_i(\omega) \right) e^{j\omega t_k} d\omega = \sum_{i=1}^M B_i \frac{1}{\sqrt{2\pi}} \int_{-\infty}^{\infty} \Psi_i(\omega) e^{j\omega t_k} d\omega. \quad (5)$$

Let us introduce the notation

$$G_{k,i} = \frac{1}{\sqrt{2\pi}} \int_{-\infty}^{\infty} \Psi_i(\omega) e^{j\omega t_k} d\omega, \quad (6)$$

where  $G_{k,i}$  is an element of the so called Jacobian matrix of the size  $N$ -by- $M$  ( $N$  is the number of time domain data and  $M$  is the number of unknown expansion coefficients). It is important for later considerations to note, that the Jacobian can be written as the inverse Fourier transform (in  $t = t_k$ ) of the  $\Psi_i$  basis function. The theoretical values take the linear form

$$u_k^{\text{theor}} = \sum_{i=1}^M B_i G_{k,i}. \quad (7)$$

The parameterization is always an important step in constructing an inversion algorithm. In Fourier transformation the frequency spectrum is defined over the interval  $(-\infty, \infty)$ , so the set of basis functions should be defined in the same domain. In addition, the use of orthonormal functions for the series expansion is also proposed to the parameterization of the model. Because of these reasons we have chosen the set of scaled Hermite functions for discretization (their square-integrability ensures the existence of their Fourier transform).

If one tries to extend the concept of inversion-based Fourier transform for two-dimensional (2D) (or even multidimensional) case, a quick and simpler way of calculation can be advantageous. For this reason, consider the basic formulae of Hermite polynomials and Hermite functions.

The basic Hermite polynomials can be defined by the Rodriguez formula

$$h_n^{(0)}(\omega) = (-1)^n e^{\omega^2} \left( \frac{d}{d\omega} \right)^n e^{-\omega^2}, \quad n = 0, 1, 2, \dots, \quad (8)$$

and also can be generated by the recursive formula

$$h_{n+1}^{(0)}(\omega) = 2\omega h_n^{(0)}(\omega) - 2n h_{n-1}^{(0)}(\omega), \quad (9)$$

where  $h_0^{(0)}(\omega) = 1$ ,  $h_1^{(0)}(\omega) = 2\omega$ . The Hermite polynomials fulfill the orthogonality condition

$$\int_{-\infty}^{\infty} e^{-\omega^2} \cdot h_n^{(0)}(\omega) \cdot h_m^{(0)}(\omega) d\omega = 2^n n! \sqrt{\pi} \delta_{nm}, \quad \delta_{nm} = \begin{cases} 0, & n \neq m \\ 1, & n = m \end{cases}, \quad (10)$$

where  $\delta_{nm}$  denotes the Kronecker symbol. Based on this formula, the basic Hermite functions can be defined as

$$H_n^{(0)}(\omega) = \frac{e^{-\frac{\omega^2}{2}} \cdot h_n^{(0)}(\omega)}{\sqrt{\sqrt{\pi} n! 2^n}}, \quad n = 0, 1, 2, \dots \quad (11)$$

Afterward the function  $H_n^{(0)}(\omega)$  is not only a complete orthogonal but an orthonormal system

$$\int_{-\infty}^{\infty} H_n^{(0)}(\omega) \cdot H_m^{(0)}(\omega) d\omega = \delta_{nm}, \quad \delta_{nm} = \begin{cases} 0, & n \neq m \\ 1, & n = m \end{cases}. \quad (12)$$

There is an important special feature of Hermite functions, namely that they are the eigenfunctions of the Fourier transform [13]

$$\mathcal{F}\{H_n^{(0)}(t)\} = (-j)^n H_n^{(0)}(\omega), \quad (13)$$

and for the inverse Fourier transform, respectively

$$\mathcal{F}^{-1}\{H_n^{(0)}(\omega)\} = (j)^n H_n^{(0)}(t). \tag{14}$$

As it was given in reference [14], the Hermite functions have to be modified by scaling because in geophysical applications the frequency covers wide ranges. The Rodriguez formula for modified Hermite polynomials takes the form

$$h_n(\omega, \alpha) = (-1)^n e^{\alpha \omega^2} \left(\frac{d}{d\omega}\right)^n e^{-\alpha \omega^2}, \tag{15}$$

and can be also generated by the recursive formula

$$h_{n+1}(\omega, \alpha) = 2\omega\alpha h_n(\omega, \alpha) - 2n\alpha h_{n-1}(\omega, \alpha), \tag{16}$$

where  $\alpha$  is the scale factor and  $h_0(\omega, \alpha) = 1$ ,  $h_1(\omega, \alpha) = 2\alpha\omega$  [15]. The normalizing equation is

$$\int_{-\infty}^{\infty} e^{-\alpha\omega^2} \cdot h_n^{(0)}(\omega, \alpha) \cdot h_m^{(0)}(\omega, \alpha) d\omega = \sqrt{\frac{\pi}{\alpha}} (2\alpha)^n n! \delta_{nm}, \quad \delta_{nm} = \begin{cases} 0, & n \neq m \\ 1, & n = m \end{cases}. \tag{17}$$

Thus, the scaled Hermite functions can be defined as

$$H_n(\omega, \alpha) = \frac{e^{-\frac{\alpha}{2}\omega^2} \cdot h_n(\omega, \alpha)}{\sqrt{\frac{\pi}{\alpha}} n! (2\alpha)^n}. \tag{18}$$

In this case the normalizing equation is

$$\int_{-\infty}^{\infty} H_n(\omega, \alpha) \cdot H_m(\omega, \alpha) d\omega = \delta_{nm}, \quad \delta_{nm} = \begin{cases} 0, & n \neq m \\ 1, & n = m \end{cases}. \tag{19}$$

Introducing the notation  $\omega' = \sqrt{\alpha}\omega$  the  $h_n(\omega, \alpha)$  modified Hermite polynomials can be traced back to the  $h_n^{(0)}$  base polynomials. Substituting  $\omega'$  into Eq. (15) we obtain

$$h_n(\omega, \alpha) = (\sqrt{\alpha})^n (-1)^n e^{\omega'^2} \left(\frac{d}{d\omega'}\right)^n e^{-\omega'^2} = (\sqrt{\alpha})^n h_n^{(0)}(\omega') = (\sqrt{\alpha})^n h_n^{(0)}(\sqrt{\alpha}\omega). \tag{20}$$

Similarly, the modified Hermite function can also be traced back to the basic case ( $H_n^{(0)}$ ). According to Eq. (18), we get the following formula

$$H_n(\omega, \alpha) = \frac{e^{-\frac{\omega'^2}{2}} (\sqrt{\alpha})^n h_n(\omega')}{\sqrt{\sqrt{\pi} \frac{1}{\sqrt{\alpha}} n! 2^n \alpha^n}} = \sqrt[4]{\alpha} \frac{e^{-\frac{\omega'^2}{2}} h_n(\omega')}{\sqrt{\sqrt{\pi} n! 2^n}} = \sqrt[4]{\alpha} H_n^{(0)}(\omega') = \sqrt[4]{\alpha} H_n^{(0)}(\sqrt{\alpha}\omega). \tag{21}$$

Expanding the spectrum by means of the modified Hermite functions, in accordance with Eq. (6) the Jacobian matrix can be written as the inverse Fourier transform of the  $H_n(\omega, \alpha)$  basis functions

$$G_{kn} = \frac{1}{\sqrt{2\pi}} \int_{-\infty}^{\infty} H_n(\omega, \alpha) \cdot e^{j\omega t} d\omega. \quad (22)$$

Using Eq. (21) one finds

$$G_{kn} = \frac{1}{\sqrt{2\pi}} \int_{-\infty}^{\infty} \sqrt[4]{\alpha} H_n^{(0)}(\omega') \cdot e^{j\omega' t} d\omega', \quad (23)$$

or taking the notations  $\omega t = \omega' t'$ ,  $\omega' = \sqrt{\alpha}\omega$  and  $t' = \frac{t}{\sqrt{\alpha}}$  into account we have

$$G_{kn} = \frac{1}{\sqrt[4]{\alpha}} \frac{1}{\sqrt{2\pi}} \int_{-\infty}^{\infty} H_n^{(0)}(\omega') \cdot e^{j\omega' t'} d\omega' = \frac{1}{\sqrt[4]{\alpha}} \mathcal{F}^{-1}\{H_n^{(0)}(\omega')\}. \quad (24)$$

Using the properties of the base Hermite functions from Eq. (14) Eq. (24) can be rewritten in the following form

$$G_{kn} = \frac{1}{\sqrt[4]{\alpha}} (j)^n H_n^{(0)}(t') = \frac{1}{\sqrt[4]{\alpha}} (j)^n H_n^{(0)}\left(\frac{t}{\sqrt{\alpha}}\right). \quad (25)$$

This is a very important result in further developing the inversion-based Fourier transform method because the Jacobian matrix can be produced quickly, as the procedure do not require integration. This is especially important in case of 2D (or higher dimensional) Fourier transform.

In accordance with Eq. (7) the theoretical data can be obtained as a linear expression of the expansion coefficients using the easily calculated elements of the Jacobian matrix. The general element of the deviation vector can be given in the following form

$$e_k = u_k^{\text{measured}} - u_k^{\text{theor}}. \quad (26)$$

In the framework of inverse problem theory, various methods are given for the minimization of appropriately chosen norm of the deviation vector resulting in an estimation of the expansion coefficients ( $B_i^{\text{estimated}}$ ). After this, the real and imaginary part of the estimated spectrum can be calculated at any frequency as

$$U^{\text{estimated}}(\omega) = \sum_{i=1}^M B_i^{\text{estimated}} H_i(\omega, \alpha). \quad (27)$$

### 3. Theoretical background for 2D algorithm

For the two-dimensional case the Fourier transform is defined as

$$U(\omega_x, \omega_y) = \frac{1}{2\pi} \int_{-\infty}^{\infty} \int_{-\infty}^{\infty} u(x, y) e^{-j(\omega_x x + \omega_y y)} dx dy, \quad (28)$$

where  $x, y$  denotes the spatial coordinates,  $\omega_x, \omega_y$  are the (angular) spatial frequencies and  $j$  is the imaginary unit. The frequency spectrum  $U(\omega_x, \omega_y)$  is the Fourier transform of a real valued function  $u(x, y)$  and it is generally a complex valued continuous function. In two dimensions the forward problem giving the theoretical values of the space domain data can be defined by the two-dimensional inverse Fourier transform

$$u(x, y) = \frac{1}{2\pi} \int_{-\infty}^{\infty} \int_{-\infty}^{\infty} U(\omega_x, \omega_y) e^{j(\omega_x x + \omega_y y)} d\omega_x d\omega_y, \quad (29)$$

where  $U(\omega_x, \omega_y)$  denotes the 2D spatial frequency spectrum, which will be discretized using the scaled Hermite functions defined above

$$U(\omega_x, \omega_y) = \sum_{n=1}^N \sum_{m=1}^M B_{n, m} H_n(\omega_x, \alpha) H_m(\omega_y, \beta), \quad (30)$$

where

$$H_n(\omega_x, \alpha) = \frac{e^{-\frac{\alpha}{2} \omega_x^2} h_n(\omega_x, \alpha)}{\sqrt{\sqrt{\frac{\pi}{\alpha}} n! (2\alpha)^n}}, \quad h_n(\omega_x, \alpha) = (-1)^n e^{\alpha \omega_x^2} \left(\frac{d}{d\omega_x}\right)^n e^{-\alpha \omega_x^2}, \quad (31)$$

$$H_m(\omega_y, \beta) = \frac{e^{-\frac{\beta}{2} \omega_y^2} h_m(\omega_y, \beta)}{\sqrt{\sqrt{\frac{\pi}{\beta}} m! (2\beta)^m}}, \quad h_m(\omega_y, \beta) = (-1)^m e^{\beta \omega_y^2} \left(\frac{d}{d\omega_y}\right)^m e^{-\beta \omega_y^2}. \quad (32)$$

Using Eq. (29) the data calculated at the point  $(x_k, y_l)$

$$u(x_k, y_l) = \frac{1}{2\pi} \int_{-\infty}^{\infty} \int_{-\infty}^{\infty} \sum_{n=1}^N \sum_{m=1}^M B_{n, m} H_n(\omega_x, \alpha) H_m(\omega_y, \beta) e^{j(\omega_x x_k + \omega_y y_l)} d\omega_x d\omega_y, \quad (33)$$

where  $k = (1, 2, \dots, K), l = (1, 2, \dots, L)$  denote the sequence numbers of the measurement points along the  $x$  and  $y$  directions, respectively. By introducing the Jacobian matrix, we can write

$$u(x_k, y_l) = \sum_{n=1}^N \sum_{m=1}^M B_{n, m} G_{k, l}^{n, m}, \quad (34)$$

where

$$\begin{aligned}
G_{k,l}^{n,m} &= \frac{1}{2\pi} \int_{-\infty}^{\infty} \int_{-\infty}^{\infty} H_n(\omega_x, \alpha) H_m(\omega_y, \beta) e^{j(\omega_x x_k + \omega_y y_l)} d\omega_x d\omega_y \\
&= \frac{1}{\sqrt{2\pi}} \int_{-\infty}^{\infty} H_n(\omega_x, \alpha) e^{j\omega_x x_k} d\omega_x \frac{1}{\sqrt{2\pi}} \int_{-\infty}^{\infty} H_m(\omega_y, \beta) e^{j\omega_y y_l} d\omega_y.
\end{aligned} \tag{35}$$

Similar to Eq. (21)

$$H_n(\omega_x, \alpha) = \sqrt[4]{\alpha} H_n^{(0)}(\sqrt{\alpha}\omega_x), \quad H_m(\omega_y, \beta) = \sqrt[4]{\beta} H_m^{(0)}(\sqrt{\beta}\omega_y), \tag{36}$$

and the Jacobian takes the form

$$G_{k,l}^{n,m} = \frac{\sqrt[4]{\alpha\beta}}{\sqrt{2\pi}} \int_{-\infty}^{\infty} H_n^{(0)}(\sqrt{\alpha}\omega_x) e^{j\omega_x x_k} d\omega_x \frac{1}{\sqrt{2\pi}} \int_{-\infty}^{\infty} H_m^{(0)}(\sqrt{\beta}\omega_y) e^{j\omega_y y_l} d\omega_y. \tag{37}$$

Using the notations

$$\omega_x x_k = \omega_x' x_k', \quad \omega_x' = \sqrt{\alpha}\omega_x, \quad x_k' = \frac{x_k}{\sqrt{\alpha}}, \quad \omega_y y_l = \omega_y' y_l', \quad \omega_y' = \sqrt{\beta}\omega_y, \quad y_l' = \frac{y_l}{\sqrt{\beta}}, \tag{38}$$

we can write

$$\begin{aligned}
G_{k,l}^{n,m} &= \frac{1}{\sqrt[4]{\alpha\beta}\sqrt{2\pi}} \int_{-\infty}^{\infty} H_n^{(0)}(\omega_x') e^{j\omega_x' x_k'} d\omega_x' \frac{1}{\sqrt{2\pi}} \int_{-\infty}^{\infty} H_m^{(0)}(\omega_y') e^{j\omega_y' y_l'} d\omega_y' \\
&= \frac{1}{\sqrt[4]{\alpha\beta}} \mathcal{F}^{-1}\{H_n^{(0)}(\omega_x')\} \mathcal{F}^{-1}\{H_m^{(0)}(\omega_y')\}
\end{aligned} \tag{39}$$

and applying the well-known Eq. (14), the Jacobian matrix can be written in its final form (without integration)

$$G_{k,l}^{n,m} = \frac{(j)^{n+m}}{\sqrt[4]{\alpha\beta}} H_n^{(0)}(x_k') H_m^{(0)}(y_l'). \tag{40}$$

The programming of the algorithm is quite simple after using the transformation of the indices  $i = n + (m-1)N$ ,  $s = k + (l-1)K$ . With these notations, the total number of the unknown expansion coefficient is  $I = N + (M-1)N = NM$  and that of the measured data is  $S = K + (L-1)K = KL$ . The theoretical data can be calculated as

$$u_s^{\text{theor}} = \sum_{i=1}^I B_i G_{s,i}, \tag{41}$$

and the general element of the deviation vector can be given in the following form

$$e_s = u_s^{\text{measured}} - \sum_{i=1}^I B_i G_{s,i} \quad (42)$$

with  $(i = 1, \dots, I, \quad s = 1, \dots, S)$ . After this, the inverse problem can be formulated in a straightforward manner.

#### 4. Inversion algorithms

If the measured data set contains Gaussian noise, the minimization of the  $L_2$  norm of the deviation vector is applied. This is the case of the least squares method when

$$E_2 = \sum_{k=1}^N e_k^2 \quad (43)$$

is minimized resulting in the well-known set of the normal equations

$$\mathbf{G}^T \mathbf{G} \vec{B} = \mathbf{G}^T \vec{u}^{\text{measured}}. \quad (44)$$

By solving these normal equations, we can give an estimate for the complex expansion coefficients, and both the real and imaginary parts of the LSQ estimated Fourier transform (LSQ-FT) can be calculated at any frequency by using

$$U^{\text{estimated}}(\omega) = \sum_{i=1}^M B_i^{\text{estimated}} \Psi_i(\omega). \quad (45)$$

As is well-known, the least squares method gives optimal results only when the data-noise follows Gaussian distribution. This distribution seldom occurs in practice so other norms of the deviation vector are introduced. In order to define a robust inversion algorithm, the minimization of the weighted norm

$$E_w = \sum_{k=1}^N w_k e_k^2. \quad (46)$$

with the so-called Cauchy weights

$$w_k = \frac{\sigma^2}{\sigma^2 + e_k^2}. \quad (47)$$

is suggested (here  $\sigma^2$  is an accordingly chosen positive number). Using this norm for the solution of inverse problems provides reliable results even if the input data sets contain outliers [9].

There is a problem with inversion procedures involving Cauchy weights, namely the scale parameter should be *a priori* given. This difficulty can easily be solved by using Steiner weights

[4]. In the framework of Steiner's most frequent value method, the scale parameter  $\sigma^2$  is derived from data residuals in an internal iteration loop. In the  $(j + 1)$ th step of this procedure Steiner's scale factor  $\varepsilon_{j+1}^2$  (called dihesion) can be calculated from  $\varepsilon_j^2$  as

$$\varepsilon_{j+1}^2 = 3 \frac{\sum_{k=1}^N \frac{e_k^2}{(\varepsilon_j^2 + e_k^2)^2}}{\sum_{s=1}^N \left( \frac{1}{\varepsilon_j^2 + e_s^2} \right)^2}, \quad (48)$$

where the  $\varepsilon_0$  starting value in the 0th step is given as

$$\varepsilon_0 \leq \frac{\sqrt{3}}{2} (e_{\max} - e_{\min}). \quad (49)$$

The stop criterion can be defined on an experimental basis (for example, a fixed number of iterations). After this the Cauchy weights are modified by using the (Steiner's) scale parameter (Cauchy-Steiner weights)

$$w_k = \frac{\varepsilon^2}{\varepsilon^2 + e_k^2}. \quad (50)$$

In the case of Cauchy-Steiner weights the misfit function given in Eq. (46) is nonquadratic (because  $e_k$  contains the unknown expansion coefficients) and so the inverse problem is nonlinear which can be solved again by applying the method of the iteratively reweighted least squares [2]. In the framework of this algorithm a 0th order solution  $\bar{B}^{(0)}$  is derived by using the (nonweighted) LSQ method and the weights are calculated as

$$w_k^{(0)} = \frac{\varepsilon^2}{\varepsilon^2 + (e_k^{(0)})^2}. \quad (51)$$

with  $e_k^{(0)} = u_k^{\text{measured}} - u_k^{(0)}$ , where  $u_k^{(0)} = \sum_{i=1}^M B_i^{(0)} G_{ki}$  and the expansion coefficients are given by the LSQ method. In the first iteration the misfit function

$$E_w^{(1)} = \sum_{k=1}^N w_k^{(0)} e_k^{(1)2} \quad (52)$$

is minimized resulting in the linear set of normal equations

$$\mathbf{G}^T \mathbf{W}^{(0)} \mathbf{G} \bar{B}^{(1)} = \mathbf{G}^T \mathbf{W}^{(0)} \bar{u}^{\text{measured}} \quad (53)$$

of the (linear) weighted least squares method where the  $\mathbf{W}^{(0)}$  weighting matrix (independent of  $\bar{B}^{(1)}$ ) is of the diagonal form  $W_{kk}^{(0)} = w_k^{(0)}$ . Solving Eq. (53) one finds

$$\bar{B}^{(1)} = (\mathbf{G}^T \mathbf{W}^{(0)} \mathbf{G})^{-1} \mathbf{G}^T \mathbf{W}^{(0)} \bar{u}^{\text{measured}} \quad (54)$$

$$u_k^{(1)} = \sum_{i=1}^M B_i^{(1)} G_{ki}, \quad e_k^{(1)} = u_k^{\text{measured}} - u_k^{(1)}, \quad w_k^{(1)} = \frac{\varepsilon^2}{\varepsilon^2 + (e_k^{(1)})^2}. \quad (55)$$

The minimization of the new misfit function

$$E_w^{(2)} = \sum_{k=1}^N w_k^{(1)} e_k^{(2)2} \quad (56)$$

gives  $\bar{B}^{(2)}$  which serves again for the calculation of  $w_k^{(2)}$ . This procedure is repeated giving the typical  $j$ th iteration step

$$\mathbf{G}^T \mathbf{W}^{(j-1)} \mathbf{G} \bar{B}^{(j)} = \mathbf{G}^T \mathbf{W}^{(j-1)} \bar{u}^{\text{measured}} \quad (57)$$

with the  $\mathbf{W}^{(j-1)}$  weighting matrix

$$W_{kk}^{(j-1)} = w_k^{(j-1)}. \quad (58)$$

(Here we note that each step of these iterations contain an internal loop for the determination of the Steiner's scale parameter.) This iteration is repeated until a proper stop criterion is met.

## 5. Numerical investigations

In order to test our inversion-based Fourier transform we generated a 2D data set in a rectangular test area of the size  $[-1,1]$  units in both  $x$  and  $y$  directions (**Figure 1**). In the homogeneous background (with the theoretical model value  $u = 0$ ), there is a rectangular anomaly (with  $u = 1.0$ ) in the center of size  $[-0.2, 0.2]$  units in both directions. The sampling intervals were  $dx = dy = 0.04$  units so the number of data is  $N = 51 \times 51$ . The 2D Fourier spectrum of the (noise-free) discrete data set was calculated by means of 2D DFT algorithm, **Figure 2** shows its absolute value (amplitude spectrum).

To test the outlier sensitivity of the Fourier transformation algorithms, the noisy data set I was generated, in which random noise of Cauchy distribution (with 0 location and 0.02 scale parameters) were added to the noise-free data set shown in **Figure 1**. Data set I containing outliers is shown in **Figure 3** and its DFT (amplitude) spectrum is shown in **Figure 4**. It can be seen that compared to **Figure 2** the DFT spectrum is highly distorted proving a sufficient noise sensitivity to the traditional DFT.

For quantitative characterization of the results we introduce the RMS distance between two data sets (for example noisy and noiseless) as

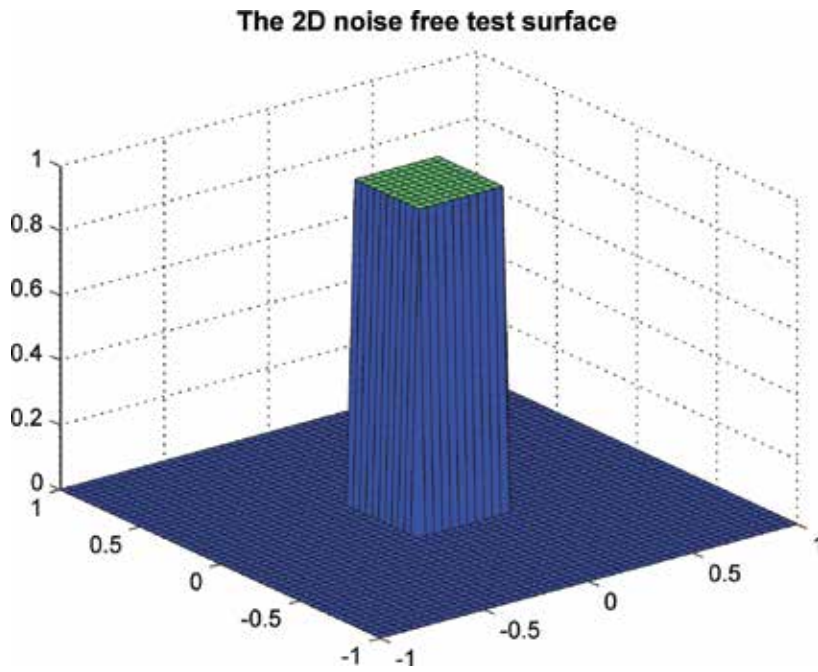


Figure 1. The noise-free test surface.

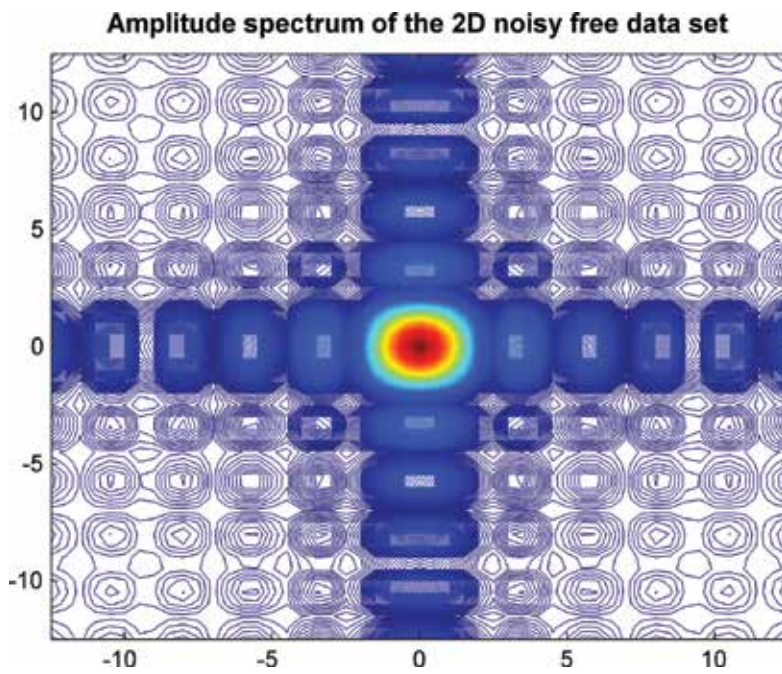


Figure 2. The 2D amplitude spectrum of the noise-free data set calculated by DFT.

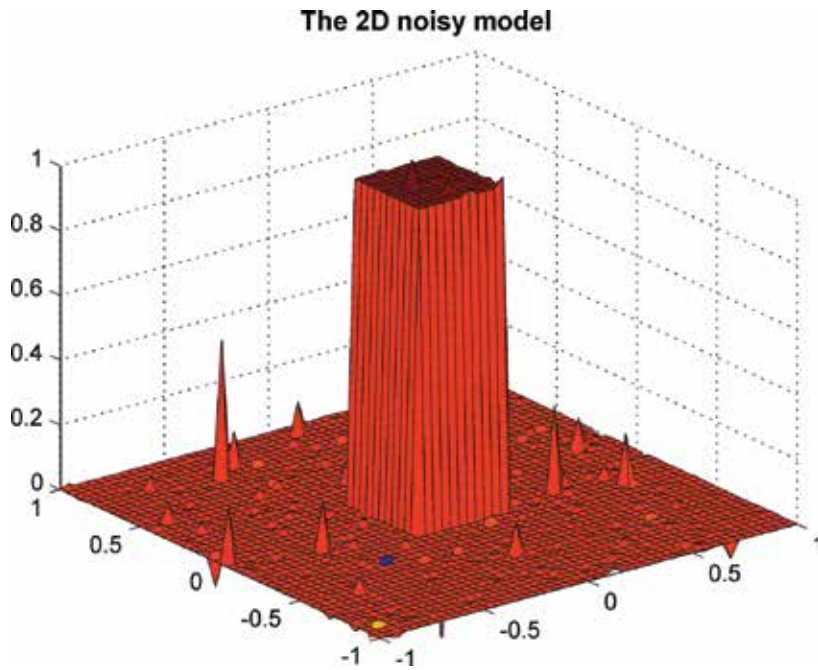


Figure 3. The noisy test surface.

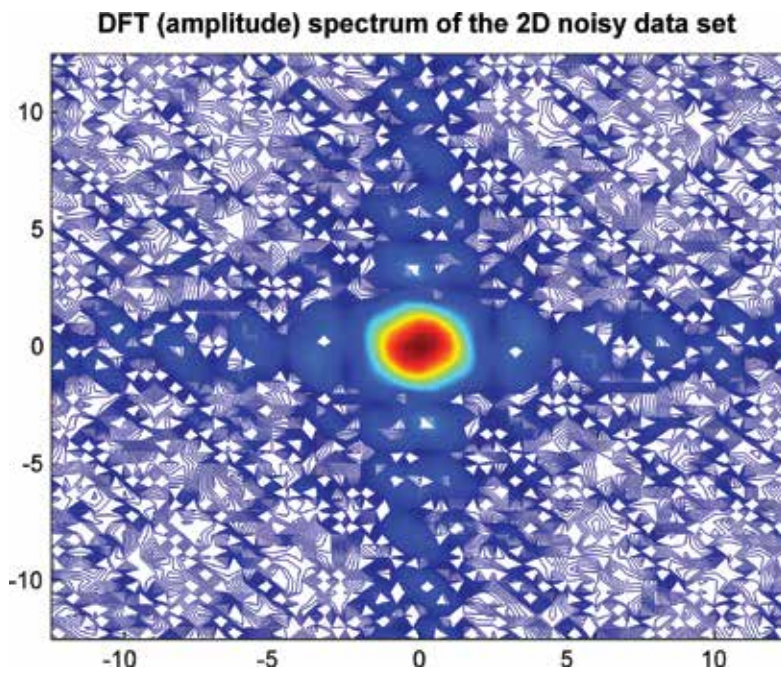


Figure 4. The 2D amplitude spectrum of the noisy data set calculated by DFT.

$$d = \sqrt{\frac{1}{N} \sum_{i=1}^{N_x} \sum_{j=1}^{N_y} [u^{\text{noiseless}}(x_i, y_j) - u^{\text{noisy}}(x_i, y_j)]^2} \quad (59)$$

in the space domain ( $N, N_x, N_y$  are relevant numbers of data point in the 2D test area) and the model distance

$$D = \left[ \frac{1}{M} \sum_{i=1}^{M_x} \sum_{j=1}^{M_y} \left( \text{Re}[U^{\text{noisy}}(\omega_{xi}, \omega_{yi})] - \text{Re}[U^{\text{noiseless}}(\omega_{xi}, \omega_{yi})] \right)^2 + \frac{1}{M} \sum_{i=1}^{M_x} \sum_{j=1}^{M_y} \left( \text{Im}[U^{\text{noisy}}(\omega_{xi}, \omega_{yi})] - \text{Im}[U^{\text{noiseless}}(\omega_{xi}, \omega_{yi})] \right)^2 \right]^{\frac{1}{2}} \quad (60)$$

in the spatial frequency domain ( $M, M_x, M_y$  are relevant numbers of data points). The distance between the noisy and noiseless data sets is  $d = 0.0984$ . Using Eq. (60) we find the model distance between the DFT spectra of the noisy (contaminated with Cauchy noise) and the noiseless data sets:  $D = 0.0713$ .

If we apply our inversion based (IRLS-FT) method for the same noisy data set we get an estimated spectrum shown in **Figure 5**. Compared to the DFT spectrum (**Figure 4**) this figure represents sufficient improvement characterized by the model distance between the noiseless and the noisy (given by IRLS-FT) spectra:  $D = 0.00128$ .

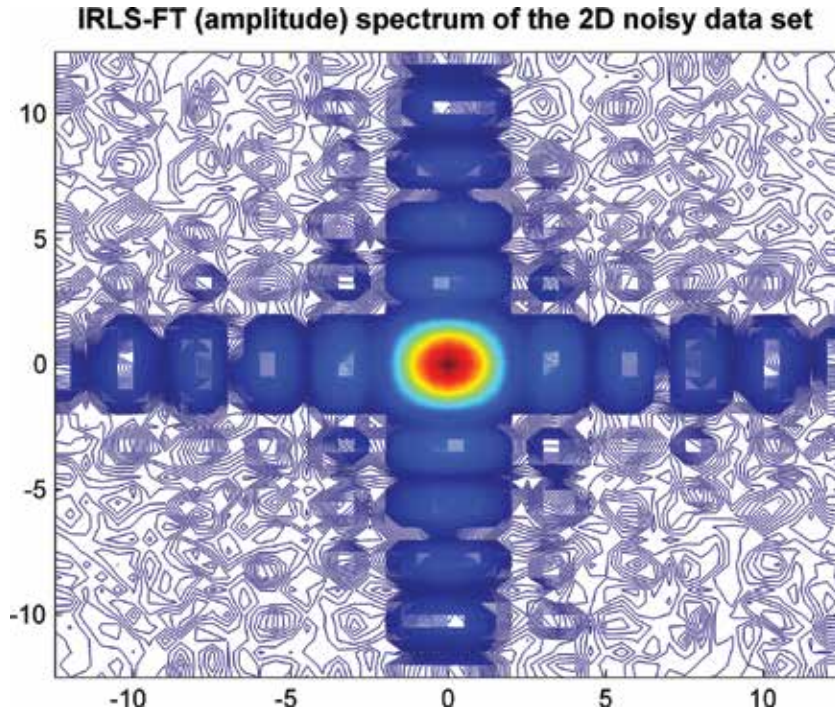


**Figure 5.** The 2D amplitude spectrum of the noisy data set calculated by IRLS-FT.

**The 2D noisy model computed by inverse IRLS-FT**

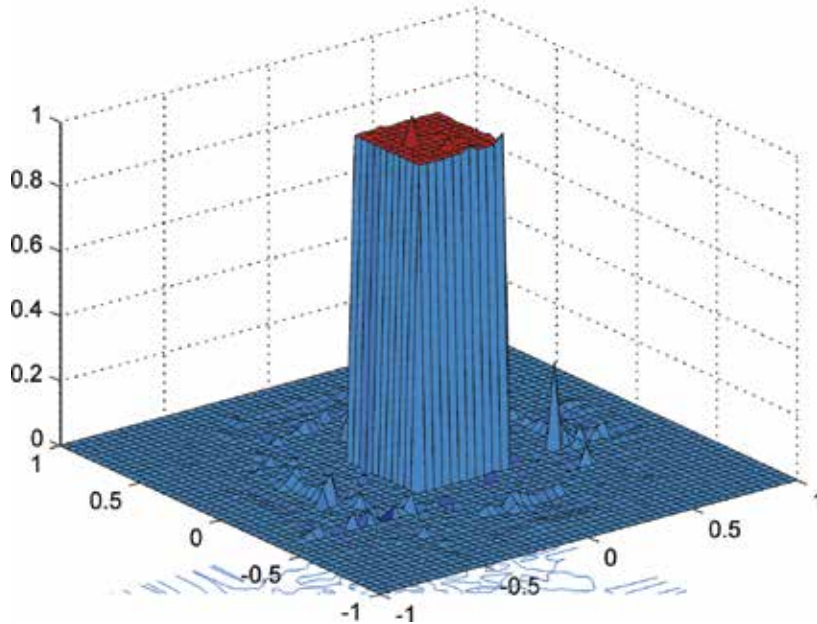


**Figure 6.** The 2D inverse FT of the estimated spectrum.

It is well known that DFT and inverse DFT sequentially retrieve the noisy input data set exactly. In our inversion-based robust Fourier transform method we solve an overdetermined set of equations. In this case, it is important to see the space domain data set given by the inverse Fourier transform of the IRLS-FT spectrum. This is the so-called calculated data introduced previously in defining the IRLS-FT algorithm

$$u_s^{\text{theor}} = \sum_{i=1}^I B_i G_{s,i}. \quad (61)$$

The result is shown in **Figure 6**. Compared to the noisy data set, the new inversion-based Fourier transform method has appreciable noise rejection capability. This is characterized by the data distance between the noiseless data set and the space domain data calculated by the IRLS-FT method:  $d = 0.0140$ . It can be seen, that compared to the common DFT our inversion-based 2D Fourier transformation method has around 6–7 times lower noise sensitivity both in space domain and frequency domain.

## 6. Application

The Fourier transformation is widely used in solving scientific or technical problems. Here we present a geophysical application in the field of processing geomagnetic data set. It is well known that the magnetic field has generally dipolar nature. It means that a magnetic body (i.e., wall fragments buried with soil in an archeo-geophysical measurement) usually produces

doubled anomaly (positive and negative) in the magnetic map depending on the geographical position of the measurement area. The only exceptions are the northern and the southern magnetic poles of the Earth and the magnetic equator. In order to simplify the interpretation of magnetic maps an elegant way was developed: the reduction to pole. This is a transformation resulting a magnetic data set that one would measure above the same magnetic body on the north (or southern) pole.

In order to apply our robust 2D IRLS-FT method a synthetic data set was generated. The measurement area was defined on the surface between (-100, 100) m in both of  $x$  and  $y$  direction. An anomaly of magnetization 100 nT (with  $D = 2.5^\circ$  declination and  $I = 63^\circ$  inclination) was assumed between the  $z$ -coordinates (20, 10) m. A rectangular measurement system was assumed with 5 m spacing in both directions (resulting in 1681 “measurement” data). The surface magnetic data calculated by means of the method of Kunaratnam [16] are shown in **Figure 7**. As it was mentioned, the interpretation of magnetic measurements is often supported by reducing the data to  $I = 90^\circ$  pole. This can be done in the spatial frequency domain by applying the formula

$$R(u, v) = T(u, v)S(u, v), \quad (62)$$

where  $T(u, v)$  is the 2D Fourier transform of the magnetic data set,  $S(u, v)$  is the frequency domain operator of the pole reduction. The reduced data set in space domain can be found by inverse Fourier transformation of the  $R(u, v)$  data set. This is shown in **Figure 8** using noise-free magnetic data and the traditional DFT in 2D Fourier transformation.

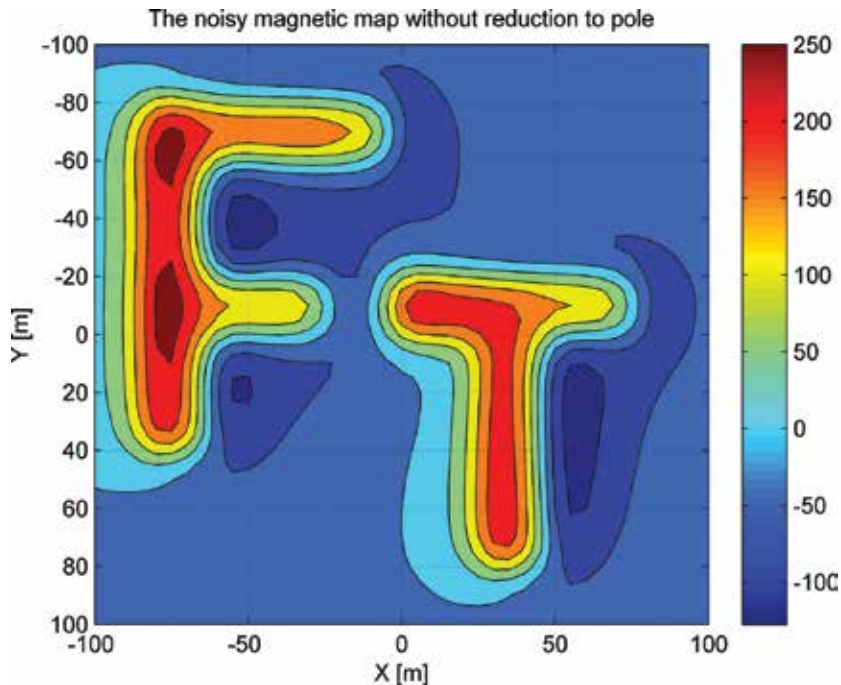


**Figure 7.** The noise-free synthetic data set.

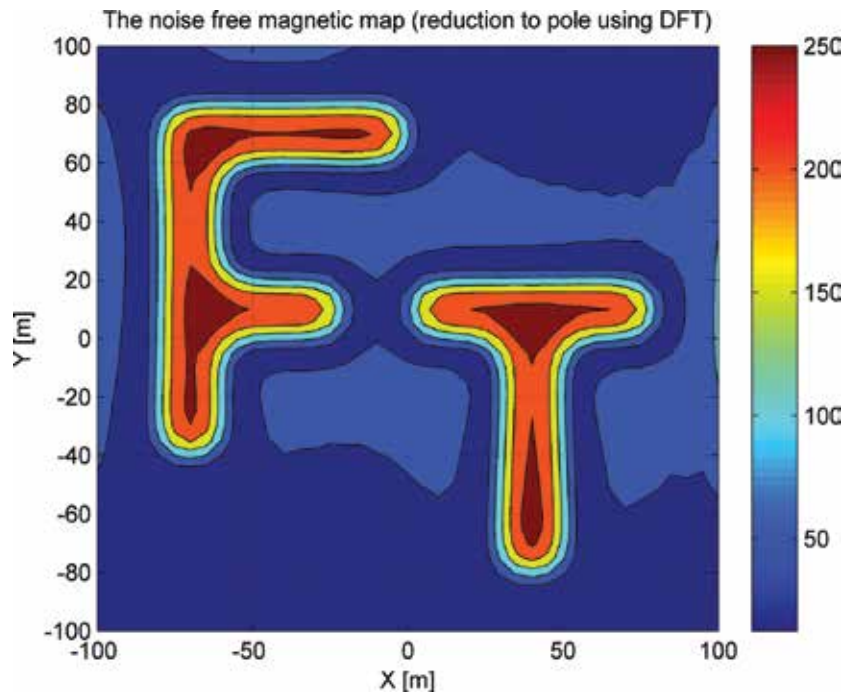


Figure 8. The data after reduction to pole (using DFT).

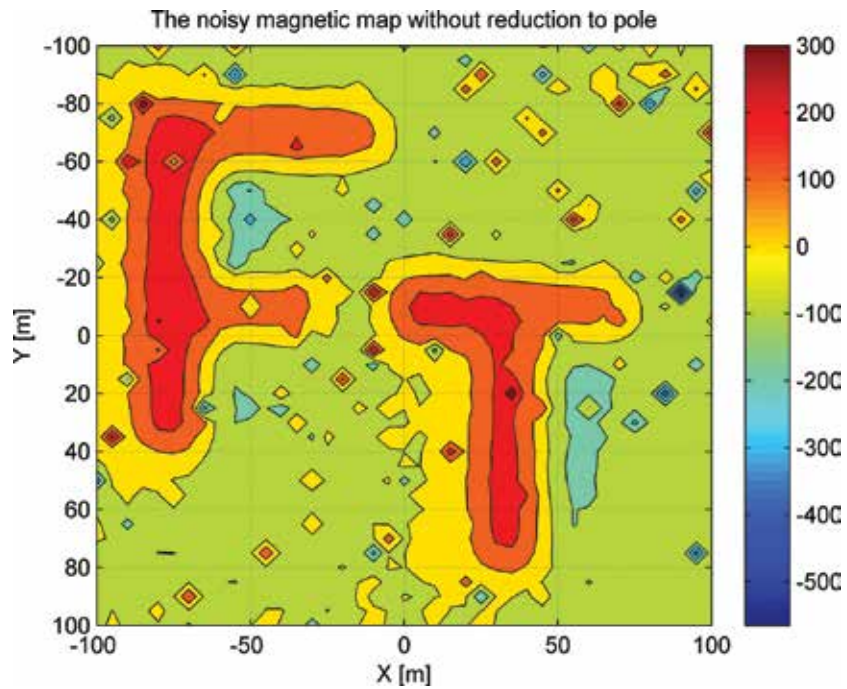


Figure 9. The noisy synthetic data set.

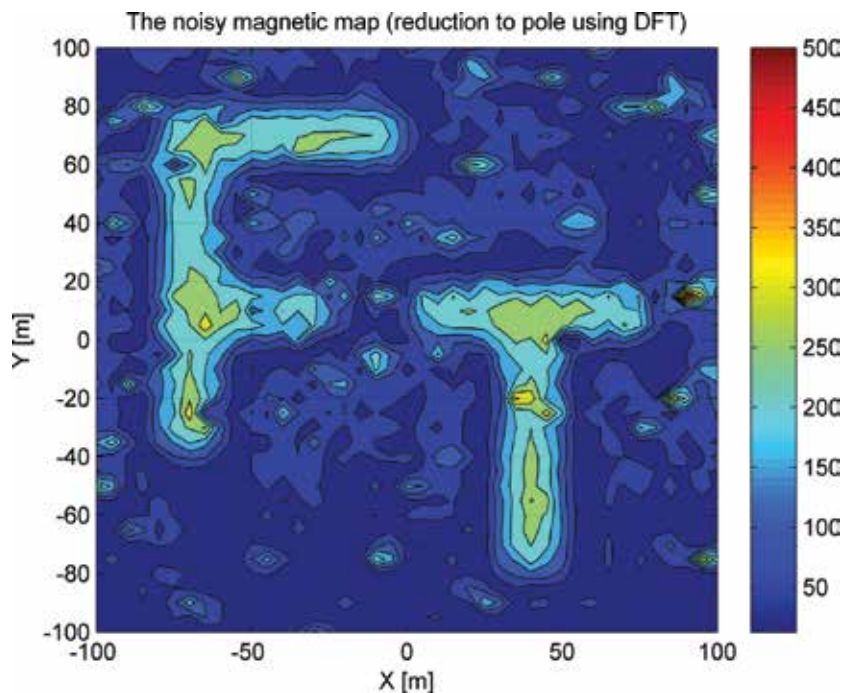


Figure 10. The pole reduced data set (using DFT).

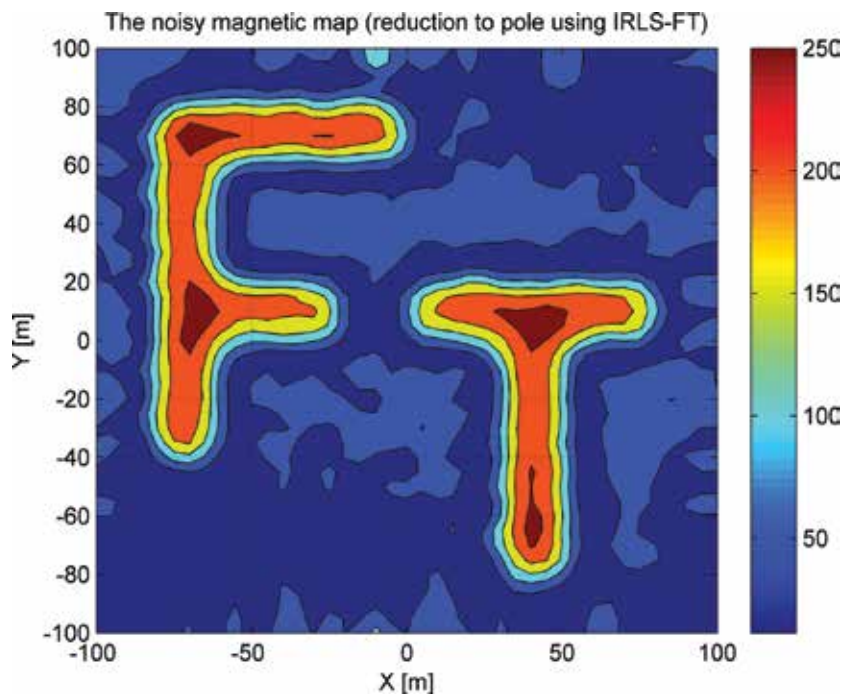


Figure 11. The pole reduced data set (using IRLS-FT).

In order to simulate noisy data set the magnetic data were contaminated with random noise following Cauchy distribution. The noisy data set and the result of pole reduction (using again the traditional DFT) is shown in **Figures 9** and **10**. It can be seen, that the pole reduction is highly distorted, which is caused by the low noise reduction capability of the 2D DFT algorithm proved in the previous chapter.

In contrary, the result of reduction to pole with the use of our new inversion-based 2D Fourier transformation algorithm is presented in **Figure 11**. In this case, we used Hermite function with 900 unknown expansion coefficients (considering the number of data, the inverse problem is sufficiently overdetermined). **Figure 11** demonstrates high noise reduction capacity (compared to **Figure 10**, where the traditional 2D DFT was used for Fourier transformation). It can be seen that the pole-reduced data set is close to that shown in **Figure 8** (noise-free data), and the limits of magnetization data are  $[0,250]$  in both cases. The result proves the successful applicability of our inversion-based 2D IRLS-FT algorithm.

## 7. Discussion

We presented a new algorithm for the 2D Fourier transform. Our purpose was to increase the noise rejection capacity of the Fourier transform. To do this, we applied the tools of inverse problem theory. In order to discretize the continuous function of the complex spectrum, series expansion was used. It was shown, that the Jacobian matrix of the inverse problem can be written as the inverse FT of the basis functions used in the discretization. Because of this reason Hermite functions were chosen as they are eigenfunctions of the Fourier transformation. This selection gave the possibility of very quick computation of the Jacobian even in 2D problems.

The unknown parameters (series expansion coefficients) are determined by solving an overdetermined inverse problem. For having a robust 2D FT method Cauchy-Steiner weights were applied in a robust iteratively reweighted least squares algorithm. In order to characterize the accuracy and the noise rejection capacity of the new Fourier Transform method we made numerical test using synthetic data sets containing random noise of Cauchy distribution and the characteristic distance between spectra calculated by means of noisy data as well as noise-free ones was calculated. It was shown that compared to the traditional DFT the characteristic distances were reduced by a factor of 6–7 so the noise reduction capability of the new inversion-based Fourier transform method (for abbreviation we used IRLS-FT) was clearly demonstrated.

Fourier transformation is widely used in science and techniques, so the new robust 2D Fourier transform method seems to be applicable on various fields of data processing dealing with noisy data sets, especially those containing outliers. As an example, we presented its application in reduction to pole, which is a frequently used operation in the interpretation of geomagnetic data sets. By our experience, the new method shows sufficient noise rejection capability compared to the traditional reduction to pole algorithm using the well-known DFT.

## 8. Conclusions

It was shown that considering the 2D Fourier transformation as an overdetermined inverse problem could result in a procedure with increased noise rejection capability. In order to find a robust method the iteratively reweighted least squares procedure using Cauchy-Steiner weights is proposed. In the framework of the new inversion-based FT method series expansion is used for discretization of the complex Fourier spectrum. The procedure is relatively quick, due to the appropriate choice of the set of basis function: the Hermite functions are involved, as they are eigenfunctions of the Fourier transformation.

## Acknowledgements

The research was supported by the National Research Development and Innovation Office (project no. K109441) and by the GINOP-2.3.2-15-2016-00010 "Development of enhanced engineering methods with the aim at utilization of subterranean energy resources" project in the framework of the Széchenyi 2020 Plan, funded by the European Union, co-financed by the European Structural and Investment Funds.

## Author details

Mihály Dobróka\*, Hajnalka Szegedi and Péter Vass

\*Address all correspondence to: dobroka@uni-miskolc.hu

University of Miskolc, Miskolc Egyetemváros, Hungary

## References

- [1] Dobróka M, Szegedi H, Vass P, Turai E. Fourier transformation as inverse problem—an improved algorithm. *Acta Geodaetica et Geophysica Hungarica*. 2012;**47**(2):185–196. DOI: 10.1556/AGeod.47.2012.2.7
- [2] Scales JA, Gersztenkorn A, Treitel S. Fast Lp solution of large, sparse, linear systems: application to seismic travel time tomography. *Journal of Computational Physics*. 1988;**75**:314–333.
- [3] Amundsen L. Comparison of the least-squares criterion and the Cauchy criterion in frequency-wavenumber inversion. *Geophysics*. 1991;**56**:2027–2038.
- [4] Steiner F. Most frequent value procedures (a short monograf). *Geophysical Transactions*. 1988;**34**:139–260.

- [5] Steiner F. Optimum methods in statistics. Budapest: Academic Press; 1997.
- [6] Dobróka M, Gyulai A, Ormos T, Csókás J, Dresen L. Joint inversion of seismic and geoelectric data recorded in an under-ground coal mine. *Geophysical Prospecting*. 1991;**39**:643–665.
- [7] Szűcs P, Civan F, Virág M. Applicability of the most frequent value method in ground-water modelling. *Hydrogeology Journal*. 2006;**14**:31–43. DOI: 10.1007/s10040-004-0426-1
- [8] Dobróka M, Szegedi H. On the generalization of seismic tomography algorithms. *American Journal of Computational Mathematics*. 2014;**4**(1):37–46. DOI: 10.4236/ajcm.2014.41004
- [9] Szegedi H, Dobróka M. On the use of Steiner's weights in inversion-based Fourier transformation: robustification of a previously published algorithm. *Acta Geophysica*. 2014;**49**(1):95–104. DOI: 10.1007/s40328-014-0041-0
- [10] Szabó NP. Shale volume estimation based on the factor analysis of well-logging data. *Acta Geophysica*. 2011;**59**(5):935–953. DOI: 10.2478/s11600-011-0034-0
- [11] Szabó NP. Hydraulic conductivity explored by factor analysis of borehole geophysical data. *Hydrogeology Journal*. 2015;**23**(5):869–882. DOI: 10.1007/s10040-015-1235-4
- [12] Turai E. Data processing method developments using TAU-transformation of time-domain IP data II. Interpretation results of field measured data. *Acta Geodaetica et Geophysica Hungarica*. 2011;**46**:391–400.
- [13] Duoandikoetxea J. *Fourier Analysis*. Graduate studies in Mathematics. Rhode Island: American Mathematical Society 29. Providence; 1995.
- [14] Vass P. Random noise reduction capability of the hermit polynomial based least squares Fourier transform method. *Acta Geodaetica et Geophysica Hungarica*. 2012;**47**:328–343.
- [15] Gröbner W, Hoffreiter N. *Integraltafel. Zweiter Teil. Bestimmte Integrale*. Wien und Innsbruck: Springer-Verlag; 1958.
- [16] Kunaratnam K. Simplified expressions for the magnetic anomalies due to vertical rectangular prisms. *Geophysical Prospecting*. 1981;**29**:883–890.



---

# Single Bin Sliding Discrete Fourier Transform

---

Carlos Martin Orallo and Ignacio Carugati

Additional information is available at the end of the chapter

<http://dx.doi.org/10.5772/66337>

---

## Abstract

The conventional method for spectrum analysis is the discrete Fourier transform (DFT), usually implemented using a fast Fourier transform (FFT) algorithm. However, certain applications require an online spectrum analysis only on a subset of  $M$  frequencies of an  $N$ -point DFT ( $M < N$ ). In such cases, the use of single-bin sliding DFT (Sb-SDFT) is preferred over the direct application of FFT. The purpose of this chapter is to provide a concise overview of the Sb-SDFT algorithms, analyze their performance, and highlight advantages and limitations. Finally, a technique to mitigate the spectral leakage effect, which arises when using the Sb-SDFT in nonstationary conditions, is presented.

**Keywords:** discrete Fourier transform, spectral leakage, digital signal processing, Cramér-Rao lower bound, total vector error

---

## 1. Introduction

The estimation of frequency, amplitude and phase of single-frequency and multifrequency signals has applications in many fields of engineering. In general, estimation methods are based on Fourier analysis or parametric modeling. The advantage of Fourier-based methods is their computational efficiency, compared with the mathematical complexity of the parameters-based algorithms, which demand a high amount of computational resources. The standard method for Fourier analysis in digital signal processing is the discrete Fourier transform (DFT). For some real-time applications, the direct application of the conventional DFT may result in an excessive computational cost. However, certain applications require an online spectrum analysis only over a subset of  $M$  frequencies of an  $N$ -point DFT ( $M < N$ ). For this scenario, the common practice is to utilize a single-bin sliding DFT (Sb-SDFT) technique. These recursive algorithms efficiently calculate a unique spectral component of an  $N$ -point DFT. Nevertheless, the direct application of DFT-based methods for spectral analysis may lead to inaccuracies due to the spectral leakage phenomenon. These unwanted effects are related to the frequency variation and improperly selected sampling time window. This problem can be

solved using an adaptive coherent sampling mechanism. One of these mechanisms is known as variable sampling period technique (VSPT) and is characterized for the dynamic adjustment of the sampling period to exactly  $N$  times the fundamental frequency, thereby avoiding the above-mentioned problems.

The chapter is organized as follows: Section 2 presents a brief review of Sb-SDFT. Section 3 evaluates and compares the four selected Sb-SDFT algorithms in diverse operational conditions, identifying the similarities between them. In order to mitigate the inaccuracies resulting from the spectral leakage effect, a scheme for coherent sampling based on VSPT is introduced in Section 4. Altogether a unified model is also presented to generalize this scheme to all Sb-SDFT along with simulation results. Finally, the conclusions of this chapter are drawn in Section 5.

## 2. Single-bin sliding discrete Fourier transform

The discrete Fourier transform (DFT) is a numerical approximation of the theoretical Fourier transform (FT) of a continuous and infinite duration signal. It represents the most common tool for engineers to extract the frequency content of a finite and discrete signal sequence, obtained from the periodic sampling of a continuous wave form in time domain.

Let us consider a continuous time signal  $x(t)$  that is sampled at the rate  $f_s = N \times f_o$  (where  $f_o$  is the fundamental frequency of  $x(t)$ ) to produce the time sequence  $x[n]$ . Then the DFT of the sequence  $x[n]$  is defined as:

$$X(k) = \sum_{n=0}^{N-1} x[n] W_N^{-k n} \quad (1)$$

where  $X(k)$  is the DFT output coefficient,  $W_N = e^{j2\pi/N}$  is the complex twiddle factor,  $N$  is the sequence length,  $k$  is the frequency domain index ( $0 \leq k \leq N-1$ ), and  $n$  is the time domain index [1].

If Eq. (1) is not properly designed and implemented, the DFT calculation in real-time might represent a considerable bottleneck when developing a DFT-based estimation algorithm, in terms of both measurement reporting latencies and achievable reporting rates. In this respect, in order to improve both latencies and throughput, several efficient techniques to compute the DFT spectrum have been proposed in literature, which can be classified as nonrecursive and recursive algorithms. Among the nonrecursive class, the fast Fourier transform (FFT) algorithm is extensively used for harmonic analysis over an extended portion of the spectrum. When, on the other hand, only a subset of the overall DFT spectrum is necessary to accomplish the desired estimate, the so-called single-bin sliding DFT (Sb-SDFT) turns out to be very effective.

The DFT can also be computed by recursive algorithms which are characterized by a minor number of operations to calculate a single DFT bin. Regardless of this advantage with respect to the class of nonrecursive algorithms, the performances of the two categories usually are not

the same. Especially, most of the algorithms in the recursive category suffers of errors due to either the approximations made to perform the recursive update or the accumulation of the quantization errors related to a finite word-length precision [2, 3].

In what follows, four of the most efficient techniques to compute a portion of the DFT spectrum, namely the sliding discrete Fourier transform (SDFT), the sliding Goertzel transform (SGT), the Douglas and Soh algorithm (D&S), and the modulated sliding discrete Fourier transform (mSDFT) will be presented and described.

### 2.1. Sliding discrete Fourier transform

A very effective Sb-SDFT method for sample-by-sample DFT bin computation is the so-called sliding discrete Fourier transform (SDFT) technique [4]. Starting from Eq. (1), the DFT can be potentially updated every time-step  $n$ , based on the most recent set of samples within a sliding window  $\{x[n-N + 1], x[n-N + 2], \dots, x[n]\}$ . The time window is advanced one sample at a time, and a new  $N$ -point DFT is calculated. **Figure 1(a)** illustrates the time domain indexing within the sliding window by showing the input samples used to compute  $k$ -bin of an  $N$ -points DFT when  $n = n_0$ . The principle used for SDFT is known as the DFT shifting theorem, or the circular shift property [1].

Based on this property, the SDFT can be recursively implemented to calculate Eq. (1) for a desired  $k$ -bin, as:

$$X_k [n] = W_N^k X_k [n-1] - x[n-N] + x[n] \tag{2}$$

where  $X_k[n]$  is calculated by phase shifting the sum of the previous  $X_k[n-1]$  with the difference between the current and delayed input sample,  $x[n]$  and  $x[n-N]$ , respectively [4, 5]. The complex output of the SDFT could be rewritten as:

$$X_k [n] = X_{rk} [n] + jX_{ik} [n] \tag{3}$$

where  $X_{rk} [n]$  and  $X_{ik} [n]$  are real and imaginary components of the DFT output coefficient, respectively. The SDFT provides an accurate estimation for the  $k$ th component as its amplitude ( $A_k [n]$ ) and phase ( $\varphi_k [n]$ ) can be determined by computing the modulus and the argument of the complex result  $X_k [n]$ , as stated by

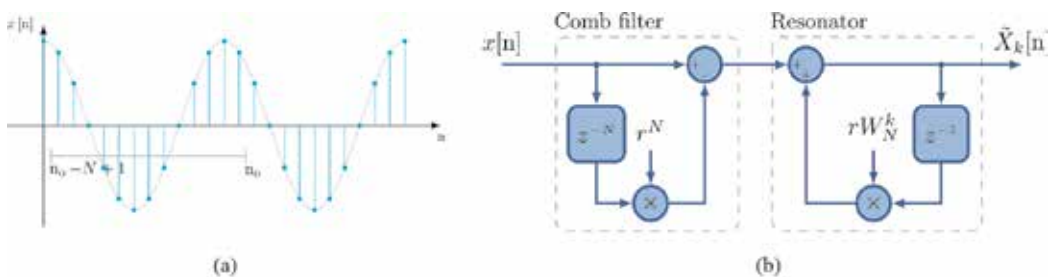


**Figure 1.** (a) Samples used to compute  $X_k[n]$  within a sliding window, when  $n = n_0$ . (b) Guaranteed-stable SDFT implementation as IIR filter as given by (5).

$$A_k[n] = \frac{2}{N} \text{abs} (X_k [n]) \quad (4a)$$

$$\varphi_k[n] = \text{arg} (X_k [n]) \quad (4b)$$

SDFT is computationally efficient, as it only requires one (complex) multiplication and two additions per time instant. Nevertheless, the implementation of Eq. (2) as an infinite impulse response (IIR) filter in a system with finite word-length precision brings about a rounding error in the implementation of the  $W_N^k$  coefficient, which may turn the algorithm unstable and/or increment the estimation error. The first one is a direct consequence of wrong cancellations between singularities and by poles displacement outside the unit circle [2, 3]. Commonly, a damping factor ( $r$ , with  $0 < r < 1$ ) is used to ensure that all singularities are placed inside the unit circle, hence instability is no longer an issue. Then, the intrinsically stable version of the SDFT is

$$\tilde{X}_k [n] = rW_N^k \tilde{X}_k [n-1] - r^N x[n-N] + x[n] \quad (5)$$

where  $\tilde{X}_k [n]$  is the estimated DFT output coefficient. While Eq. (5) is numerically stable, it no longer computes the exact value of  $X(k)$  in Eq. (1), since a small error is induced by the damping factor. The  $z$  domain transfer function for the estimated  $k$ th bin of the SDFT is

$$H_{\text{SDFT}}(z) = \frac{1-r^N z^{-N}}{1-rW_N^k z^{-1}} \quad (6)$$

The stable SDFT algorithm given by Eq. (5) leads to the filter structure shown in **Figure 1(b)**. This structure is basically an IIR filter that comprises a comb filter followed by a complex resonator. The comb filter makes the transient response  $N-1$  samples in length; therefore, the output will reach steady state when the stored waveform equals the input signal.

## 2.2. Sliding Goertzel transform

The number of multiplications required in the SDFT can be reduced by creating a new pole/zero pair in its  $H_{\text{SDFT}}(z)$  system function. This is achieved by multiplying the numerator and denominator of  $H_{\text{SDFT}}(z)$  in Eq. (6) by the factor  $(1-rW_N^{-k} z^{-1})$  yielding:

$$H_{\text{SGT}}(z) = \frac{(1-rW_N^k z^{-1})(1-r^N z^{-N})}{1-2r \cos(2\pi k/N)z^{-1} + r^2 z^{-2}} \quad (7)$$

The transfer function represented by Eq. (7) is commonly known as the sliding Goertzel transform (SGT). Because the poles are placed on the  $z$  domain unit circle, the SGT implementation is also potentially unstable. Once more a damping factor  $r$  can be used in Eq. (7), to move the singularities inside the unit circle and to ensure the system stability.

This method can be implemented by the following pair of finite difference equations:

$$v[n] = C_1 v[n-1] - C_2 v[n-2] + x[n] - r^N x[n-N] \tag{8a}$$

$$\tilde{X}_k[n] = v[n] - rW_N^{-k} v[n-1] \tag{8b}$$

where  $C_1 = 2r \cos(2\pi k/N)$  and  $C_2 = r^2$ , with  $0 < r < 1$ . The SGT is implemented as an IIR filter that consists of a comb filter followed by the standard Goertzel filter, as depicted in **Figure 2(a)**. The resulting system only has real coefficients so its computational complexity is decreased in relation to that of the SDFT [6, 7].

### 2.3. Douglas and Soh algorithm

The implementation of a SDFT or SGT requires a damping factor to guarantee the algorithm stability. The trade-off for the system stability is that the calculated value is no longer exactly equal to the  $k$ th-bin of an  $N$ -point DFT in Eq. (1). In Ref. [8], a technique that significantly reduces this error, without compromising the stability, is developed. This method is a periodically time-varying system designed to generate an  $\tilde{X}_k[n]$  output that is mathematically equal to  $X(k)$  in Eq. (1) at every  $N$ th time instant.

This technique is implemented by the following pair of finite difference equations:

$$\tilde{X}_k[n] = \begin{cases} rW_N^k \tilde{X}_k[n-1] - rx[n-N] + x[n], & (n \bmod N) = 0 \quad \text{(a)} \\ W_N^k \tilde{X}_k[n-1] - rx[n-N] + x[n], & \text{else} \quad \text{(b)} \end{cases} \tag{9}$$

The algorithm described by Eq. (9) will be referred to as the Douglas and Soh algorithm (D&S). The filter implementation of Eq. (9), shown in **Figure 2(b)**, requires two multiplications and two additions as well as the control logics to determine when  $n \bmod N = 0$ . In the figure, the

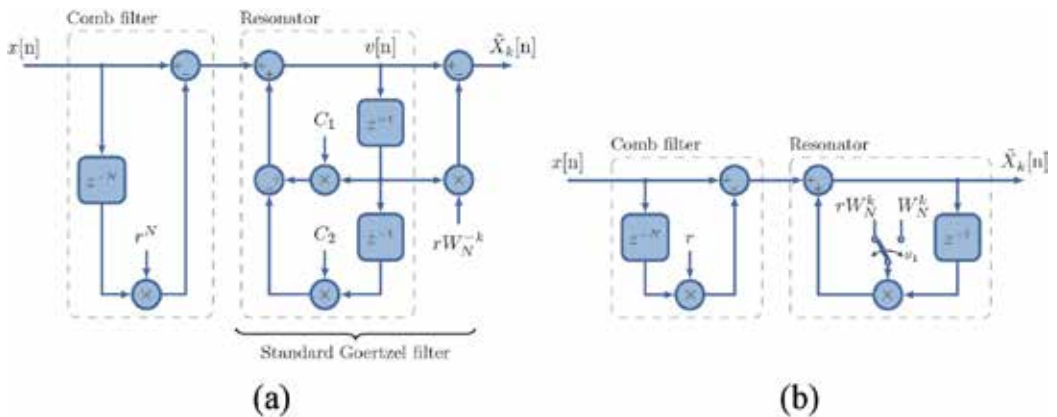


**Figure 2.** (a) Guaranteed-stable SGT implementation as IIR filter as given by (8). (b) Guaranteed-stable D&S algorithm implemented as IIR filter as given by (9).

change between Eqs. (9a) and (9b) is performed by switch  $S_1$ . Therefore, the switching period of  $S_1$  in **Figure 2(b)** is equal to  $N \times T_s$ , where  $T_s$  is the sampling period, and its duty cycle is equal to one sample. It is worth mentioning that the effect of the nonlinear operation of D&S algorithm in the dynamic response is negligible as it only changes its structure every  $N$  samples.

**2.4. Modulated sliding discrete Fourier transform**

There is an alternative way of avoiding the reduction in accuracy generated by the damping factor, without compromising stability. SDFT implementation in Eq. (2) is marginally stable, however, for the particular case of  $k = 0$  (DC component estimation). It takes the following form:

$$X_0[n] = X_0[n-1] - x[n-N] + x[n] \tag{10}$$

The absence of the  $W_N^k$  coefficient, which typically leads to stability issues when it is represented with finite precision, allows to implement the recursive expression without the damping factor  $r$ . Therefore, the recurrence in Eq. (10) is unconditionally stable and does not accumulate errors. The modulated sliding discrete Fourier transform (mSDFT) algorithm uses the Fourier modulation property to effectively shift the DFT bin of interest to the position  $k = 0$  and then use Eq. (10) for computing that DFT bin output. This is accomplished by the multiplication of the input signal  $x[n]$  by the modulation sequence  $W_N^{-kn}$ . This approach allows to exclude the complex twiddle factor from the resonator and avoids accumulated errors and potential instabilities [9]. The recursive realization of the mSDFT is:

$$X_k^0[n] = X_k^0[n-1] - x[n-N]W_N^{-k(n-N)} + x[n]W_N^{-kn} \tag{11a}$$

$$X_k[n] = W_N^{kn} X_k^0[n] \tag{11b}$$

where  $X_k^0[n]$  is a complex constant related to the phase of the complex twiddle factor, since the modulation moves the desired  $k$ th-bin to  $k = 0$  (0 Hz). The relation between the desired  $X_k[n]$  and the computed  $X_k^0[n]$  is given by Eq. (11b). It is worth noticing that if the application only requires DFT magnitude estimation, the complex multiplication in Eq. (11b) is unnecessary because  $|X_k^0[n]|$  is equal to  $|X(k)|$ . The filter structure of the mSDFT algorithm in Eq. (11) is depicted in **Figure 3(a)**. In contrast of traditional recursive DFT algorithms, the mSDFT method

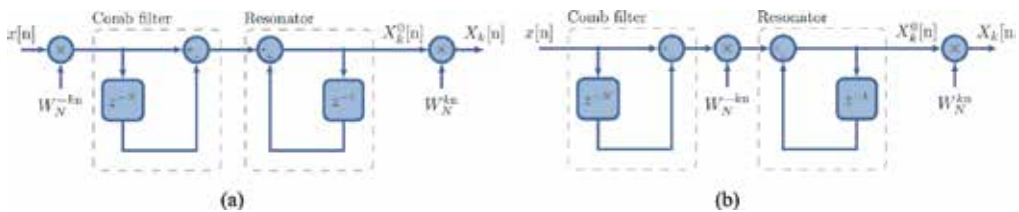


**Figure 3.** (a) Guaranteed-stable mSDFT implementation as IIR filter as given by (11). (b) Guaranteed-stable mSDFT implementation as IIR filter as given by (12).

is unconditionally stable and does not accumulate errors because its singularities are exactly placed on the unit circle, regardless of the finite precision used. These advantages are possible due to the removal of the complex twiddle factor from the resonator loop.

If multiple DFT frequency bins are to be computed, the mSDFT in Eq. (11) requires a comb filter for each frequency bin. On the other hand, given the periodicity of  $W_N^{-kn}$ , as shown in Ref. [9], Eq. (11) can be rewritten as

$$X_k^0 [n] = X_k^0 [n-1] + W_N^{-kn}(-x[n-N] + x[n]) \tag{12a}$$

$$X_k [n] = W_N^{kn} X_k^0 [n] \tag{12b}$$

Whenever multiple DFT frequency bins are to be computed, Eq. (12) becomes a more efficient approach as only one comb filter is needed (**Figure 3(b)**).

### 3. Performance comparison

This section discusses the key features of each of the Sb-SDFT that were presented in Section 2. The aim of this analysis is to find underlying similarities and differences between these methods. To this end, a study on statistical efficiency and accuracy is presented in the following subsections. Finally, the section ends with a discussion over the limitations and inaccuracies of the Sb-SDFT inherited by every DFT-based method.

#### 3.1. Statistical efficiency

It is common knowledge that the statistical efficiency and noise performance of estimators is determined by comparison with the Cramer-Rao lower bound (CRLB). The CRLB deals with the estimation of the quantities of interest from a given finite set of measurements that are noise corrupted. It assumes that the parameters are unknown but deterministic, and provides a lower bound on the variance of any unbiased estimation. The CRLB is useful because it provides a way to compare the performance of unbiased estimators. Furthermore, if the performance of a given estimator is equal to the CRLB, the estimator is a minimum variance unbiased (MVU) estimator [10].

Computer simulations have been performed to evaluate the performance of the SDFT, the SGT, the mSDFT and D&S algorithm for a single real sinusoid polluted with white Gaussian noise:

$$x[n] = A \cos(\omega n + \phi) + \text{wgn}[n] \tag{13}$$

where  $A$  and  $\phi$  are the amplitude and initial phase, respectively,  $n$  is the time domain index,  $\omega$  denotes the normalized angular frequency ( $\omega = 2\pi f_o/f_s$ ) and  $\text{wgn}[n]$  is a zero-mean white Gaussian noise of variance  $\sigma_n^2$ . For this case the CRLB for amplitude estimation is approximated by Kay [10]:

$$\text{CRLB}_A = \frac{2\sigma_n^2}{N} \tag{14}$$

Parameters were assigned to  $A = 1$ ,  $f_o = 50\text{Hz}$ ,  $f_s = 6.4 \text{ KHz}$   $N = 128$  and  $\phi$  is a constant uniformly distributed between  $[0, 2\pi)$ . The signal-to-noise ratio (SNR) is equal to  $A^2/(2\sigma_n^2)$ , whereas different SNR levels were obtained by properly scaling the noise variance  $\sigma_n^2$ . All simulation results provided are the averages of 1000 independent runs.

**Figure 4(a)** and **(b)** shows the variance in the estimate of  $A$  ( $\sigma_{\hat{A}}$ ) versus SNR for two different damping factors. In **Figure 4(a)**, the damping factor was fixed at  $r = 0.999$  for SDFT, SGT and D&S algorithm. In this figure, for SNR levels below  $-10 \text{ dB}$  can be observed that the  $\sigma_{\hat{A}}$  values are beneath the CRLB limit. Therefore, beyond this threshold level, the estimations made by the Sb-SDFT techniques cease to be consistent with those of an unbiased estimator. From this threshold level and up to  $15 \text{ dB}$ , the Sb-SDFT algorithms are efficient MVU estimators, because their  $\sigma_{\hat{A}}$  values reach the CRLB. For higher levels of SNR, the  $\sigma_{\hat{A}}$  for SDFT and SGT remains

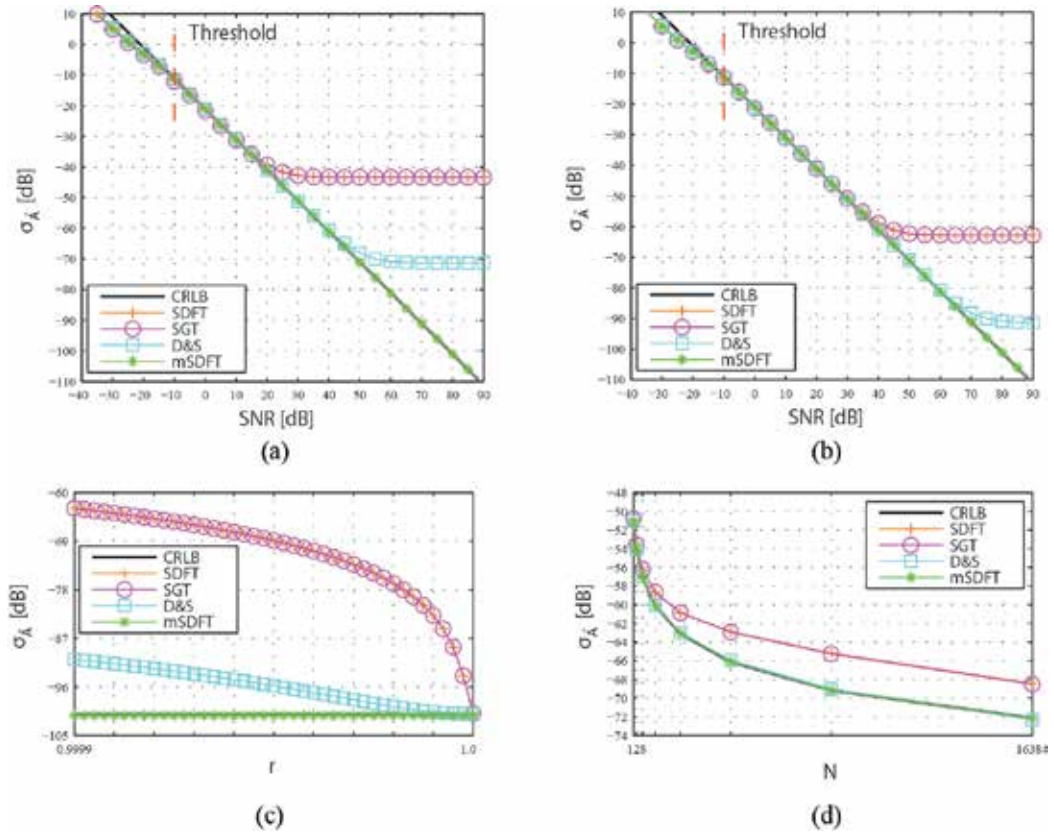


**Figure 4.** (a) Variance of  $\hat{A}$  versus SNR levels for the analyzed estimators with  $N = 128$  and  $r = 0.999$ . (b) Variance of  $\hat{A}$  versus SNR levels for the analyzed estimators with  $N = 128$  and  $r = 0.9999$ . (c) Variance of  $\hat{A}$  versus  $r$  for the four estimators at SNR=80 dB. (d) Variance of  $\hat{A}$  versus  $N$  for the four estimators, with  $r = 0.9999$  and SNR=30 dB.

above the CRLB and asymptotically approximate the  $-43.5$  dB bound. This is mainly due to the fact that the inaccuracy caused by the damping factor in Eqs. (5) and (8) is more relevant than the consequence of SNR level. The D&S algorithm exhibits the same behavior, but beginning at SNR = 60 dB and with  $\sigma_{\hat{A}}$  asymptotically approaching the  $-91$  dB bound for higher levels.

When compared to the performances of the SDFT and the SGT, the D&S algorithm behaves as an MVU estimator for a wider range of SNR, at the cost of a slightly increased computational complexity and a nonlinear functioning. For the range of SNR levels shown in **Figure 4(a)** beyond the threshold, the variance in  $\hat{A}$  computed by the mSDFT remains on CRLB curve, so its performance corresponds to an MVU estimator.

This test was repeated for  $r = 0.9999$ , and the results are shown in **Figure 4(b)**. It is seen that the performances of the SDFT, SGT and D&S algorithm are better than exhibited in the previous case. This improvement is reflected through an increase in the range of SNR values for which the estimations correspond to an MVU estimator. The results obtained for mSDFT are consistent with those obtained previously, because this estimator does not require a damping factor to ensure stability.

The effect of the damping factor on the  $\sigma_{\hat{A}}$  is shown in **Figure 4(c)**. The simulation is performed for SNR = 80 dB because at this level, SDFT, SGT and D&S algorithms do not lie on CRLB curve and have converged to their final values listed in **Figure 4(b)**. For this scenario, the  $\sigma_{\hat{A}}$  of the mSDFT is constant and equal to the CRLB, because it does not require a damping factor to achieve stability. Instead, for  $r \rightarrow 1$  and SNR beyond threshold level, the  $\sigma_{\hat{A}}$  for SDFT, SGT and D&S algorithm approximates the CRLB as it is reflected by **Figure 4(c)**. From the analysis of this figure, it is possible to conclude that for the ideal situation ( $r = 1$ ) and SNR levels beyond the threshold, all reviewed algorithms reach the CRLB and therefore their statistical efficiency is identical.

Finally, the  $\sigma_{\hat{A}}$  versus  $N$  at SNR = 30 dB are illustrated in **Figure 4(d)**. As expected,  $N$  increase, that is, the length of the sliding window reduces the variance of  $\hat{A}$  in the four methods. This is mainly because the estimations are computed in a larger sliding time window, that is, more samples are used for the estimation.

### 3.2. Accuracy analysis

In this section, the accuracy of the Sb-SDFT methods on the estimation of a single-frequency signal, both in steady-state and dynamics conditions, is analyzed through simulations. The adopted accuracy index is the so-called total vector error (TVE) that combines the effect of magnitude, angle and time synchronization errors on the desired component estimation accuracy. The TVE is defined in the Standard IEEE C37.118.1-2011 [11] as

$$\text{TVE} = 100 \times \sqrt{\frac{(\hat{X}_r[n] - X_r[n])^2 + (\hat{X}_i[n] - X_i[n])^2}{X_r[n]^2 + X_i[n]^2}} \quad (15)$$

where  $\hat{X}_r[n]$  and  $\hat{X}_i[n]$  are the sequences of estimations given by the Sb-SDFT method under test,  $X_r[n]$  and  $X_i[n]$  are the sequences of theoretical values of the input signal at the instants of

time ( $n$ ), and the subscripts  $r$  and  $i$  identify the real and imaginary parts of the desired component, respectively. The TVE is a real number that expresses the Euclidean distance between the true frequency domain complex bin and estimated one.

3.2.1. Steady-state condition

At first, the analysis is assessed in steady-state conditions assuming an input signal equal to Eq. (13). Parameters were assigned to  $A = 1$ ,  $f_o = 50\text{Hz}$ ,  $f_s = 6.4 \text{ KHz}$   $N = 128$  and  $\phi = 0$  rad and the damping factor is set to  $r = 0.9999$ . The curves plotted in **Figure 5(a–d)** show the estimated amplitude of the test signal for all Sb-SDFT algorithms in steady state, where the reference value is displayed with a black solid line. **Figure 5(e)** shows the TVE values as a function of time. SDFT and SGT have the same steady-state TVE values; this error has a mean value with an overlaid ripple that is a direct consequence of the use of a damping factor in Eqs. (5) and (8). For both algorithms, the maximum TVE value is 0.7335%. The D&S algorithm significantly reduces the TVE and maintains the same damping factor than the two previous cases, resulting in improved system performance, with a maximum TVE value of 0.01%. In **Figure 5(c)**, it is shown that when  $(n \bmod N) = 0$ , the estimation is accurate, which is consistent with the period of the fundamental component of the test signal. On the other hand, mSDFT provides precise estimation with a 0% TVE, since it does not require a damping factor to ensure stability.

3.2.2. Dynamic condition

The accuracy under dynamic condition of the SDFT, the SGT, the mSDFT and D&S algorithm are evaluated through multiple simulations under the effect of various transient disturbances. The comparison is performed by means of the following test signal:

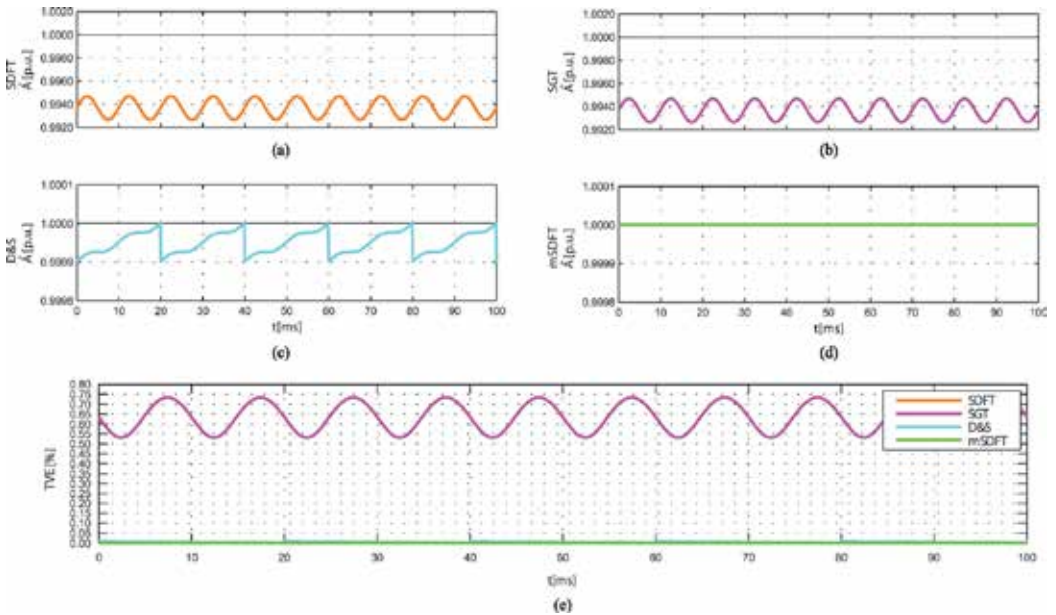


**Figure 5.** (a)–(d) Amplitude estimation of the test signal (13) in steady-state condition using the selected Sb-SDFT algorithms with  $N = 128$ ,  $r = 0.9999$  and  $f_s = 6.4 \text{ kHz}$ . (e) TVE exhibited by the Sb-SDFT algorithms in steady-state.

$$x[n] = A_o \{1 + \delta_s u[n-n_o] + \delta_r(n-n_o)u[n-n_o] + \delta_{am} \cos[\omega_{am}(n-n_o)]u[n-n_o]\} \cos(\omega n + \omega_g n u[n-n_o] + \phi) \quad (16)$$

where  $A_o$  is the nominal amplitude,  $\delta_s$  is the amplitude step depth factor,  $\delta_r$  is the amplitude ramp slope factor,  $\delta_{am}$  is the modulation depth factor,  $\omega_{am}$  is the normalized modulating angular frequency ( $\omega_{am} = 2\pi f_{am}/f_s$ ),  $\omega$  denotes the normalized nominal angular frequency ( $\omega = 2\pi f_o/f_s$ ),  $\omega_g$  is the normalized off-nominal angular frequency offset ( $\omega_g = 2\pi f_g/f_s$ ) and  $\phi$  is the initial phase. In the following, the performance of the Sb-SDFT is evaluated under the effect of amplitude step, amplitude ramp, amplitude modulation and static frequency offsets. The accuracy is assessed exhaustively, by varying the test signal parameters over a suitable range, in order to determine the maximum TVE values. This approach leads to a fair performance comparison between the considered techniques. Unless otherwise stated, parameters were assigned to  $A_o = 1$ ,  $f_o = 50$  Hz,  $f_s = 6.4$  KHz,  $N = 128$ ,  $\phi = 0$  rad,  $r = 0.9999$ ,  $\delta_s = 0$ ,  $\delta_r = 0$ ,  $\delta_{am} = 0$ ,  $\omega_{am} = 0$ ,  $\omega_g = 0$  and  $n_o = 0$ .

First, the step response of the Sb-SDFT estimators is evaluated. For this purpose, the parameters of Eq. (16) are set to:  $\delta_s = 0.1$  and  $n_o = 640$ . **Figure 6(a)** shows the estimated amplitude ( $\hat{A}$ )

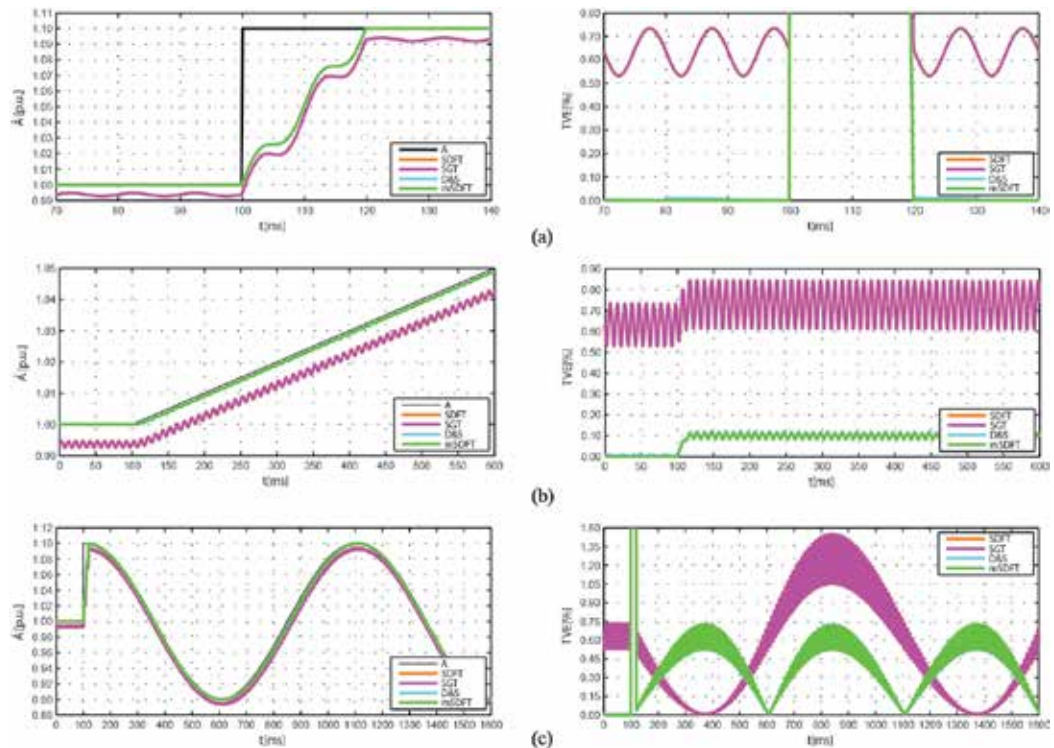


**Figure 6.** Transients for the estimation of the amplitude of (16) and the evolution of the TVE for the selected Sb-SDFT algorithms, under different test conditions. (a) A step change in amplitude with  $\delta_s = 0.1$ ,  $\delta_r = 0$ ,  $\delta_{am} = 0$  and  $\omega_g = 0$ . (b) A ramp-change in amplitude with  $\delta_s = 0$ ,  $\delta_r = 0.1$ ,  $\delta_{am} = 0$  and  $\omega_g = 0$ . (c) A sudden amplitude modulation with  $\delta_s = 0$ ,  $\delta_r = 0$ ,  $\delta_{am} = 0.1$ ,  $\omega_{am} = 2\pi/f_s$  and  $\omega_g = 0$ .

and TVE values as a function of time when the amplitude step occurs in  $x[n]$ . Ignoring small differences, related to the damping factor effect, the dynamic response during the transient is the same for all the algorithms. This transient has a duration that is equal to the length of the sliding window for all the Sb-SDFT. After the transient, the TVE values provided by the Sb-SDFT estimators are equal to the steady-state values shown in **Figure 5(e)**. Further, simulation results (not reported here for the sake of brevity) confirm that the TVE value in steady state, due to an amplitude step, is the same regardless of the value of  $\delta_s$ .

The accuracy of the considered estimators is analyzed in **Figure 6(b)**, assuming that the waveform  $x[n]$  is subjected to linear variation of its amplitude. Therefore, the parameters of Eq. (16) were adjusted as follows:  $\delta_r = 0.1$  and  $n_o = 640$ , to create ramp change in the amplitude of the test signal. Once more, the Sb-SDFT exhibit similar dynamics in their amplitude estimation performance. **Figure 7(a)** shows the worst-case TVE values, after the transient response, returned by the four considered estimators as a function of  $\delta_r$  in the range  $[0,0.1]$  p. u.. As can be seen, the maximum TVE value achieved by the Sb-SDFT worsens linearly with this parameter. In addition, a gap of 0.78% is observed, between the SDFT, SGT and the other two algorithms, which remains constant for the analyzed range.

The effect of a modulating signal on the estimation accuracy is analyzed in **Figure 6(c)**. Hence, the parameters of Eq. (16) were adjusted as follows:  $\delta_{am} = 0.1$ ,  $\omega_{am} = 2\pi/f_s$  and  $n_o = 640$ . The figure shows the estimated amplitude ( $\hat{A}$ ) and TVE values as a function of time when the amplitude modulation of 10% with a frequency of 1 Hz occurs in  $x[n]$ . As expected, the dynamic behavior displayed by the Sb-SDFT estimators is similar, with the mSDFT the most accurate of the reviewed algorithms. The curves in **Figure 7(b)** show the worst case TVE values

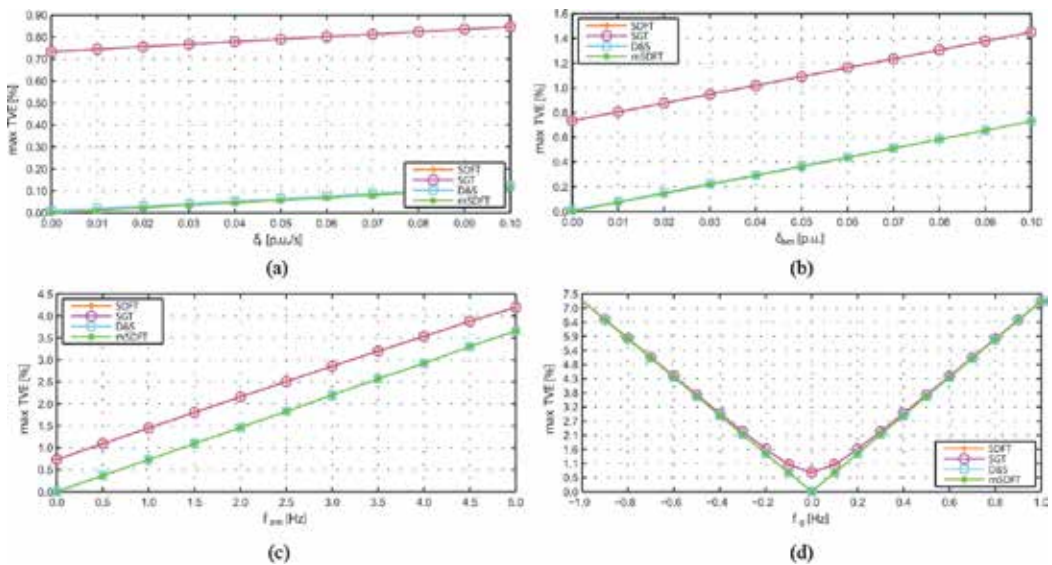


**Figure 7.** (a) Maximum TVE curves versus amplitude ramp slope factor  $\delta_r$ . (b) Maximum TVE curves versus amplitude modulation depth factor  $\delta_{am}$  for a modulating frequency  $f_{am}$  of 1 Hz. (c) Maximum TVE curves versus amplitude modulating frequency  $f_{am}$  with  $\delta_{am} = 0.1$  p.u. (d). Maximum TVE curves versus static frequency offset  $f_g$ .

returned by the four considered estimators as a function of  $\delta_{am}$  in the range  $[0, 0.1]$ p. u. with  $f_{am} = 1$  Hz. **Figure 7(c)** shows the worst case TVE values given by the Sb-SDFT as a function of  $f_{am}$  in the range  $[0, 5]$  Hz with  $\delta_{am} = 0.1$ p. u. Note that the TVE increment linearly with  $\delta_{am}$  or  $f_{am}$ , and that the behavior of the Sb-SDFT estimators is very similar.

Finally, the influence of a simple static off-nominal frequency offset on the Sb-SDFT estimators' performance is analyzed in **Figure 7(d)**. The figure shows the maximum TVE values, in steady state, when the signal (Eq. 16) phase varies as a function of the off-nominal frequency offset  $f_g$  in the range  $[-1, 1]$  Hz. As expected, the accuracy of all the considered estimators degrades monotonically as the frequency offset increases due to the spectral leakage effect.

The similarities between the Sb-SDFT algorithms found through **Figures 6** and **7** are explained by the fact that all implementations of this type of algorithms result from applying Fourier properties and mathematical operations to standard DFT definition (Eq. 1).

### 3.3. Sb-SDFT limitations

The direct application of Sb-SDFT may lead to inaccuracies due to aliasing and spectral leakage, common pitfalls inherited by every DFT-based method. Aliasing is generally corrected by employing anti-aliasing filters or increasing the sampling frequency to a value that satisfies the Nyquist sampling criterion. Instead, when the sampling is not synchronized with the signal under analysis, the DFT is computed over a noninteger number of cycles of the input signal which leads to the spectral leakage phenomenon [1]. Spectral leakage is typically reduced (not eliminated) by selection of the proper nonrectangular time domain windowing functions, to weigh the sequence data at a fixed sampling frequency [12]. This process increases the computational complexity and does not take advantage of the recursive nature of Sb-SDFT methods. Otherwise, spectral leakage can be avoided entirely by ensuring that sequence of samples is equal to an integer number of periods of the input signal [13].

## 4. Coherent sampling approach

In order to avoid the spectral leakage phenomenon, the sequence of samples within a sliding window of a Sb-SDFT must be equal to an integer number of fundamental periods of the input signal. An integer number of periods will be sampled if and only if the coherence criterion holds:

$$\frac{f_o}{f_s} = \frac{m}{N} \quad (17)$$

where  $f_o$  is the signal frequency,  $f_s$  is the sampling frequency,  $N$  is the sampled sequence length and  $m$  is an integer number. This is equivalent to ensuring that an integer number  $m$  of sine periods is present in the data sample of length  $N$ , and in that case there is no spectral leakage. If Eq. (17) holds,  $f_s$  is referred to as coherent or synchronous sampling frequency.

A variable sampling period approach, named variable sampling period technique (VSPT), was developed by the authors to design synchronization methods that maintain a coherent sampling with the input signal fundamental frequency [14]. This technique has recently been adapted to dynamically adjust the sampling frequency in a harmonic measurement method based on mSDFT [15]. In Ref. [16], the VSPT is generalized so as to be used with any Sb-SDFT algorithm.

In this section, the technique of variable sampling period is briefly described, and a unified small-signal model, which allows to use the VSPT with any Sb-SDFT, is also presented.

#### 4.1. Variable sampling period technique

VSPT allows to adapt the sampling frequency to be  $N$  times the fundamental frequency of a given input signal. This technique has proven to be efficient both in three-phase and in single-phase applications yielding a robust synchronization mechanism, whose effectiveness has been tested under different conditions and scenarios [14, 17].

**Figure 8(a)** illustrates the basic VSPT scheme for single-phase implementation, where the input signal is sampled and the input phase  $\varphi_u[n]$  is extracted by the phase detector. Concomitantly with the input sampling, the reference generator provides a signal called reference phase:

$$\varphi_{\text{ref}}[n] = \frac{2\pi n}{N} \quad (18)$$

The method achieves a null phase error ( $e_\varphi[n]$ ) between  $\varphi_{\text{ref}}[n]$  and  $\varphi_u[n]$ , by varying the sampling period  $T_S[n]$  as a function of  $e_\varphi[n]$ . The controller  $G_c(z)$  provides the value of the sampling period and then the sampling generator produces a clock signal (CLK) that starts the conversion and increments the reference phase. The implementation of the phase detector and phase error calculation is key for the proper functioning of this technique. The operating principle is based on the dynamic adjustment of the sampling frequency. An exhaustive explanation of the key elements of this technique can be found in Refs. [14, 17].

#### 4.2. Unified small-signal model

VSPT allows to adapt the sampling rate to a multiple of the fundamental frequency of a given input signal, so the coherence criterion holds, thereby preventing the DFT's shortcomings when is used to analyze nonstationary signals. An error signal, related to the phase difference between the fundamental component of the input signal and the reference phase, is needed to adapt the sampling period. Based on this, phase error is feasible to develop a closed-loop control to synchronize the sampling period.

As mentioned in Section 3, when  $r \rightarrow 1$  and for a real input signal, the Sb-SDFT algorithms become equivalent. Therefore, for this scenario and for small-signal conditions, these methods supply the same estimation of the  $k$ th-bin of an  $N$ -points DFT. Based on this concept, **Figure 8(b)** shows a phase error estimation scheme that employs an Sb-SDFT algorithm, which allows to estimate the phase difference between the fundamental component of the input signal and the reference phase. This scheme obtains the phase error signal from three basic operations, first an

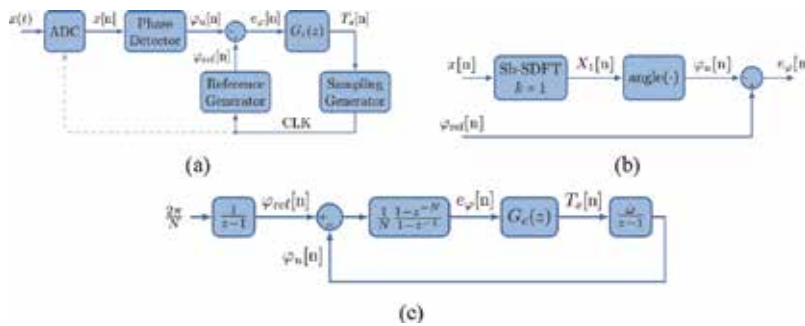


**Figure 8.** (a) General scheme of the variable sampling period technique, (b) phase error estimation scheme based on Sb-SDFT and (c) system model for Sb-SDFT with coherent sampling adjustment based on VSPT.

Sb-SDFT algorithm with  $k = 1$  is used to estimate the fundamental component ( $X_1[n]$ ) of an  $N$ -points DFT, from a given input sequence of samples ( $x[n]$ ). Then the phase of the input signal ( $\varphi_u[n]$ ) is estimated by computing the argument of the complex result  $X_1[n]$ , as stated by Eq (4b). Finally, a simple subtraction operation is used to estimate the phase error ( $e_\varphi[n]$ ) between the incoming signal and the reference.

Since all the Sb-SDFT methods are derived from Eq. (1), for small-signal condition, they are mathematically equivalent, and the system phase error ( $e_\varphi[n]$ ) for small deviation is approximately equal. Therefore, a mathematical model can be extrapolated for implement the VSPT scheme shown in **Figure 8(a)** with the phase error estimation scheme shown in **Figure 8(b)**. **Figure 8(c)** presents the small signal model of a coherent sampling scheme for the Sb-SDFT algorithms based on the VSPT, which allows to avoid the spectral leakage phenomenon. The complete mathematical derivation of this model is available in Ref. [16].

### 4.3. Validation

The specifications and requirements to be met by the controller ( $G_c(z)$ ) are determined by the application. Several applications require zero phase error and frequency synchronization for normal operation. In these cases, the controller must be proportional integral to achieve zero phase error in steady state; the resulting system being a type II system.

Then the transfer function for the controller in the  $z$  domain is

$$G_c(z) = K \left( \frac{z-a}{z-1} \right) \quad (19)$$

As an example of design,  $\bar{\omega} = 2\pi \times 50$  rad/s and  $N = 128$  are adopted. Concerning dynamics, a phase margin of  $45^\circ$  and maximum bandwidth are adopted as design criteria for  $G_c(z)$ . Based on this, and using the design methodology proposed in Ref. [15], the parameters of the controller are  $K = 1.7304 \cdot 10^{-5}$  and  $a = 0.9974$ , with a bandwidth of 5.905 Hz.

The estimations obtained by the Sb-SDFT algorithms with coherent sampling supplied by the VSPT, in situations where the input signal frequency deviates from its nominal value, are evaluated in two possible scenarios. The first simulation analyzes the effect of a frequency step

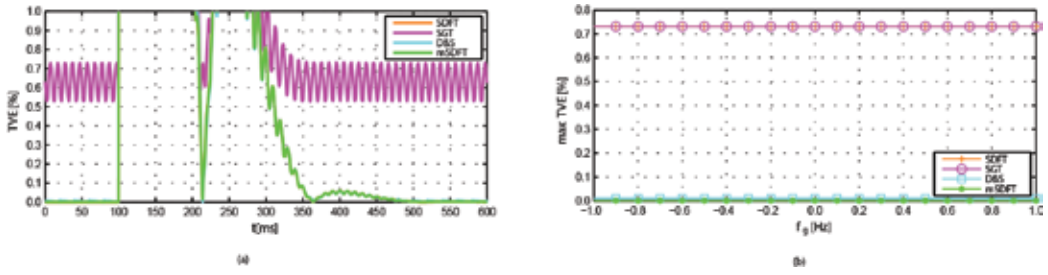


**Figure 9.** (a) Evolution of the TVE for the selected Sb-SDFT algorithms when a sudden  $-0.5$  Hz step change in the nominal frequency occurs. (b) Maximum TVE curves versus static frequency offset  $f_g$ .

of  $-0.5$  Hz on the performance of the proposed method. Hence, the parameters of Eq. (16) were adjusted as follows:  $A_o = 1$ ,  $f_o = 50$  Hz,  $\phi = 0$  rad,  $\delta_s = 0$ ,  $\delta_r = 0$ ,  $\delta_{am} = 0$ ,  $\omega_{am} = 0$ ,  $f_g = -0.5$  Hz and  $n_o = 640$ . The Sb-SDFT algorithms are set with  $f_s = 6.4$  KHz,  $N = 128$ ,  $r = 0.9999$  and  $k = 1$ . The parameters used in the controller  $G_c(z)$ , for the VSPT close loop, are those presented in the previous example of design. **Figure 9(a)** depicts the effect of the frequency step change on the TVE values given by the estimated  $X[n]$  component. During the transient, an oscillatory behavior is noticed, which may be attributed to spectral leakage given by the noncompliance of the coherence criterion (Eq. 17) at the step change. Variations in the estimated values are extinguished once the sampling frequency is properly adjusted by the VSPT method to  $f_s = N \times (f_o - f_g)$ . Then, under a steady-state condition, the TVE values given by the four Sb-SDFT are equal to those previous to the frequency step.

To complete the evaluation of the accuracy of coherent sampling achieved by the VSPT, the influence of a simple static off-nominal frequency offset on the Sb-SDFT estimators performance is analyzed in **Figure 9(b)**. The figure shows the maximum TVE values, in steady state, when fundamental frequency of Eq. (16) varies as a function of the off-nominal frequency offset  $f_g$  in the range  $[-1,1]$  Hz. Due to the VSPT, in steady-state sampling, frequency is coherent with the fundamental frequency of the test signal, ensuring that exactly one period is present in the data sample of length  $N$ , and in that case, the Sb-SDFT avoids the spectral leakage phenomenon. Therefore, compared with the results shown in **Figure 7(d)**, the TVE values do not worsen with  $f_g$ , instead remain constant and equal to those shown in **Figure 5(e)**.

## 5. Conclusions

In this work, a comparative study of four Sb-SDFT algorithms is conducted. The comparison includes filter structure, stability, statistical efficiency, accuracy analysis, dynamic behavior and implementation issues on finite word-length precision systems limitations. Based on theoretical studies as well as on simulations, it is deduced that all reviewed Sb-SDFT techniques are equivalent, primarily due to the fact that they are derived from the traditional DFT, therefore in various applications can be applied indistinctly.

It proves that SDFT and SGT have identical performances, in regard to disturbance rejection and precision on spectral estimation. Both of these techniques are used extensively due to their

straightforward implementation, although the two have an error in accuracy due to the use of a damping factor. For applications requiring greater precision, this error can be reduced by using the D&S algorithm. On the other hand, it can be eliminated by using mSDFT due to the absence of damping factor, resulting in better performance. The results of the study have shown that mSDFT is the best option when it comes to precision and noise rejection.

The direct application of a Sb-SDFT may lead to inaccuracies due to the spectral leakage phenomenon, common pitfall inherited by every DFT-based method. Spectral leakage arises when the sampling process is not synchronized with the fundamental tone of the signal under analysis and the DFT is computed over a noninteger number of cycles of the input signal. In this sense, a unified small-signal system model is presented, which can be used to design a generic adaptive frequency loop that is based on a variable sampling period technique. The VSPT allows to obtain a sampling frequency coherent with the fundamental frequency of the analyzed signal, avoiding the error introduced by the spectral leakage phenomenon.

## Author details

Carlos Martin Orallo\* and Ignacio Carugati

\*Address all correspondence to: [orallo@fi.mdp.edu.ar](mailto:orallo@fi.mdp.edu.ar)

Instituto de Investigaciones Científicas y Tecnológicas en Electrónica (ICYTE), Consejo Nacional de Investigaciones Científicas y Técnicas (CONICET) and Universidad Nacional de Mar del Plata (UNMdP), Mar del Plata, Argentina

## References

- [1] Oppenheim A and Schaffer R. *Discrete-time Signal Processing*. Prentice-Hall Signal Processing Series. Pearson, Upper Saddle River, New Jersey, US, 2009. ISBN: 9780131988422.
- [2] Kim JH and Chang TG. "Analytic derivation of the finite wordlength effect of the twiddle factors in recursive implementation of the sliding-DFT". In: *IEEE Transactions on Signal Processing* 48.5, Piscataway, New Jersey, US, (May 2000), pp. 1485–1488. ISSN: 1053-587X. DOI: 10.1109/78.839998.
- [3] Darwish HA and Fikri M. "Practical Considerations for Recursive DFT Implementation in Numerical Relays". In: *IEEE Transactions on Power Delivery* 22.1, Piscataway, New Jersey, US, (Jan. 2007), pp. 42–49. ISSN: 0885–8977. DOI: 10.1109/TPWRD.2006.874642.
- [4] Lyons R. "The Sliding DFT". In: *IEEE Signal Processing Magazine* 20.2 Piscataway, New Jersey, US, (Mar. 2003), pp. 74–80. ISSN: 1053–5888. DOI: 10.1109/MSP.2003.1184347.
- [5] Hartley R and Welles K. "Recursive Computation of the Fourier Transform". In: *Circuits and Systems, 1990, IEEE International Symposium on*. Piscataway, New Jersey, US, (May 1990), pp. 1792–1795 vol.3. DOI: 10.1109/ISCAS.1990.111983.

- [6] Chicharo JF and Kilani MT. "A sliding Goertzel algorithm". In: *Signal Processing* 52.3 Piscataway, New Jersey, US, (1996), pp. 283–297. ISSN: 0165–1684. DOI: [http://dx.doi.org/10.1016/0165-1684\(96\)00066-7](http://dx.doi.org/10.1016/0165-1684(96)00066-7).
- [7] Lyons RG. *Streamlining Digital Signal Processing*. Ed. by Lyons RG. Hoboken, NJ, USA: John Wiley & Sons, Inc. (June 2012). ISBN: 9781118316948. DOI: 10.1002/9781118316948.
- [8] Douglas SC and Soh JK. "A numerically-stable sliding-window estimator and its application to adaptive filters". In: *Conference Record of the Thirty-First Asilomar Conference on Signals, Systems & Computers, Piscataway, New Jersey, US, 1997*. Vol. 1. (Nov. 1997), pp. 111–115. DOI: 10.1109/ACSSC.1997.680039.
- [9] Duda K. "Accurate, Guaranteed Stable, Sliding Discrete Fourier Transform". In: *IEEE Signal Processing Magazine* November Piscataway, New Jersey, US, (Nov. 2010), pp. 124–127. ISSN: 1053–5888. DOI: 10.1109/MSP.2010.938088.
- [10] Kay SM. *Fundamentals of Statistical Signal Processing: Estimation Theory*. Prentice-Hall, Inc., Upper Saddle River, New Jersey, US, 1993. ISBN: 0-13-345711-7.
- [11] "IEEE Standard for Synchrophasor Measurements for Power Systems". In: *IEEE Std C37.118.1-2011 (Revision of IEEE Std C37.118-2005)* Piscataway, New Jersey, US, (Dec. 2011), pp. 1–61. DOI: 10.1109/IEEESTD.2011.6111219.
- [12] Lyons RG. *Understanding Digital Signal Processing*. 3rd ed. Pearson, Upper Saddle River, New Jersey, US, 2010. ISBN: 9780137028528.
- [13] Manolakis D and Ingle V. *Applied Digital Signal Processing: Theory and Practice*. Cambridge University Press, Shaftesbury Road, Cambridge CB2 8BS, UK, 2011. ISBN: 9781139495738.
- [14] Carugati I, Maestri S, Donato PG, Carrica D, and Benedetti M. "Variable Sampling Period Filter PLL for Distorted Three-Phase Systems". In: *IEEE Transactions on Power Electronics* 27.1 Piscataway, New Jersey, US, (Jan. 2012), pp. 321–330. ISSN: 0885–8993. DOI: 10.1109/TPEL.2011.2149542.
- [15] Orallo CM, Carugati I, Maestri S, Donato PG, Carrica D, and Benedetti M. "Harmonics Measurement With a Modulated Sliding Discrete Fourier Transform Algorithm". In: *IEEE Transactions on Instrumentation and Measurement* 63.4 Piscataway, New Jersey, US, (Apr. 2014), pp. 781–793. ISSN: 0018–9456. DOI: 10.1109/TIM.2013.2287801.
- [16] Orallo CM, Carugati I, Donato PG, and Maestri S. "Study on Single-bin Sliding DFT algorithms: Comparison, stability issues and frequency adaptivity". In: *Measurement* 69, Radarweg 29, 1043 NX Amsterdam, The Netherlands, (2015), pp. 9–19. ISSN: 0263-2241. DOI: 10.1016/j.measurement.2015.03.011.
- [17] Carugati I, Donato P, Maestri S, Carrica D, and Benedetti M. "Frequency Adaptive PLL for Polluted Single-Phase Grids". In: *IEEE Transactions on Power Electronics* 27.5 Piscataway, New Jersey, US, (May 2012), pp. 2396–2404. ISSN: 0885-8993. DOI: 10.1109/TPEL.2011.2172000.

---

# Fourier Analysis for Harmonic Signals in Electrical Power Systems

---

Emmanuel Hernández Mayoral,  
Miguel Angel Hernández López,  
Edwin Román Hernández,  
Hugo Jorge Cortina Marrero,  
José Rafael Dorrego Portela and  
Victor Ivan Moreno Oliva

Additional information is available at the end of the chapter

<http://dx.doi.org/10.5772/66730>

---

## Abstract

The harmonic content in electrical power systems is an increasingly worrying issue since the proliferation of nonlinear loads results in power quality problems as the harmonics is more apparent. In this paper, we analyze the behavior of the harmonics in the electrical power systems such as cables, transmission lines, capacitors, transformers, and rotating machines, the induction machine being the object of our study when it is excited to nonsinusoidal operating conditions in the stator winding. For this, a model is proposed for the harmonic analysis of the induction machine in steady-state regimen applying the Fourier transform. The results of the proposed model are validated by experimental tests which gave good results for each case study concluding in a model proper for harmonic and nonharmonic analysis of the induction machine and for “harmonic” analysis in an electrical power system.

**Keywords:** harmonic, power quality, induction machine, nonsinusoidal, power systems

---

## 1. Introduction

Electrical power systems are an area that is receiving a great deal of attention recently. The issues and considerations associated with electrical power systems are often misunderstood. With the growth and expansion of power electronics and proliferation of nonlinear loads in

---

electrical power system applications, the harmonics and their effects on power quality are a topic of concern. Currently in the United States, only 15–20% of the utility distribution loading consists of nonlinear loads.

Nowadays, the recommendation from IEEE Std. 519 imposed by utilities is becoming stricter due to the increase in proportion of nonlinear load. The problems of harmonic in the electrical power systems are low, but their analysis can help to increase plant power system reliability. The harmonics are a problem when their magnitude produces an electrical power system resonance.

The analysis and modeling of the harmonics are supported for the Fourier analysis. In the eighteenth and nineteenth century, J. B. Joseph Fourier (1768–1830) and other mathematicians performed basic calculations of harmonics. In the 1920s and 1930s, the distortion in voltage waveforms caused by power converters was noticed and studied. In the 1950s and 1960s, the study of harmonics in power converters extended to the transmission of voltage in the electrical power system. Currently, the electrical power systems have a large number of nonlinear elements that generate other waves at different frequencies. They generate these waves from sinusoidal waveforms to network frequency. This causes a phenomenon known as harmonics. Harmonics are phenomena that cause problems for both the users and the electricity suppliers. They have various harmful effects on the equipment in the electrical network.

## 2. Definition of harmonics

The term *harmonic* comes from acoustics. It refers to the vibration of a column of air at a frequency which is a multiple of the basic frequency of repetition.

In electric signals, a harmonic is defined as the signal content at a specific frequency, which is a multiple integral of the current frequency system or main frequency produced by the generators. With an oscilloscope, it is possible to observe a complex signal in the domain of time. At any moment in the given time, the amplitude of the waveform is displayed. If the same signal is applied to a high-fidelity amplifier, the result in sounds is a mix of frequencies. The phase relationship does not affect the audible effects, which is acceptable in acoustics. But this is not the case with electric signals. The position of harmonics and the phase relationship in the harmonic from a different source can considerably alter the effects in electric signals. To define harmonic, it is important to first define the quality of the voltage wave, which must have a constant amplitude and frequency, as well as the sinusoidal form. **Figure 1** depicts the waveform without any content of harmonics, with a constant frequency of 60 Hz and a constant amplitude of 1 pu.

When a periodic wave does not have a sinusoidal form, it is said to have a harmonic content. This can alter its peak value and/or its RMS value causing alterations in the normal functioning of any equipment that undergoes this voltage. The frequency of the periodic wave is known as the fundamental frequency and the harmonics are the signals whose frequency is an integer multiple of this frequency. **Figure 2** shows a voltage wave with a content of 30% of the fifth harmonic.

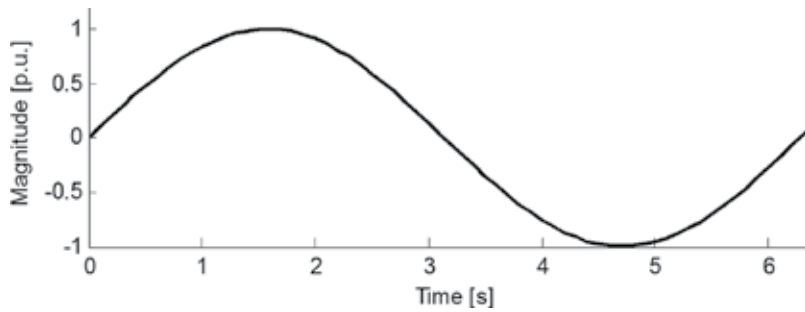


Figure 1. Wave without harmonic content.

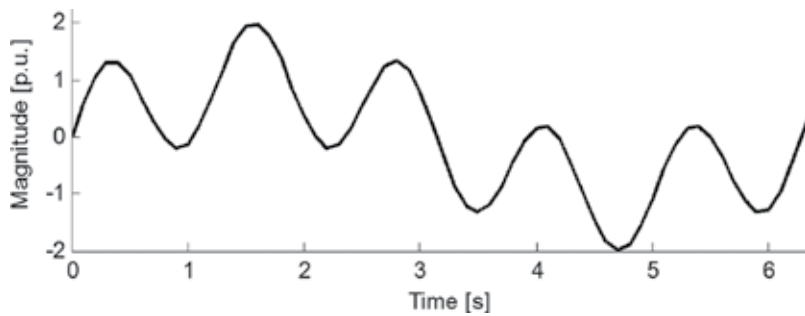


Figure 2. Voltage waveform with harmonic content.

### 3. Fourier analysis

The analysis of harmonics is the process of calculating the magnitudes and phases of the fundamental and high order harmonics of the periodic waveforms. The resulting series is known as Fourier series. It establishes a relation between a function in the domain of time and a function in the domain of frequency.

The Fourier's theorem states that every nonsinusoidal periodic wave can be decomposed as the sum of sine waves through the application of the Fourier series, given the following conditions:

- The integral over one period of the function is a finite value.
- The function possesses a finite number of discontinuities in a period.
- The function possesses a finite number of maxima and minima in a period.

*Coefficients and Fourier series.* The Fourier series of a periodic function  $x(t)$  is expressed as:

$$x(t) = a_0 + \sum_{n=1}^{\infty} \left( a_n \cos\left(\frac{2\pi nt}{T}\right) + b_n \sin\left(\frac{2\pi nt}{T}\right) \right) \quad (1)$$

This constitutes a representation of periodic function in the domain of the frequency.

In this expression,  $a_0$  is the average value of the function  $x(t)$ , where  $a_n$  and  $b_n$  are the coefficients of the series besides being the rectangular components of the  $n$  harmonic. For the corresponding  $n$  harmonic its vector is:

$$A_n \angle \phi_n = a_n + jb_n \quad (2)$$

With a magnitude and an angle of phase:

$$A_n = \sqrt{a_n^2 + b_n^2}, \phi_n = \tan^{-1} b_n \quad (3)$$

#### 4. Harmonic sources

Harmonics are the result of nonlinear loads which give a nonsinusoidal response to a sinusoidal signal. The main sources of harmonics are:

- Arc furnaces and other elements of arc discharge, such as fluorescent lamps. Arc furnaces are considered as voltage harmonic generators more than current generators. Typically all harmonics (2nd, 3rd, 4th, 5th,...) appear but the odd harmonics are predominant with typical values with regard to the fundamental harmonic:
  - The third harmonic represents 20%, and the fifth harmonic represents 10%.
  - The seventh harmonic represents 6%, and the ninth harmonic represents 3%.
- Magnetic cores in transformers and rotating machines require third harmonic current to excite the iron.
- The inrush current of transformers produces second and fourth harmonics.
- Adjustable speed controllers used in fans, pumps, and process controllers.
- Solid-state switches which modulate control currents, light intensity, heat, etc.
- Controlled sources for electronic equipment.
- Rectifiers based on diodes and thyristors for welding equipment, battery chargers, etc.
- Static reactive power compensators.
- DC high voltage transmission stations.
- AC to DC converters (inverters).

The AC electrical power system harmonic issues are mainly due to the substantial increase of nonlinear loads due to technological advances, such as the use of power electronics circuits and devices, in AC/DC transmission links, or loads in the control of power systems using power electronic or microprocessor controllers. Such equipment creates load-generated harmonics throughout the electrical power system.

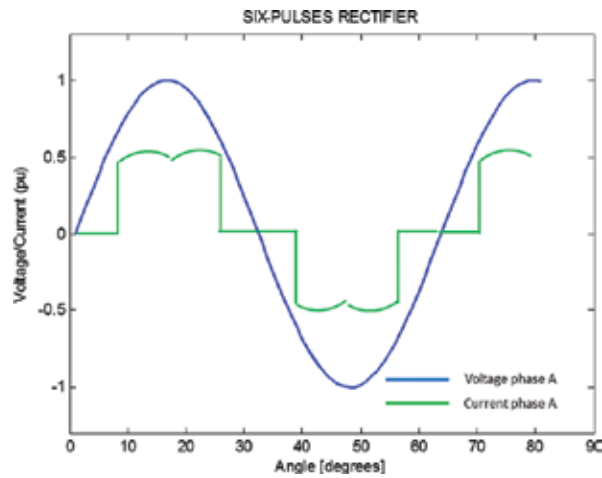


**Figure 3.** Current and voltage of a typical six-pulse rectifier input.

In the case of a motor drive, the AC current at the input to the rectifier looks more like a square wave than a sine wave (see **Figure 3**).

The rectifier can be thought of as a harmonic current source and produces roughly the same amount of harmonic current over a wide range of electrical power system impedances. The characteristic current harmonics that are produced by a rectifier are determined by the pulse number. The following equation allows determination of the characteristic harmonics for a given pulse number:

$$h = kq \pm 1 \tag{4}$$

where:

$h$  is the harmonic number (integer multiple of the fundamental),

$k$  is any positive integer, and

$q$  is the pulse number of the converter.

The harmonics 5th, 7th, 11th, 13th, 17th, 19th, 23rd, 25th, etc., are the harmonics that a 6-pulse rectifier will exhibit and which are multiples of the fundamental. The quotient of the fundamental current and the harmonic number will result in the magnitudes of the harmonic currents (e.g., the magnitude of the 5th harmonic would be about 1/5th of the fundamental current). When it comes to a 12-pulse systems, a small amount of the 5th, 7th, 17th, and 19th harmonics will be present (the magnitudes will be approximately a 10 percent of those for a 6-pulse drive). The induction machines are quite affected by the harmonic currents produced by inverters. Most of these harmonics produced are integer multiples of the inverter frequency and their magnitude will depend on the algorithm switching power semiconductors of the inverter. It is common that there are “interharmonics” currents at the input or the output of the inverter but they do not necessarily occur at integer multiples of the power

supply or inverter fundamental frequency. For this reason, it needs a good design of DC link to minimize the presence of interharmonics.

Some authors [1] agree to classify the sources of harmonic distortion in three groups: small and predictable (harmonics generated by residential consumers), large and transient (voltage fluctuations produced by arc furnaces), and large and predictable (SVC and HVDC transmission causing characteristic and uncharacteristic harmonics). Now, if at a point common coupling harmonic currents are not within the permissible limits, it is necessary to take appropriate measures to comply with regulations. For example the IEEE 519-1981, "*IEEE Guide for Harmonic Control and Reactive Compensation of Static Power Converters*," originally established levels of voltage distortion acceptable to the distribution system for individual nonlinear loads. This distortion is a steady-state deviation from a sine wave of power frequency called waveform distortion [2]. Fourier series is generally used to analyze this nonsinusoidal waveform.

## 5. Effects of harmonics

Normally, the presence of harmonic signals in the electrical power system is rare but it is possible that a large number of undesirable effects occur. High levels of harmonic distortion can cause undesirable effects in the transformer, capacitor, motor or generator heating, disoperation of electronic equipment, interference with telephone circuits, etc., and it gets worse if a resonant condition is presented. Resonance occurs when a harmonic frequency produced by a nonlinear load closely coincides with the natural frequency of the electrical power system. There are two forms of resonance which can occur: parallel resonance and series resonance.

*Parallel resonance:* The parallel resonance occurs when the natural frequency of the inductive components of the system, connected in parallel with capacitive reactive impedance components are too close to the harmonic frequency of the system. If this frequency coincides with a frequency generated by the harmonic source, it causes severe complications leading to excessive voltages and currents, causing damage to capacitors or overheating transformer and other electrical equipment (see **Figure 4**).

*Series resonance:* It occurs when the source harmonic current is connected in series with the combination, also in series, of the inductive impedance of the system and the capacitive reactance of a capacitor bank (usually connected to the end of a branch supply), its impedance being very low.

The effect of a series resonance can be a high-voltage distortion between the inductive impedance and the capacitive reactance (see **Figure 5**).

### 5.1. Effects on cables

The current distribution through the cross section of a conductor is uniform only when the current is a direct one. In alternating current as the frequency increases, the nonuniformity of the current distribution becomes steeper.

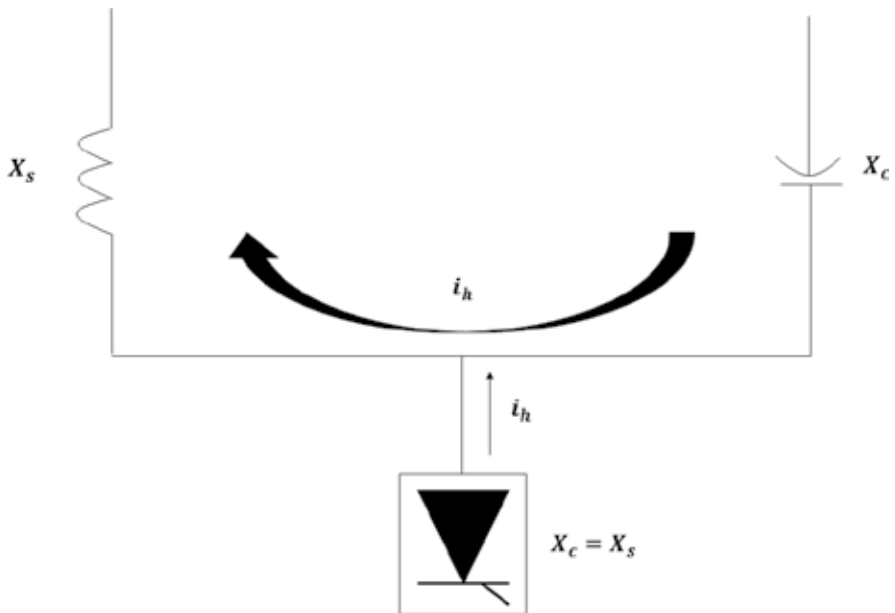


Figure 4. Parallel resonance.

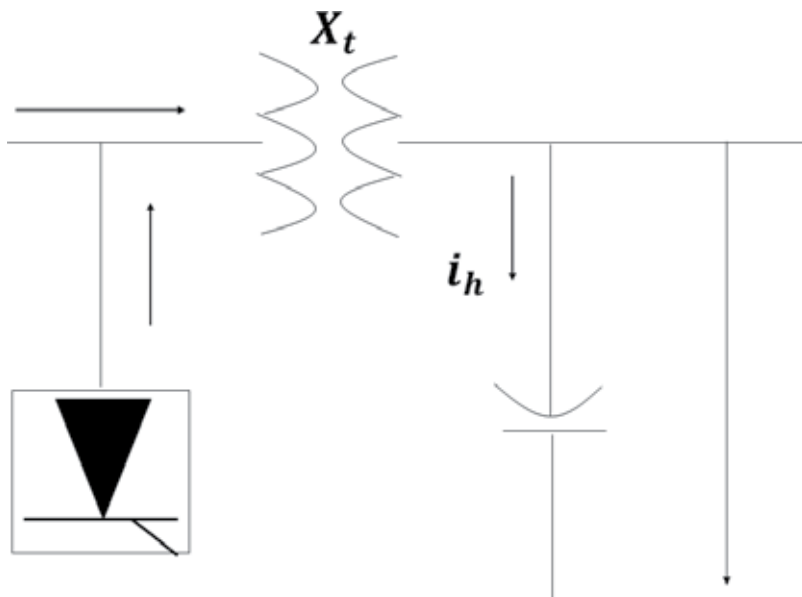
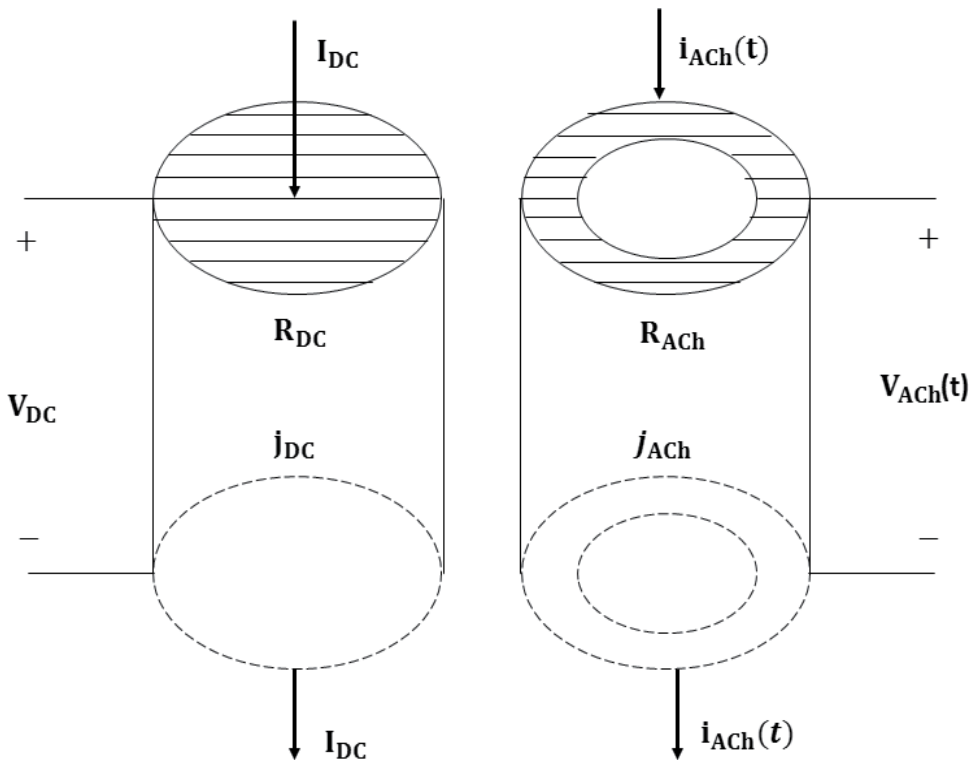


Figure 5. Series resonance.

In circular conductors, the current density increases from the center to the surface. The outer layers are less bounded by the magnetic flow than the inner layers. This means that more voltage is longitudinally induced with alternating current inside the conductor than on the surface. Therefore the current density is increasing from the interior to the outer layers of the conductor. This phenomenon is called the skin effect.

**Figure 6** shows the variation of the ratio  $r_{ac}/r_{dc}$  with regard to frequency for some wire sizes used in electrical installations. The figure shows how the skin effect becomes more pronounced with a higher caliber (less  $r_{dc}$ ). If a conductor with a cross section  $a_{cond}$  conducts a DC current  $I_{DC}$ , the current density  $j_{DC} = I_{DC}/a_{cond}$  is uniform within the conductor and a resistance  $R_{DC}$  can be assigned to the conductor representing the ratio between the applied voltage  $V_{DC}$  and the resulting current  $I_{DC}$ , that is,  $R_{DC} = V_{DC}/I_{DC}$ . For (periodic) AC currents,  $i_{ACh}(t)$ , the current flows mostly near the surface on the conductor and the current density  $j_{ACh}$  is nonuniform within the conductor (**Figure 6**). In general,  $R_{DC}/R_{ACh}$ , the higher the order  $h$  of the harmonic current  $i_{ACh}(t)$  the larger is the skin effect.



**Figure 6.** DC resistance  $R_{DC}$  versus AC resistance  $R_{ACh}$ .

### 5.2. Effects on transformers

The normal operating conditions of the transformer is a well-researched subject. In fact, many steady-state and transient models are available. The transformer can be modeled into

two-state regime: transient model and steady-state model. The transient model needs much computation time, while the steady-state model requires less amount of computation time as it takes place in phasor analysis in the frequency domain to analyze the behavior of the transformer.

However, the material with which the core of the transformers is built has nonlinear characteristics. These nonlinear characteristics are neglected by the transformer models that use linear techniques. They exhibit three types of nonlinearities that make their analysis difficult: saturation effect, hysteresis (major and minor) loops, and eddy currents. The factors that influence additional losses and the generation of harmonic signals in the transformer are the temperature and possible resonance between transformer winding inductance and supply capacitance. In addition, if the losses in the transformer are considered, then the modeling becomes complicated, for that reason those losses are neglected according to the following expression,

$$P_{fe} = P_{hys} + P_{eddy} = K_{hys} (B_{max})^s f + K_{eddy} (B_{max})^2 f^2 \quad (5)$$

Where  $P_{hys}$ ,  $P_{eddy}$ ,  $B_{max}$  and  $f$  are hysteresis losses, eddy-current losses, flux density, and fundamental frequency system, respectively.  $K_{hys}$  is the constant of the type of iron used and  $K_{eddy}$  is the eddy-current constant for the conductive material.  $S$  is the Steinmetz exponent ranging from 1.5 to 2.5 depending on the operating point of transformer core. **Figure 7** illustrates a relatively simple and accurate frequency-based linear model.

In **Figure 7**,  $R_c$  is the core loss resistance,  $L_m$  is the magnetizing inductance, and  $R_p$ ,  $R'_s$ ,  $L_p$  and  $L'_s$  are the resistances and inductances of the primary and secondary windings of the transformer,

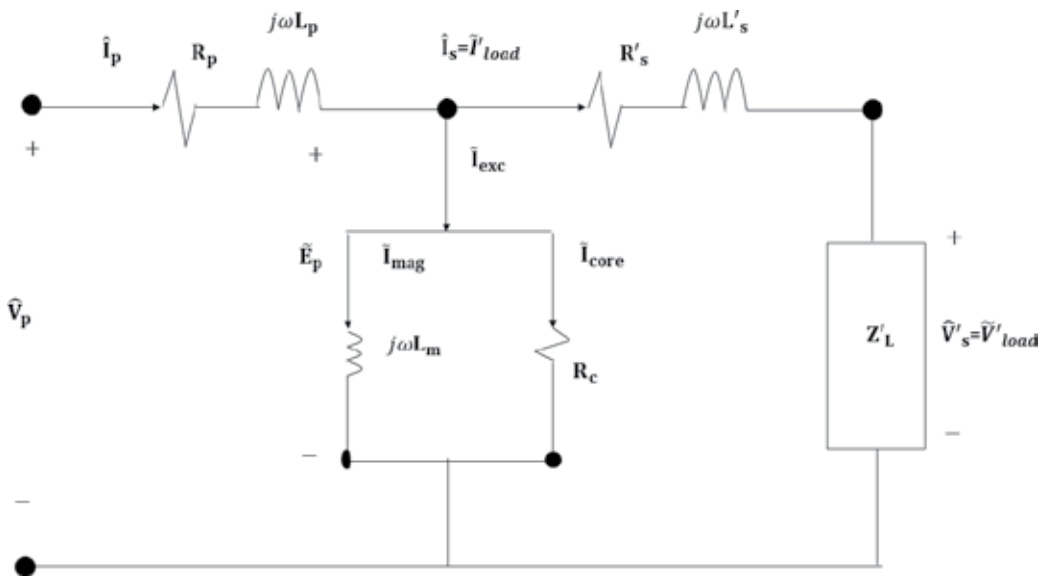


**Figure 7.** Linear single-phase, steady-state transformer model for sinusoidal analysis.

respectively. Superscript ' is used for quantities referred from the secondary winding to the primary winding of the transformer. Losses in transformers consist of losses with no-load or core and load losses, which include  $I^2R$  losses, eddy current losses, and additional losses in the tank, fasteners, or other iron parts. The effect of the harmonics on each type of loss is explained below:

- No-load or core losses: they are produced by the excitation voltage in the core. The voltage waveform in the primary winding is considered as sinusoidal independently of the load current. Thus, the losses are not expected to increase when load currents are nonsinusoidal. Although, the magnetizing current contains very weak harmonics compared with the harmonics current load, so their effects on the total losses are minimal.
- Joule losses: if the load current contains harmonics, these losses will also increase due to the skin effect.
- Eddy current losses: these losses at fundamental frequency are proportional to the square of the current load and the square of the frequency. Then, there might be an excessive increase of losses in the windings conducting nonsinusoidal current loads (and thus also in its temperature).
- Additional losses: these losses cause the temperature to increase in the structural parts of the transformer and, depending on the type of transformer, they will or will not contribute to the hottest temperature in the winding.

The generation of harmonic signals in the transformer plays an important role in the model of such electrical machines. The methodology for the harmonic design of a transformer is as follows: First is the construction and design where mainly the nonlinearity of the core is analyzed that causes nonsinusoidal magnetizing and core-loss currents. The relationship between the parameters and variables of the model of the transformer with respect to the generated harmonic frequencies would be the next step. In the following references, several harmonic models for transformers have been proposed and implemented with respect to time-domain simulation [3–8], frequency-domain simulation [9–12], combined frequency- and time-domain simulation [13, 14], and numerical (e.g., finite-difference, finite-element) simulation [15–21]. Most previous references considered the influence of skin effects and proximity effects in the harmonic model. The problem with this model is the determination of the magnetizing currents and losses in the core, as these are the main harmonic sources in the transformer (see **Figure 8**).

In the previous figure,  $R_p$ ,  $i_p$ , and  $V_p$  are the resistance, current, and voltage of the primary winding,  $L_{pl}$  is the leakage inductance,  $i_{exc}$ ,  $i_{core}$  and  $i_{mag}$  is the excitation, core, and magnetization currents and  $e_p$  is the potential difference in the primary. For the second winding of transformer correspond to the variables:  $R_s$ ,  $i_s$  and  $V_s$  are the resistance, current, and voltage of the secondary winding and  $L_{sl}$  is the leakage inductance. The triplen (i.e., 3rd, 9th, 15th...) harmonic currents cannot propagate in distribution transformers downstream but circulate in the primary delta winding of the transformer causing localized overheating. With linear loading, the three-phase currents will cancel out in the neutral conductor called homopolar currents. However, when nonlinear loads are being supplied, the triplen harmonics in the phase cur-

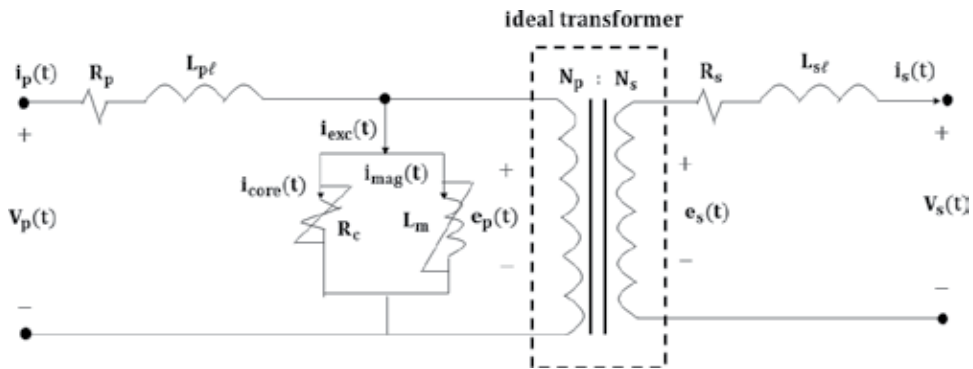


Figure 8. General harmonic model of a transformer.

rents do not cancel out, but instead add cumulatively in the neutral conductor at a frequency of predominately 180 Hz (3rd harmonic), overheating the transformers and occasionally causing overheating and burning of neutral conductors. Typically, the uses of appropriate “K factor” rated units are recommended for nonlinear loads.

### 5.3. Effects on the capacitors

The capacitors are used in the electrical power systems for voltage control, reactive power compensation, filtering of signals, and in many cases power-factor correction. For this latter topic, there are two different types of power factor that must be considered in the case when voltage and current waveforms are nonsinusoidal. The first type of power factor is the input displacement factor (IDF), which refers to the cosine of the angle between the fundamental frequency of the voltage and current waveforms. If the harmonic content increases, then the distortion factor will decrease as the total power factor (PF) being the product of the input displacement factor and the distortion factor.

The use of systems and control equipment have increased considerably since the 1990s including electronic loads fed by residential feeders, arc furnaces in industrial networks, etc, resulting in a power quality poor of electrical power systems and an increase in the harmonic disturbances operating to low power-factors, which causes increases line losses, poor voltage regulation, and other factors. The capacitor is very important in the harmonic analysis because it provides the response system at fundamental and harmonic frequencies and it is in the capacitor banks where the issues with harmonics often occur resulting in fuse blowing and/or capacitor failure.

For this reason, it is important to know whether capacitors form either series or parallel resonant circuits, which increase and distort their electrical variables. There are many solutions to these problems: changing location capacitors as well as its size, producing an alteration in the frequency of system response, also altering source characteristics, and designing harmonic filters. The presence of series/parallel resonances can result in unacceptable stresses regarding the equipment installation so it is recommended to use joint capacitor banks for power-factor correction and reactive power compensation, although excessive use of capacitors in

the power networks causes problems that affect power quality, especially in the presence of harmonics.

In summary, the capacitors are important components within an electrical power system because they offer power-factor correction, voltage control/regulation, and filters with special design although its use continue may cause problems associated with capacitor switching and series resonance. In most cases, triplen (multiples of 3) and even harmonics do not exist in a three-phase system because they are uncoupled (see **Figure 9**). There are some cases in which harmonic triplen of zero sequence may exist within the three-phase power systems because the triplen harmonics are very dominant in single-phase systems, unlike even harmonics because these are mostly negligibly small within single- and three-phase systems. Both factors are equal when harmonic is not present.

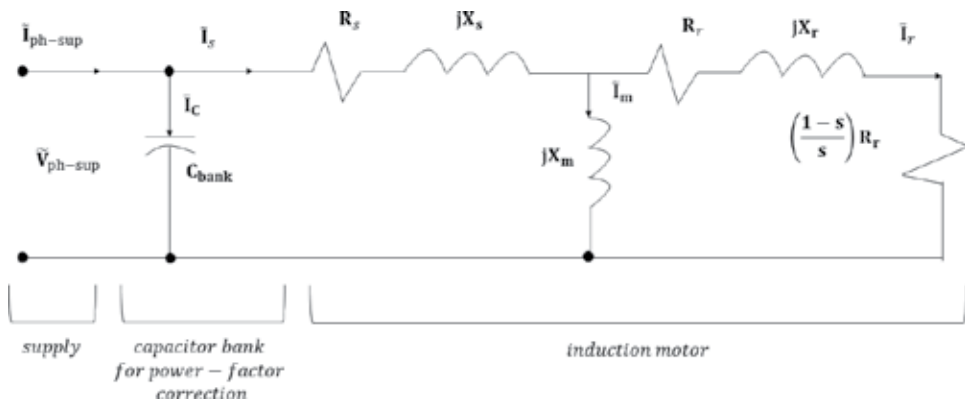


**Figure 9.** Equivalent circuit of induction motor with displacement FP correction capacitor bank.

### 5.4. Effects on rotating machines

Fourier Transform offers a method that allows the expression of the nonsinusoidal periodic input signals as a sum of the sinusoids. Each one of these sinusoidal components is supposed to be applied to a linear system. Their particular response as a sinusoid is determined by means of phasors and  $H(j\omega)$ . If there is a unique pulse instead of a stream of periodic repetitive waves, the phasors and the Fourier series cannot be used to express such pulses. In order to express them, the Fourier series needs to be generalized in the Fourier Transform. In this way, the series can operate not only with all periodic input signals, but also with many other types of nonperiodic pulses.

The Fourier Transform is the analytical tool that finds the way in which such functions of time, for example the sinusoids, the impulses, etc., can be expressed in the domain of frequency.

This Fourier Transform can be used for the analysis and the detection of failure in induction machines. The most likely faults in induction machines are broken rotor bars, bearing damage, short circuits, and eccentricity. Most failures in induction machines can be sorted in two groups: isolation failures and mechanical failures. The coil short-circuits in the stator winding are characteristic in isolation failures, while mechanical faults has to do with the rotor. Among

the most significant rotor failures are the bearing damage, rotor broken bars and rings, static and dynamics eccentricities, voltage unbalances, etc. The electrical faults in machines are dominated by failures in bearings and stator coils. These failures are summarized in **Figure 10**.

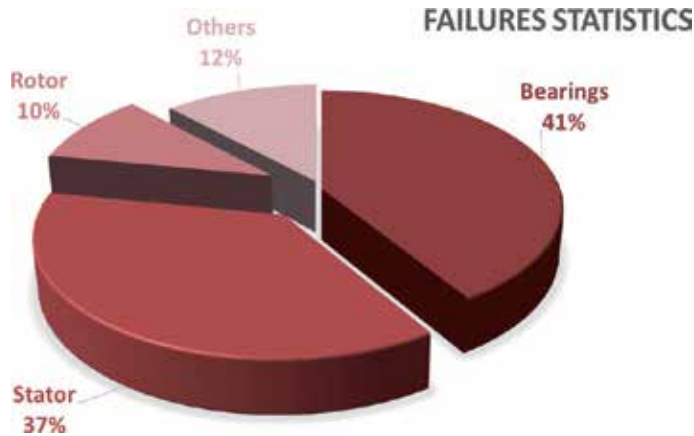


**Figure 10.** Failure statistics in induction machines.

To establish the level of failures in the induction machines it is necessary to develop a methodology that consists of finding the machine slip using only the stator current. This parameter could be used for many applications, but in this case the focus is on fault detection based on the fact that an unbalanced machine, when supplied with a three-phase balanced voltage, produces specific components in the stator current whose magnitude and frequency depends on the asymmetry level and the nature of the fault. This is based on the current signal spectrum decomposition, analyzed via the Fourier Transform. Another very important aspect of induction machines to establish the level of failures is the detection monitoring of the mechanical faults [22–24]. Vibration monitoring is the most reliable method for assessing the overall health of a rotor system. The spectral analysis of vibrations has been used in rotating machines fault diagnosis for decades as this method, in time domain, is more effective for calculating some simple quantities as root mean square (RMS), kurtosis, crest factor, etc., but the problem is that they often do not offer enough information on the vibrations for a thorough diagnosis [25].

To the analysis of the systems in the harmonic domain of the polyphase AC, the concept was presented by Nikola Tesla [26] in 1888, there was a competition between AC and DC systems. Steinmetz [27], Richter [28], Kron [29], Veinott [30], Schuisky [31], Bodefeld [32], Alger [33], Umans et al. [34], Lyon [35], and Say [36] were the pioneers in the study of single- and three-phase induction machines which published in this area of expertise, being the most recent Matsch [37], Chapman [38], and Fuchs et al. [39, 40].

The studies were carried out under transient and steady-state conditions. Currently, electrical power systems are affected by the insertion of nonlinear components and loads and the three-phase machines are subjected to nonsinusoidal operating conditions not taking into account the harmonic signals generated in voltage and/or current on three-phase induction

machines causing a poor power quality and these in turn, abnormal operation, static and dynamic rotor eccentricities, excessive saturation of iron cores, one-sided magnetic pull due to DC currents, shaft fluxes and associated bearing currents, mechanical vibrations, dynamic instability when connected to weak systems, increasing copper losses, reduction of overall efficiency, generation of inter- and subharmonic torques, production of (harmonic) resonance and ferroresonance conditions, failure of insulation due to high voltage stress caused by quick changes in supply current and lightning surges, unbalanced operation due to an imbalance of power systems voltage caused by harmonics, etc. For that reason, it is necessary to analyze the machine and get a harmonic model of induction machine for loss calculations, harmonic torque calculations, and harmonic power flow studies.

**5.5. Three-phase induction machine model**

**Figure 11** illustrates an equivalent circuit simple and accurate frequency-based linear model to fundamental frequency and **Figure 12** shows a complete linear of a three-phase induction machine for harmonic analysis. The nomenclature is the following:  $\omega_{es}$  is the fundamental angular frequency (or velocity) and  $s$  is the fundamental slip. The core-loss resistance are neglected,  $L_M$  is the (linear) magnetizing inductance,  $r_s, L_{ls}, r'_r \wedge L_{lr}$  are the stator and the rotor (reflected to the stator) resistances and leakage inductances, respectively [41].

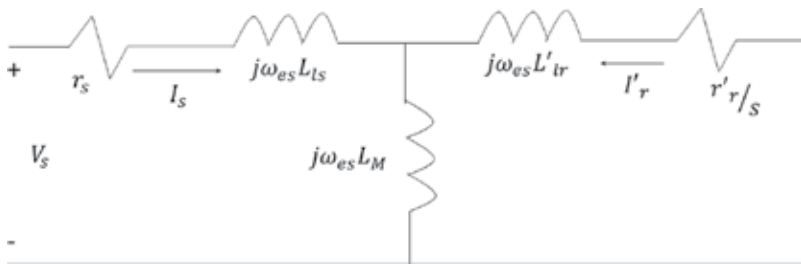


**Figure 11.** Complete linearity of a three-phase induction machine for sinusoidal analysis.

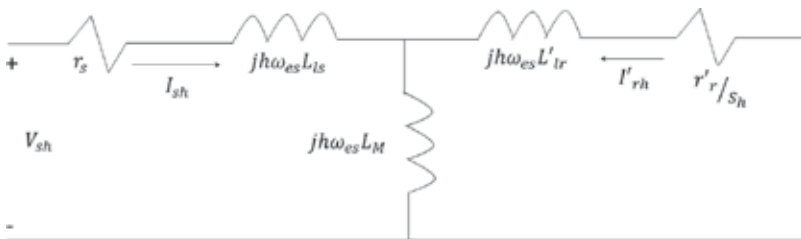


**Figure 12.** Complete linearity of a three-phase induction machine for harmonic analysis.

When the concept changes, i.e., when it is a doubly fed induction machine, the harmonics can be generated by both windings of the machine: harmonics generated in the stator winding voltage source with frequencies  $f_{sh} = hf_{es}$  and harmonics generated in the rotor winding voltage source with frequencies  $f_{rh} = hf_{er}$ , where  $h$  is an integer number. However, it is necessary to know

that the harmonics induced in the rotor winding, due to harmonics in the stator winding, are not harmonics of the rotor fundamental frequency and therefore they cannot be called harmonics but subharmonic or interharmonic.

When a harmonic voltage source with frequency  $hf_{es}$  fed to the stator winding of the induction machine the rotor is short circuited. This machine's model is a well-accepted steady-state, with all the parameters seen from the stator, as showed in the circuit in **Figure 12**. Then the equation that represents the circuit is:

$$\begin{bmatrix} V_{sh} \\ 0 \end{bmatrix} = \begin{bmatrix} r_s + jh \omega_{es} (L_{ls} + L_M) & jh \omega_{es} L_M \\ jh \omega_{es} L_M & r_r/s_h + jh \omega_{es} (L_{lr} + L_M) \end{bmatrix} \begin{bmatrix} I_{sh} \\ I_{rh} \end{bmatrix} \quad (6)$$

$$s_h = \frac{\pm h \omega_{es} - \omega_r}{\pm h \omega_{es}} \quad (7)$$

where:

The sign - is used for negative and + for positive sequence, respectively. Harmonics have different behavior for each sign, i.e., for negative is  $h = 3k - 1$  for  $k = 1, 2, 3, \dots$  and the positive sequence behavior are  $h = 3k + 1$  where the most common harmonics are the 5, 7, 11, 13, 15, 17... known as the characteristic harmonics. Solving the equation of the voltage equation we obtain the harmonic phasors current of a harmonic voltage source in the stator winding. If it analyzed it in its own winding with an analysis in the time domain, we have,

$$i_{sh} = |I_{sh}| \cos(h \omega_{es} t + \varphi_{sh}) \quad (8)$$

$$i_{rh} = I_{rh} \vee \cos(s_h h \omega_{es} t + \varphi_{rh} \mp \theta_{ef}) \quad (9)$$

If zero sequence corresponding to the harmonic  $h = 3k$ , then the circuit of **Figure 12** is invalid since the induction machine zero sequence works with two uncoupled windings observed in **Figure 13**, where the voltages are given by,

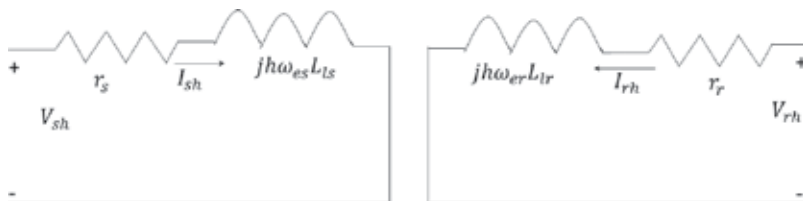


**Figure 13.** Induction machine triplex harmonic model seen from stator.

$$V_{sh} = (r_s + jh \omega_{es} L_{ls}) I_{sh} \quad (10)$$

$$V_{rh} = (r_r + jh \omega_{er} L_{lr}) I_{rh} \quad (11)$$

The solution of the last equation gives the harmonic current phasors because of their respective voltage sources: i.e.,  $I_{sh} = |I_{sh}| \angle \phi_{sh}$  and  $I_{rh} = |I_{rh}| \angle \phi_{rh}$ . Their representations in the time domain in their respective windings are:

$$i_{sh} = |I_{sh}| \cos(h \omega_{es} t + \phi_{sh}) \quad (12)$$

$$i_{rh} = |I_{rh}| \cos(h \omega_{er} t + \phi_{rh}) \quad (13)$$

The general solution for balance conditions including voltage sources at fundamental and harmonic frequencies in the stator and rotor are:

$$i_s = \sum_{h=1}^H |I_{sh}| \cos(h \omega_{es} t + \phi_{sh}) + \sum_{h=1,3k+1}^H |I'_{sh}| \cos(s_{rh} h \omega_{er} t + \phi'_{sh} + \theta_{ef}) + \sum_{h=3k-1}^H |I'_{sh}| \cos(s_{rh} h \omega_{er} t + \phi'_{sh} - \theta_{ef}) \quad (14)$$

The first summation includes all harmonic current generated in the nonsinusoidal source voltage in the stator winding, which contains positive, negative, and zero sequence harmonics. The second summation includes all the current harmonics generated for the induction effect of the positive sequence voltage source harmonics in the rotor winding. The third summation includes all the current harmonics generated for induction effect of the negative sequence voltage source harmonics in the rotor winding [42]. This procedure is the same for the rotor winding:

$$i_r = \sum_{h=1}^H |I_{rh}| \cos(h \omega_{er} t + \phi_{rh}) + \sum_{h=1,3k+1}^H |I'_{rh}| \cos(s_{rh} h \omega_{es} t + \phi'_{rh} - \theta_{ef}) + \sum_{h=3k-1}^H |I'_{rh}| \cos(s_{rh} h \omega_{es} t + \phi'_{rh} + \theta_{ef}) \quad (15)$$

To validate the proposed model, a three-phase induction machine of ¼ H.P., 208 V, and 1.3 A is utilized for experimental validation. It is important to mention that a three-phase programmable voltage source of 200/208V at 50/60Hz and 24A capable of generating harmonic signals is used as the main voltage source to supply induction machine.

**Table 1** shows the parameters of the induction machine. The proposed model in steady-state model is compared with the dynamic equations of the induction machine and the results of experimentation. It should be considered that for all the study cases a mechanical torque of 0.3 N·m was used.

The results from the proposed model (steady-state) are compared with those obtained in the laboratory (measurement) and compared with those obtained from the simulated complete model (dynamic), once the steady-state has been attained.

### 5.5.1. Case I. Stator-fed induction machine and rotor short-circuited

In this case, a sinusoidal three-phase balanced voltage source of 80 V at 60 Hz in the stator winding excites the induction machine with the connections in the rotor in short-circuit. The

results of the waveforms of the stator and rotor harmonic currents of both the simulation and the experimentation are shown in **Figures 14** and **15**, respectively and we can see that the results match in the analysis.

Parameters	0.23 H.P/175 W
Number of poles	4
Inertia	0.0068 kg·m <sup>2</sup>
Nominal line current	1.3 Amps
Nominal line-to-line voltage	120 Vrms
Nominal torque	2.481 N·m
Nominal frequency	60 Hz
Stator resistance, $r_s$	14 Ω
Stator inductance, $L_{ls}$	9 H
Rotor resistance, $r_r$	7.7 Ω
Rotor inductance, $L_{lr}$	9 H
Magnetizing inductance, $L_{mr} = L_{ms}$	155 H
Rotor speed	1500 rpm

**Table 1.** Induction machine parameters.

### 5.5.2. Case II. Stator-fed induction machine at harmonic frequencies

For this case, the nonsinusoidal voltage source at 120 V at 60 Hz which excites the stator winding contains harmonic of the third, fifth and seventh order while the rotor winding is short-circuited. The voltage harmonic components magnitude and angle are  $40 \angle 113^\circ$  V,  $24 \angle 42.85^\circ$  V, and  $17.1428 \angle 137.15^\circ$  V for the third, fifth, and seventh harmonic, respectively. **Figures 16** and **17** show the resulting currents in the stator and rotor of the induction machine. The results in steady-state clearly match those obtained by measurement and with the dynamic model.

The harmonic slips for each harmonic component are  $s_{0.3342}$ ,  $s_5 = 1.1332$  and  $s_7 = 0.9047$ . The induced frequencies in the rotor are obtained with  $(s_h \times h \times \omega_{es})/2\pi$ : the fundamental frequency in the stator induces  $(0.3342 \times 377)/2\pi = 20$  Hz in the rotor; the fifth harmonic in the stator induces  $(1.1332 \times 5 \times 377)/2\pi = 340$  Hz in the rotor; and the seventh harmonic in the stator induces  $(0.9047 \times 7 \times 377)/2\pi = 380$  Hz in the rotor. These frequencies are not harmonics of the fundamental frequency in the stator (integer multiples of 60 Hz), but the seventeenth and nineteenth harmonic of the rotor fundamental frequency (integer multiples of 20 Hz). These frequencies induced in the rotor cannot be called as harmonic frequencies are not integer multiples of the fundamental frequency but are to be noted that the harmonic seventeenth and nineteenth of the fundamental frequency of the rotor.

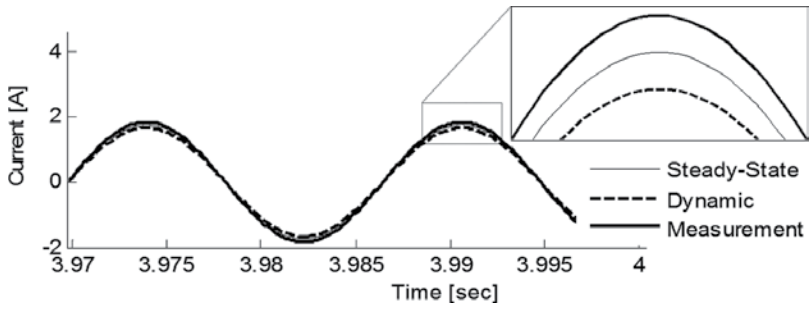


Figure 14. Stator current at fundamental frequency.

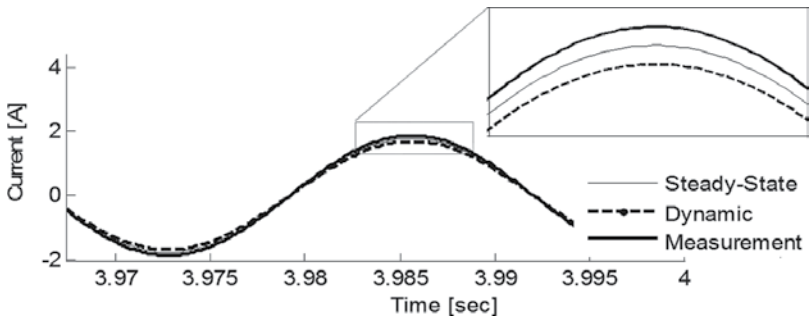


Figure 15. Rotor current at fundamental frequency.

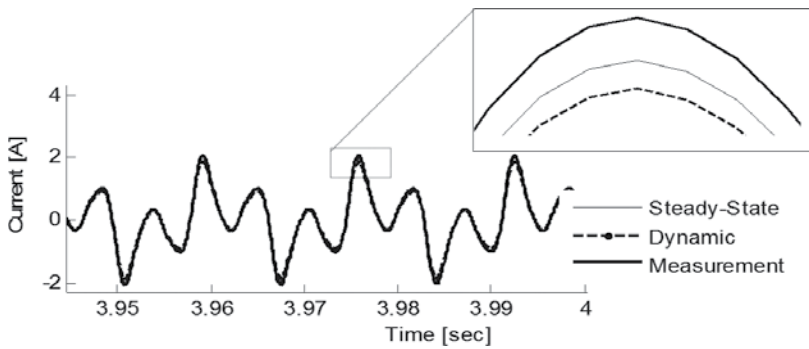


Figure 16. Stator current at harmonic frequencies.

5.5.3. Case III. Stator-fed induction machine with six-pulse voltage source

It is considered that a nonsinusoidal three-phase balanced voltage source of 120 V at 60 Hz excites to the induction machine in the stator winding with the rotor windings in short-circuit. The voltage source is six-pulse as shown in **Figure 18** with harmonics components in **Table 2**.

Figures 19 and 20 show the current waveforms obtained from measurement and from simulation.

Table 3 summarizes the harmonic currents in the induction machine for the case studies. Note that the waveform current has been attained from the current shown in this table, which have been obtained from the solution of the equations mentioned in the previous section.

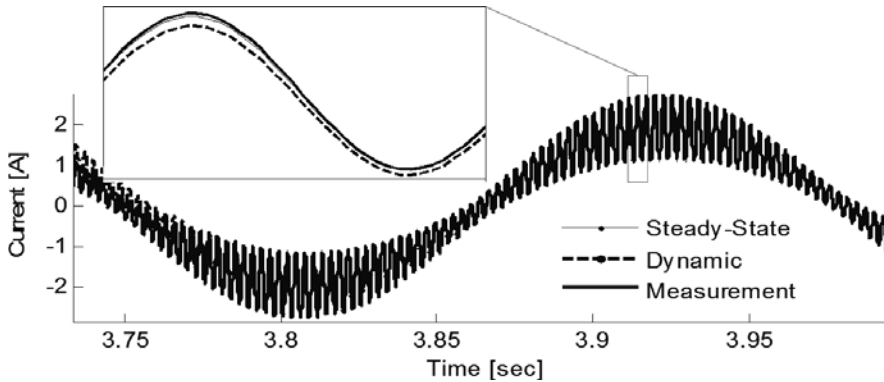


Figure 17. Rotor current at harmonic frequencies.

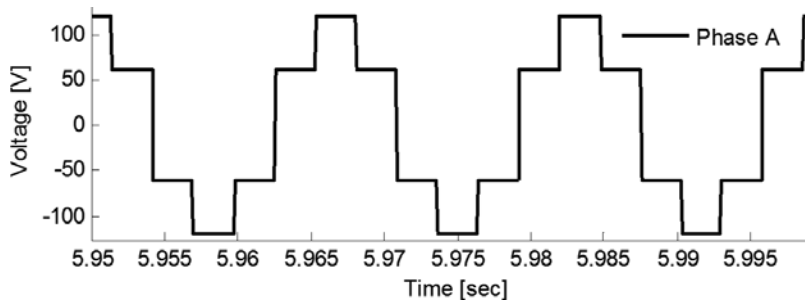


Figure 18. Three-phase voltage source.

	Harmonic components							
	5th	7th	11th	13th	17th	19th	23th	25th
Voltage (%)	20.3	13.8	9.35	7.17	6.3	4.6	4.4	2.3
Degrees	163	88.1	175	83.7	-17	88	-166	101

Table 2. Harmonic components.

Harmonic analysis in the electrical power systems becomes increasingly necessary since by the proliferation of nonlinear loads the problems of power quality and especially the harmonics signals are more apparent. The proposed model analyzes the behavior of the induction machine under nonsinusoidal operating conditions for the inclusion of harmonics signals in the stator winding voltage source. In the end, the results of the steady-state proposed model

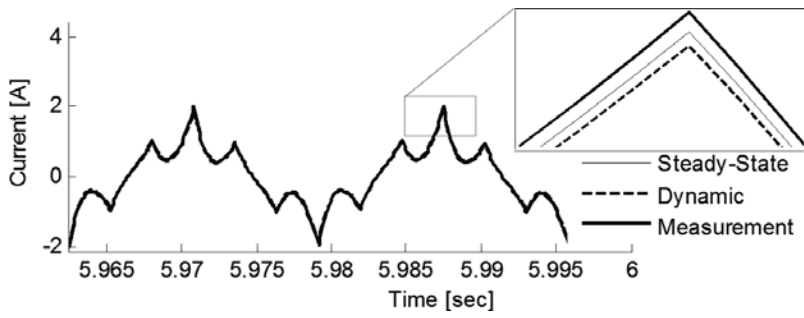


Figure 19. Stator current with six-pulse voltage source.

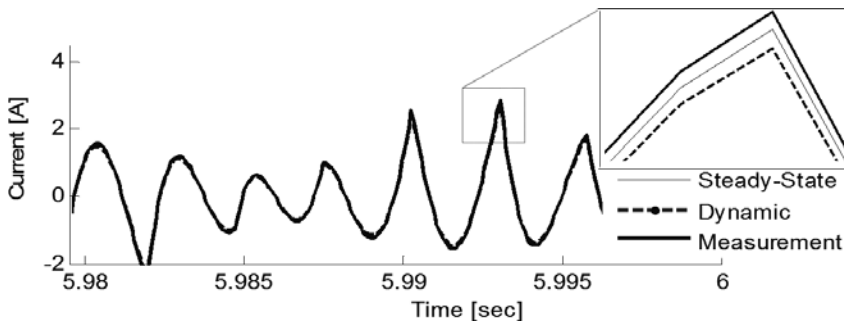


Figure 20. Rotor current with six-pulse voltage source.

Case study	Stator current				Rotor current			
	Seq. (+,-,0)	Magnitude	Angle	Frequency (Hz)	Sequence (+,-,0)	Magnitude	Angle	Frequency (Hz)
Case I	+	0.588	-0.72	60	+	3	2.57	19.8
Case II	+	0.588	0.72	60	+	3	2.57	19.8
	+	0.111	-1.39	420	+	0.2	1.8	322.9
	-	0.216	-1.34	300	-	0.17	1.74	397
	0	1.07	-1.09	180				
Case III	+	2.1	14.1	60	+	1.8	40.9	9.6
	-	0.79	4.2	300	-	1.32	222.9	48
	+	0.38	178	420	+	2.81	-42.1	67.2
	-	0.152	166.9	660	-	0.80	28.6	105.6
	+	0.115	-16.4	780	+	0.56	117.5	124.8
	-	0.067	-24.3	1020	-	0.15	204	163.2
	+	0.057	150.1	1140	+	0.24	-63.3	182.4
	-	0.032	142.1	1380	-	0.12	14.1	220.8
	+	0.029	-38.6	1500	+	0.13	92.2	240

Table 3. Summary of the harmonic currents for the cases studies.

are compared with the results obtained in transient-state and both models are validated by experimental tests in the laboratory getting the same results for each case validating the precision and accuracy of the proposed model besides that this model is proper for harmonic and nonharmonic analysis of the induction machine exciting only to the stator winding. This model also can be used for “harmonic” analysis in an electrical power system.

## Author details

Emmanuel Hernández Mayoral\*, Miguel Angel Hernández López, Edwin Román Hernández, Hugo Jorge Cortina Marrero, José Rafael Dorrego Portela and Victor Ivan Moreno Oliva

\*Address all correspondence to: [emanuel.mayoral7@gmail.com](mailto:emanuel.mayoral7@gmail.com)

Universidad del Istmo, Santa Cruz, Tehuantepec, Oaxaca, Mexico

## References

- [1] Arrillaga, J.; Watson, N. R.; and Chen, S. *Power System Quality Assessment*. 2nd ed. University of Michigan: John Wiley & Sons, 2000; 2007. 300 p. DOI: 0471988650.
- [2] Gonen T. *Electrical Power Transmission System Engineering: Analysis and Design*, 3rd ed. California State University, Sacramento: CRC Press; 2015. 1093 p. DOI: 1482232235.
- [3] Dommel, H. Digital computer solution of electromagnetic transients in single and multi-phase network. *IEEE Transactions on Power Apparatus and Systems*. 2007;**PAS-88**(4):388–399. DOI: 10.1109/TPAS.1969.292459.
- [4] Dommel, H. Transformer models in the simulation of electromagnetic transient. In: IEEE, editor. *5th Power Systems Computation Conference*; September 1–5; Cambridge. England: Paper 3.1/4; 1975. pp. 1–16.
- [5] Hatziantoniou, C.; Galanos, G. D.; and Miliadis-Argitis, J. An incremental transformer model for the study of harmonic overvoltages in weak AC/DC systems. *IEEE Transactions on Power Delivery*. 1988;**3**(3):1111–1121.
- [6] Dolinar, D.; Pihler, J.; and Grcar, B. Dynamic model of a three-phase power transformer. *IEEE Transactions on Power Delivery*. 1993;**8**(4):1811–1819.
- [7] Leon, F.; and Semlyen, A. Complete transformer model for electromagnetic transients. *IEEE Transactions on Power Delivery*. 1994;**9**(1):231–239. DOI: 10.1109/61.277694.
- [8] García, S.; Medina, A.; and Pérez, C. A state space single-phase transformer model incorporating nonlinear phenomena of magnetic saturation and hysteresis for transient and periodic steady-state analysis. *IEEE Power Engineering Society Summer Meeting*, 2000. 2000;**4**:2417–2421. DOI: 10.1109/PESS.2000.867369.
- [9] Huang, S.-R.; Chung, S. C.; Chen, B.-N.; and Chen, Y.-H. A harmonic model for the nonlinearities of single-phase transformer with describing functions. *IEEE Transactions on Power Delivery*. 2003;**18**(3):815–820. DOI: 10.1109/TPWRD.2003.813878A.

- [10] Medina, A.; and Arrillaga, J. Generalised modelling of power transformers in the harmonic domain. *IEEE Transactions on Power Delivery*. 2002;7(3):1458–1465. DOI: 10.1109/61.141865.
- [11] Semlyen, A.; Acha, E.; and Arrillaga, J. Newton-type algorithms for the harmonic phasor analysis of nonlinear power circuits in periodical steady state with special reference to magnetic nonlinearities. *IEEE Transactions on Power Delivery*. 2002;3(3):1090–1098. DOI: 10.1109/61.193891.
- [12] Pedra, J.; Corcoles, F.; Sainz, L.; and López R. Harmonic nonlinear transformer modelling. *IEEE Transactions on Power Delivery*. 2004;19(2):884–890. DOI: 10.1109/TPWRD.2004.825254.
- [13] Dugui, W.; and Zheng, X. Harmonic model of power transformer. In: *POWERCON '98. 1998 International Conference on, editor. Power System Technology, 1998. Proceedings; 18–21 Aug; Hangzhou, China. IEEE; 1998.* DOI: 10.1109/ICPST.1998.729244.
- [14] Greene, J. D.; and Gross, C. A. Nonlinear modelling of transformers. *IEEE Transactions on Industry Applications*. 1988; 24(3):434–438. DOI: 10.1109/28.2892.
- [15] Fuchs, E. F.; Masoum, M. A. S.; and Roesler, D. J. Large signal nonlinear model of anisotropic transformers for nonsinusoidal operation. I.  $\lambda$ -i characteristics. *IEEE Transactions on Power Delivery*. 1991;6(1):1874–1886. DOI: 10.1109/61.103773.
- [16] Masoum, M. A. S.; Fuchs, E. F.; and Roesler, D. J. Large signal nonlinear model of anisotropic transformers for nonsinusoidal operation. II. Magnetizing and core-loss currents. *IEEE Transactions on Power Delivery*. 1991; 6(4):1509–1516. DOI: 10.1109/61.97686.
- [17] Stensland, T.; Fuchs, E. F.; Grady, W. M.; and Doyle, M. T. Modelling of magnetizing and core-loss currents in single-phase transformers with voltage harmonics for use in power flow. *IEEE Transactions on Power Delivery*. 1997; 12(2):768–774. DOI: 10.1109/61.584366.
- [18] Yamada, S.; Bessho, K.; and Lu, J. Harmonic balance finite element method applied to nonlinear AC magnetic analysis. *IEEE Transactions on Magnetics*. 1989; 25(4):2971–2973. DOI: 10.1109/20.34341.
- [19] Silvester, P.; and Chari, M. V. K. Finite element solution of saturable magnetic field problems. *IEEE Transactions on Power Apparatus and Systems*. 1970; PAS-89(7):1642–1651. DOI: 10.1109/TPAS.1970.292812.
- [20] Enokizono, M. and Soda, N. Finite element analysis of transformer model core with measured reluctivity tensor. *IEEE Transactions on Magnetics*. 1997; 33(5):4110–4112. DOI: 10.1109/20.619679.
- [21] Wu, J.-C.; Jou, H.-L.; Wu, K.-D.; and Shen, N. C. Power converter-based method for protecting three-phase power capacitor from harmonic destruction. *IEEE Transactions on Power Delivery*. 2004;19(3):1434–1441. DOI: 10.1109/TPWRD.2004.829926

- [22] Albrecht, P. F.; Appiarius, J. C.; McCoy, R. M.; Owen, E. L.; and Sharma, D. K. Assessment of the reliability of motors in utility applications – updated. *IEEE Transactions on Energy Conversion*. 1986;**EC-1**(1):39–46. DOI: 10.1109/TEC.1986.4765668.
- [23] Thompson, W. T. (1999). *A Review of On-Line Condition Monitoring Techniques for Three-Phase Squirrel-Cage Induction Motors – Past, Present and Future*, The Robert Gordon University, Schoolhill, Aberdeen, Scotland.
- [24] Eschmann, P. editor. *Ball and Roller Bearings: Their Theory, Design, and Application*. 1st ed. University of Michigan: Heyden; 2007. 375 p.
- [25] Harris, T. A. editor. *Rolling Bearing Analysis*. 4th ed. University of Michigan: Wiley; 2001. 1086 p.
- [26] Neidhoefer, G; “Early three-phase power,” *IEEE Power & Energy*, vol. 5, no. 5, September/October 2007, pp. 88-112.
- [27] Steinmetz, C. P. *Steinmetz on Induction-Motor*. New York: AIEE Trans; 1898. 300 p.
- [28] Richter, R. *Elektrische Maschinen: Zweiter Band: Synchronmaschinen und Einankerumformer*. 3rd ed. Germany: Springer-Verlag; 2013. 707 p. DOI: 3034841396.
- [29] Kron, G. The generalized theory of electrical machinery. *AIEE Transactions*. 1930;**49**(4):666-683.
- [30] Veinott, C. G; “Performance calculation of induction motors,” *AIEE Transactions*, 1932, pp. 743-755.
- [31] Schuisky, W.; *Calculation of electrical machines*, Springer-Publishing, Wien, 1960.
- [32] Bödefeld, T.; and Sequenz, H.; *Electrical machines*, Springer-Publishing, Wien, 1962.
- [33] Alger, P. L. *The Nature of Polyphase Induction Machines*. 1st ed. University of Michigan: John Wiley & Sons; 2006. 397 p.
- [34] Umans, S.; Fitzgerald, A.; and Kingsley, C. *Electric Machinery*. 5th ed. New York: McGraw-Hill Higher Education; 2013. 631 p.
- [35] Lyon, W. V. *Transient Analysis of Alternating-current Machinery: An Application of Method of Symmetrical Components*. 1st ed. New York: Technology Press of Massachusetts Institute of Technology, and Wiley; 2006. 310 p.
- [36] Say, M. G. *Alternating Current Machines*. 5th ed. Michigan: Wiley; 1983. 632 p.
- [37] Matsch, L. W.; and Morgan, J. D. *Electromagnetic and Electromechanical Machines*. 3rd ed. Michigan: Wiley; 1986. 592 p.
- [38] Chapman, S. *Electric Machinery Fundamentals*. 3rd ed. Massachusetts: McGraw-Hill Companies, Incorporated; 2005. 746 p.

- [39] Fuchs, E. F. Optimization of Induction Motor Efficiency: Single-Phase Induction Motors. 4th ed. Colorado: Electric Power Research Institute; 1985. 385 p.
- [40] Blanus, B. New Trends in Efficiency Optimization of Induction Motor Drives. 1st ed. Spain: INTECH Open Access; 2010. 953 p.
- [41] Krause, P. C.; Wasynczuk, O.; and Sudhoff, S. D. Analysis of Electric Machinery. 2nd ed. Michigan: IEEE Press; 1995. 564 p.
- [42] Hernandez , E.; and Madrigal, M. A step forward in the modeling of the doubly-fed induction machine for harmonic analysis. IEEE Transactions on Energy Conversion. 2014;**29**(1):149–157. DOI: 10.1109/TEC.2013.2290297.

---

# High Resolution Single-Chip Radix II FFT Processor for High-Tech Application

---

Rozita Teymourzadeh

Additional information is available at the end of the chapter

<http://dx.doi.org/10.5772/66745>

---

## Abstract

Electrical motors are vital components of many industrial processes and their operation failure leads losing in production line. Motor functionality and its behavior should be monitored to avoid production failure catastrophe. Hence, a high-tech DSP processor is a significant method for electrical harmonic analysis that can be realized as embedded systems. This chapter introduces principal embedded design of novel high-tech 1024-point FFT processor architecture for high performance harmonic measurement techniques. In FFT processor algorithm pipelining and parallel implementation are incorporated in order to enhance the performance. The proposed FFT makes use of floating point to realize higher precision FFT. Since floating-point architecture limits the maximum clock frequency and increases the power consumption, the chapter focuses on improving the speed, area, resolution and power consumption, as well as latency for the FFT. It illustrates very large-scale integration (VLSI) implementation of the floating-point parallel pipelined (FPP) 1024-point Radix II FFT processor with applying novel architecture that makes use of only single butterfly incorporation of intelligent controller. The functionality of the conventional Radix II FFT was verified as embedded in FPGA prototyping. For area and power consumption, the proposed Radix II FPP-FFT was optimized in ASIC under Silterra 0.18  $\mu\text{m}$  and Mimos 0.35  $\mu\text{m}$  technology libraries.

**Keywords:** FFT, butterfly, Radix, floating point, high speed, FPGA, Embedded, VLSI

---

## 1. Introduction

The prevalent subject of Fourier analysis encompasses a vast spectrum of mathematics where parts may appear quite different at first glance. In Fourier analysis, the term Fourier transform often refers to the process that decomposes a given function into the harmonics domain. This process results in another function that describes what frequencies are in the original function.

---

Meanwhile, the transformation is often given a more specific name depending upon the domain and other properties of the function being transformed.

## 2. Fourier transform fundamental

Fourier transform was introduced with the main concepts of discrete Fourier transform (DFT) [1] in the heart of most DSP processor. The DFT is a Fourier representation of a finite-length sequence which is the most important fundamental operation in digital signal processing and communication system [2, 3]. However, the computation complexity of the direct evaluation of an  $N$ -point DFT involves a long phase computational time and large power consumption [4]. As a result of these problems, it is important to develop a fast algorithm. There are numerous viewpoints that can be taken toward the derivation and interpretation of the DFT representation of a finite-duration sequence. The sequence of  $\tilde{x}(n)$  that is periodic with period  $N$  so that  $\tilde{x}(n) = \tilde{x}(n + kN)$  functions for any integer value of  $k$ . It is possible to represent  $\tilde{x}(n)$  in terms of Fourier series that is represented by the sum of sine and cosine values or equivalently complex exponential sequences with frequencies that are integer multiplies of the fundamental frequencies  $2\pi/N$  associated with the periodic sequence. The same representation can be applied to finite-duration sequence. The resulting Fourier representation for finite duration sequences will be referred to as the DFT. Sequence of length  $N$  by a periodic sequence can be represented by a periodic sequence with period  $N$ , one period of which is identical to the finite-duration sequence. The sampled sequence signal in frequency is defined as

$$X(\omega) = \sum_{n=-\infty}^{\infty} x(n)e^{-j\omega n} \quad (1)$$

The DFT  $X(\omega)$  is a function of continuous-frequency variable  $\omega$ , and the summation in Eq. (1) extends toward positive and negative infinitively. Therefore, the DFT is a theoretical Fourier transform of a digital signal. However, it cannot be implemented for real applications. It is the sample of the signal in time domain at a particular time and can be expressed as:

$$x(n) = \int_0^{\infty} x(t)\delta(t - t_n) \quad (2)$$

The frequency analysis of a finite-length sequence is equal to the sample of continuous frequency variable  $\omega$  at  $N$  equally spaced frequencies  $\omega_k = 2\pi k/N$  for  $k = 0, 1, 2, \dots, N - 1$  on the unit circle. These frequency samples are expressed as:

$$X(k) = X(\omega_k), \quad \omega_k = \frac{2\pi k}{N} \quad (3)$$

$$X(k) = \sum_{n=0}^{N-1} x(n)e^{-\frac{j2\pi kn}{N}} = \sum_{n=0}^{N-1} x(n)W_N^{kn}, \quad k = 0, 1, \dots, N - 1$$

where the twiddle factors are defined as:

$$W_N^{kn} = e^{-j\left(\frac{2\pi}{N}\right)kn} = \cos\left(\frac{2\pi kn}{N}\right) - j \sin\left(\frac{2\pi kn}{N}\right) \quad (4)$$

The DFT is based on the assumption that the signal  $x(n)$  is periodic. Therefore,  $X(k)$  for  $k = 0, 1, \dots, N - 1$  can uniquely represent a periodic sequence  $x(n)$  of period  $N$ . The inverse DFT is the

reversed process of the DFT. It converts the frequency spectrum  $X(k)$  back to the time domain signal  $x(n)$  [5]:

$$x(n) = \frac{1}{N} \sum_{k=0}^{N-1} X(k)e^{j\frac{2\pi kn}{N}} = \frac{1}{N} \sum_{k=0}^{N-1} X(k)W_N^{-kn}, \quad n = 0, 1, \dots, N-1 \quad (5)$$

Direct computation of an  $N$ -point DFT according to Equation Eq. (5) requires  $N(N-1)$  complex additions and  $N(N-1)$  complex multiplications. The complexity for computing an  $N$ -point DFT is therefore  $O(N^2)$ . High computation complexity in DFT algorithm and need for having efficient Fourier processor leads for introduction of a fast Fourier transform (FFT) processor.

### 2.1. Fast Fourier transform (FFT) algorithm

In 1965 Cooley and Tukey [6] developed the use of FFT in order to save time and avoid unnecessary complex calculations. FFT algorithm computes an  $N$ -point forward DFT or inverse DFT (IDFT) where  $N$  is 2 power of  $M$ . FFT algorithm divides  $N$ -point data into two  $N/2$ -point series and performs the DFT on series individually results in the order of  $O(N/2)^2$  complexity as compared with the original  $N^2$  operations in an  $N$ -point DFT. The process of dividing can be continued until a 2-point DFT is reached. FFT algorithm computes an  $N$ -point forward DFT or inverse DFT (IDFT) where  $N$  is 2 power of  $m$ . The FFT is a family of algorithms that efficiently implements the DFT. **Table 1** shows the comparison between the calculation of direct DFT and FFT when a different number of  $N$  is applied.

Number of points	DFT		Radix II FFT	
	Complex addition	Complex multiplication	Complex addition	Complex multiplication
$N$	$N(N-1)$	$N^2$	$N\log_2 N$	$(N/2)\log_2 N$
4	12	16	8	4
8	56	64	24	12
16	240	256	64	32
32	992	1024	160	80
64	4032	4096	384	192
127	16,256	16,384	896	448

**Table 1.** Computation complexity of DFT and FFT algorithm.

To calculate FFT algorithm, there are two well-known methods identified as DIT-FFT and DIF-FFT calculations [7–9]. In general, FFT processor has many types in terms of Fourier calculation. Taking into account different types of FFT algorithms are:

- Different Radixes, such as Radix II, Radix IV, etc., and mixed-radix algorithms.
- DIT and DIF.
- Real and complex algorithm.

Here, further detail is provided for DIT and DIF processor.

2.1.1.1. DIT Radix II butterfly FFT processor

The FFT structure divides input series into odd and even sequences. The number of stream in FFT is  $N = 2^m$  when  $m$  is a positive integer:

$$\begin{aligned} x_e(n) &= x(2m), m = 0, 1, \dots, \left(\frac{N}{2}\right)-1 \\ x_o(n) &= x(2m + 1), m = 0, 1, \dots, \left(\frac{N}{2}\right)-1 \end{aligned} \tag{6}$$

Based on the DFT definition and combination of the FFT concept,  $X(k)$  can be written as:

$$X(k) = \sum_{n=0}^{N-1} x(n)W_N^{kn} = \sum_{m=0}^{\left(\frac{N}{2}\right)-1} x(2m)W_N^{2mk} + \sum_{m=0}^{\left(\frac{N}{2}\right)-1} x(2m + 1) W_N^{(2m+1)k} \tag{7}$$

Since  $W_N^{2mk} = W_{N/2}^{mk}$ , the equation will be simplified as:

$$X(k) = \sum_{m=0}^{\left(\frac{N}{2}\right)-1} x_e(m)W_{\frac{N}{2}}^{mk} + W_N^k \sum_{m=0}^{\left(\frac{N}{2}\right)-1} x_o(m)W_{\frac{N}{2}}^{mk} \quad k = 0, 1, \dots, N-1 \tag{8}$$

where  $W_N^k$  is complex twiddle factor with unit amplitude and different phase angles. The 8-point FFT utilizes the twiddle factors from  $W_N^0$  to  $W_N^7$ . The first twiddle factor  $W_N^0 = 1$ . All twiddle factors are distributed around the unit circle. **Figure 1** shows the twiddle factor for 8-point Fourier transform. The twiddle factor  $W_N^k$  repeats itself after every multiple of  $N$ . The twiddle factors are periodic and for 8-point FFT twiddle factor 0 and 8 are equal.

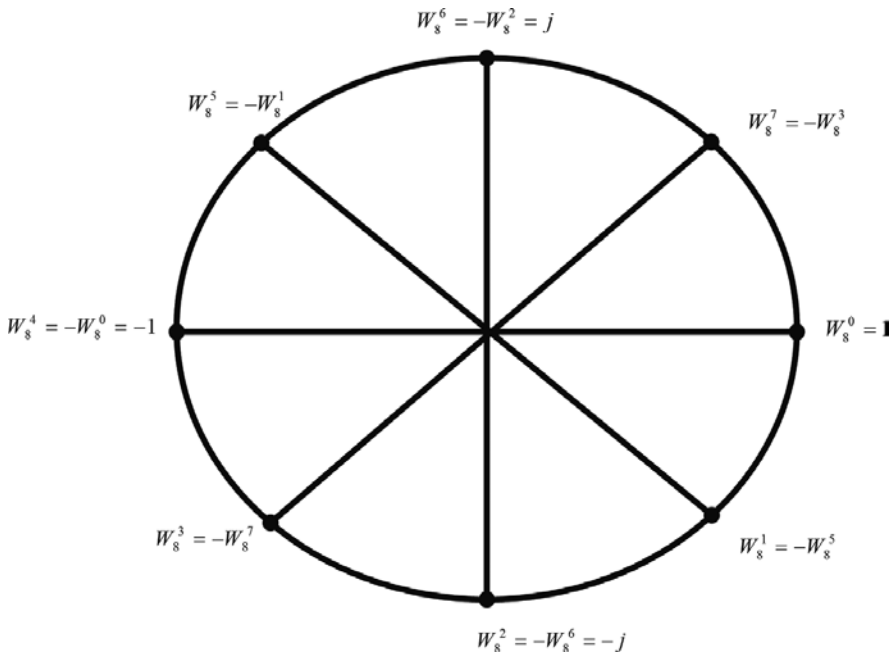
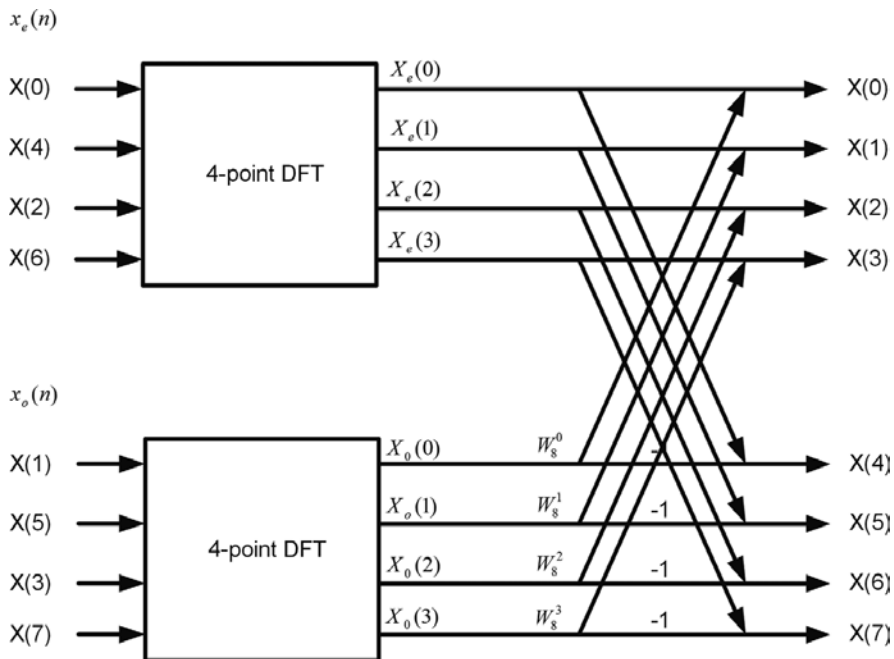


Figure 1. 8-point FFT twiddle factor.

By assuming  $X_e(k) = \sum_{m=0}^{(\frac{N}{2})-1} x_e(m) W_{N/2}^{mk}$  and  $X_o(k) = \sum_{m=0}^{(\frac{N}{2})-1} x_o(m) W_{N/2}^{mk}$ , this symmetric property provides a reduction in calculations as:

$$X(k) = \begin{cases} X_e(k) + W_N^k X_o(k), & k = 0, 1, \dots, (\frac{N}{2}) - 1 \\ X_e(k) - W_N^k X_o(k), & k = (\frac{N}{2}), \dots, N - 1 \end{cases} \quad (9)$$

Butterfly calculation is the fundamental concept of the FFT algorithm and 8-point butterfly structure is shown in **Figure 2**.



**Figure 2.** Decomposition of 8-point DIT FFT structure.

Radix II butterfly FFT is decomposed into  $M$  stages, where  $M = \log_2^N$ . In each stage,  $N/2$  complexes are multiplied by the twiddle factors where  $N$  complex additions are required. Therefore, the total computational requirement is  $(N \log_2^N)/2$  complex multiplications and  $N \log_2^N$  complex additions. Consequently, expanding Radix II butterfly calculation into 8 data is shown in **Figure 3**.

### 2.1.2. DIF Radix II butterfly FFT processor

DIF-FFT calculation is similar to the DIT-FFT algorithm. As far as FFT calculation is involved, the time domain sequence is divided into two subsequences with  $N/2$  samples: The DFT concept of  $x(n)$  expressed as:

$$X(k) = \sum_{n=0}^{(\frac{N}{2})-1} x(n) W_N^{nk} + \sum_{n=\frac{N}{2}}^{N-1} x(n) W_N^{nk} = \sum_{n=0}^{(\frac{N}{2})-1} x(n) W_N^{nk} + \sum_{n=0}^{(N/2)-1} x(n + N/2) W_N^{nk} W_N^{(\frac{N}{2})k} \quad (10)$$

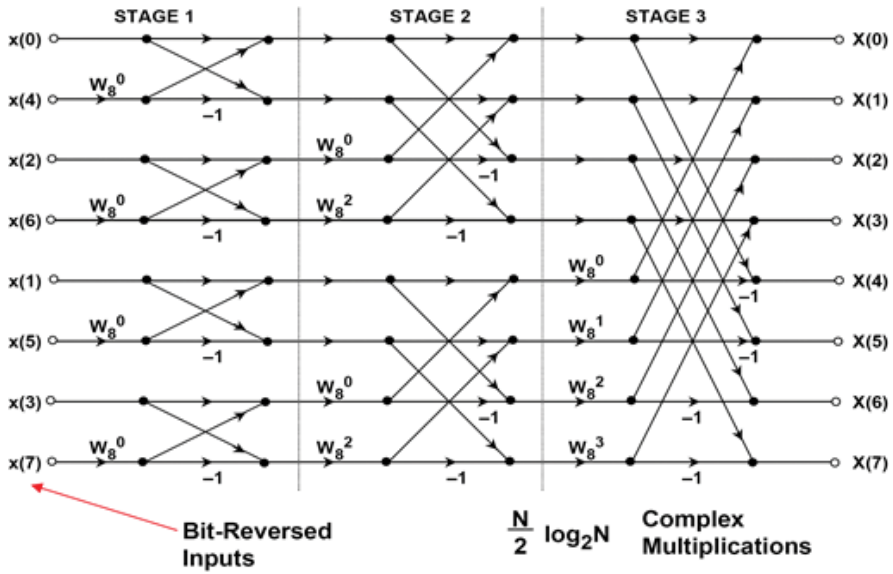


Figure 3. Decomposition of 8-point DIT-FFT.

Given that  $W_N^{(\frac{N}{2})k} = (-1)^k$ , Eq. (10) can be simplified to:

$$X(k) = \sum_{n=0}^{(\frac{N}{2})-1} [x(n) + (-1)^k x(n + N/2)] W_N^{nk} \tag{11}$$

Later, Eq. (11) is expanded into two parts including even  $X(2k)$  and odd  $X(2k + 1)$  sam\ twidle factor characteristic, Eq. (11) is simplified to:

$$\begin{aligned}
 W_n^{2kn} &= W_{N/2}^{kn} W_n^{(2k+1)n} = W_N^n W_{N/2}^{kn} \\
 X(2k) &= \sum_{n=0}^{(\frac{N}{2})-1} \left[ x(n) + x\left(n + \frac{N}{2}\right) \right] W_{N/2}^{nk} = \sum_{n=0}^{(\frac{N}{2})-1} x_1(n) W_{N/2}^{nk} \\
 X(2k + 1) &= \sum_{n=0}^{(\frac{N}{2})-1} \left[ x(n) - x\left(n + \frac{N}{2}\right) \right] W_N^{nk} W_{N/2}^{nk} = \sum_{n=0}^{(\frac{N}{2})-1} x_2(n) W_N^n W_{N/2}^{nk} \quad k = 0, 1, \dots, \left(\frac{N}{2}\right) - 1
 \end{aligned} \tag{12}$$

Similarly, 8-point DIF FFT structure is shown in **Figure 4** with detail complex calculation in three stages. The output sequence  $X(k)$  of the DIF-FFT is bit-reversed, while the input sequence  $x(n)$  of the DIT-FFT is bit-reversed. In addition, there is a slight difference in the calculation of butterfly architecture. As shown in **Figure 4**, the complex multiplication is performed before the complex addition or subtraction in the DIT-FFT processor. In contrast, the complex subtraction is performed before the complex multiplication in the DIF-FFT. The process of decomposition is continued until the last stage is reduced to the 2-point DFT. Since the frequency samples in the DIF-FFT are bit-reversed, it is required to apply bit-reversal algorithm to the frequency samples. Likewise, the DIF-FFT algorithm also uses in-place computation.

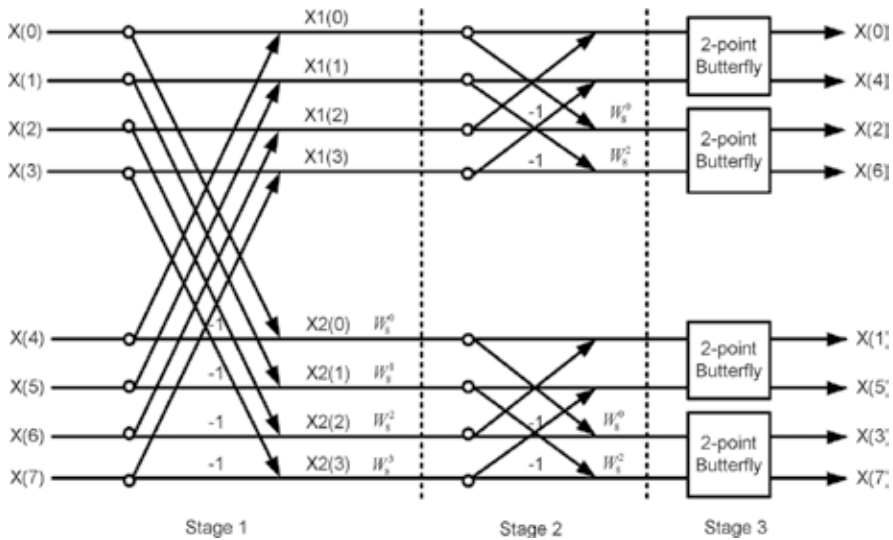


**Figure 4.** Internal calculation of 8-point DIF-FFT processor.

Unlike the DIF structure, input data in DIT-FFT is in bit-reverse format while the output is sorted. On the other hand, both the DIT and DIF can go from normal to shuffled data or vice versa. In order to apply Radix II FFT structures, DIT and DIF algorithms require the same number of operations and bit-reversal to compute the FFT calculation. The overall performance of the FFT processor is dependent on the application, hardware implementation, and convenience. If the design is focused on high speed structure, the processor has to take the most efficient approach and algorithm to perform the FFT calculation accordingly. In this chapter DIT-FFT architecture is considered for floating-point implementation.

## 2.2. Floating point FFT algorithm

Measured frequency by FFT will be subjected to quantization noise error with respect to the real frequency. This is caused by the fact that the FFT only computes the spectrum at discrete frequencies. This error is said to affect the accuracy. In addition, spectral leakage effect becomes very significant when small amplitude harmonics are close to large amplitude ones since they become hidden by the energy distribution of the larger harmonics. Furthermore, the fixed internal arithmetic calculation generates white noise in frequency domain. To reduce the generated noise effect and enhance signal strength, floating-point technique is designed and implemented. The floating-point technique allows numbers to be represented with a large dynamic range. Therefore, floating-point arithmetic enables the reduction of overflow problems that occur in fixed-point arithmetic. Although it is at the expense of throughput and chip area size, the new architecture is designed and investigated to avoid undesired effects in floating-point FFT algorithm. Floating-point arithmetic provides higher precision and a much larger dynamic range under IEEE 754 standard [10]. Therefore, floating-point operations support more accurate DSP operations. **Table 2** compares the efficiency between fixed-point and the floating-point FFT processor.

Fixed-point FFT	Floating-point FFT
16-bit or 24-bit	32-bit
Limited dynamic range	Large dynamic range
Overflow and quantization errors	Less error
Higher frequency	Low frequency
Less silicon area	More silicon area
Cheaper	More expensive
Low power consumption	High power consumption

**Table 2.** Fixed-point and floating-point FFT processor properties.

In floating-point format, the data are translated based on power and mantissa in the decimal system. This notation can be expanded into the binary system. Representing the data in power and mantissa system gives the data the capability of storing a much greater range of numbers than if the binary points were fixed. Floating point refers to the “truth” of the Radix point, which refers to the decimal point or in computers it is known as the binary point that has the capability to float. This entails the event to occur anywhere that is relative to the significant digit of the number. Thus, a floating-point representation, with its position indicated separately in the internal representation, is a computer's recognition of a scientific concept. Although the benefit of floating-point representation over fixed-point (and integer) representation is much wider in range of values, but the floating-point format needs more storage. Hence, the implementation of high performance system requires applying efficient and fast floating-point processor, which is competitive with the fixed-point processor. Various types of floating-point representation have been used in computers in the past. However, in the last decade, the IEEE 754 standard [10] has defined the representation. According to the IEEE 754 standard [10], the single precision is chosen to represent the floating-point data. The IEEE standard specifies a way in which the three values described can be represented in a 32-bit or a 64-bit binary number, referred to single and double precision, respectively [11, 12]. In this project, single precision is selected to function. For the 32-bit numbers, the first bit (MSB) specifies the sign, followed by 8 bits for the exponent, and the remaining 23 bits are used for the mantissa. This arrangement is illustrated in **Figure 5**. The sign bit is set to zero if the number is positive, and the bit is set to 1 if the number is negative. The mantissa bits are set to the fractional part of the mantissa in the original number in bits 22 to 0.



**IEEE-754 Standard**

**Figure 5.** Floating-point structure in IEEE 754 standard [10].

Floating-point algorithm finds huge demand in industry. To conclude this section, **Table 3** summarizes the FFT algorithm application in fixed-point and floating-point architectures.

Fixed-point FFT	Floating-point FFT
Low resolution disk drive	Radar, Image processing
Consumer audio application	High-end audio application, ambient acoustics simulators
Channel coding	Professional audio encoding/decoding and audio mixing
Communication device	Sound synthesis in professional audio and video coding/decoding
	Prototyping
	4G OFDM Transceiver
	High resolution motor monitoring

**Table 3.** Fixed and floating-point FFT application.

### 2.3. Pipeline/parallel FFT algorithm

In 2009, Xilinx Logic core [13] introduced the FFT processor using the Radix structure on a chip. The introduced FFT processors were designed to offer a trade-off between core sizes and transform time. These architectures are classified below:

- FFT Processor with Radix II pipelined serial I/O architecture
- FFT Processor with Radix IV, parallel I/O (burst) architecture
- FFT Processor with Radix II, parallel I/O (burst) architecture
- FFT Processor Radix II lite, parallel I/O (burst) architecture

The pipeline serial I/O allows to continue data processing, whereas the burst parallel I/O loads and processes data separately by using the iterative approach. It is smaller in size than the parallel but has a longer transform time. In the case of Radix II algorithm, it uses the same iterative approach as Radix IV with the difference of smaller butterfly size that differentiates it. Yet, the transformation time is longer. Finally, for the last category, based on Radix II architecture, this variant uses a time multiplexed approach to the butterfly for an even smaller core, at the expense of longer transformation time. **Figure 6** shows the throughput versus resource among the four architectures.

#### 2.3.1. FFT processor with Radix II pipelined, serial I/O

In this design,  $n$ -stage of Radix II butterfly is connected as a serial structure. Each unit of Radix II butterfly has its own RAM memory to upload and download data. The input data are stored in the RAM while the processor simultaneously performs transform calculations on the current frame of data and loads input data for the next frame of data and unloads the result of the previous frame of data. Input data are presented in sorted order. The unloaded output data can either be in bit-reversed order or in sorted order. When sorted output data are selected, an additional memory resource is utilized. **Figure 7** illustrates the architecture of the pipeline serial I/O with individual memory bank, which connects in a serial structure.

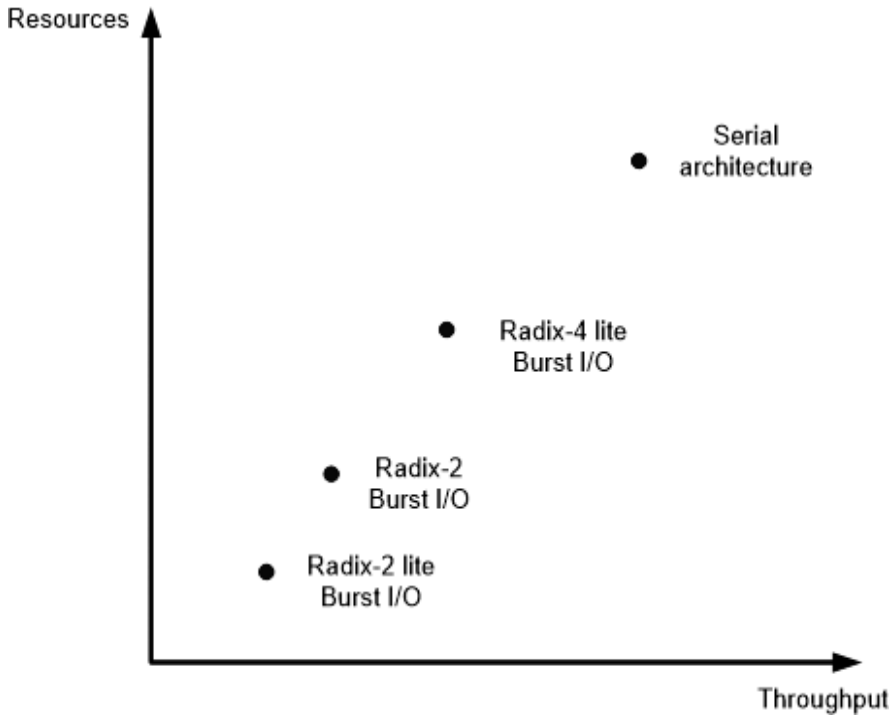


Figure 6. FFT architecture resources vs. throughput.

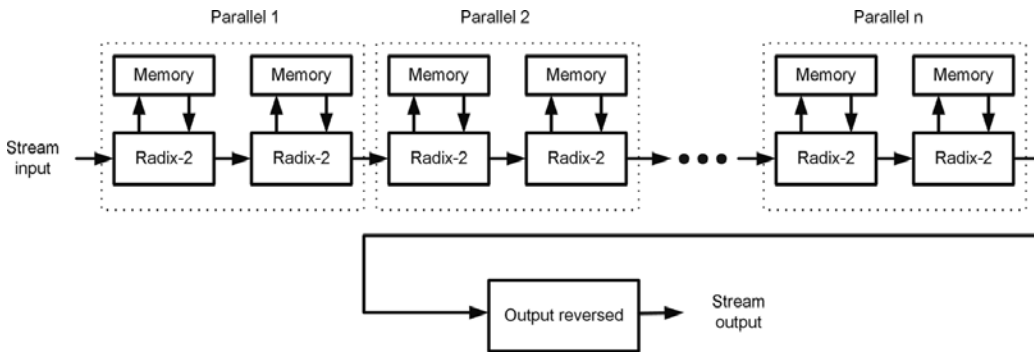


Figure 7. FFT processor with Radix II pipelined, serial I/O [13].

2.3.2. FFT processor with Radix IV, burst I/O

Radix IV structure accepts 4 input data simultaneously whereas Radix II takes only 2 input data at the time to perform FFT calculation. Radix IV input data uploaded into the FFT processor, cannot be uploaded while the calculation is underway. When the FFT is started, the data are loaded. After a full frame has been loaded, the core computes the transformation. The result can be downloaded after the full process is over. The data loading and unloading processes can be overlapped if the data are unloaded in digit-reversed order. **Figure 8** shows the Radix IV structure when 4 input data are loaded for FFT calculation.

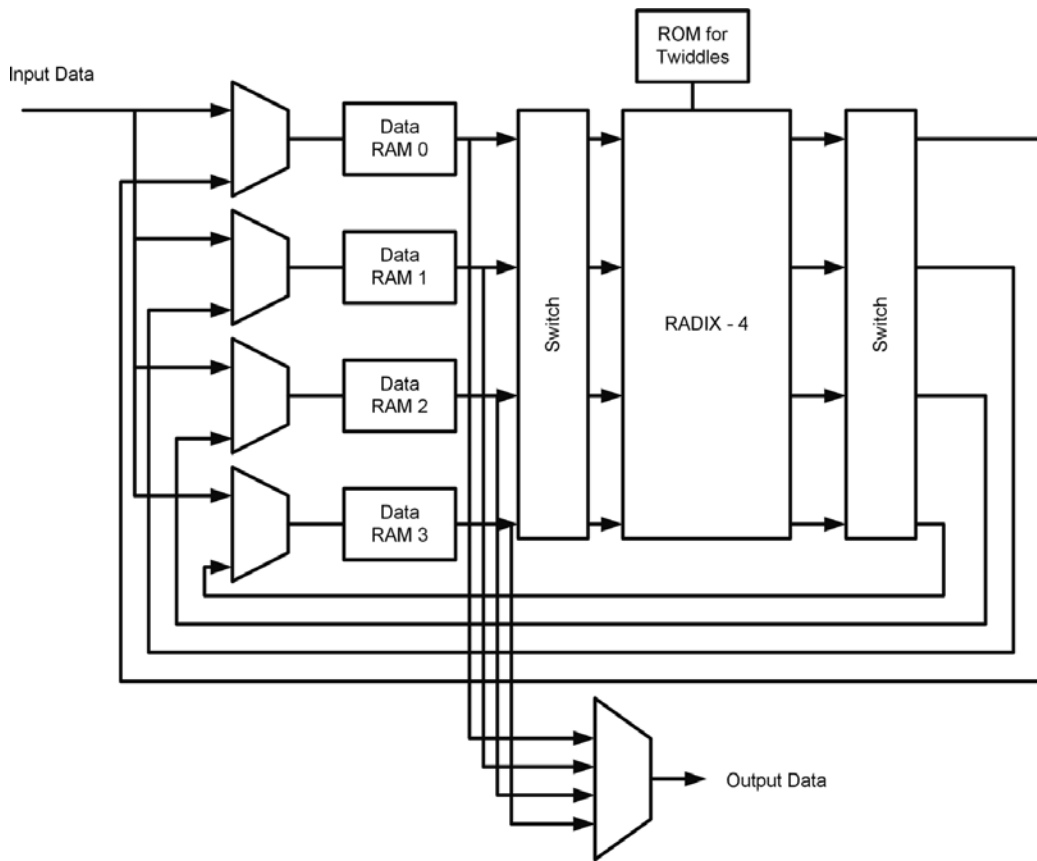


Figure 8. FFT processor with Radix IV architecture [13].

### 2.3.3. FFT processor with Radix II, burst I/O

FFT processor with burst I/O architecture utilizes Radix II butterfly calculation to execute the arithmetic structure. In spite of Radix IV with burst I/O processor, which the input data cannot be loaded and unloaded simultaneously, the Radix II processor accepts the input data during the FFT processor and data can be used concurrently when the output samples are in bit-reversed order. The twiddle factors are stored in the ROM blocks while the output and input data are stored in a separate or mixed RAM blocks. **Figure 9** shows the Radix II structure when 2 input data are loaded for FFT calculation.

### 2.3.4. FFT processor with Radix II lite, burst I/O

FFT processor with Radix II lite architecture uses one shared RAM, hence reducing resources at the expense of an additional delay per butterfly calculation. The multiplier in this structure multiplies the real part of complex number in one clock cycle and the imaginary in the next. In this architecture, the data can be simultaneously loaded and unloaded if the output samples are in bit-reversed order. In this architecture, sine and cosine twiddle factor coefficient will be saved in the ROM and the output data will be saved in a single RAM. Although this proposed architecture saves the resources, the throughput is significantly limited by the FFT structure

due to the sequence calculations. **Figure 10** shows the Radix II lite structure when 2 input data are loaded for FFT calculations.

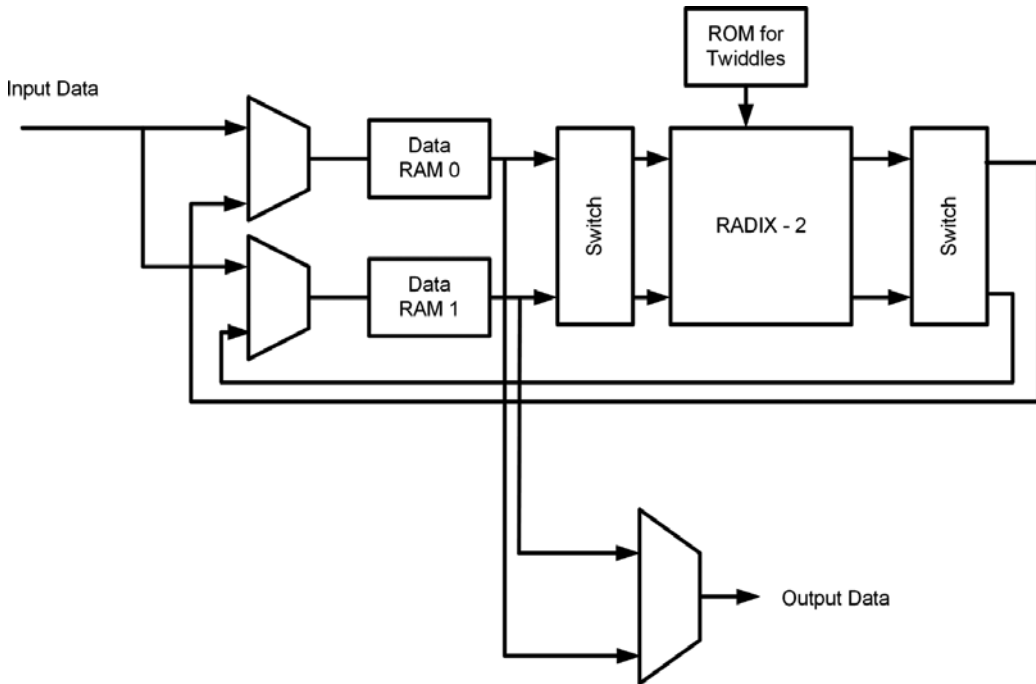


**Figure 9.** FFT processor with Radix II burst I/O architecture [13].

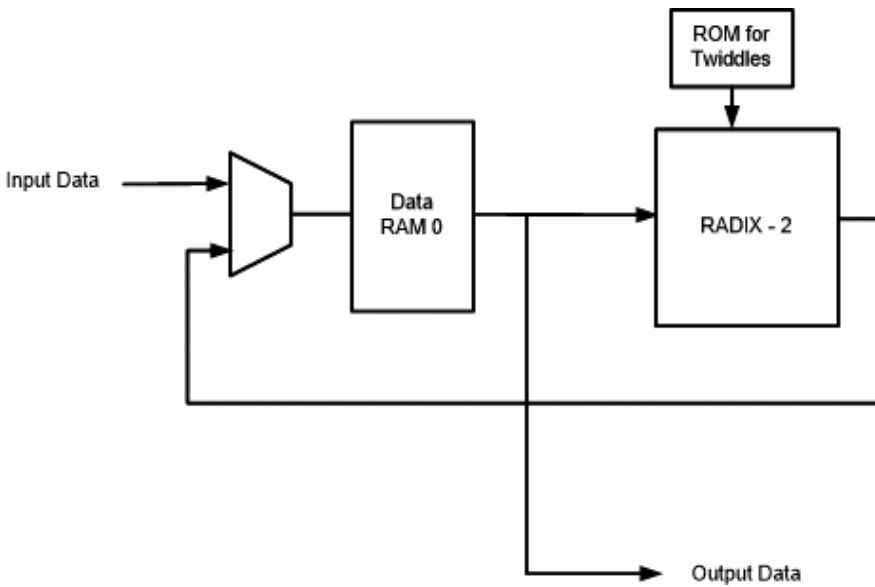


**Figure 10.** FFT processor with Radix II lite burst I/O architecture [13].

### 3. Advanced high-tech fast Fourier transform algorithm

In Section 2, FFT fundamental was discussed and elaborated. Furthermore, different FFT architectures were provided with the detail on IO configuration. Here, advance FFT processor with the focus on 1024 floating-point parallel architecture for high performance application is provided.

#### 3.1. Stage realization of 1024-point parallel pipeline FFT structure

High-tech FFT principle is based on Radix II algorithm in floating-point format to conduct 1024 point FFT structure. **Figure 11** illustrates the main block diagram of the 1024-point Radix II floating-point parallel pipeline (FPP) FFT processor in detail.

As shown in **Figure 11**, there are six major subprocessor units in the high-tech 1024 point Radix II FPP-FFT algorithm. These units are shared memory, bit reverse, butterfly arithmetic, smart controller, ROM, and finally address generator unit. The floating-point input data act as a variable streaming configuration into the processor. The variable streaming configuration allows continuous streaming of input data and produces continuous stream of output data. **Figure 12** shows the internal schematic of the pipeline butterfly algorithm with the parallel architecture at a glance.

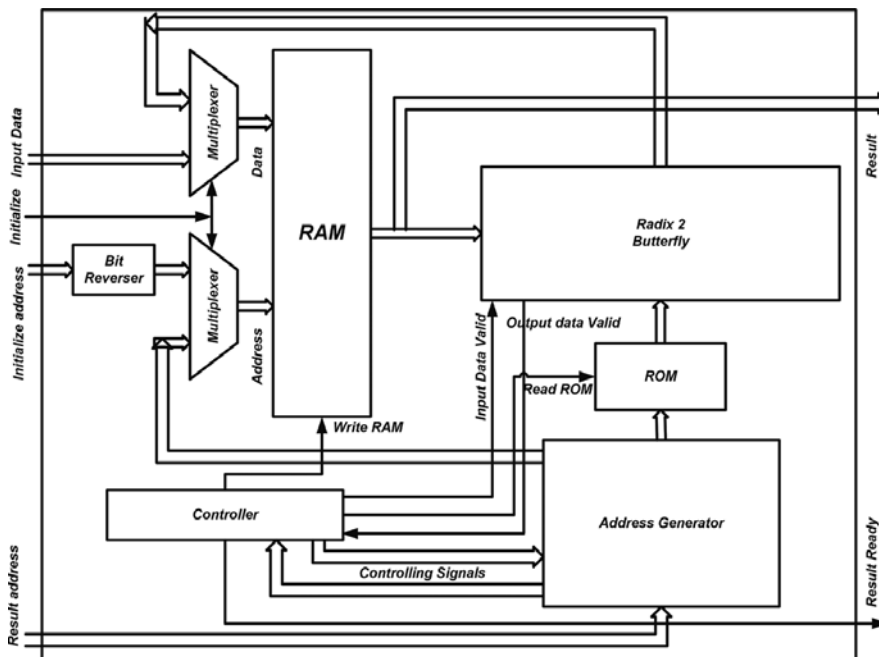


**Figure 11.** 1024 point Radix II FPP-FFT block diagram.

To enhance the speed of calculation in Radix II butterfly algorithm, the pipeline registers are located after each addition, subtraction, and multiplication subprocessors. Hence, the pipeline butterfly algorithm keeps the final result in the register to be transferred into the

RAM by the next clock cycle. Additionally, the parallel architecture splits the data in real and imaginary format and increases the speed of FFT calculation by 50%. As a result of the design algorithm, Radix II FPP-FFT processor calculates 1024 point floating-point FFT exactly after  $O(N/2 \log_2^N) + 11$  clock a pulse which proves the performance improvement in comparison with similar Radix II FFT architecture. The existence of 11 clock pulses delay is due to 11 pipeline registers in adder, subtraction, and multiplier in a serial butterfly block. Additionally, parallel design of the FFT algorithm decreases the calculation time significantly.

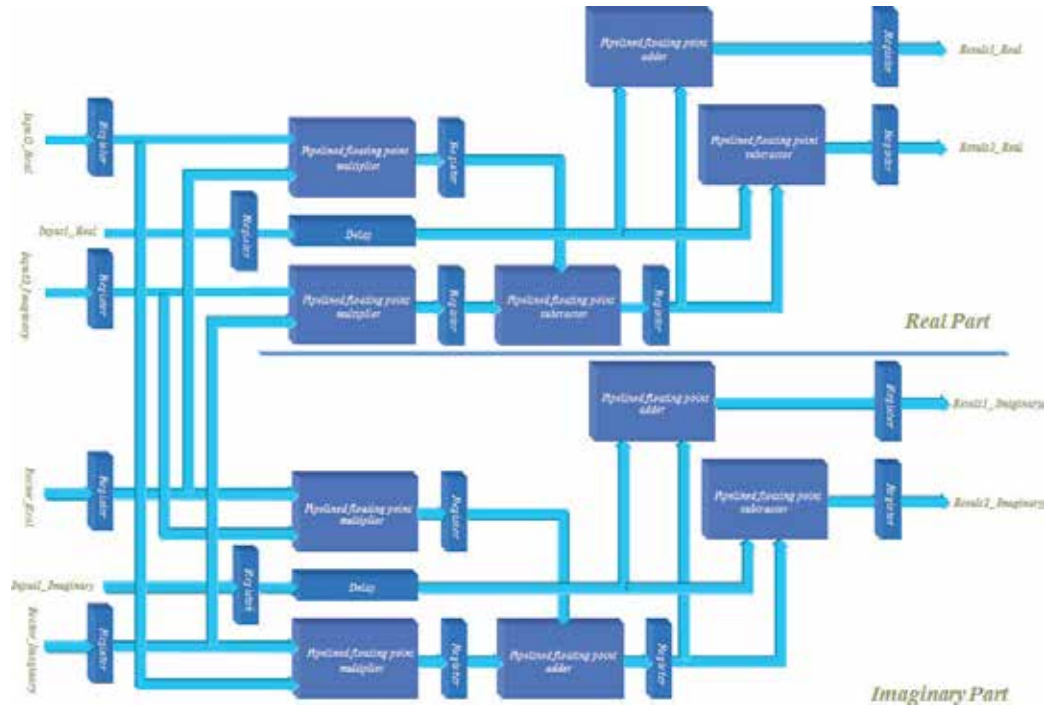
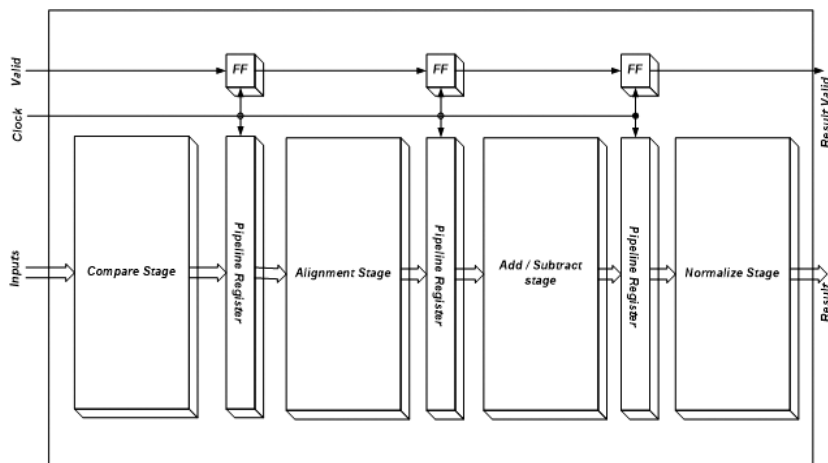


Figure 12. Designed FPP Radix II butterfly structure.

Radix II butterfly unit is responsible for calculating the complex butterfly equations as  $output1 = input1 + W^k \times input2$  and  $output2 = input1 - W^k \times input$ . To calculate the butterfly equation, it is necessary to initiate the RAM with bit-reverse format and the external processor loads the data in the RAM. Since butterfly equation deals with complex data, thus each butterfly requires four multiplication units (two for the real and two for the imaginary) and six additional units (three for the real and three for the imaginary). Fixed point implementation of such complex calculation does not satisfy high-tech application of FFT processor due to the generated noise of round-off, overflow, and coefficient quantization errors [14]. Consequently in order to reduce the error as well as to achieve high-resolution output, the floating-point adders and subtractors are used to replace the fixed-point arithmetic units.

### 3.1.1. Floating point adder/subtraction

Butterfly processor efficiency greatly depends on its arithmetic units, and high-speed floating-point adder is the bottle neck of butterfly calculation. Based on IEEE-754 standard [10] for floating-point arithmetic, 32-bit data register is considered to allocate mantissa, exponent, and sign bit in a portion of 23, 8, and 1 bits, respectively. The advantages of floating-point adder are that the bias power is applied to complete the calculation and avoid using unsigned value. Additionally, the floating-point adder unit performs the addition and subtraction using substantially the same hardware as used for the floating-point operations. This functionality minimizes the core area by minimizing the number of elements. Furthermore, each block of floating-point adder/subtraction operates the arithmetic calculation within only one clock cycle that results high-throughput and low latency for the entire FFT processor. **Figure 13** shows the novel structure of the floating-point adder when it is divided into four separate blocks while detail algorithm is presented in **Figure 14**.



**Figure 13.** Schematic diagram of advance floating-point adder.

The purpose of having separate blocks is to share the total critical path delay into three equal blocks. These blocks calculate the arithmetic function within one clock cycle. However, the propagation delay can be associated with continuous assignment to increase the overall critical path delay and for the slowing down of the throughput. Based on combinational design, the output of each stage depends on its input value at the time. The unique structure of floating-point adder enables feeding of the output result in the pipeline registers after every clock cycles. Hence, the sequential structure is applied for the overall pipelined add/subtraction algorithm to combine the stages. The processing flow of the floating-point addition/subtraction operation consists of comparison, alignment, addition/subtraction, and normalization stages.

The comparison stage compares two input exponents. This unit compares two exponents and provides the result for the next stage. The comparison is made by two subtraction units and the result is revealed by *compare\_sign* bit.

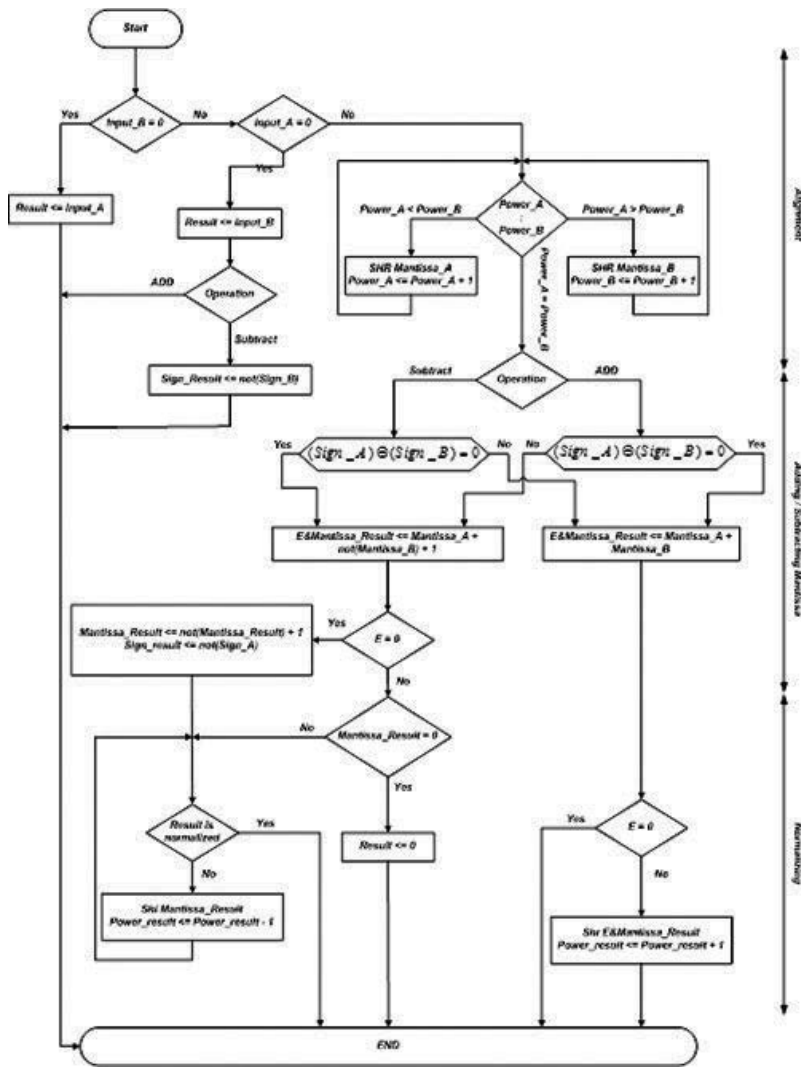


Figure 14. Flowchart of advance floating-point adder.

According to the results of the comparison stage, the alignment stage shifts the mantissa and transfers it to the adder/subtraction stage. The number of shifting will be selected by the comparison stage output. Consequently, each stage of the floating-point adder algorithm is executed within one clock cycle. Floating-point adder/subtraction unit satisfies high speed and efficiency of arithmetic unit in cost of die area size. The floating-point arithmetic unit is designed to calculate entire numbers regardless of the number sign. As shown in Figure 15, there is a logic gate involved with the stages, which cause higher delay propagation through the circuit.

Floating-point numbers are generally stored in registers as normalized numbers. This means that the most significant bit of the mantissa has a nonzero value. Employing this method allows the most accurate value of a number to be stored in a register. For this purpose, the

normalized stage is required. This unit is located after the add/sub stage. The output signal representing the add/sub block leads to zero digits of an unnormalized result of the calculation operation. The normalized block ignores the digital value of zero from the MSB of the mantissa and shifts the mantissa to imply value of one in digital as MSB in mantissa.

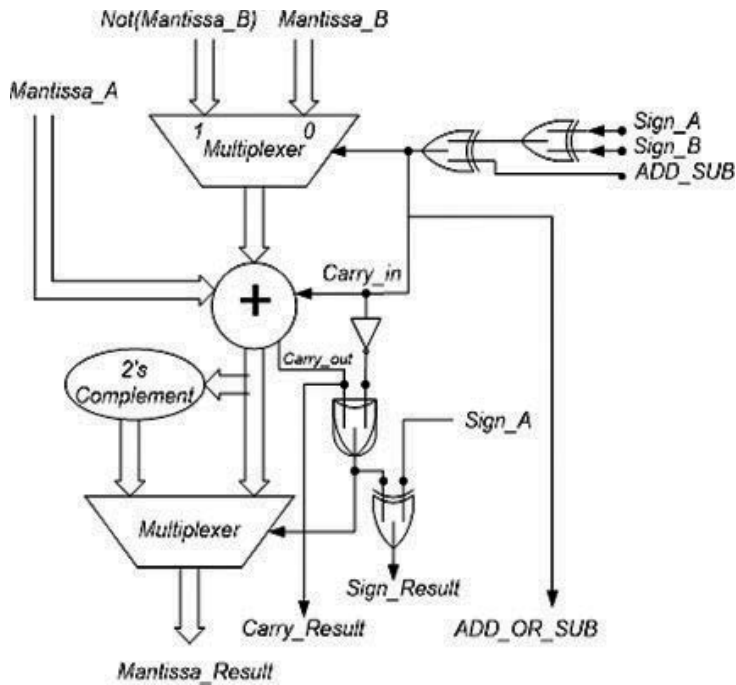


Figure 15. Addition/subtraction structure.

### 3.1.2. Floating-point multiplier

In a floating-point multiplier, numbers are represented in single-precision normalized mantissa and 8-bit exponent format defined by the IEEE 754 standard. This structure has developed the architecture for partial-product reduction for the IEEE standard floating-point multiplication, leading to a structured high-speed floating-point multiplier. The shortening of the data path is desirable because they require shorter wires and therefore support faster operation. The former approach uses a reduction scheme based on combination unit and connects it as parallel architecture. Implementing floating-point multiplier is simpler than floating-point adder since it does not require alignment stage. The processing flow of the floating-point multiplication operation consists of multiple stage and normalized stage. Figure 16 shows the overall block diagram of the floating-point multiplier while the flowchart of the functionality of the multiplier is shown in Figure 17.

In a floating-point multiplier, the bias power format is applied to avoid having negative exponent in the data format. Additionally, the multiplier is designed as pipelined structure to

enhance speed calculation, with the intention of the initial result appearing after the latency period where the result can then be obtained after every clock cycle. The multiplier offers low latency and high throughput and is IEEE 754 compliant. This design allows a trade-off between the clock frequency and the overall latency by adding the pipeline stage.

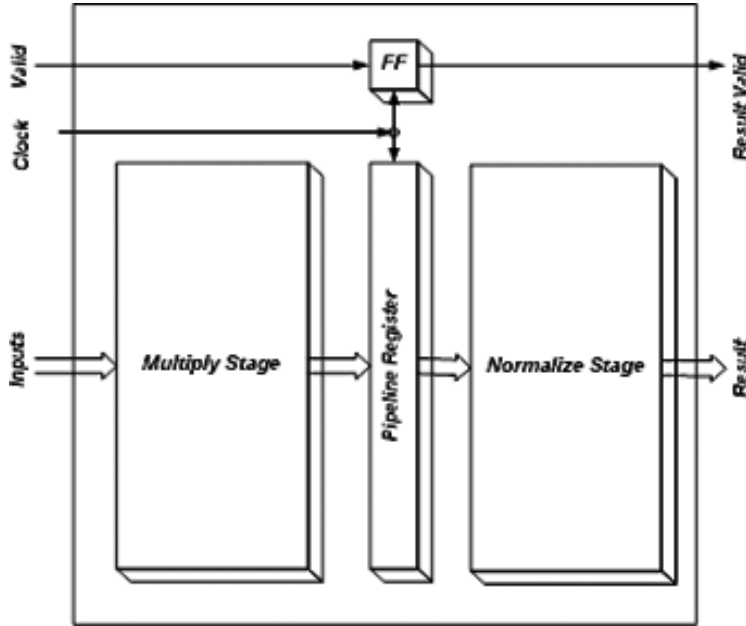


Figure 16. Floating-point multiplier block diagram.

### 3.1.3. Smart controller structure

Smart controller unit significantly affects the efficiency of the 1024 Radix II FPP-FFT processor. As such, small die area can be achieved by designing high performance controller for the FFT processor. In this architecture, FFT controller is designed with the pipeline capability. The global controller unit provides the signal control to the different parts of the FFT processor. Additionally, several paths are switched between the data input and data output in architecture design and the data path is controlled. To calculate the 1024 point Radix II FFT processor, it is necessary to have  $\log_2 N$  stages, which are 10 stages for 1024-point data. Furthermore, each stage calculates  $\frac{N}{2}$  butterfly that is 512 butterfly calculations in the design. Hence, there are two counter in corporation with the controller to count the stage number of the processor and the number of butterfly calculation. Smart controller with collaboration of address generator unit calculates 1024 point floating-point FFT by using only one butterfly structure. This functionality has great contribution on power supply as well as saving die area size. **Figure 18** shows the smart controller state machine, which controls the flow of the 1024 floating-point Radix II FFT processor.

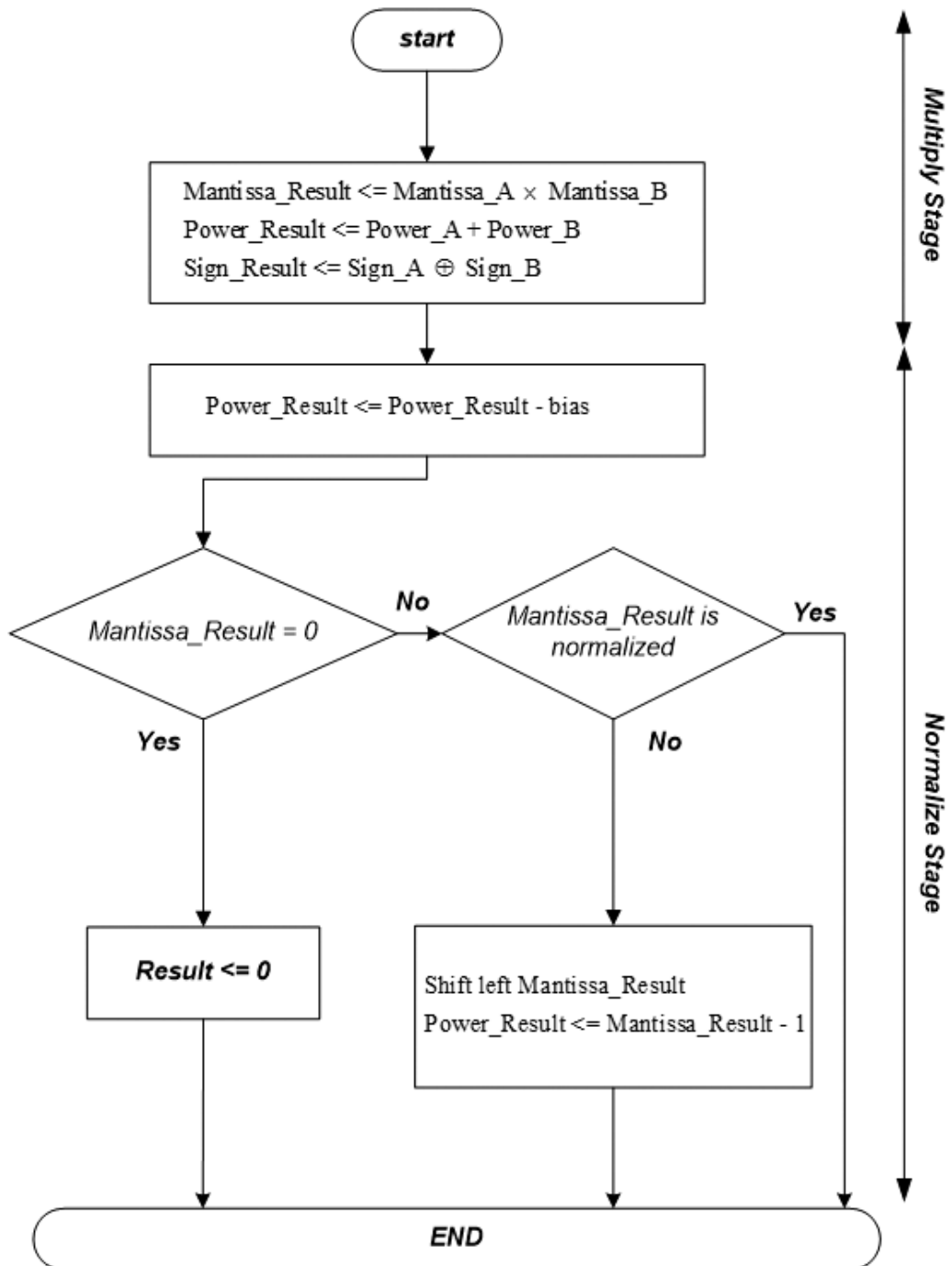


Figure 17. Floating-point multiplier flow chart.

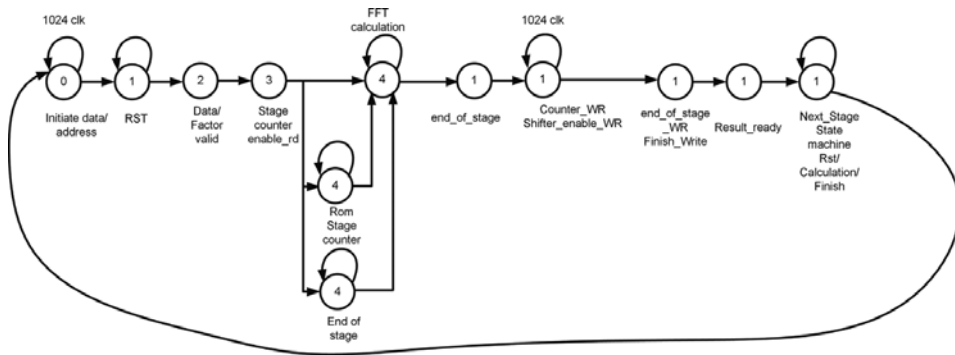


Figure 18. Smart controller state machine.

There are several control signals in smart controller to clarify the presence of correct output after finishing the current cycle of FFT calculation. The control signals transfer information through the RAM, ROM, butterfly preprocessor, and address generator. The designed controller operates according to the provided state machine (Figure 18) and makes the high performance FFT calculation feasible for implementation. The controller unit is structured into the subblocks such as in sequential and combination units. Sequential unit is responsible for updating the state of the processor, while the combinational unit performs the states individually. The state machine waits for processor core to complete the entire FFT calculations and then records data points into the memory. Reset state is received every time the reset input is asserted then holds the entire calculation. The processor gets activated after the reset input signal is removed.

### 3.1.4. Memory and address generator

Address generator has a significant task in Radix II FFT processor, since it delivers the address of the input/output data for each computational stage in an appropriate way. Address generator architecture consists of ROM address generator, Read address generator, and Write address generator. ROM address generator produces the reading address for the ROM module. The reading address represents the address of the twiddle factor, which must be taken to feed the butterfly structure. This address generator is designed to select the specific twiddle factor for the butterfly calculations. Meanwhile, the Write address generator is designed to save the result of the butterfly calculation in the proper location in the complex RAM. The proposed smart address generator is designed to provide the correct result for the next stage of the butterfly in 1024-point Radix II FFT calculations. The architecture of the Read address generator is similar to the Write address generator. The butterfly will save the data result after reading from the certain address and input it to the butterfly, in the previous address line. The reading RAM select control signal ensures the correct location of data in the complex RAM. On the other hand, memory modules are used for the storing input and output results with 1024 complex long words of 32-bit registers. The implemented architecture for the memory is shown in Figure 19. The capacity of the memory is 1024-point data for real and imaginary data. In high-tech implementation, shared RAM architecture is designed and implemented in a single-chip FFT processor. The high-tech design makes the Radix II FFT architecture entirely independent of the type of FPGA board since it has on

board memory system. Furthermore, each complex RAM has the capability of saving real and imaginary input data separately. The module is programmed with a dual-in-line header to provide the appropriate location for storing input and output result in each stage consequently. It is composed of two delay memories and multiplexer, which allows straight through or crossed input-output connection as required in the pipeline algorithm. Memory unit similarly contains the controller trig. The controller, which is connected directly to the memory modules, takes the responsibility of transferring data through the memory and arithmetic blocks ensuring that no data conflict occurs within the complete process of the FFT calculations. This is another advantage of high-tech smart memory modules, by which data can be read and written in the memory simultaneously without sending bubble data in the FFT processor.

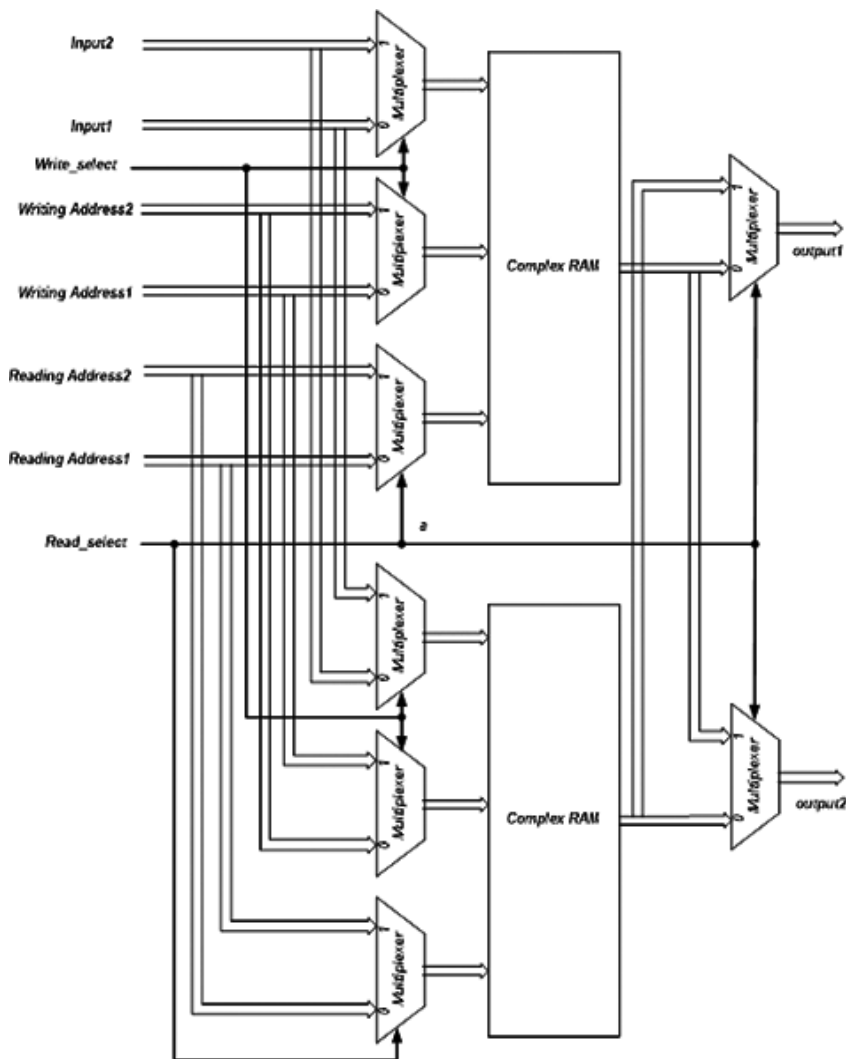


Figure 19. RAM internal architecture.

### 3.2. Advantages of 1024-point parallel pipeline FFT structure

Design algorithm of the 1024 point Radix II FPP-FFT processor was based on the smart sub-blocks where the result was optimized accordingly. The designed processor takes the advantages of (i) shared memory to store the input and output data and makes the system as single chip. Hence, it reduces hardware complexity. Furthermore, (ii) the entire individual arithmetic unit is designed to operate within one clock cycle to increase the maximum clock frequency. Additionally, (iii) the butterfly structure is in parallel and pipelined architecture to minimize delay caused by the FFT calculations, and finally, (iv) the strong controller with collaboration of address generator unit ignores the need of using  $N$  numbers of butterfly unit, since Radix II calculation is carried out within one butterfly unit that results reduction of power consumption, area, and avoid system complexity. The high performance processor is implemented with optimizing the architecture to enable the system in maintaining a reasonable clock rate and with low latency of  $(N/2 \log_2 N) + 11$ . The throughput of the operation is limited by the amount of available logic in the target device.

## 4. 1024 point FPP-FFT implementation

Section 4 details the implementation of introduced 1024-point floating-point parallel pipeline Radix II FFT algorithm. Hardware implementation of the algorithm as system on chip (SOC) is presented here.

### 4.1. Hardware implementation

In order to verify the functionality of the 1024-point FPP-FFT processor, the VHDL code for the overall processor is developed. Register transfer level (RTL) behavior description of the processor is generated for downloading into FPGA prototyping. The procedure is continued by attaching the library cell and constraint file for ASIC implementation. High performance FFT is transferred into the gate level synthesis to complete postsimulation stage. The design moves forward to the back-end implementation by 0.18  $\mu\text{m}$  Silterra technology and 0.35 Mimos technology library. Generated netlist with constraint file is transferred to complete floor planning and place and route stage. The implementation process is summarized in **Figure 20**.

The high-tech 1024-point FPP-FFT specification generated by Xilinx ISE synthesis report is provided in **Table 4**.

As stated in **Table 4**, high-tech FFT processor operates with the maximum clock frequency of 227.7 MHz and the total latency of 5131 clock cycles (**Figure 21**) to prove the computation complexity derived from  $(N/2\log_2 N) + 11$  when  $N = 1024$ .

Place and route (PAR) process was completed and the processor routed successfully on silicon chip (**Figure 22**).

Later, the 1024-point FPP-FFT processor was optimized in Silterra 0.18  $\mu\text{m}$  and Mimos 0.35  $\mu\text{m}$  technology for power consumption and die size measurement in maximum clock frequency.

**Table 5** shows the optimization result of FFT processor implementation in Silterra 0.18  $\mu\text{m}$  and Mimos 0.35  $\mu\text{m}$  technology library.

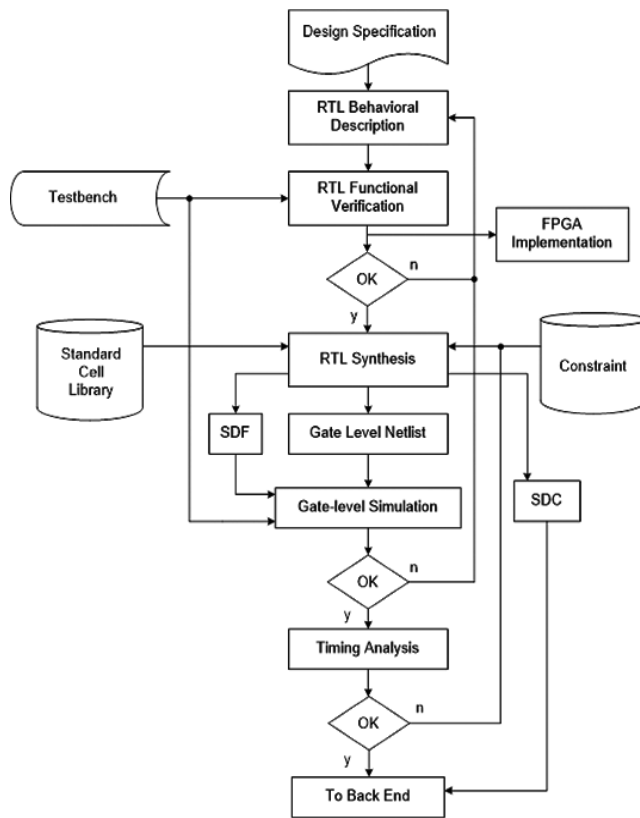


**Figure 20.** Flowchart of hardware implementation.

HDL synthesis report		Timing summary	
Registers flip-flops	1175	Minimum period (ns)	4.391
Shift registers	43 (6%)	Maximum frequency (MHz)	227.747
LUTs slice	4419 (23%)	Min. input arrival time (ns)	3.788
Logic slice	2584 (13%)	Max. output required time (ns)	6.774
RAM cells	1835 (35%)	Total equivalent gate count	998678
IOs	88 (40%)	Total number of path	220310
Memory usage (MB)	254 (40%)	Total number of destinations	5926
Multiplexers	77		
Tri-states	98		

**Table 4.** 1024-point FPP-FFT specification.

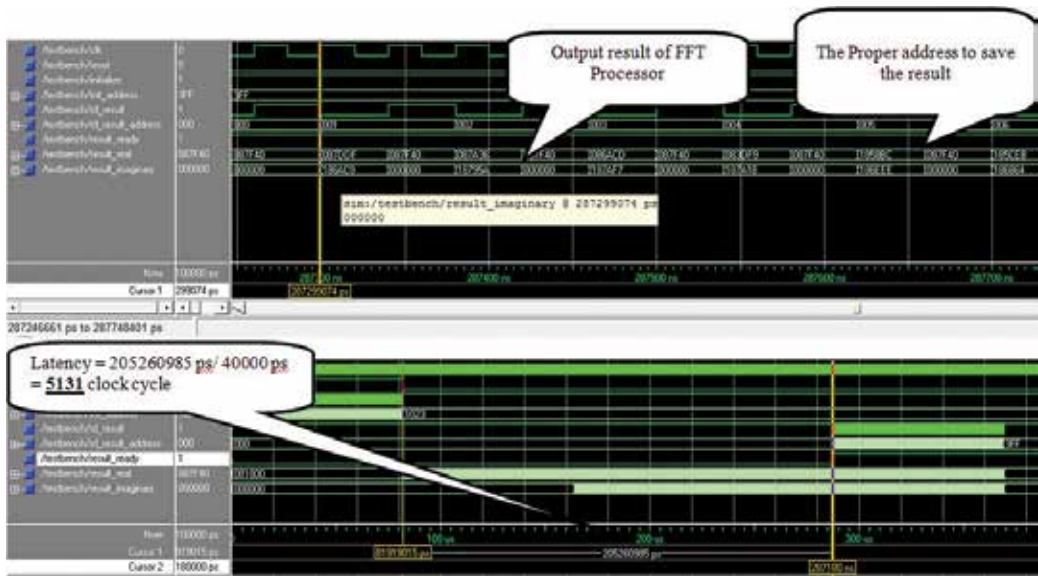


Figure 21. 1024-point FPP-FFT processor output signal.

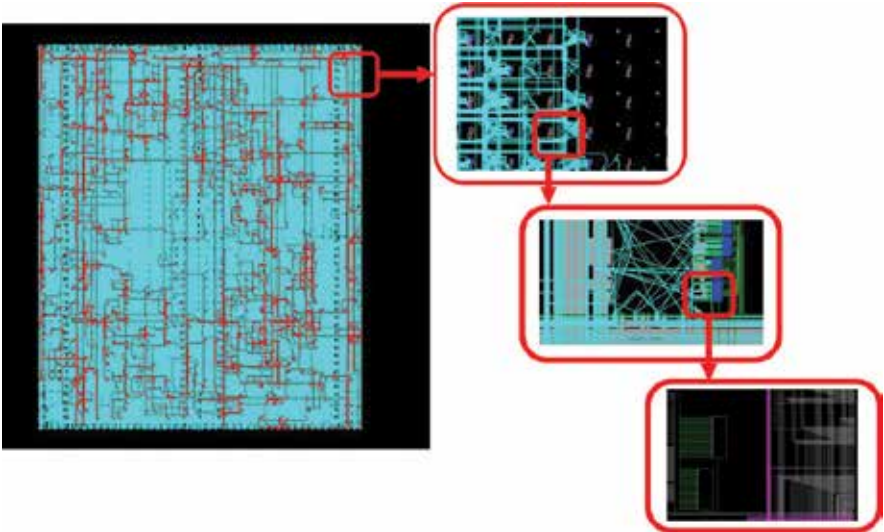
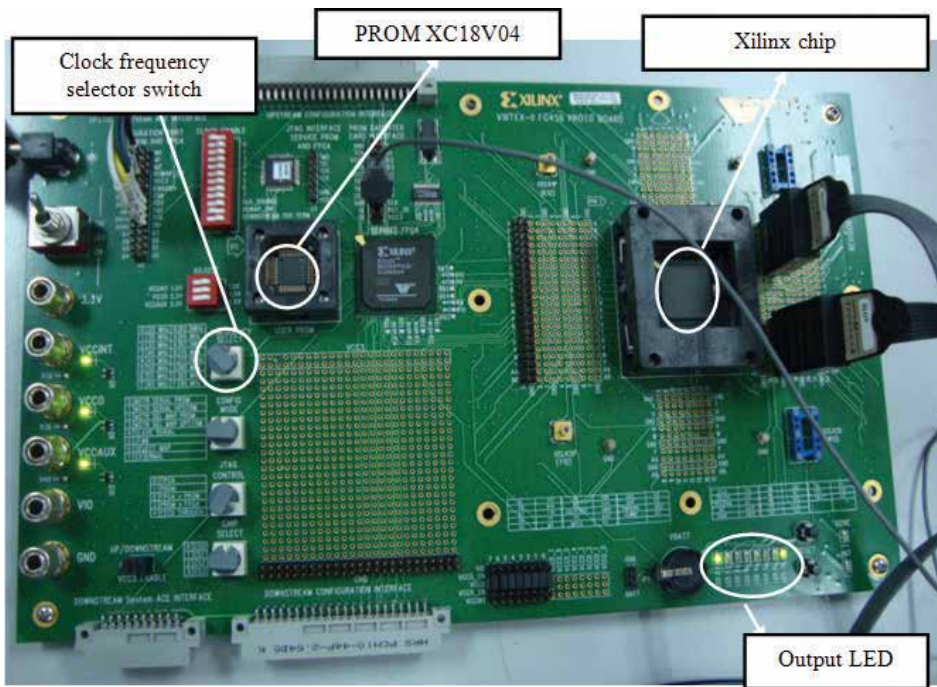


Figure 22. Chip layout of high-tech FFT processor.

FFP-FFT specification	Silterra 0.18 $\mu\text{m}$ technology	Mimos 0.35 $\mu\text{m}$ technology
Active core area ( $\text{mm}^2$ )	2.32 $\times$ 2.32	4.256 $\times$ 4.256
Power consumption (mW)	640	1198

Table 5. Optimized power consumption and die area size in different technology library.

To conclude, after FPGA implementation and ASIC optimization and with considering available software and hardware resources, the high-tech 1024-point Radix II FPP-FFT processor was implemented and tested in FPGA prototyping under Xilinx ISE software and CAD tools in synopsis. **Figure 23** shows relevant FPGA board, and **Table 6** summarizes the design property.



**Figure 23.** FPGA implementation of high-tech FFT processor.

Parameters	Unit	specification
Processor machine		Radix II
Calculation type		Floating-point
Latency ( $\mu$ s)		22
Maximum precision		32-bit
No. of input data		1024
Data rate (ms/s)		25
Max. clock frequency	$f_{s,max}$	227 MHz
Signal to noise ratio	SNR	192 dB
Power consumption (Silerra 0.18 $\mu$ m library)	$P_o$	640 mW
Active core area (Silerra 0.18 $\mu$ m library)	mm	$2.32 \times 2.32$
Accuracy		$\leq 0.01$

**Table 6.** High-tech 1024 point FFT specification.

## 5. Summary and conclusion

In this chapter, high-tech 1024-point Radix II FFT processor was implemented. The design was launched with introducing 32-bit data single precision floating-point parallel pipeline architecture. Then, it was followed by implementing the subcomponents such as Radix II butterfly and smart controller. The implementation result of high-tech 1024-point Radix II FPP FFT processor was provided accordingly. Designing high speed floating-point arithmetic unit such as adder/subtraction (278 MHz), multiplier (322 MHz), implementing smart controller to save area and increase system efficiency, design processor as single chip by implementing complex dual memory, and providing pipeline and parallel architecture lead to present a high-tech 1024-point Radix II FPP FFT processor. In addition, the processor was synthesized using the Xilinx ISE platform. From synthesis report, it was found that the FPP FFT processor shows the maximum clock frequency of 227 MHz. The latency for calculating 1024-point FFT is 22  $\mu$ s. After FPGA implementation, the proposed processor was optimized in ASIC under Silterra 0.18  $\mu$ m and Mimos 0.35  $\mu$ m technology libraries. The estimation power consumption was reported 640 mW in Silterra and 1.198 W in Mimos technology library with sample rate of 25 ms/s. The procedure was followed by defining the constraints and the netlist (gate level) to produce the ASIC layout. The design compiler result shows the die size of  $2.32 \times 2.32$  mm<sup>2</sup> in Silterra 0.18  $\mu$ m technology and  $4.256 \times 4.256$  mm<sup>2</sup> in Mimos 0.35  $\mu$ m technology. From the given specification, it was found that the high-tech 1024-point Radix II FPP FFT processor is suitable for high performance DSP application.

## Author details

Rozita Teymourzadeh

Address all correspondence to: rozita.teymourzadeh@neonode.com

Neonode Inc., San Jose, California, USA

## References

- [1] Bergland, G. D. A guided tour of the fast Fourier transform. IEEE Spectrum Conference. 1969; pp. 41–52.
- [2] Gold, B., Radar, C. Digital Processing of Signals. New York: McGraw-Hill; 1969.
- [3] Smith, J. O. Mathematics of the Discrete Fourier Transform (DFT) with Audio Applications. 2nd ed. W3K Publishing; Stanford, California; 2007. DOI: ISBN 978-0-9745607-4-8
- [4] Alegre P. Low Power QDI Asynchronous FFT. 2016 22nd IEEE International Symposium on Asynchronous Circuits and Systems (ASYNC). 2016;978-1-4673-9008-8; pp. 87–88. DOI: <http://doi.ieeecomputersociety.org/10.1109/ASYNC.2016.17>

- [5] Kuo, S. M., Gan, W.-S. *Digital Signal Processors, Architecture, Implementations and Applications*. Pearson Education International: Prentice Hall; Singapore; 2005. DOI: ISBN: 0131277669
- [6] Cooley, J. W., Tukey, J. W. An algorithm for the machine computation of complex Fourier Series. *Mathematics of Computation Journal*. 1965;19:297–301.
- [7] Hemmert, K. S., Underwood, K. D. An Analysis of the Double-Precision Floating-point FFT on FPGAs. In: *13th IEEE Symposium on Field-Programmable Custom Computing Machines*; 2005. pp. 171–180.
- [8] Zheng, S., Yu, D. Design and Implementation of a Parallel Real-Time FFT Processor. In: *7th IEEE Conference on Solid-State and Integrated Circuits Technology*; IEEE; 2004. Vol. 3. pp. 65–168.
- [9] Thulasiram, R. K., Thulasiraman, P. Performance evaluation of a multithreaded fast Fourier transform algorithm for derivative pricing. *Journal of Supercomputing*. 2003;26(1):43–58.
- [10] IEEE Std. 1985. For Binary Floating-Point Arithmetic. IEEE Standard 754-1985. 1985;1–17.
- [11] Madeira, P. A Low Power 64-point Bit-Serial FFT Engine for Implantable Biomedical Applications. *IEEE 2015 Euromicro Conference on Digital System Design (DSD) (2015)*. 2015; 978-1-4673-8034-8; pp. 383–389. DOI: <http://doi.ieeecomputersociety.org/10.1109/DSD.2015.30>
- [12] Ahmedabad. Implementation of Input Data Buffering and Scheduling Methodology for 8 Parallel MDC FFT. *2015 19th International Symposium on VLSI Design and Test (VDATE) (2015)*. 2015;978-1-4799-1742-6; pp. 1–6. DOI: <http://doi.ieeecomputersociety.org/10.1109/ISVDATE.2015.7208107>
- [13] Xilinx Logic core. Fast Fourier transform. Xilinx; 2009; Version 7.0.DS260; pp. 1–64.
- [14] Ifeachor, E. C., Jervis, B. V. *Digital Signal Processing: A Practical Approach*. 2nd ed. Prentice Hall; 2002.



---

# Memristor Threshold Logic FFT Circuits

---

Alex Pappachen James

Additional information is available at the end of the chapter

<http://dx.doi.org/10.5772/66583>

---

## Abstract

One of the possible approaches to achieve more than Moore's law with signal processing circuits is to inspire from functioning of human brain to mimic neural functions by exploring emerging technologies such as memristor circuits. While fast Fourier transform (FFT) implementations are largely based on CMOS gates, they are limited by the computation speed and availability limits on the number of Boolean variables it can handle at a given time. Biological neurons and networks on the other hand are generalized in nature and can handle both analogue and digital signals. Through this chapter, memristor-based resistive threshold logic family of gates that inspire from brain-like large variable logic functions is introduced. This logic consists of a memristors acting as weights to the inputs followed by threshold operations emulating neuronal synapse. Using this Boolean logic, a processing unit that can compute Fourier transform of a given set of inputs was developed. Various comparisons of the circuit are found to be advantageous in implementing neuromorphic circuits. The existing logic families were carried out and the proposed logic family was found too advantageous in many ways.

**Keywords:** memristors, threshold logic, circuits, Fourier, FFT

---

## 1. Processing in brain

Human brain is the processing centre of human nervous system. Average adult human brain weighs about 1.5 kg and [1, 2] is composed of about 10 billion nerve cells or neurons. On average, each neuron is connected to other neurons through about 10,000 synapses. The brain's network of neurons forms a massively parallel information processing system.

On the other hand, approximates arithmetic, such as the ability to calculate whether '26 + 32' is closer to 60 or 75, is not processed in the same manner or in the same part of your brain. Memorization of the results of operations such as multiplication tables reduces the need to use complex cognitive processing, such as going through the learning processes every time

---

the task is given. The idea of storing for long-term retrieval is supported by the long-term memories in the human brain, where the retrieval of results from the memory reduces the effort on cognitive processes.

The ability of the brain to process computational operations in real time is reflective of an active working memory. In many of the mental calculations, one makes on a day-to-day basis can be analysed by looking into the activities in the prefrontal cortex (see **Figure 1**). The studies using neuroimages indicate 10 separate regions in the brain that contribute to even simple task of subtraction of two numbers. The main areas of activation for this simple task include fusiform gyrus, parietal cortices, lateral and medial parts of the temporal lobe and inferior parts of the frontal lobes.

The interconnections between the modules and the way they interact with each other for different set of arithmetic operations are different. It is also found that there is a separate network for estimation (bilateral inferior parietal cortex) as opposed to computation (left parietal and frontal cortices). These features point out the fact that there is one specific unit for performing computation; instead it is a collaborative effort between various regions in the brain.

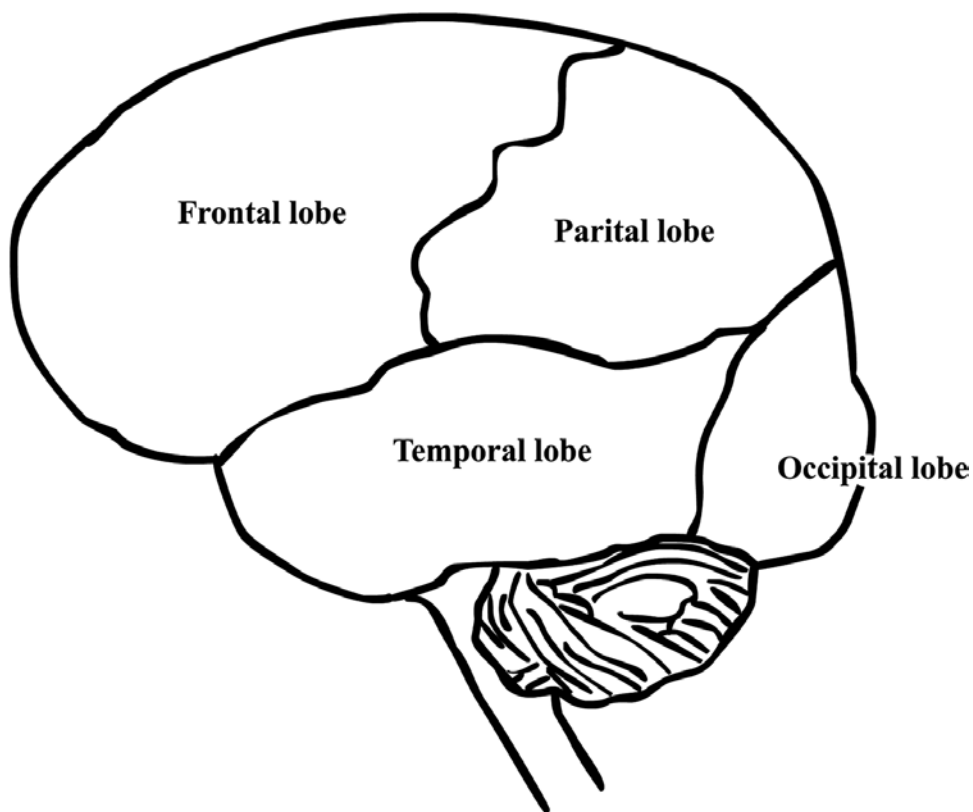


**Figure 1.** Functional units in brain.

These features of brain are similar to the normal CPU architecture—a separate unit for arithmetic and logic functions, with a difference in the mode of operation. Instead of doing algorithmic approach, the brain works based on what it learned or we can say that the patterns it has learned. If we can implement this key feature of brain in hardware, then we can have a brain-like fast processing unit.

In the brain the basic functional unit is a cell, called neuron. For each function, there will be separate set of neuron cells, which are learned to do that particular task. If we can develop a neuromorphic circuit for the neuron cell and can make it learn to do particular tasks, we can use it to develop a brain-like processing unit, that is what is achieved through this project work.

## 2. Neurons

Neurons are the basic building blocks of the nervous system, which includes brain, spinal cord and peripheral ganglia. Neurons are electrically excitable cells and they process and transmit information through electrochemical signals. Neurons connect together to form what is known as neural networks.

The basic structure of a biological neuron is shown in **Figure 2**. It consists of a cell body, dendrites and axons. Cell body or the soma is bulbous in shape and contains the nucleus. The cell body or the soma contains many cell organelles, including Nissl granules that are the site of protein synthesis. Nissl granules contain endoplasmic reticulum and free polyribosomes.

Dendrites arise from the cell body, branches into what is known as the 'dendritic tree'. Dendrites are the branched projections of the neuron arising from the cell body and its function is to receive the electrochemical simulations from other neurons and to conduct it to

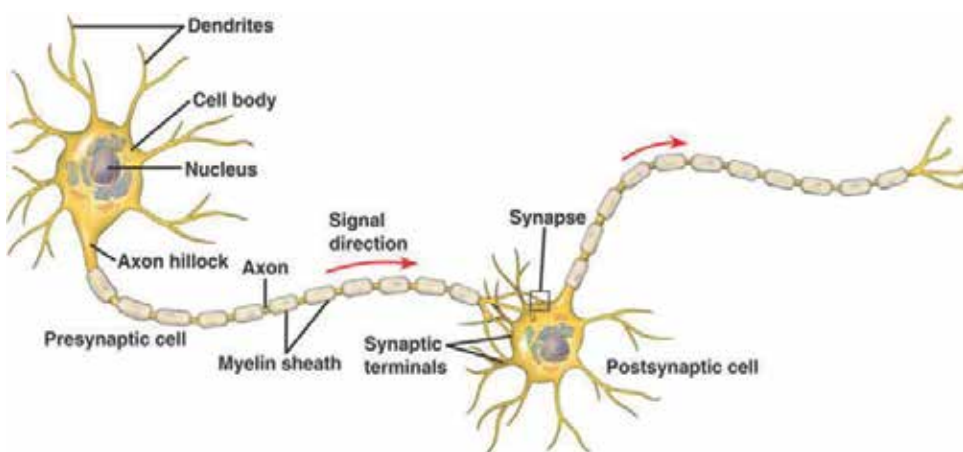


**Figure 2.** Biological neurons.

the cell body. The electrical simulations are transmitted from one neuron to the dendrite of another neuron at the synaptic terminals.

Another important part of the neuron is the axon. Axon arises from the cell body at a site called axon hillock and extends to over 1 m in length. A neuron can have multiple dendrites, but only one axon. Axon is covered by a layer of dielectric material myelin, known as myelin sheath. Before termination, the axon gets divided into a large number of branches.

The axon terminals of one neuron connect to the dendrites of another neuron through synapses. Electrochemical signals are transmitted from one neuron to another through synapses. Chemicals known as neurotransmitters are released from the presynaptic neuron, which binds to the receptors located at the dendrites of the postsynaptic neurons. These neurotransmitters are initially present in small bag-like structures known as synaptic vesicles that are found at the axonic terminals of the neurons. These synaptic vesicles, when excited, migrate towards the synapse and get attached to the synapse and release the chemical ions through the semipermeable membrane of the synapses.

The major ions that are involved in the process are sodium, potassium, chlorine and calcium. Once released, these ions diffuse through the semipermeable membrane and binds to the receptors which are present on the dendrites of the post-synaptic neurons. The basic structure of a synapse is shown in **Figure 3**.

Due to the ion exchange between neurons, a gradient in the ion concentration arises on either side of the semipermeable membrane. Due to this ion concentration difference, a potential will be generated, known as Nernst potential. Changes in the cross-membrane voltage between the intra-cellular and extra-cellular potential will alter the function of the voltage-dependence

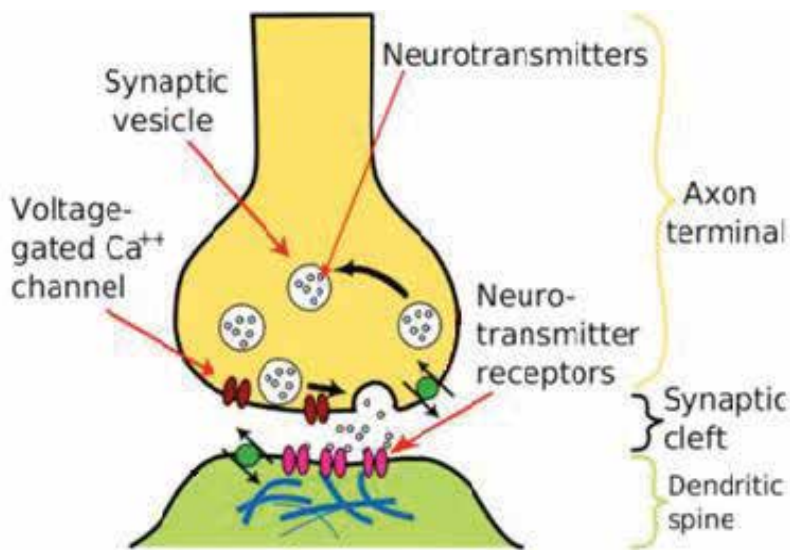


**Figure 3.** Structure of synapse.

channels. As the difference in ion concentration increases, the resultant Nernst potential also increases and when this potential reaches a particular threshold value, the post-synaptic neuron fires and an action potential is generated which moves from cell body to the next neuron through the axon. This is how a biological neuron transmits signals.

There are several differences between the processing in human brain and processing in a computer. One of the most important differences is that brain is analogue whereas the computers are digital. The computers work with 0's and 1's whereas neuron signals are not bi-state. But we can find a superficial similarity between neurons and digital circuits in the aspect that neurons fire an action potential when they reach a threshold value. In computers, information in memory is accessed by polling its precise memory address. This is known as byte-addressable memory whereas brain uses content-addressable memory.

Human brain can be considered as a massively parallel machine, where different functions are carried out simultaneously in different parts of the brain. Brain has got several dedicated modules for carrying out different functions. But if we consider the case of computers, the processing is in modular and serial in nature.

The brain has got a body at its disposal. This may seem to be trivial, but this is a major difference which gives the humans a clear advantage over the computers. Once the brain takes a decision based on the input signals, the brain directs the body to respond to the signals. But in computers, although it can take decisions based on the input signals, there is no body so that it can respond to the stimulus.

Although there are several other differences, one of the most important differences between brain and computing processors is that there exists no distinction between memory and processing architecture in brain. These two important activities are not separable. As the neurons process information, they also modify their synapses that are the substrate of memory. But in computers there exist a clear distinction between processor and memory.

### 3. Memristor

Memristor is considered to be the fourth fundamental electronic component. The basic state variables in any circuit are voltage ( $V$ ), current ( $I$ ), charge ( $q$ ) and flux ( $\phi$ ). The state variables and relations between them are shown in **Figure 4**. Prior to the 1970s, only resistor, capacitor and inductor were known. No component showing the property of memristance was known to the scientific community. It was in 1971 that Leon Chua gave the scientific and logical basis for the existence of a two terminal circuit element called memristor (memristor is the shortened form of 'memory resistor') [3]. He reasoned the existence of the fourth element through symmetry arguments. Although he showed that the memristor has many interesting and valuable circuit properties, he was unable to implement the memristor in the form of a physical device without an internal power supply.

The six different mathematical relations connect the four fundamental circuit variables: voltage ( $V$ ), current ( $I$ ), charge ( $q$ ) and magnetic flux ( $\phi$ ). These relations are indicated in **Figure 4**.

Since there were no devices that reflected a relation for long between the charge and flux, the memristor was referred to as the missing element, with memristance ( $M$ ), with  $d\phi = Mdq$ .

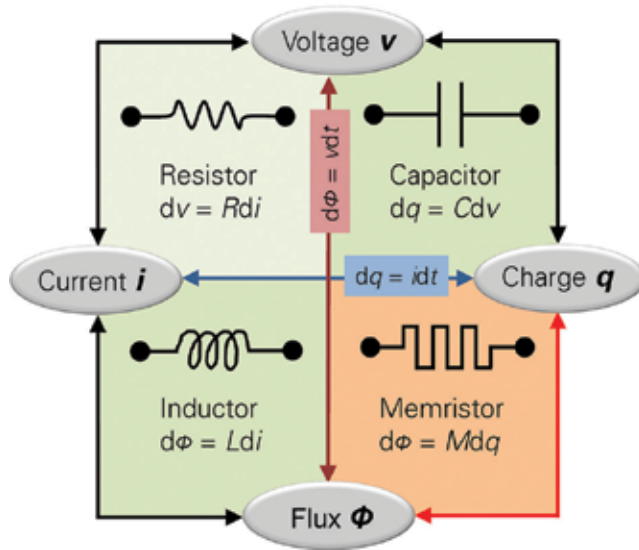


Figure 4. Relation between various state variables in an electronic circuit.

One of the most advertised and commercially inclined versions of the memristor was developed by HP Labs that was based on a thin film of titanium dioxide [4, 5]. The main reason that gained attention for this device was the possibility to scale the device beyond the traditional CMOS limits. While, there is debate on the charge transport mechanisms and resistance switching behaviours, the hypothesis is that the hysteresis requires some sort of atomic rearrangement that modulates the electronic current. The HP memristor device consists of a thin film of titanium dioxide ( $TiO_2$ ) sandwiched between two platinum electrodes, with one side of the titanium dioxide doped with oxygen vacancies,  $TiO_{2-x}$  (see Figure 5).

The undoped region is insulated and has higher resistance than the doped region. The effective resistance within the memristor is determined by the boundary between the doped and

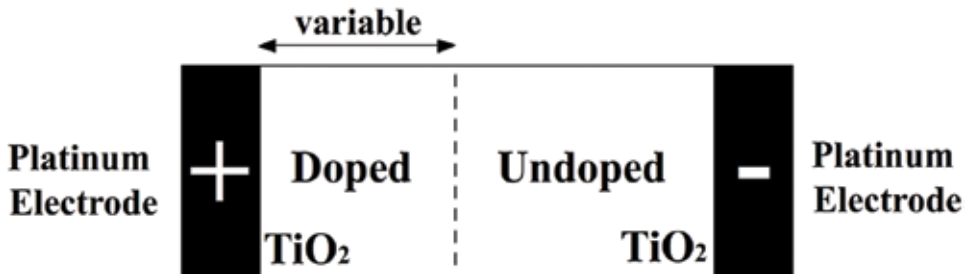


Figure 5. Memristor modelled by HP.

undoped regions. Let  $D$  be the total width of the  $\text{TiO}_2$  layer and  $W$  be the width of the doped region. Then the effective resistance of the device is given by  $M_{\text{eff}} = (W/D)R_{\text{ON}} + (1 - (W/D))R_{\text{OFF}}$ , where  $R_{\text{ON}}$  is the resistance of the device if it is completely doped and  $R_{\text{OFF}}$  is the resistance of the device if it is completely undoped, see **Figure 6**.

Under the situation, when a positive voltage at the side of the doped region and negative voltage at the side of the undoped region, the oxygen vacancies move from the doped side to the undoped side, thus, increasing the width ( $W$ ) of the doped region. This results in the overall resistance of the memristor.

If the polarity of applied voltage is reversed, that is, positive potential is applied to the undoped side and negative potential is applied to the doped side, then the width of the undoped region increases, thereby increasing the effective resistance of the device.

When input voltage is withdrawn or when there is no potential difference between the terminals, the memristor maintains the boundary between the doped and undoped region, since the oxygen ions remain immobile after removal of the input voltage. Thus, the resistance will be maintained at the same value before withdrawing the input voltage.

The resistance of the memristor increases when current flows through it in one direction and the resistance value decreases when the current flows through it in the opposite direction. It can retain the resistance value it had at that point of time, if the current is stopped.

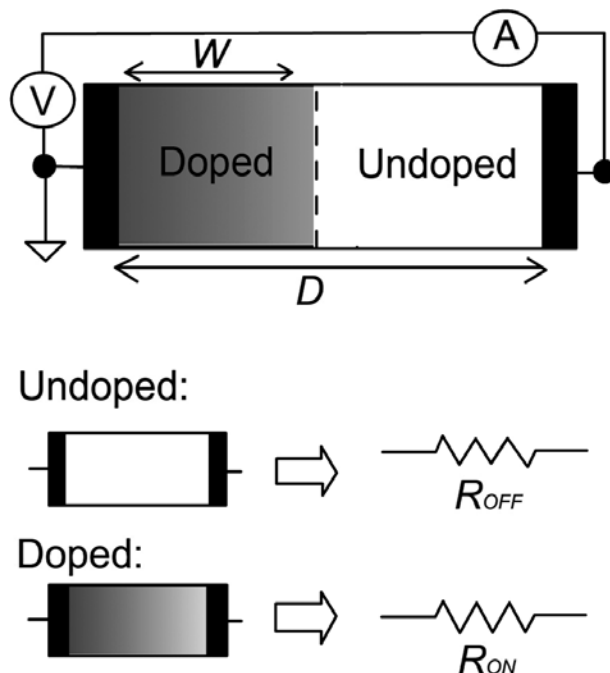


**Figure 6.** Working of a memristor.

We can see from  $i = v/M(q)$  that when there is no voltage difference across the memristor, there is no current through the memristor. When the potential applied is reversed, the width of the undoped region increases resulting in an increase in effective resistance. The high resistance blocks any reverse leakage current and adding more inputs, the collective current does not increase significantly as the effective resistance remains constant.

The  $V$ - $I$  characteristics of the memristor are shown in **Figure 7**. Generally, indicative of a pinched hysteresis effect [3, 4, 6], the changes in the slope indicate the switching behaviour, with each of the switch having at least two resistance states. With change in operating frequencies, the resistance values of the state become equal at high frequencies. The frequency dependence of memristor is shown in **Figure 7**.

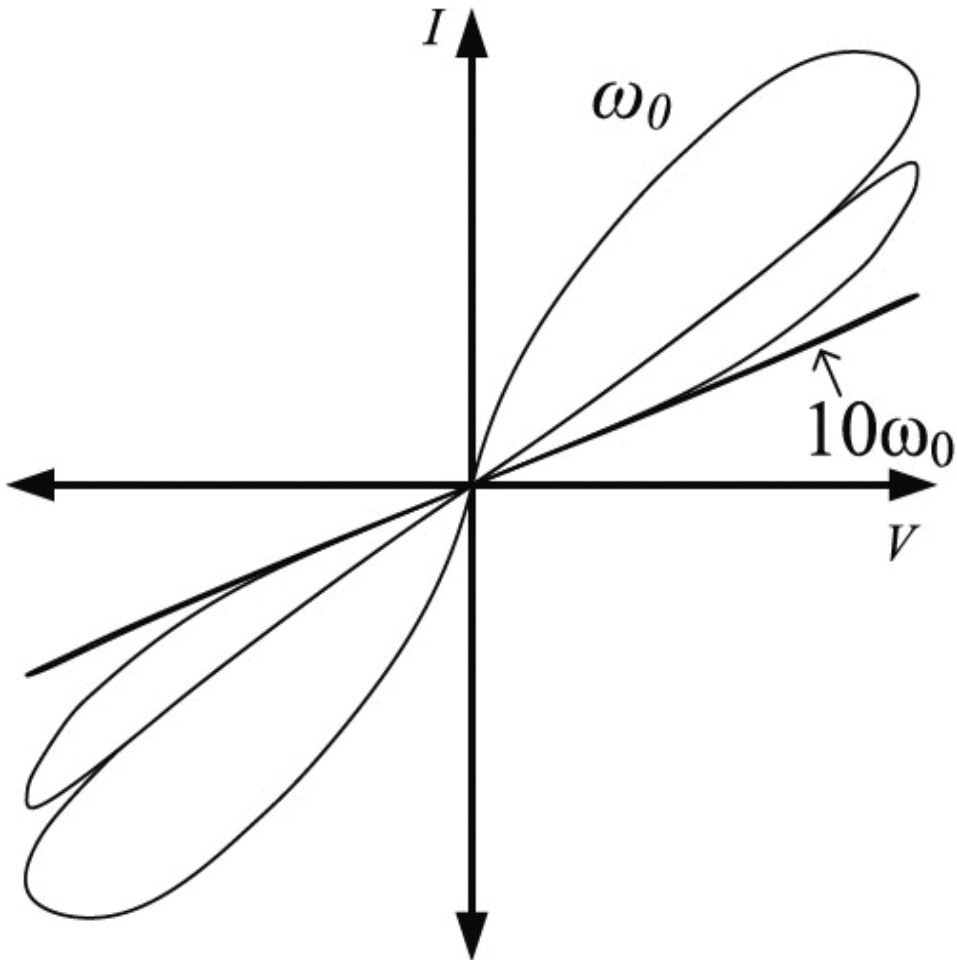


**Figure 7.** The  $V$ - $I$  characteristics of the memristor device.

Over the years, there have been several efforts to manufacture memristors. The various attempts include polymeric or ionic memristors, resonant tunnelling diode memristors, manganite memristors and spintronic memristors. In addition to the memristor devices, there are circuits that emulate the memristor behaviour, generally referred to as memristive systems.

The crossbar architecture with memristor is used to build ultra-dense memory cells (RRAM—resistive random-access memory). Another application is the use of memristor for emulating neural circuits that can help develop a range of hardware-based machine learning methods. The memristors can be also used to implement multilevel memories [7, 8] and analogue memories [9]. They also find application in configurable logic arrays [10].

#### 4. Resistive threshold logic

Resistive threshold logic [11, 12] is a new logic family based on a resistive voltage divider and threshold logic, which is the hardware implementation of the neuron cell by configuring the cognitive memory network [13]. This circuit is capable of doing all Boolean logic [14, 15].

Two-input basic resistive threshold logic cells are shown in **Figure 8**. For a straight forward approach, we started by using semiconductor resistors for the resistive divider. The input to the resistive divider is voltage levels that can be equated to the logic inputs [10] of a digital logic gate. Based on the logic functionality required, predefined threshold levels will be used in the thresholding part.

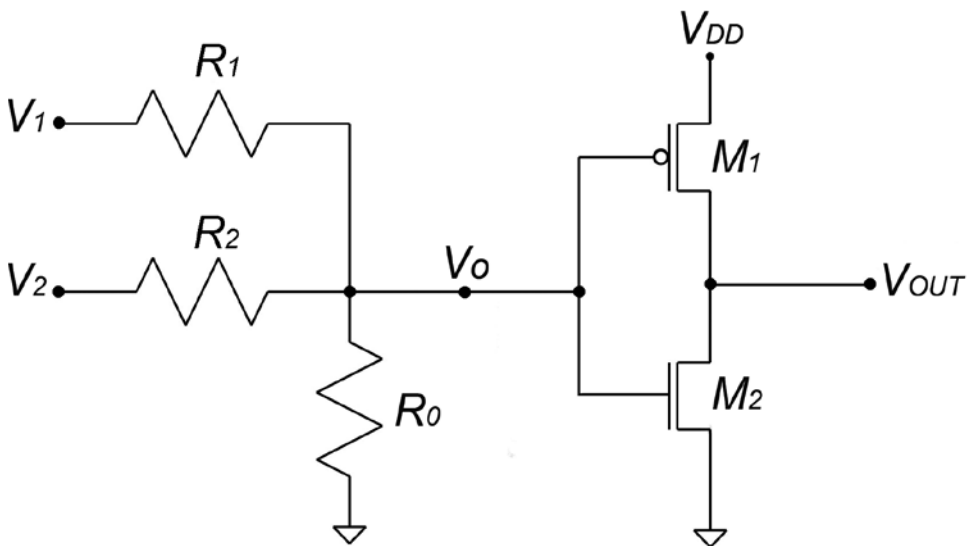


**Figure 8.** Two-input basic resistive threshold logic cell.

An  $N$ -input resistance divider circuit consist of  $N$  input resistors  $R_i$  and one reference resistor  $R_0$ . The output voltage  $V_0$  for  $N$ -input voltages  $V_i$  is shown in Eq. (1),

$$V_0 = \frac{\sum_{i=1}^N \frac{V_i}{R_i}}{\left(\frac{1}{R_0} + \sum_{i=1}^N \frac{1}{R_i}\right)} \tag{1}$$

We keep equal values to  $R_i$ 's and  $R_0 = m R_i$ , which results in:

$$V_0 = \frac{\sum_{i=1}^N V_i}{\frac{1}{m} + N} \tag{2}$$

The inverter with a threshold  $V_{th}$  and a two-input resistive divider is used to implements the NAND and NOR gates shown in **Table 1**. Given that,  $V_{dd} = 1V$ ,  $V_H = 1V$ ,  $V_L = 0V$ , (see **Table 1**), when the threshold voltage of the inverter is set between 0 and  $1/3 V$ , the cell functions as NOR logic, while between  $1/3$  and  $2/3 V$  the cell functions as NAND logic. This implies that varying the threshold voltage of the inverter a single cell structure can be used to implement NAND and NOR logic.

In general, the range of threshold voltage,  $V_{th}$  of NOR gate is  $\frac{Nm V_L}{1+Nm} \leq V_{th} \leq \frac{(V_H + (N-1)V_L) m}{Nm+1}$  and NAND gate is,  $\frac{m(V_L + (N-1)V_H)}{Nm+1} \leq V_{th} \leq \frac{mNV_H}{Nm+1}$ .

To find the  $m$  value in Eq. (2), the lower limit of NAND gate threshold range  $\frac{m(V_L + (N-1)V_H)}{Nm+1}$  is equated to  $\frac{V_H + V_L}{2}$ . And to solve the equation  $V_L$  is taken as 0 V. So we get the  $m$  value as  $\frac{1}{N-2}$ . Now we can say that the threshold voltage of NAND gate must be between  $\frac{V_H + V_L}{2}$  and  $\frac{mNV_H}{Nm+1}$ .

But there are certain drawbacks in using semiconductor resistors for building the voltage divider. One of the most important factors is the large leakage current of the semiconductor resistors. When the number of inputs increases the problem of leakage current becomes prohibitively high. Another drawback of using semiconductor resistor is that a change in the resistance value of the resistor due to second-order implementation effects, such as improper junctions and defects. This change in the resistance value is generally termed as the tolerance

Input voltage ( $V_i$ )		Output voltage	NAND	NOR
$V_1$	$V_2$	$V_0$	$\frac{V_L + V_H}{3} < V_{th} < \frac{2V_H}{3}$	$\frac{2V_L}{3} < V_{th} < \frac{V_L + V_H}{3}$
$V_L$	$V_L$	$\frac{2V_L}{3}$	$V_H$	$V_H$
$V_L$	$V_H$	$\frac{V_L + V_H}{3}$	$V_H$	$V_L$
$V_H$	$V_L$	$\frac{V_L + V_H}{3}$	$V_H$	$V_L$
$V_H$	$V_H$	$\frac{2V_H}{3}$	$V_L$	$V_L$

**Table 1.** Truth table of two-input resistive divider for NAND and NOR gates.

value of a resistors, which is usually  $\pm 10\%$ . This change in the resistance value may not create any problem when we are considering two-input or three-input circuits. But in practical implementations having a large number of inputs, these changes in the resistance value will have an adverse effect on the output of the circuit.

To overcome these drawbacks, semiconductor resistors were replaced with memristors developed by HP, which had negligible leakage current. Thus, the logic gate was modified as shown in **Figure 9**. The advantage of using op-amp in the circuit is that it can act as a buffer and isolates the inputs from output of the circuit thus enabling realistic implementations of a large number of inputs per gate. As the number of inputs shown in **Figure 8** increases, the threshold voltage will change. This change can affect the functionality of the gate. This problem can also be avoided by using the circuit shown in **Figure 9**. Here, the op-amp will boost the signal before applying it to the inverter. Thus, it offers the advantage of scalability over the number of inputs.

The op-amp reference voltage for NOR logic,  $V_{REF}$  is fixed as  $V_{L+\Delta}$  and for NAND logic,  $V_{REF}$  is fixed as  $V_{H-\Delta}$ , where  $\Delta$  is a small voltage defined to ensure the bounds of  $V_{th}$ . The op-amp shifts the voltage to a high value or low value depending on the input voltage,  $V_0$ .

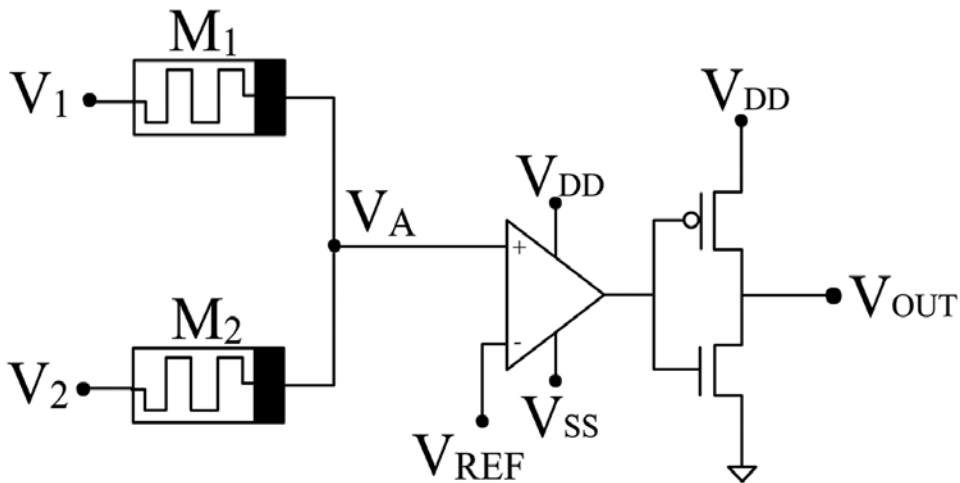


**Figure 9.** Resistive threshold logic.

The universal gate circuit using resistive threshold logic is shown in **Figure 10**. For the cell to work as a NAND logic, the switches S1 and S4 are closed and the output is taken from  $v_{out}$ . To implement AND logic, the switches S1 and S3 are closed and the output is taken from  $v'_{out}$ . If the switches S2 and S4 are closed, we get a NOR logic from  $v_{out}$ . If both S2 and S3 are closed, OR logic can be implemented.

**Figure 11** shows the circuit diagram of an  $N$ -input resistive threshold logic gate. Here  $\{V_1, V_2, V_3, \dots, V_N\}$  represents the inputs to the cell.  $\{M_1, M_2, M_3, \dots, M_N\}$  represents the input memristors. Depending on the values of the inputs, a potential  $V_A$  is generated which is given

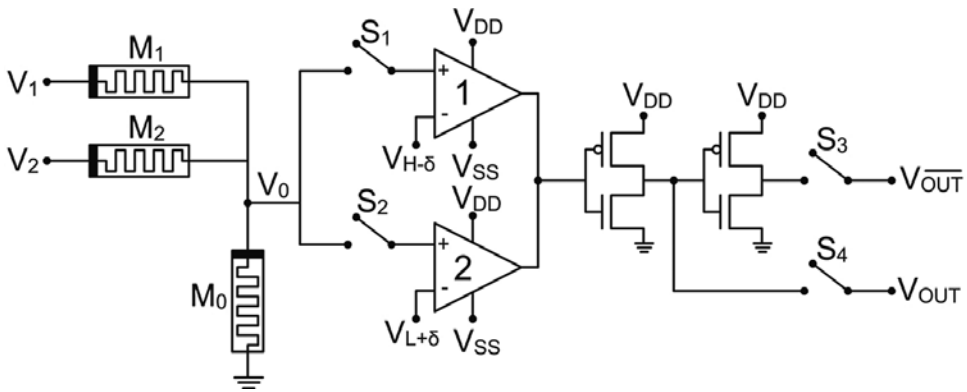


Figure 10. The universal gate structure that implements NAND, NOR, AND, OR and NOT logic functions.

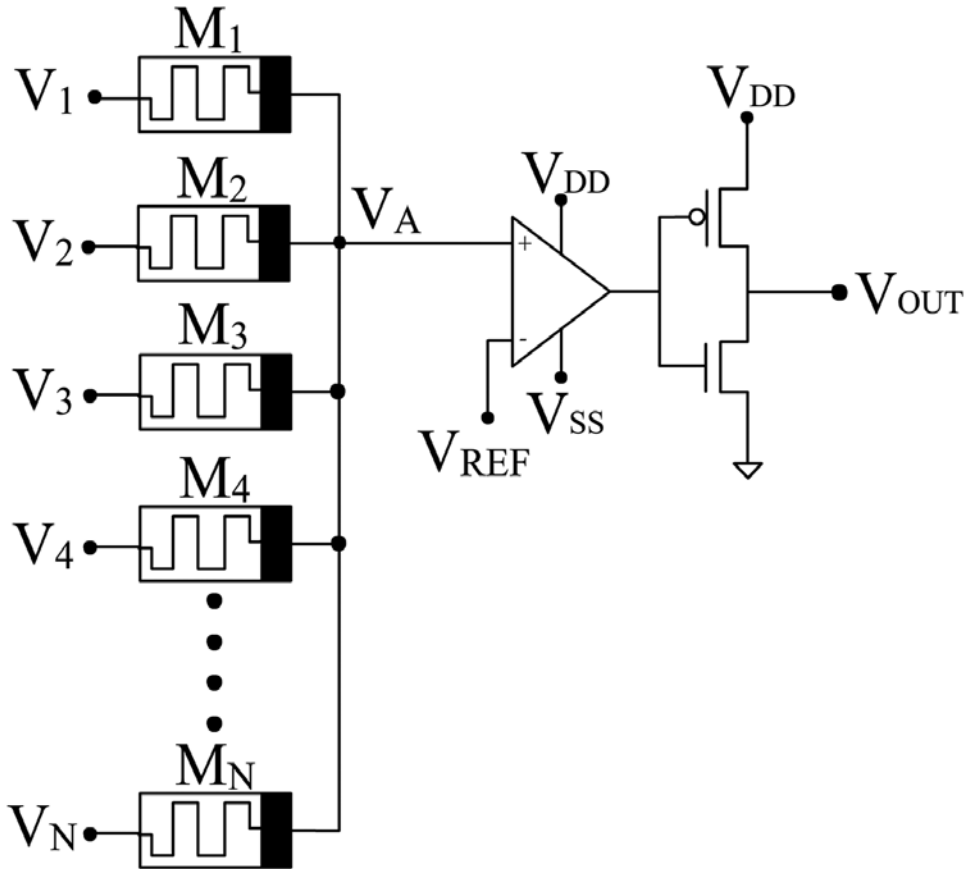


Figure 11. N-input resistive threshold logic gate.

to the non-inverting terminal of the op-amp. To the inverting terminal of the op-amp, a  $V_{REF}$  is given depending upon which the cell acts as either  $N$ -input NOR gate or  $N$ -input NAND gate. If the  $V_{REF}$  is fixed at  $V_L + \Delta$  then the circuit acts as NOR gate and for NAND logic,  $V_{REF}$  is fixed as  $V_H - \Delta$ , where  $\Delta$  is a small voltage defined to ensure the bounds of  $V_{th}$ . Thus, an  $N$ -input logic gate can be implemented using memristor-based resistive threshold logic. Here, as the number of inputs increase, only the number of memristors increases. The area consumed by a memristor is very small. Hence, even a very large input logic gate can be implemented in a very small area using the proposed resistive threshold logic.

## 5. Fast Fourier transform circuits

The chapter summarizes our previous work on the use of threshold logic in developing a hardware implementation of Fast Fourier transform [16]. Fast Fourier transform/inverse fast Fourier transform (FFT/IFFT) is widely used algorithm to compute the discrete Fourier transform and its inverse of a given set of inputs. FFT/IFFT is mainly used in digital signal processing applications such as communication systems including orthogonal frequency division multiplexing (OFDM), spectrum analysis, DSL modems, speech coding, HDTV etc. Due to the large number of applications, it is important to design a FFT circuit which can handle large number of inputs and at the same time it should be small in area and should not become too complex.

The basic equation of four-point DFT is

$$X(k) = \sum_{n=0}^3 x(n) e^{-j\frac{2\pi nk}{4}}, \quad k = 0, 1, 2, 3 \tag{3}$$

Eq. (3) can be rewritten as an N-by-N multiplication as

$$X = Wx \tag{4}$$

Eq. (4) can be expanded in matrix form as given below.

$$\begin{bmatrix} X(0) \\ X(1) \\ X(2) \\ X(3) \end{bmatrix} = \begin{bmatrix} 1 & 1 & 1 & 1 \\ 1 & -j & -1 & j \\ 1 & -1 & 1 & 1 \\ 1 & j & -1 & j \end{bmatrix} \begin{bmatrix} x(0) \\ x(1) \\ x(2) \\ x(3) \end{bmatrix} \tag{5}$$

In the above matrix multiplication,  $X(k)$ ,  $k = 0, 1, 2, 3$  are the DFT outputs whereas  $x(k)$ ,  $k = 0, 1, 2, 3$  are the inputs. Using this matrix equation, we can represent the signal flow graph of four-point DFT, as shown in **Figure 12**. The exponential term  $e^{-j\frac{2\pi nk}{4}} = \pm 1$  or  $\pm j$ . Since multiplications with  $\pm 1$  and  $\pm j$  are trivial, no multipliers are needed to implement them, i.e. they can be simply realized with bypass, inversion, and/or swap for 2's complement numbers. Hence, it does not

require any multiplier to construct a butterfly element for a four-point DFT (radix-4 butterfly). From **Figure 12**, it can be seen that we can implement the processor using adders and inverters.

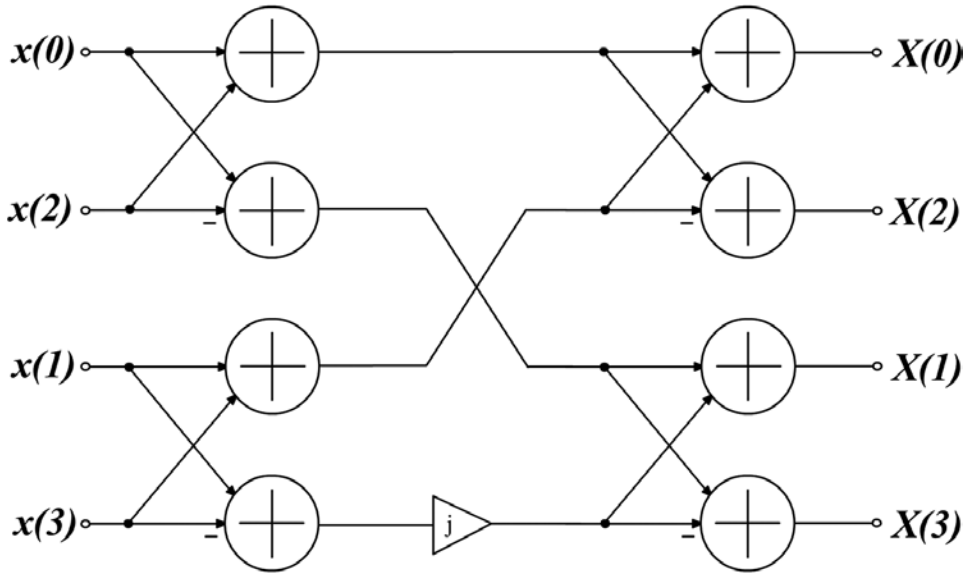


**Figure 12.** Signal flow graph of a four-point FFT.

Implementation of the FFT processor can be done, as shown in **Figure 13** where  $x(0)$ ,  $x(1)$ ,  $x(2)$  and  $x(3)$  are the inputs and  $X(0)$ ,  $X(1)$ ,  $X(2)$  and  $X(3)$  are the outputs of the FFT circuits. The circuits are capable of handling complex numbers and the complex numbers are separated into real and imaginary part and are given into the circuit. All the inputs to the circuit are 8 bits long.

All the FFT units take in four inputs and give the corresponding FFT output. Inputs are given to the FFT units according to **Figure 12**. From the signal flow graph of the four-point FFT, we can see that FFT outputs are obtained by equations of the form

$$X(k) = a + b + c + d \tag{6}$$

or

$$X(k) = a + b - c - d \tag{7}$$

So it is understood that certain inputs need to be subtracted in order to get the Fourier transform output. In digital circuits, subtraction is carried out by taking the 2's complement of the subtrahend and then adding it to the minuend to get the difference. For obtaining 2's complement of a number, first of all, 1's complement of the number has to be found out and then add one to it.

From **Figure 12**, it can be seen that the real and the imaginary part of the first output, i.e.  $X(0)$ , in four-point FFT is obtained by computations of the form Eq. (6). So it requires addition operations only. Hence, the inputs to the first two FFT units are not complimented, as shown in **Figure 13**.

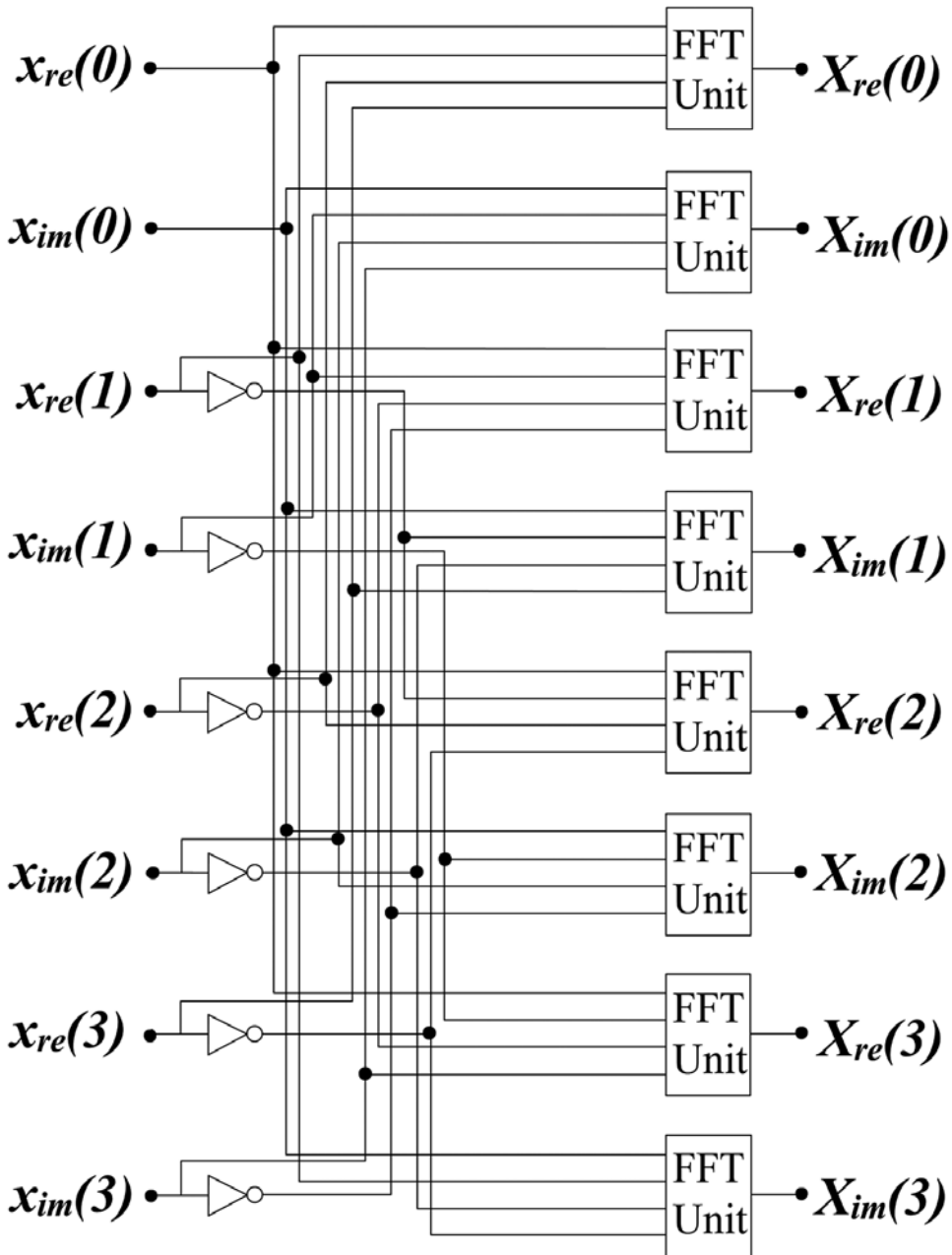
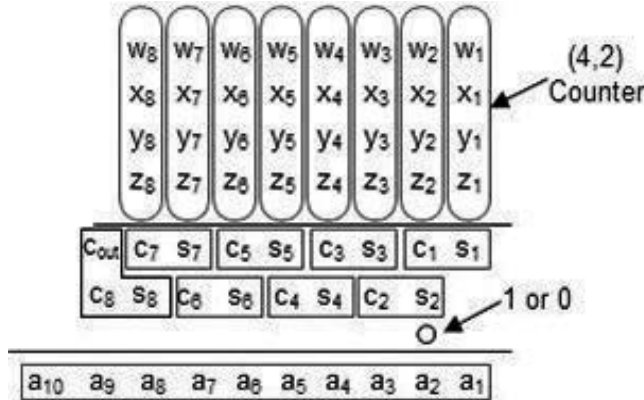


Figure 13. General block diagram of a four-point FFT circuit.

However, all other outputs of the four-point FFT are obtained by computations of the form Eq. (7), see Figure 12. So it consists of addition as well as subtractions. In order to implement subtraction, two's complement of the inputs is taken and is added. For taking 2's complement, first of all, the signals need to be inverted. This is obtained by the inverters shown in Figure 13.

Since all the inputs are of 8-bit length, 8-bit inverters are used in the circuit. The output of these inverters will be the 1's compliment of the input signals. To get 2's complement one must be added to the 1's compliment. Since two signals are to be complimented according to Eq. (7), two must be added to their sum. It is equivalent to adding one be the (LSB + 1)th place of their sum. This is done inside their corresponding FFT units, see **Figure 14**.



**Figure 14.** General block diagram of a FFT unit.

Let the four inputs to an FFT unit be denoted as  $w$ ,  $x$ ,  $y$  and  $z$ . All these inputs are 8-bit long. So the input  $w$  can be represented as  $w_8 w_7 w_6 w_5 w_4 w_3 w_2 w_1$ . Similarly,  $x$ ,  $y$  and  $z$  can be represented as  $x_8 x_7 x_6 x_5 x_4 x_3 x_2 x_1$ ,  $y_8 y_7 y_6 y_5 y_4 y_3 y_2 y_1$  and  $z_8 z_7 z_6 z_5 z_4 z_3 z_2 z_1$ , respectively. For the FFT units that are computing real and imaginary parts of  $X(0)$ , namely  $X_{re}(0)$  and  $X_{im}(0)$ , only additions are involved. Hence  $w$ ,  $x$ ,  $y$  and  $z$  need to be added to get  $X(0)$ . Addition of four binary numbers can be done using (4, 2)-counters or (4, 2)-compressors. So in order to implement a FFT unit, eight (4, 2)-counters are required.

The basic block diagram of a (4, 2)-counter is as shown in **Figure 15**. This circuit takes in four inputs and gives 3 outputs - sum, carry and carry out. A parallel arrangement of eight such (4, 2)-counters are needed to implement a single FFT unit. As seen from **Figure 15**, these (4, 2)-counters are implemented using the basic logic gates. All these logic gates are implemented using the proposed memristor-based resistive threshold logic.

The OR gate presented in **Figure 15** is implemented as shown in **Figure 16**, where A and B represent the inputs,  $V_L + \Delta V$  represent the reference voltage and  $V_{out}$  represents the output of the gate.

AND gate can be obtained either from inverting the output of the NAND gate or by giving inverted inputs to the NOR gate. **Figure 17** shows the AND gate, used in **Figure 15** which is obtained by giving inverted inputs to the resistive threshold NOR gate.

XOR logic gate is implemented as shown in the circuit diagram of **Figure 18**. It is implemented using NOR logic. Thus, by using the circuits of **Figures 16–18**, a (4, 2)-counter can be implemented. By using a parallel implementation of eight such (4, 2)-counters, a single FFT unit can be implemented. For implementing a full FFT circuit, we require eight FFT units, four for the real parts and four for the imaginary parts of the outputs.

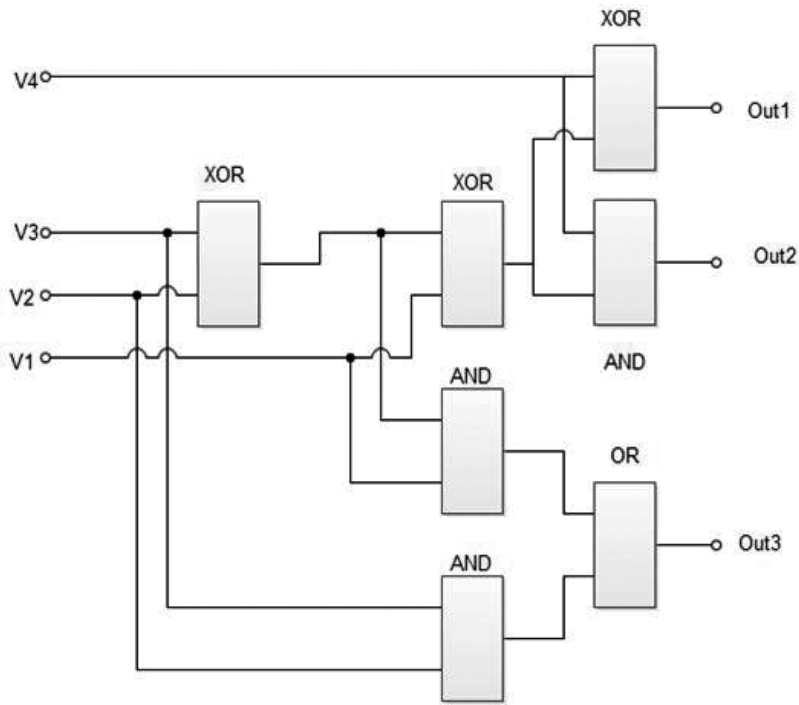


Figure 15. Block diagram of a single (4, 2)-counter.

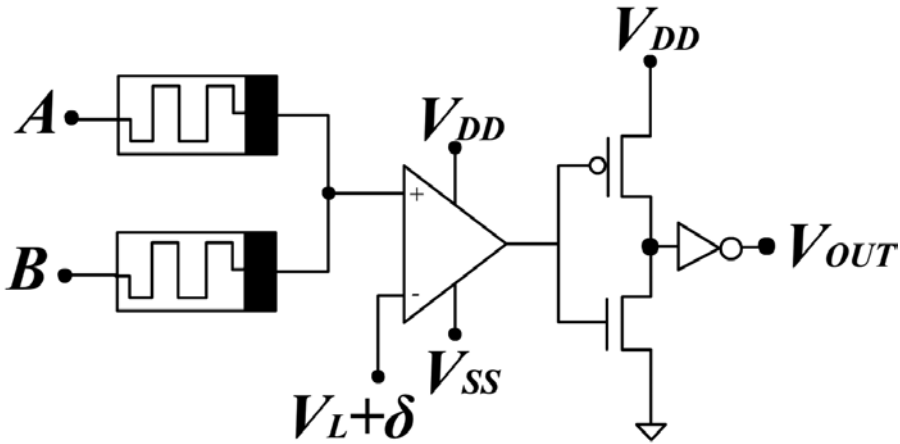


Figure 16. Circuit diagram of OR gate using memristor-based resistive threshold logic.

But while implementing the FFT units for real and imaginary parts of outputs  $X(1)$ ,  $X(2)$  and  $X(3)$ , the implementations involve subtraction. For subtractions, 2's complement of the subtrahend is taken and added. For taking 2's complement, first of all, the signal is inverted and then one is added. Inversion of the signal is carried out using an 8-bit inverter, as shown in Figure 13. The addition of one is done inside the FFT unit. Since two signals are to be subtracted per FFT unit, one has to be added twice which is equivalent to adding two or in binary terms, adding one to the (LSB+1)th position. This addition is shown in Figure 14.

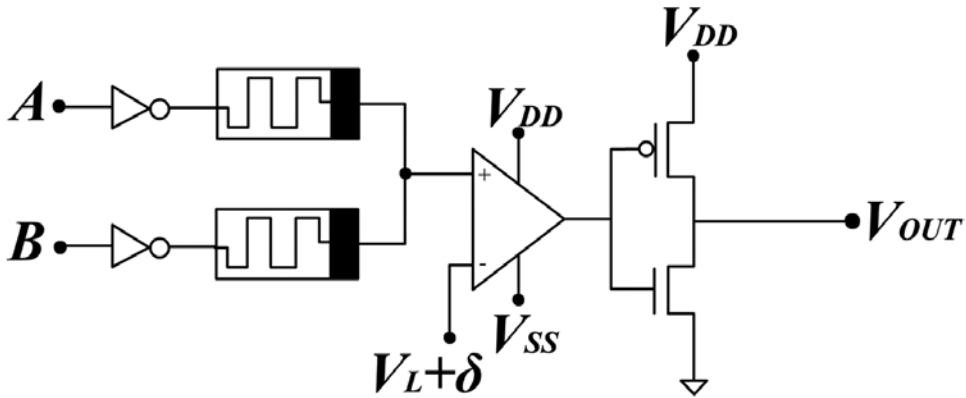


Figure 17. Circuit diagram of AND gate using memristor-based resistive threshold logic.

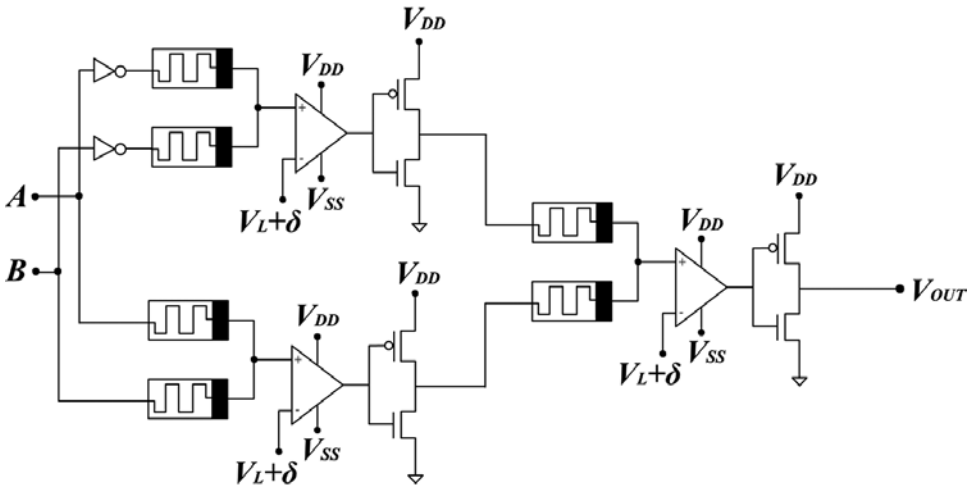


Figure 18. Circuit diagram of XOR gate using memristor-based resistive threshold logic.

## 6. Results and discussion

The proposed resistive threshold logic and FFT computing architecture have been tested and compared with corresponding CMOS [14], dynamic MOS and pseudo-NMOS circuits. Propagation delay, total harmonic distortion, area, power dissipation and leakage power were compared. For the fairness in comparison the technology, sizes of all components in the circuit are kept same.

Comparisons of the memristor-based resistive threshold logic with other logic families were carried out. **Tables 2** and **3** give the comparison results of propagation delay of NAND and NOR gates, respectively, implemented using various logic families. Comparison of resistive threshold logic with CMOS, pseudo-NMOS and dynamic-MOS logic families was carried out. The experiment was carried out for various numbers of inputs. The general trend in the

existing logic family is that the propagation delay of a gate increases as the number of inputs increases. This is due to the fact that the increase in the number of inputs means the increase in the number of input transistors. More transistors in the path lead to increase in the propagation delay of the gate.

But in the case of resistive threshold logic, this problem can be avoided. This is due to the fact that when the number of inputs increases, the number of memristors increases, but in a parallel fashion. This does not increase the path between input and output. Thus, the increase in the number of inputs does not affect the propagation delay of the overall circuit. This leads to lower propagation delay in the resistive threshold logic compared to other logic families, as the number of inputs increases. Comparison of propagation delay is shown for both NAND and NOR gates (see **Tables 2** and **3**).

Logic family	3i/p	10i/p	100i/p
CMOS logic	0.47 μs	0.54 μs	0.65 μs
Pseudo NMOS	0.48 μs	0.60 μs	0.85 μs
Dynamic MOS	0.48 μs	0.51 μs	0.75 μs
Resistive threshold logic	0.45 μs	0.45 μs	0.45 μs

**Table 2.** Comparison of propagation delay of NAND gate various logic families.

Logic family	3i/p	10i/p	100i/p
CMOS logic	0.50 μs	0.52 μs	0.66 μs
Pseudo NMOS	0.51 μs	0.58 μs	0.72 μs
Dynamic MOS	0.51 μs	0.58 μs	0.75 μs
Resistive threshold logic	0.60 μs	0.60 μs	0.60 μs

**Table 3.** Comparison of propagation delay of NOR gate various logic families.

Another comparison that shows the advantage of the proposed logic family is that of total harmonic distortion (THD). The total harmonic distortion gives the measure of harmonic distortion present in a circuit. Consider a signal of frequency  $x$ , the harmonics of the signals are signals containing frequencies  $2x, 3x, 4x$  and so on. These harmonics cause distortion in the output of the circuit. The total amount of distortion caused by the harmonics is measured as total harmonic distortion. It can be defined as the ratio of powers of all harmonics to the power of the fundamental frequency.

Let the power of the fundamental frequency signal be  $P_1$ . Let the powers of the harmonics be  $P_2, P_3, P_4, \dots, P_n$ . Then the total harmonic distortion can be expressed as Eq. (8).

$$THD = \frac{\sum_{i=2}^{\infty} P_i}{P_1} \tag{8}$$

So higher the THD value means higher the distortion caused by the harmonics. When comparing the values in **Table 4**, it can be seen that the total harmonic distortion of the proposed

memristor-based resistive threshold logic is less when compared to other existing logic families. Thus, it can be seen that the proposed logic family has several advantages when compared to the existing logic families. Various comparisons were carried out for the fast Fourier transform circuits of **Figure 13**. **Table 5** gives the comparison of area of the FFT circuit implemented using different logic families.

Logic family	THD of NAND (%)	THD of NOR(%)
CMOS logic	71.2091	107.4098
Pseudo NMOS	76.2288	97.9864
Dynamic MOS	51.0608	146.7818
Resistive threshold logic	61.7043	85.2743

**Table 4.** Comparison of total harmonic distortion of NOR and NAND gate various logic families.

Logic family	Area ( $\mu\text{m}^2$ )
CMOS logic	83.5200
Pseudo NMOS	53.0496
Dynamic MOS	58.4852
Resistive threshold logic	58.1292

**Table 5.** Comparison of the total area of FFT circuits using various logic families.

The area comparison clearly shows that the circuit implements using the proposed logic family require less area compared to most of the other existing logic families. Another comparison was carried out regarding the power dissipation of the circuit, the results of which are shown in **Table 6**.

Logic family	Power
CMOS logic	19.3842 $\mu\text{W}$
Pseudo NMOS	14.6467 $\mu\text{W}$
Dynamic MOS	03.9515 nW
Resistive threshold logic	13.7932 $\mu\text{W}$

**Table 6.** Comparison of the total power dissipation of FFT circuits using various logic families.

The proposed logic family consumes less power when compared to other logic families. In **Table 6**, the power dissipation of the circuit using dynamic MOS is much less compared to other logic families owing to the fact that the dynamic MOS is a clocked logic family.

Now, **Table 7** shows the comparison of the FFT circuit implemented using various logic gates, in respect of their leakage power. The slight increase in the leakage power of the circuit using proposed logic family is due to the presence of op-amp in the circuit.

Logic family	Leakage power
CMOS logic	8.5377 nW
Pseudo NMOS	1.0629 mW
Dynamic MOS	4.8410 nW
Resistive threshold logic	11.1378 nW

Table 7. Comparison of leakage power of FFT circuits using various logic families.

As mentioned earlier, each of the FFT unit takes in four inputs, each of which is 8-bit long. Figure 19 shows the 8th bit of the four inputs to a single FFT unit. The outputs of each FFT unit will be 10-bit long. Figure 20 shows the LSB of the outputs of FFT unit for inputs shown in Figure 19.

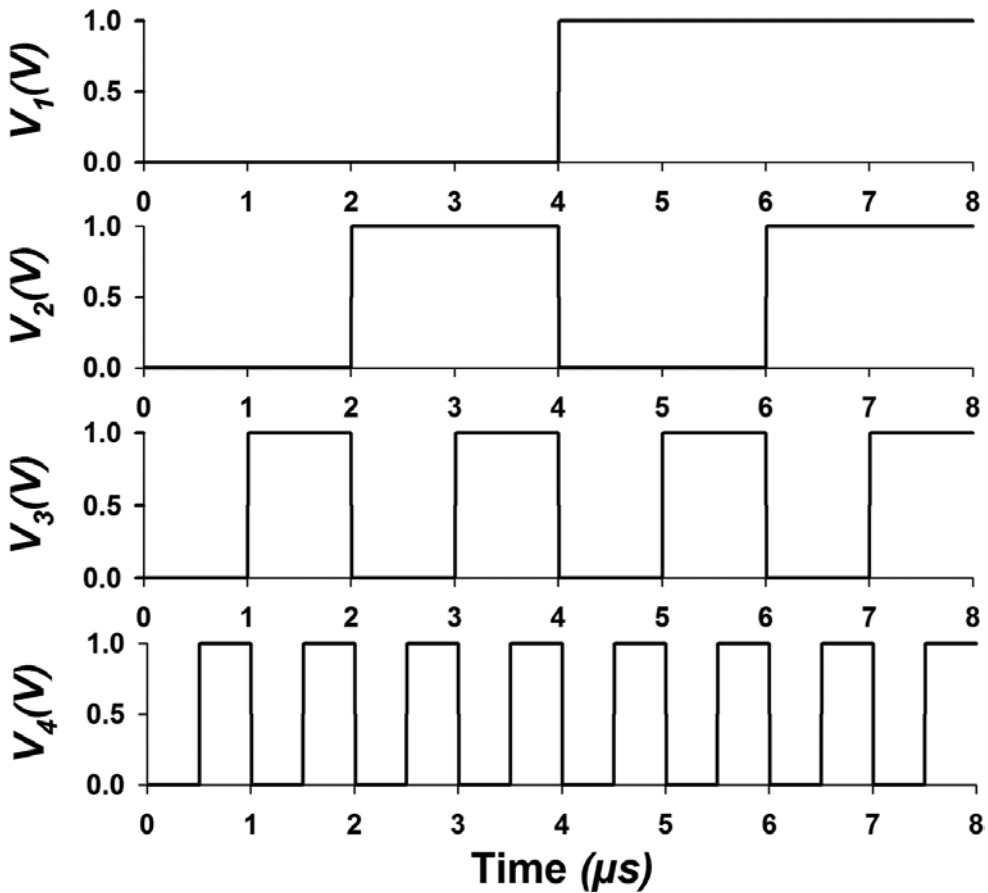


Figure 19. Eighth bit of the four inputs to a FFT unit.

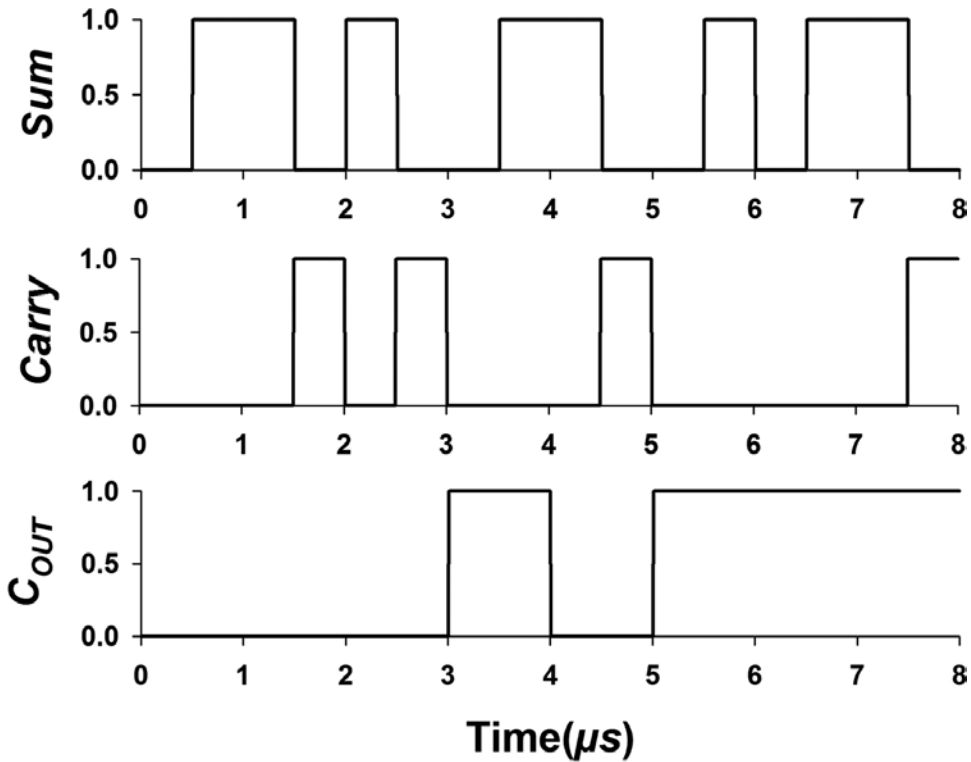


Figure 20. LSB of the output of the FFT unit is shown as sum. Carry and Cout of the LSB are also shown.

## 7. Discussion

In order to maintain practical relevance of the approach, all the results mentioned in the previous section are based on device parameters from 90 nm TSMC process. HP memristor models with  $R_{ON} = 100 \Omega$  and  $R_{OFF} = 100 \text{ k}\Omega$  were used and all the simulations were carried out using LTSpice VI.

From the results shown in the previous section, it can be seen that the proposed logic family is clearly of advantage when we are trying to implement large input circuits. The comparison of propagation delay of the logic gates showed that the memristor-based resistive threshold logic family can be used to implement brain-like large input logic functions. Moreover, it gives a clear advantage in terms of the total harmonic distortion also. After the successful implementation of the new logic family, it was used to implement a circuit that could compute the fast Fourier transform of the given set of inputs. A four-point FFT circuit was implemented. It can take in four inputs at a time and give four FFT outputs. The circuit can handle complex numbers and the complex inputs were separated into real and imaginary part for the easy computation. All the inputs considered in this project were 8-bit long.

All the circuits and gates involved in the FFT circuit were implemented using the proposed memristor-based resistive threshold logic family. The speed of operation of the circuit can be further increased and the area can be further reduced if low power and high speed op-amp designs are developed, or an alternative thresholding circuit needs to be developed. If a better op-amp can be developed, then the leakage power can also be reduced to a great extent. Moreover, in the proposed logic, we are not concentrating on the memory power of memristor. If we can use that property of memristor in our architecture to save the data, then we can implement a memory unit also.

As a future work, the memory property of the memristor can be made use of using this property, a very efficient memory unit can be implemented. Since the area required for the memristor is very small, a very compact and area-efficient memory cell can be developed which can be used as an alternative for the existing memory cells. Also, only two-state logic gates are considered in this project. But in the future, by making use of the memory property of the memristor, multi-state logic functions can also be implemented. The op-amps used in this project can be replaced by more efficient and smaller op-amps, thereby, further reducing the area and leakage power and also increase the speed of operation of the circuit.

## 8. Summary

The concept of brain-like processing unit was presented using resistive threshold logic. The proposed memristor-based resistive threshold logic gate was used to implement circuits that could compute the fast Fourier transform of a given set of inputs. The proposed logic family was found too advantageous in many ways. However, there are certain disadvantages too, like the leakage power. Further development in the thresholding circuit will help to overcome this issue. In addition, the ability of the proposed architecture to perform brain-like processing can be seen as an early step in achieving the goal of mimicking brain-like processing unit in VLSI.

## Author details

Alex Pappachen James

Address all correspondence to: [apj@ieee.org](mailto:apj@ieee.org)

Bioinspired Microelectronic Systems Lab, School of Engineering, Nazarbayev University, Astana, Republic of Kazakhstan

## References

- [1] Zaidi ZF. Gender differences in human brain: a review. *The Open Anatomy Journal*. 2010;2:37–55.

- [2] Borzenko A. Language processing in human brain. In: Proceedings of the First AGI Conference; March 1–3; Memphis. IOS Press; 2008.
- [3] Chua LO. The missing circuit element. *IEEE Tans. Circuit Theory.* 1971;**18**:507–519.
- [4] Williams RS. How we found the missing memristor. *IEEE Spectrum.* 2008;**45**:28–35.
- [5] Williams RS, Strukov DB, Snider GS, Stewart DR. The missing memristor found. *Nature.* 2008;**453**:80–83.
- [6] Joglekar YN, Wolf SJ. The elusive memristor: properties of basic electrical circuits. *European Journal of Physics.* 2009;**30**:661–675.
- [7] Kim H, Sah MP, Yang C, Chua LO. Memristor-based multilevel memory. In: 12th International Workshop on Cellular Nanoscale Networks and their Applications (CNNA 2010); February 3–5; Berkeley, CA. pp. 1–6; 2010.
- [8] Manem H, Rose GS, He X, Wang W. Design considerations for variation tolerant multi-level CMOS/Nano memristor memory. In: Proceedings of the 20th symposium on Great lakes symposium on VLSI; May 16; ACM; 2010. pp. 287–292.
- [9] Laiho M, Lehtonen E. Arithmetic operations within memristor-based analog memory. In: 12th International Workshop on Cellular Nanoscale Networks and their Applications (CNNA 2010); Feb 3; IEEE; 2010. pp. 1–4.
- [10] Xia Q, Robinett W, Cumbie MW, Banerjee N, Cardinali TJ, Yang JJ, Wu W, Li X, Tong WM, Strukov DB, Snider GS. Memristor–CMOS hybrid integrated circuits for reconfigurable logic. *Nano Letters.* 2009;**9**(10):3640–3645.
- [11] James AP, Francis LR, Kumar DS. Resistive threshold logic. *IEEE Transactions on Very Large Scale Integration (VLSI) Systems.* 2014 ;**22**(1):190–195.
- [12] Maan AK, Jayadevi DA, James AP. A survey of memristive threshold logic circuits. *IEEE Transactions on Neural Networks and Learning Systems.* 2016;**99**:1–13.DOI: 10.1109/TNNLS.2016.2547842
- [13] James AP, Dimitrijević S. Cognitive memory network. *Electronics Letters.* 2010;**46** (10):677–678.
- [14] Petrick, S.R. A direct determination of the irredundant forms of a Boolean function from the set of prime implicants. Air Force Cambridge research Center, Cambridge. Techn. Rep. AFCRC-TR-56–110, 10 (1956).
- [15] McGeer PC, Sanghavi JV, Brayton RK, Sangiovanni-Vicentelli AL. ESPRESSO-SIGNATURE: a new exact minimizer for logic functions. *IEEE Transactions on Very Large Scale Integration (VLSI) Systems.* 1993;**1**(4):432–440.
- [16] James AP, Kumar DS, Ajayan A. Threshold logic computing: memristive-CMOS circuits for fast Fourier transform and vedic multiplication. *IEEE Transactions on Very Large Scale Integration (VLSI) Systems.* 2015;**23**(11):2690–2694.

---

# Application of Fourier Series Expansion to Electrical Power Conversion

---

Irina Dolguntseva

Additional information is available at the end of the chapter

<http://dx.doi.org/10.5772/66581>

---

## Abstract

Many power electronic applications demand generation of voltage of a rather good sinusoidal waveform. In particular, dc-to-ac voltage conversion could be done by multilevel inverters (MLI). A number of various inverter topologies have been suggested so far: diode-clamped (DC) MLI, capacitor-clamped (CC) MLI, cascaded H-bridge (CHB) MLI, and others. Fourier series expansions have been used to investigate and to form a basis of different topologies comparison, to discover their advantages and disadvantages, and to determine their control. In this chapter, we discuss modulation strategies of DCMLI and CHBMLI, solve their harmonics spectra analytically, and compare them using harmonic distortion indices.

**Keywords:** Fourier series, multilevel inverters, pulse width modulation, harmonics, THD

---

## 1. Introduction

The term “power electronics” is used for a family of electrical circuits which convert electrical energy from one level of voltage/current/frequency to other using semiconductor-based switches. The switching process in power electronic converters is called *modulation*, and development of optimum modulation strategies has been the subject of research in power engineering during several past decades. Electrical power conversion has evolved as new topologies, switching devices, control, and modulation strategies have been proposed. Each group of power electronic converters has its own preferable modulation approach optimizing the circuit performance, addressing such issues as switching frequency, distortion, losses, and harmonics generation. Only voltage source inverters modulation will be discussed below.

Before turning to specific issues of modulation, one needs to establish a common basis to compare the modulation schemes. Different merits are used to evaluate a particular pulse

---

width modulation (PWM) implementation: diminished harmonics [1], filtered distortion performance factors [2], and the root-mean-square (RMS) harmonic ripple current [3]. In this text, analytical solutions to PWM strategies are used to compare magnitude of various harmonic components. This approach has a number of advantages [4].

Firstly, the conventional method of determining harmonic components of a switched waveform using fast Fourier transform (FFT) of the waveform is sensitive to the time resolution of the simulation and periodicity of the overall waveform. Moreover, it ensures that intrinsic harmonic components of PWMs are not affected by such factors as simulation round off errors, dead time, switch ON-state voltages, DC bus ripple voltages, etc.

Secondly, PWM strategies can be compared at exactly the same phase leg switching frequency.

And thirdly, the first-order weighted total harmonic distortion (WTHD) is used for a quick comparison of PWMs since it has a physical meaning (the normalized current ripple expected into an inductive load when fed from the switched waveform) and often used performance indicator.

The rest of the paper is organized as follows. In Section 2, information on the double Fourier series expansions and necessary relations is given. Essentials on PWM are provided in Section 3. Different voltage inverter topologies and their analytical PWM solutions are presented in Section 4. Harmonic distortion factors of the introduced inverter topologies, different modulation schemes are compared in Section 5, and a summary on the chapter is given in Section 6.

## 2. Double Fourier series expansion

### 2.1. Double Fourier series decomposition for a double variable function

It is well known that a periodic two variable waveform  $f(x, y)$  can be expressed in the form

$$f(x, y) = \frac{A_{00}}{2} + \sum_{n=1}^{\infty} [A_{0n} \cos ny + B_{0n} \sin ny] + \sum_{m=1}^{\infty} [A_{m0} \cos mx + B_{m0} \sin mx] \\ + \sum_{m=1}^{\infty} \sum_{\substack{n=-\infty \\ n \neq 0}}^{\infty} [A_{mn} \cos (mx + ny) + B_{mn} \sin (mx + ny)] \quad (1)$$

where the double Fourier series components can be found in a complex form:

$$C_{mn} = A_{mn} + jB_{mn} = \frac{1}{2\pi^2} \int_{-\pi}^{\pi} \int_{-\pi}^{\pi} f(x, y) e^{j(mx+ny)} dx dy. \quad (2)$$

The first term in Eq. (1) is the *DC offset* that should be zero or negligibly small. The second summation term represents the *baseband harmonics*. The first baseband harmonic,  $n = 1$ , is the *fundamental harmonic* whose magnitude defines the magnitude of the output waveform. Other baseband harmonics,  $n > 1$ , represent low-frequency undesired fluctuations about

the fundamental output and should preferably be eliminated with the modulation process. The third summation term in Eq. (1) corresponds to the *carrier harmonics* which are relatively high-frequency components. Finally, the last double summation term in Eq. (1) corresponds to groups of the *sideband harmonics* of order  $n$  located around the  $m$ th carrier harmonic component.

## 2.2. Jacobi-Anger expansion and Bessel functions relations

The magnitudes of harmonic components in Eq. (1) are to be determined for each PWM scheme for each particular combination of indexes  $m$  and  $n$ . The evaluations are based on Jacobi-Anger expansions

$$e^{\pm j\xi \cos \theta} = J_0(\xi) + 2 \sum_{k=1}^{\infty} j^{\pm k} J_k(\xi) \cos k\theta = \sum_{k=-\infty}^{\infty} j^k J_k(\xi) e^{jk\theta} \quad (3)$$

and a number of Bessel function properties:  $J_{-n}(\xi) = (-1)^n J_n(\xi)$  and  $J_n(-\xi) = (-1)^n J_n(\xi)$ , that particularly implies  $J_0(-\xi) = J_0(\xi)$  [5].

## 2.3. Parseval's theorem

Given  $f(x)$  is a periodic function with the period  $T$ , it can be represented by its Fourier series  $f(x) = a_0/2 + \sum_{n=1}^{\infty} a_n \cos n\omega t + b_n \sin n\omega t$  where  $\omega = 2\pi/T$  is the fundamental angular frequency. Then, on  $[-T/2, T/2]$ , the Parseval's theorem assumes the form

$$\frac{1}{T} \int_{-T/2}^{T/2} f^2(x) dx = \frac{a_0^2}{4} + \sum_{n=1}^{\infty} \frac{a_n^2 + b_n^2}{2}. \quad (4)$$

## 3. Pulse width modulation

To introduce the concept of PWM, let us consider a basic configuration of one-phase two-level inverter leg shown in **Figure 1**. It consists of two switches,  $S_1$  and  $S_2$ , and two diodes,  $D_1$  and  $D_2$ . Switches  $S_1$  and  $S_2$  are operating alternately at high frequency to generate a quasiperiodic output voltage  $v_a(t)$ , whose low-frequency components are intended to deliver a prescribed AC supply. When the switch  $S_1$  ( $S_2$ ) is ON, a positive voltage,  $+V_{dc}$ , (respectively, negative voltage,  $-V_{dc}$ ) is supplied to a load at the connection point  $a$ .

The essential concept of a two-level pulse-width-modulated converter system is that a low-frequency target waveform is compared against a high-frequency carrier waveform, and the comparison result is used to control the state of a switched phase leg. In case of the inverter in **Figure 1**, the phase leg is switched to the upper DC rail when the target waveform is greater than the carrier waveform, otherwise to the lower DC rail. As a result, a sequence of pulses switching between the upper and the lower DC rails is generated, which contains the target waveform as the fundamental component but also a series of unwanted harmonics arising due to the switching process.

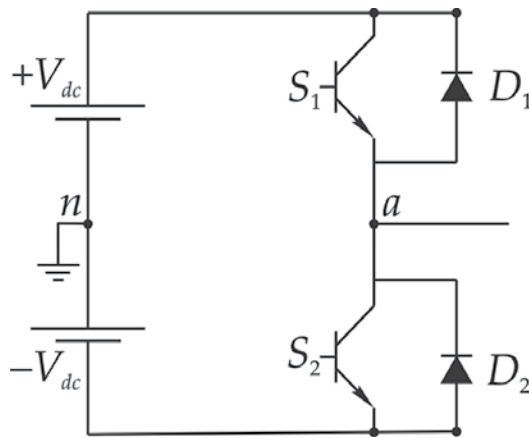


**Figure 1.** Half-bridge one phase two-level inverter leg.

The most well-known analytical method of determining the harmonic components of a PWM switched phase leg was first developed by Bowes and Bullough [1], who adopted an analysis approach originally developed for communication systems by Bennet [6] and Black [7] to modulated converter systems.

The analysis is based on the existence of two time variables  $x(t) = \omega_c t$  and  $y(t) = \omega_0 t$ , where  $\omega_0$  and  $\omega_c$  are the angular frequencies of the fundamental (target, sinusoid) low-frequency modulated waveform and the carrier high-frequency modulating waveform,  $\omega_0 \ll \omega_c$ . Variables  $x(t)$  and  $y(t)$  are considered to be independently periodic. If the ratio  $\omega_c/\omega_0$  is integer, the generated pulse width trail will be periodic [4].

The problem of finding a PWM for the modulated periodic waveform  $f(t)$  can be solved by exploring a unit cell which identifies contours within which  $f(t)$  remains constant for cyclic variations of  $x(t)$  and  $y(t)$  and is equal to the phase leg output voltage. Thus, a three-dimensional (3D) unit cell is a plot of two time variables function with  $z$  assuming values of  $f(x, y)$  where  $x$  and  $y$  vary from  $-\pi$  to  $\pi$ . Contours of  $f(x, y)$  within the unit cell depend on a particular PWM strategy which will be discussed below.

### 3.1. Carrier-based PWM schemes

#### 3.1.1. Carrier waveforms and unit cells

Since the target waveform is usually a sinusoid, PWM schemes can be categorized based on the carrier waveform: saw-tooth leading edge (**Figure 2a**), saw-tooth trailing edge (**Figure 2b**), and double edge (**Figure 2c**).

Let the modulated waveform of a phase be given  $v_a^{id} = M \cos y$ , where  $M$  is the modulation index,  $0 < M < 1$ . For the one-phase two-level inverter leg shown in **Figure 1**, unit cells with contour plots for each carrier waveform modulation are presented in **Figure 3**. The output of the modulated waveform assumes either  $+V_{dc}$  or  $-V_{dc}$ , and the regions of the constant output are bounded by reference waveforms  $\Omega(y) = \pm\pi M \cos y$ . For saw-tooth modulations, one of

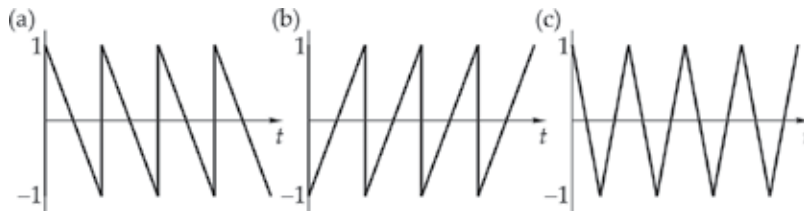


**Figure 2.** Carrier waveform: (a) saw-tooth leading edge; (b) saw-tooth trailing edge; (c) double edge.

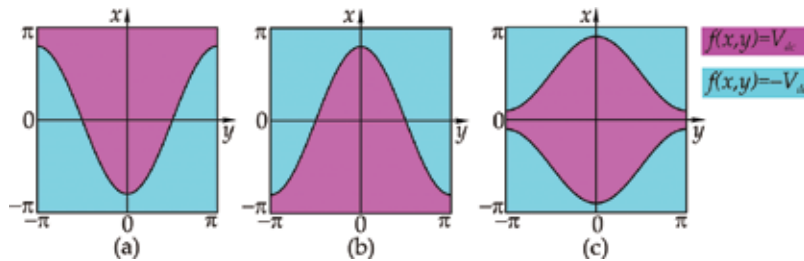


**Figure 3.** Contour plots for a sine modulated reference waveform and different carrier modulating waveform: (a) saw-tooth leading edge; (b) saw-tooth trailing edge; (c) double edge.

switching time instances (within a period of the carrier waveform) is independent of the reference waveform resulting in only one side of the contour plot to be sinusoid. The double-edge PWM both sides of the switched output are modulated providing better harmonic performance unlike saw-tooth modulations [4]. Hereinafter, only double-edge modulation is considered.

To determine the harmonics content and the output waveform of a particular PWM, the double Fourier series coefficients  $C_{mn}$  (or, equivalently,  $A_{mn}$  and  $B_{mn}$ ) are to be found using Eq. (2). To solve the problem, the periodic function  $f(x, y)$  is to be integrated over the unit cell of the PWM scheme.

### 3.1.2. PWM sampling schemes

Based on the choice of switching time instances, PWM schemes can be divided into: naturally sampled (NS), symmetrically regularly sampled (SR), and asymmetrically regularly sampled (AR) PWMs.

#### 3.1.2.1. Naturally sampled PWM

For NS PWM scheme, switching occurs at time instances corresponding to intersection of the carrier and target waveforms. Switching time instances can also be determined as the intersection between the reference waveform and the solution trajectory  $y = (\omega_0/\omega_c)x$ . For example, switching time instances for the NS double-edge modulation of the one-phase two-level inverter leg in **Figure 1** are defined from its unit cell in **Figure 3c** such that  $f(x, y)$  changes

from  $-V_{dc}$  to  $V_{dc}$  when  $x = -\pi M \cos y$ ,

from  $V_{dc}$  to  $-V_{dc}$  when  $x = \pi M \cos y$ .

### 3.1.2.2. Symmetrically regularly sampled PWM

Switching instances for SR PWM can be determined by the intersection between the sampled sinusoid waveform and the solution trajectory line  $y = y' + (\omega_0/\omega_c)x$ . The same switching instances can be determined as the intersection between the continuous sinusoid waveform and a staircase variable  $y'$  which has a constant value within each carrier interval [4]. In general, the value of  $y'$  within each carrier interval can be expressed as

$$y' = \frac{\omega_0}{\omega_c} 2p\pi, \quad p = 0, 1, 2, \dots \quad (5)$$

where  $p$  represents the  $p$ th carrier interval within a fundamental cycle. The staircase variable  $y'$  in terms of continuous variables  $x$  and  $y$  is given by

$$y' = y - \frac{\omega_0}{\omega_c} (x - 2p\pi), \quad p = 0, 1, 2, \dots \quad (6)$$

The double Fourier series coefficients for the case of SR PWM with a triangle carrier can be found analogously to NS PWM with variable  $y$  substituted by variable  $y'$  found from Eq. (6).

Considering the previous example with the one-phase two-level inverter leg shown in **Figure 1**, switching time instances for the SR double-edge modulation are defined such that  $f(x, y)$  changes

from  $-V_{dc}$  to  $V_{dc}$  when  $x = -\pi M \cos y'$ ,

from  $V_{dc}$  to  $-V_{dc}$  when  $x = \pi M \cos y'$ .

### 3.1.2.3. Asymmetrically regularly sampled PWM

Switching time instances for AR PWM are determined similarly to SR PWM. Unlike SR PWM, switching occurs twice within each carrier interval for AR PWM. The switching time instances can be determined as the intersection between the continuous sinusoid waveform and two staircase variables

$$y'_i = \frac{\omega_0}{\omega_c} \left( 2p\pi + (-1)^i \frac{\pi}{2} \right), \quad i = 1, 2, \quad (7)$$

which can be expressed in terms of continuous variables  $x$  and  $y$  as

$$y'_i = y - \frac{\omega_0}{\omega_c} \left( x - 2p\pi - (-1)^i \frac{\pi}{2} \right), \quad i = 1, 2. \quad (8)$$

To write the double Fourier series integral for AR PWM, the switched waveform in each carrier interval must be split into two sections for analysis, and with the results added by

superposition, the first section ( $i = 1$ ) has modulated “rising” edge in the first half carrier interval and a “falling” edge in the center of the carrier interval. The second section ( $i = 2$ ) has a modulated “rising” edge in the center of the carrier interval and “falling” edge in the second half carrier interval. Mathematically, this behavior can be expressed as a sum of two functions,  $f_1(x, y)$  and  $f_2(x, y)$ , representing “rising” and “falling” edges of the double-edge carrier waveform  $f(x, y) = f_1(x, y) + f_2(x, y)$ .

In the previous example with the one-phase two-level inverter leg (**Figure 1**), functions  $f_1(x, y)$  and  $f_2(x, y)$  are defined as follows:

$f_1(x, y)$  steps from  $V_{dc}$  to  $-V_{dc}$  at  $x = x(y_1') + 2p\pi$  and from  $-V_{dc}$  to  $V_{dc}$  at  $x = 2p\pi$ ;

$f_2(x, y)$  steps from  $V_{dc}$  to  $-V_{dc}$  at  $x = 2p\pi$  and from  $-V_{dc}$  to  $V_{dc}$  at  $x = x(y_2') + 2p\pi$ .

## 4. PWM for multilevel inverters

In this section, the following MLI topologies are presented: diode-clamped (DC) MLI, cascade H-bridge (CHB) MLI, and capacitor-clamped (CC) MLI. The three-level diode-clamped inverter, which is also called the neutral-point-clamped inverter, was initially introduced by Nabae et al. [8] in 1981. Thereafter, diode-clamped, cascade H-bridge, and flying capacitor MLIs with higher number of DC voltage levels have been developed [9–11].

### 4.1. Diode-clamped MLI

#### 4.1.1. DCMLI circuit topology

A three-level diode-clamped inverter is shown in **Figure 4a**. In this circuit, the DC bus voltage is split into three levels by two series-connected bulk capacitors,  $C_1$  and  $C_2$ . The middle point of the two capacitors  $n$  can be defined as a neutral point. The inverter has two complementary switch pairs:  $(S_1, S_3)$  and  $(S_2, S_4)$ ; the complementary switches cannot be turned on simultaneously. The output voltage  $v_a$  has three states:  $-V_{dc}/2$ ,  $0$ , and  $V_{dc}/2$ . For voltage level  $V_{dc}/2$ , switches  $S_1$  and  $S_2$  should be turned on; for  $-V_{dc}/2$ , switches  $S_3$  and  $S_4$  should be turned on; and for the  $0$  level, switches  $S_2$  and  $S_3$  should be turned on.

**Figure 4b** shows a five-level diode-clamped converter whose DC bus consists of four capacitors:  $C_1, C_2, C_3,$  and  $C_4$ . Here, the output voltage  $v_a$  has five levels:  $-V_{dc}/2, -V_{dc}/4, 0, V_{dc}/4,$  and  $V_{dc}/2$ . In this example, four complementary switches are  $(S_1, S_5), (S_2, S_6), (S_3, S_7),$  and  $(S_4, S_8)$ . For voltage level  $V_{dc}/2$ , all upper switches  $S_1$  and  $S_4$  should be turned on; for voltage level  $V_{dc}/4$ , three upper switches  $S_2$  and  $S_4$  and one lower switch should be turned on; for voltage level  $0$ , two upper switches  $S_3$  and  $S_4$  and two lower switches  $S_5$  and  $S_6$  should be turned on; for voltage level  $-V_{dc}/4$ , one upper switch  $S_4$  and three lower switches  $S_5$  and  $S_7$  should be turned on; and for voltage level  $-V_{dc}/2$ , all lower switches  $S_5$  and  $S_8$  should be turned on.

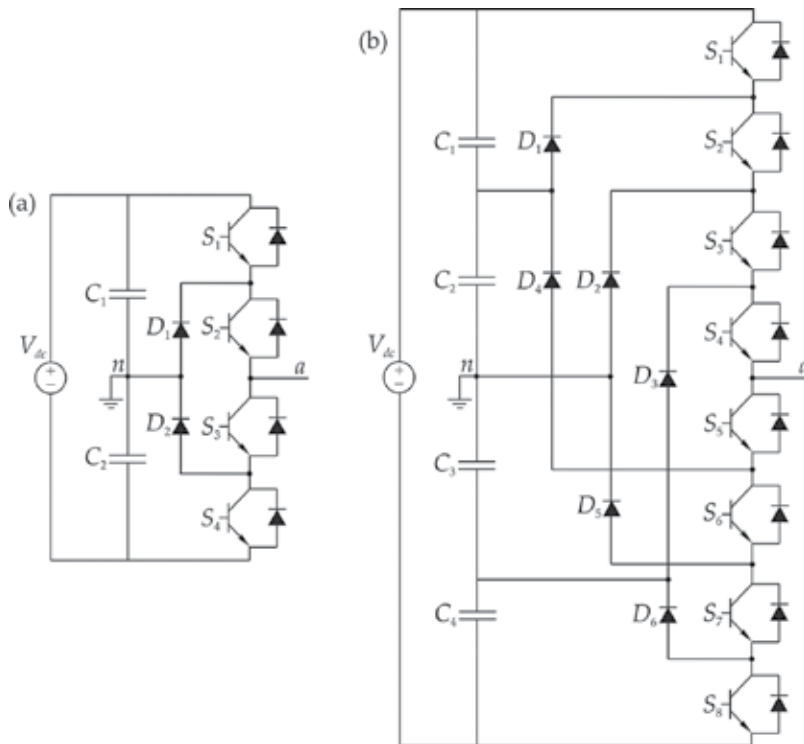


Figure 4. DCMLI circuit topologies: (a) three-level; (b) five-level.

Development of DCMLI of a higher level is constrained by diodes rating for reverse voltage blocking. The number of diodes increases quadratic in the level of inverter; therefore, construction of DCMLI beyond certain level will be impractical. Moreover, the diode recovery time is the major challenge in high-voltage high-power applications [12].

4.1.2. Carrier-based PWM schemes for DCMLIs

For DCMLIs, two or more carrier waveforms are used to modulate the target waveform. The number of waveforms depends on the level of the converter. Usually, the level of an inverter is an odd number, and if  $L$  is the level of the converter, then the number of carrier waveforms is  $L-1$ .

Carrier waveforms can be shifted with respect to each other. Based on the shift between the carrier waveforms, following modulation schemes are identified:

- phase opposition disposition (POD): all carrier waveforms above zero are in phase and  $180^\circ$  out of phase with those below zero;
- alternative phase opposition disposition (APOD): every carrier waveform is  $180^\circ$  out of phase with its neighbors;
- phase disposition (PD): all carrier waveforms are in phase.

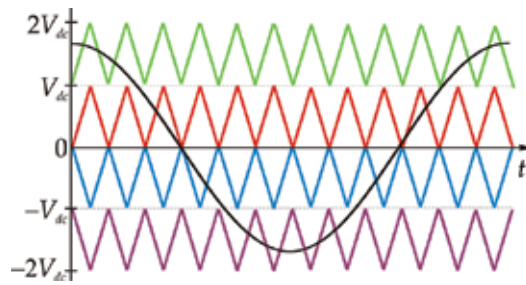


Figure 5. POD PWM scheme for a five-level inverter with the sinusoid reference waveform.

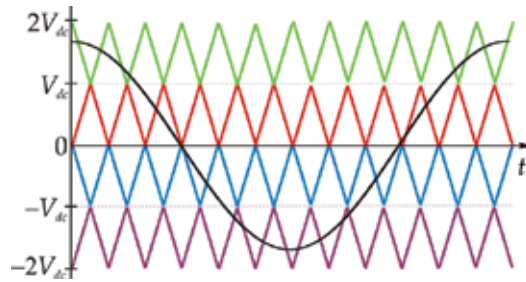


Figure 6. APOD PWM scheme for a five-level inverter with the sinusoid reference waveform.

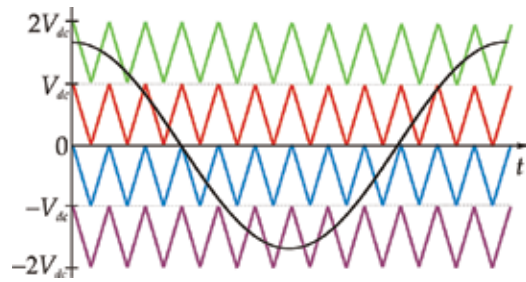


Figure 7. PD PWM scheme for a five-level inverter with the sinusoid reference waveform.

An example of each PWM scheme for a five-level inverter is shown in **Figures 5–7**. Apparently, there is no difference between POD and APOD for three-level inverters.

#### 4.1.3. Contour plots for DCMLIs

If  $L$  is the level of the inverter, it denotes  $N = (L-1)/2$ . Then, function  $f(x, y)$  of voltage level assumes one of the values:  $-NV_{dc}/(L-1)$ ,  $-(N-1)V_{dc}/(L-1)$ , ...,  $0$ , ...,  $NV_{dc}/(L-1)$ . Let us denote carrier waveforms as  $x_1^c(t)$ ,  $x_2^c(t)$ , ...,  $x_{L-1}^c(t)$  beginning from the lowest one. If the reference waveform is less than  $x_1^c(t)$ , then  $f(x, y) = -NV_{dc}/(L-1)$ ; if the reference waveform is greater than  $x_{i-1}^c(t)$  and less than  $x_i^c(t)$ ,  $i = 2, \dots, L-1$ , then  $f(x, y) = -(N-i+1)V_{dc}/(L-1)$ ; and, finally,  $f(x, y) = NV_{dc}/(L-1)$  if the reference waveform is greater than  $x_{L-1}^c(t)$ .

To determine the corresponding contour plot, interval  $[-\pi; \pi]$  of the  $y$ -axis should be divided in  $2N-1$  intervals with limits defined by  $M \cos y = m/N$ ,  $m = -N, -(N-1), \dots, N$ . One also needs to consider separately “rising” and “falling” edges of each carrier waveform corresponding to two intervals of variable  $x$ :  $-\pi \leq x \leq 0$  and  $0 \leq x \leq \pi$ . Then, the condition that the reference waveform is greater than the carrier waveform  $x_i^c(t)$  for “rising” and “falling” edges becomes, respectively:

$$NM \cos y > \frac{x_i^c}{\pi} \text{ if } 0 \leq x \leq \pi, \tag{9}$$

$$NM \cos y > -\frac{x_i^c}{\pi} \text{ if } -\pi \leq x \leq 0. \tag{10}$$

Similarly, the opposite conditions can be defined. Solving in Eqs. (9) and (10) for all values of  $f(x, y)$ , one can find the contour plot of a particular PWM scheme, accounting for the voltage level in each domain. Examples of different PWM schemes for three- and five-level diode-clamped inverter are given in **Figures 8-12**.

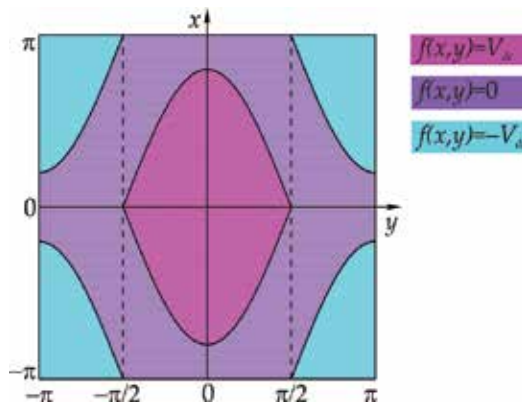


Figure 8. PD PWM scheme for a three-level diode-clamped inverter.

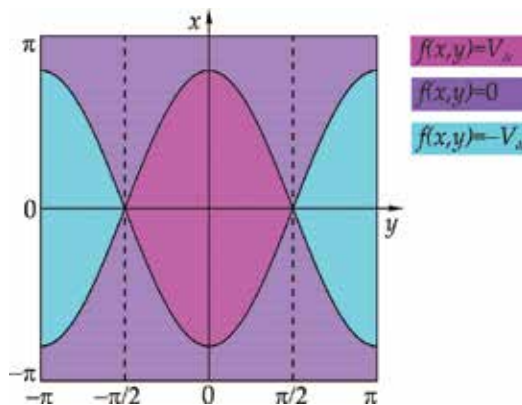


Figure 9. POD PWM scheme for a three-level diode-clamped inverter.

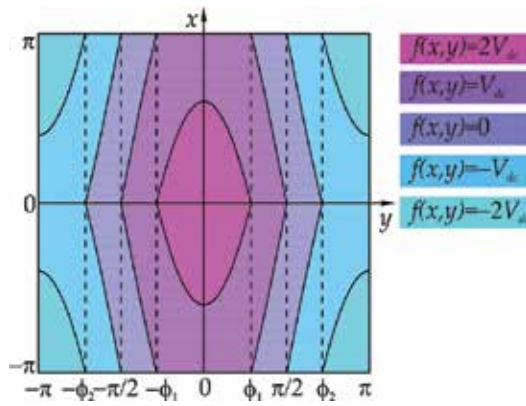


Figure 10. PD PWM scheme for a five-level diode-clamped inverter (here  $\phi_2 = \pi - \phi_1$  and  $\phi_1 = \cos^{-1}(1/2M)$ ).

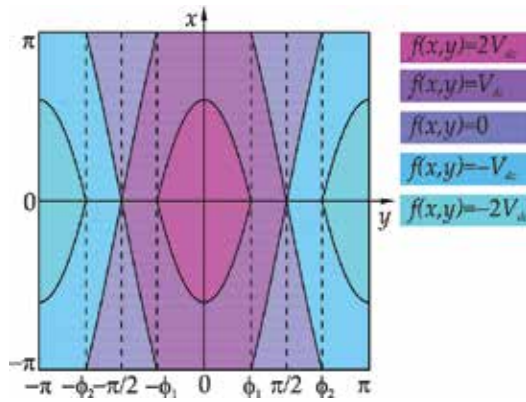


Figure 11. POD PWM scheme for a five-level diode-clamped inverter (here  $\phi_2 = \pi - \phi_1$  and  $\phi_1 = \cos^{-1}(1/2M)$ ).

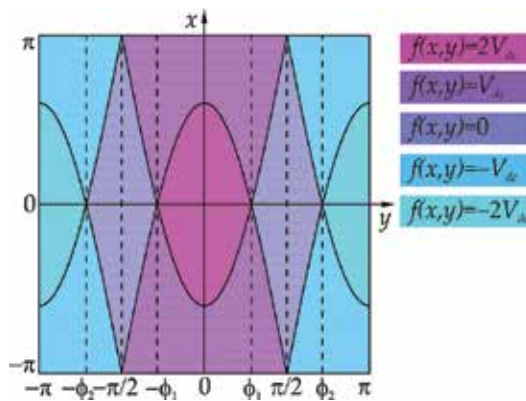


Figure 12. APOD PWM scheme for a five-level diode-clamped inverter (here  $\phi_2 = \pi - \phi_1$  and  $\phi_1 = \cos^{-1}(1/2M)$ ).

4.1.4. Harmonic spectra of DCMLIs

Once the unit cell with contour plots of voltage level domains for a particular PWM is obtained, harmonic components of the PWM can be found using Eq. (2) with the help of equations given in Section 2.2. Output voltage waveforms and their Fourier transforms are given below for three- and five-level diode-clamped inverters using different modulation strategies. Harmonic components magnitudes are plotted for first harmonic numbers assuming  $M = 0.8$  and  $\omega_c/\omega_0 = 40$ .

The output voltage of a three-level diode-clamped inverter modulated by NS POD/APOD PWM is given by

$$v_a(t) = V_{dc}M \cos(\omega_0 t) + \frac{2V_{dc}}{\pi} \sum_{m=1}^{\infty} \frac{1}{m} \sum_{p=-\infty}^{\infty} (-1)^p J_{2p+1}(m\pi M) \cos(m\omega_c t + (2p + 1)\omega_0 t) \quad (11)$$

and its harmonic components are plotted in **Figure 13**.

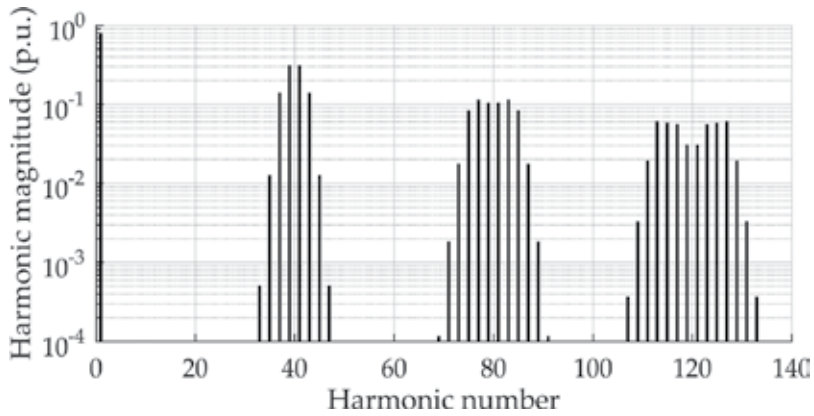


**Figure 13.** Theoretical harmonic spectrum of a three-level diode-clamped inverter modulated using NS POD/APOD PWM.

The output voltage of a three-level diode-clamped inverter modulated using NS PD PWM can be calculated as

$$v(t)a = V_{dc}M \cos(\omega_0 t) + \frac{2V_{dc}}{\pi} \sum_{q=1}^{\infty} \frac{1}{2q} \sum_{p=-\infty}^{\infty} \frac{J_{2p+1}(2q\pi M)(-1)^p}{2s + 1} \cos(2q\omega_c t + (2p + 1)\omega_0 t) + \frac{4V_{dc}}{\pi^2} \sum_{q=1}^{\infty} \frac{1}{2q-1} \sum_{p=-\infty}^{\infty} \sum_{s=-\infty}^{\infty} \frac{J_{2s+1}((2q-1)\pi M)(-1)^p}{2p + 2s + 1} \cos((2q-1)\omega_c t + 2p\omega_0 t) \quad (12)$$

and its theoretical harmonic spectrum is shown in **Figure 14**.

The output voltage of a five-level diode-clamped inverter obtained by NS POD PWM can be found as follows:

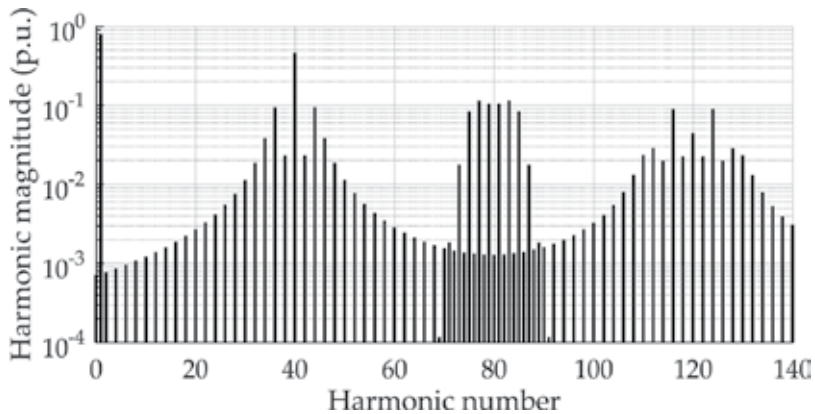


**Figure 14.** Theoretical harmonic spectrum of a three-level diode-clamped inverter modulated using NS PD PWM.

$$v_a(t) = 2V_{dc}M \cos(\omega_0 t) + \frac{2V_{dc}}{\pi} \sum_{q=1}^{\infty} \frac{1}{2q} \sum_{p=-\infty}^{\infty} (-1)^p J_{2p+1}(4q\pi M) \cos(2q\omega_c t + (2p+1)\omega_0 t) + \frac{4V_{dc}}{\pi^2} \sum_{q=1}^{\infty} \frac{1}{2q-1} \sum_{p=-\infty}^{\infty} \left[ (-1)^p J_{2p+1}(2(2q-1)\pi M) \left( \frac{\pi}{2} - 2\phi \right) + \sum_{\substack{s=-\infty \\ s+p+1 \neq 0}}^{\infty} (-1)^{s+1} J_{2s+1}(2(2q-1)\pi M) \frac{\sin(2(p+s+1)\phi)}{p+s+1} \right], \quad (13)$$

where  $\phi = \cos^{-1}(1/2M)$  and its harmonic spectrum is plotted in **Figure 15**.

The output voltage of a five-level diode-clamped inverter modulated by NS APOD PWM is given by

$$v_a(t) = 2V_{dc}M \cos(\omega_0 t) + \frac{2V_{dc}}{\pi} \sum_{m=1}^{\infty} \frac{1}{m} \sum_{p=-\infty}^{\infty} (-1)^{m+p} J_{2p+1}(2m\pi M) \cos(m\omega_c t + (2p+1)\omega_0 t) \quad (14)$$

and its harmonics are plotted in **Figure 16**.

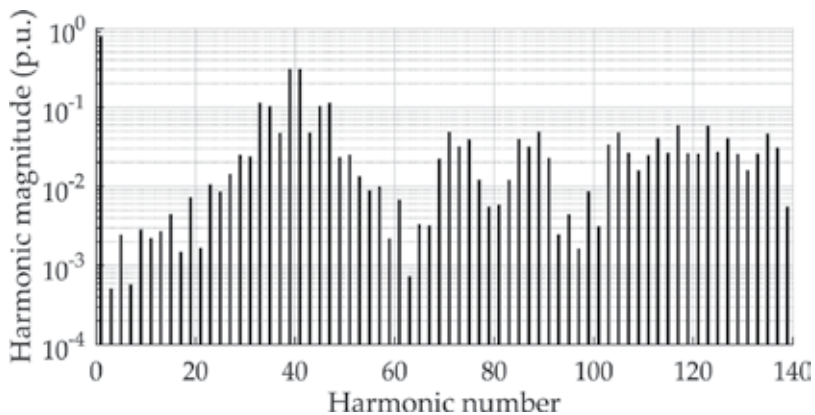


**Figure 15.** Theoretical harmonics spectrum of a five-level diode-clamped inverter modulated using NS POD PWM.

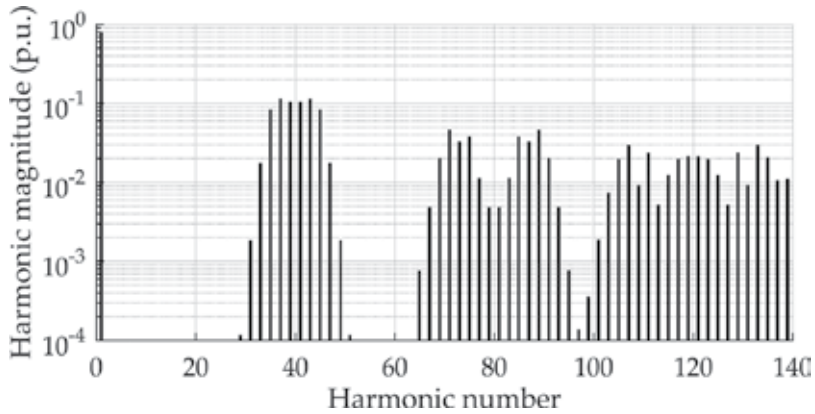


**Figure 16.** Theoretical harmonic spectrum of a five-level diode-clamped inverter modulated using NS APOD PWM.

The output voltage of a five-level diode-clamped inverter modulated using NS PD PWM is given by

$$\begin{aligned}
 v_a(t) = & 2V_{dc}M \cos(\omega_0 t) + \frac{2V_{dc}}{\pi} \sum_{q=1}^{\infty} \frac{1}{2q} \sum_{p=-\infty}^{\infty} (-1)^p J_{2p+1}(4q\pi M) \cos(2q\omega_c t + (2p+1)\omega_0 t) + \\
 & + \frac{4V_{dc}}{\pi^2} \sum_{q=1}^{\infty} \frac{1}{2q-1} \sum_{p=-\infty}^{\infty} \sum_{\substack{s=-\infty \\ 2p+2s \neq -1}}^{\infty} (-1)^s J_{2s+1}(2(2q-1)\pi M) \frac{\cos(\pi(p+s)) - 2 \sin(\phi(2p+2s+1))}{2p+2s+1} \\
 & \times \cos((2q-1)\omega_c t + 2p\omega_0 t)
 \end{aligned} \tag{15}$$

where  $\phi = \cos^{-1}(1/2M)$  and the theoretical harmonics spectrum is shown in **Figure 17**.

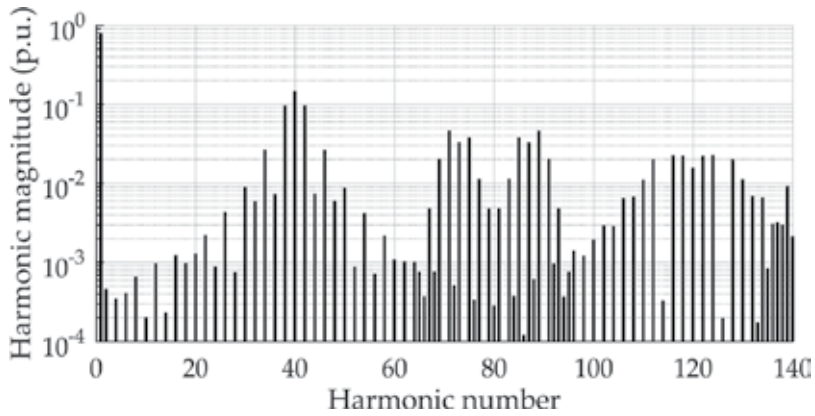


**Figure 17.** Theoretical harmonic spectrum of a five-level diode-clamped inverter modulated using NS PD PWM.

Below theoretical harmonic contents for SR and AR PWM are presented for a three-level diode-clamped inverter. The output voltage of a three-level diode-clamped inverter modulated with SR POD PWM can be found using

$$C_{m,2n+1} = \frac{2V_{dc}}{q\pi} (-1)^n J_{2n+1}(q\pi M) \tag{16}$$

where  $q = m + n\omega_0/\omega_c$ . Its harmonics content is shown in **Figure 18**.

The harmonic spectrum of a three-level diode-clamped inverter modulated with SR PD PWM can be determined by equations

$$C_{m,2p} = \frac{2V_{dc}}{\pi^2} \frac{1 - e^{jq\pi}}{q} \sum_{k=-\infty}^{\infty} (-1)^k J_{2k+1}(q\pi M) \tag{17}$$

$$C_{m,2p+1} = \frac{V_{dc}}{\pi} \frac{1 + e^{jq\pi}}{q} (-1)^p J_{2p+1}(q\pi M) \tag{18}$$

where  $q = m + n\omega_0/\omega_c$ . First harmonics are plotted in **Figure 19**.

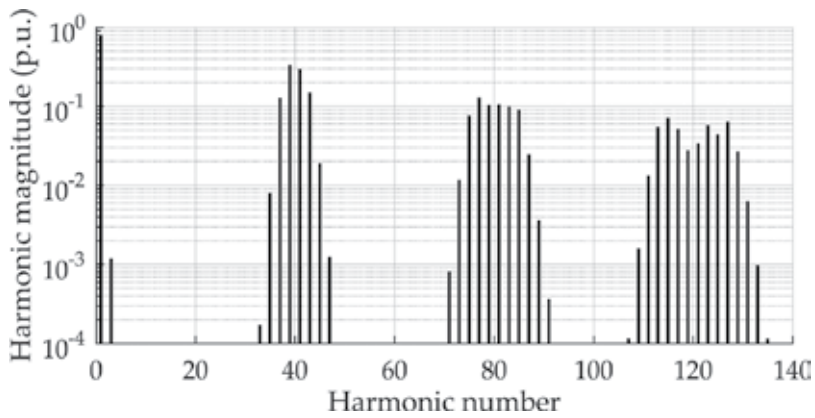


**Figure 18.** Theoretical harmonic spectrum of a three-level diode-clamped inverter modulated using SR POD PWM.

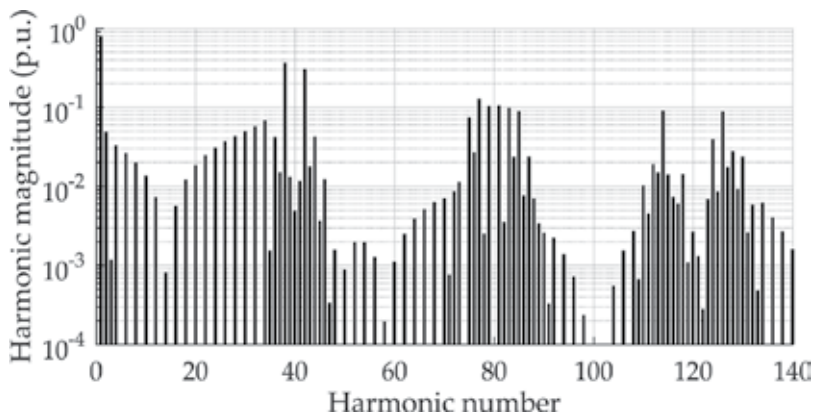


**Figure 19.** Theoretical harmonic spectrum of a three-level diode-clamped inverter modulated using SR PD PWM.

The harmonic spectrum of a three-level diode-clamped inverter modulated with AR POD PWM can be determined by equations

$$C_{mn} = \frac{2V_{dc}(1-e^{jn\pi})}{\pi^2 q} \left[ \frac{1}{n} \sin\left(n \frac{\pi \omega_0}{2\omega_c}\right) \sin\left(n \frac{\pi}{2}\right) + \frac{\pi}{2} J_n(q\pi M) \sin\left(n \frac{\pi}{2} \left[1 - \frac{\omega_0}{\omega_c}\right]\right) + \sum_{\substack{k=-\infty \\ n+k \neq 0}}^{\infty} \frac{1}{n+k} J_k(q\pi M) \sin\left(\frac{\pi}{2} \left[k - n \frac{\omega_0}{\omega_c}\right]\right) \sin\left((n+k) \frac{\pi}{2}\right) \right] \quad (19)$$

where  $q = m + n\omega_0/\omega_c$  and  $n$  is odd. A series of lower order harmonics are shown in **Figure 20**.

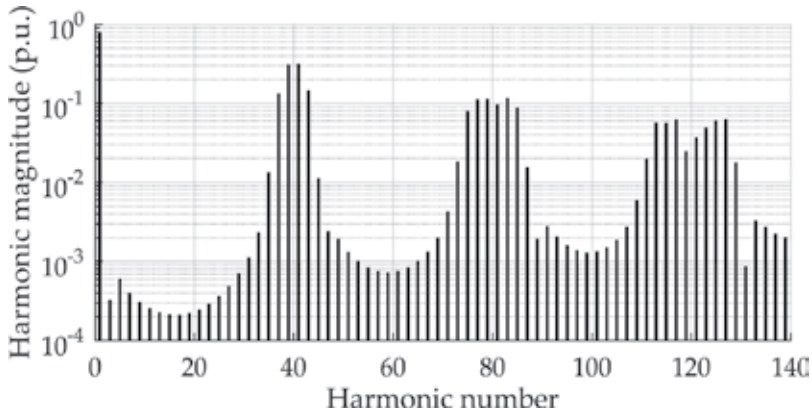


**Figure 20.** Theoretical harmonic spectrum of a three-level diode-clamped inverter modulated using AR POD PWM.

The harmonic spectrum of a three-level diode-clamped inverter modulated with AR PD PWM can be found using equations

$$C_{m0} = \frac{2V_{dc}}{\pi^2 q} \sum_{s=-\infty}^{\infty} \frac{J_{2s+1}(q\pi M)}{2s+1} \left(1 - e^{j(q+2s)\pi}\right) \quad (20)$$

$$C_{mn} = \frac{2V_{dc}(1 + e^{jq\pi})}{\pi^2 q} \left[ \frac{1}{n} \sin\left(n \frac{\pi \omega_0}{2\omega_c}\right) \sin\left(n \frac{\pi}{2}\right) + (-1)^{n+1} \frac{\pi}{2} J_n(q\pi M) \sin\left(n \frac{\pi}{2} \left[1 + \frac{\omega_0}{\omega_c}\right]\right) + \sum_{\substack{k=-\infty \\ k \neq -n}}^{\infty} \frac{(-1)^{k+1}}{n+k} J_k(q\pi M) \sin\left([n+k] \frac{\pi}{2}\right) \sin\left(\frac{\pi}{2} \left[k + n \frac{\omega_0}{\omega_c}\right]\right) \right] \quad (21)$$

where  $q = m + n\omega_0/\omega_c$  and  $n$  is odd in Eq. (21). A series of lower order harmonics are shown in **Figure 21**.

## 4.2. Cascaded H-Bridge MLI

### 4.2.1. CHBMLI circuit topology

A single-phase H-bridge inverter is shown in **Figure 22**. It is made up of two single-phase inverter legs (**Figure 1**) connected to a common DC bus. Each phase is modulated in complementary

pattern by a carrier/reference waveform comparison when the switching occurs as it is described above. A single-phase full-bridge inverter generates voltage of three levels:  $-V_{dc}$ , 0, and  $V_{dc}$ .

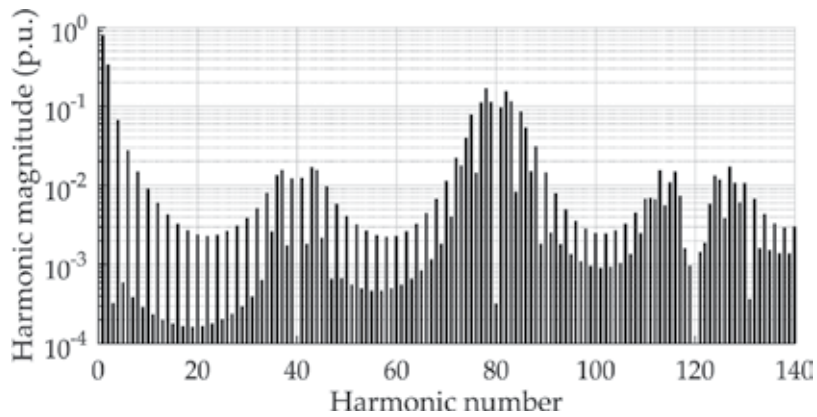


Figure 21. Theoretical harmonic spectrum of a three-level diode-clamped inverter modulated using AR PD PWM.

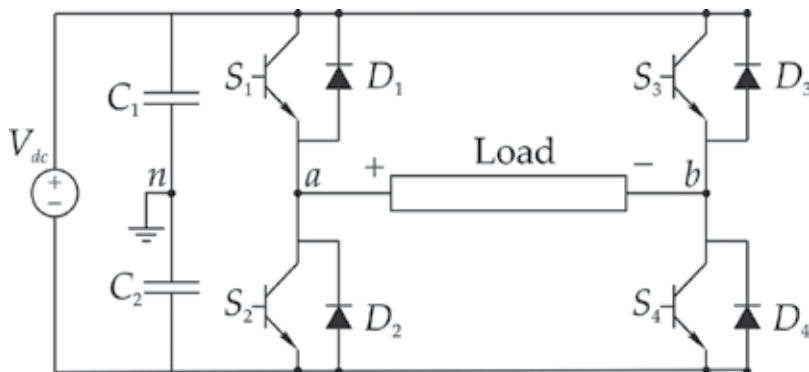
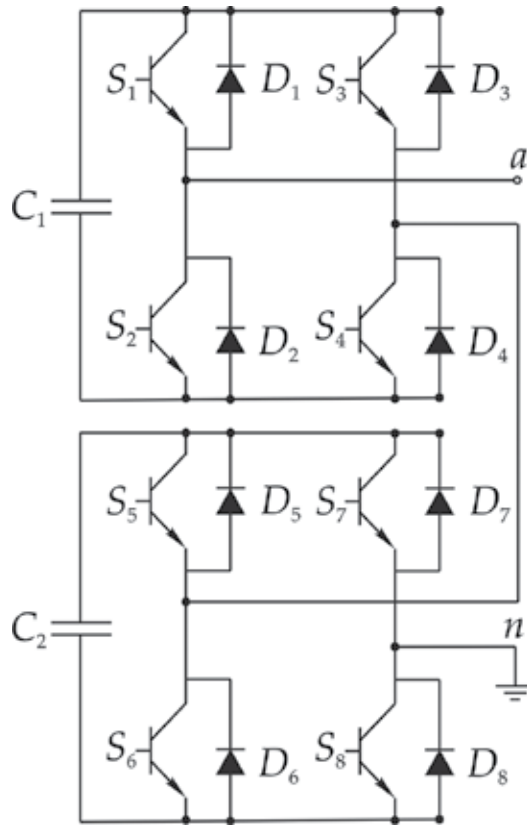


Figure 22. A single-phase H-bridge (full-bridge) inverter.

A cascaded H-bridge multilevel inverter, also called cascaded multicell inverters [12], consists of a number of series-connected single-phase H-bridge inverters connected to separate dc voltage sources. The resulting phase voltage is synthesized by addition of the voltages generated by different cells and is nearly sinusoidal even without filtering. An example of a five-level cascaded H-bridge inverter is shown in **Figure 23**.

Cascaded MLI topology has several advantages: each cell can be controlled independently from the others. Although communication between cells is required to achieve synchronized reference and carrier waveforms, controllers can be distributed. The control scheme is significantly easier than the ones for other topologies. However, it has not been used in practice in low power applications because a separate isolated dc voltage supply is needed for each full H-bridge [4].



**Figure 23.** A five-level cascaded H-bridge inverter topology.

4.2.2. Carrier-based PWM schemes for CBHMLIs

Three-level modulation of a single-phase full-bridge inverter can be obtained via combination of voltage modulations of two phase legs *a* and *b*. The phase legs are modulated with 180° opposed reference waveforms given by

$$v_a^{id}(t) = \frac{V_{dc}}{2} M \cos y, \tag{22}$$

$$v_b^{id}(t) = \frac{V_{dc}}{2} M \cos (y-\pi). \tag{23}$$

The fundamental line-to-line (*l-l*) output reference voltage for the inverter is the difference between two phase reference voltages and is equal to

$$v_{ab}^{id}(t) = v_a^{id}(t) - v_b^{id}(t) = V_{dc} M \cos y. \tag{24}$$

Then, the *l-l* output voltage harmonic components for the inverter are given by

$$v_{ab}(t) = v_a(t) - v_b(t). \tag{25}$$

Applying different PWM schemes to a single-phase half-bridge inverter, one can obtain various modulations for the full-bridge inverter: NS, SR, and AR.

#### 4.2.3. Harmonic spectra of CHBMLIs

The harmonic solution for NS PWM of a phase leg is given by

$$v_a(t) = \frac{V_{dc}}{2} + \frac{V_{dc}}{2} M \cos(\omega_0 t) + \frac{2V_{dc}}{\pi} \sum_{m=1}^{\infty} \frac{1}{m} \sum_{n=-\infty}^{\infty} J_n\left(m \frac{\pi}{2} M\right) \sin\left([m+n] \frac{\pi}{2}\right) \cos(m\omega_c t + n\omega_0 t). \tag{26}$$

Eq. (26) can be applied for each phase leg accounting for 180° phase shift of the reference waveforms resulting in the following harmonic spectrum for NS PWM of a full-bridge inverter:

$$v_{ab}^{NS}(t) = V_{dc} M \cos(\omega_0 t) + \frac{4V_{dc}}{\pi} \sum_{m=1}^{\infty} \frac{1}{2m} \sum_{n=-\infty}^{\infty} J_{2n+1}(2m\pi M) \cos([m+n]\pi) \cos(2m\omega_c t + [2n+1]\omega_0 t). \tag{27}$$

The harmonic spectrum of the output voltage of a full-bridge inverter modulated using SR PWM is equal to

$$v_{ab}^{SR}(t) = \frac{4V_{dc}}{\pi} \left[ \sum_{n=1}^{\infty} \frac{J_n\left(n \frac{\omega_0}{\omega_c} \frac{\pi}{2} M\right)}{n \frac{\omega_0}{\omega_c}} \sin\left(n \left[1 + \frac{\omega_0}{\omega_c}\right] \frac{\pi}{2}\right) \left| \sin n \frac{\pi}{2} \right| \cos(n\omega_0 t) \right. \\ \left. + \sum_{m=1}^{\infty} \sum_{n=-\infty}^{\infty} \frac{J_n\left(\left[m + n \frac{\omega_0}{\omega_c}\right] \frac{\pi}{2} M\right)}{m + n \frac{\omega_0}{\omega_c}} \sin\left(\left[m + n + n \frac{\omega_0}{\omega_c}\right] \frac{\pi}{2}\right) \left| \sin n \frac{\pi}{2} \right| \cos(m\omega_c t + n\omega_0 t) \right] \tag{28}$$

and using AR PWM it is given by

$$v_{ab}^{AR}(t) = \frac{4V_{dc}}{\pi} \left[ \sum_{n=1}^{\infty} \frac{J_n\left(n \frac{\omega_0}{\omega_c} \frac{\pi}{2} M\right)}{n \frac{\omega_0}{\omega_c}} \sin\left(n \frac{\pi}{2}\right) \cos(n\omega_0 t) \right. \\ \left. + \sum_{m=1}^{\infty} \sum_{n=-\infty}^{\infty} \frac{J_{2n-1}\left(\left[m + n \frac{\omega_0}{\omega_c}\right] \frac{\pi}{2} M\right)}{m + n \frac{\omega_0}{\omega_c}} \sin\left([m+n] \frac{\pi}{2}\right) \left| \sin n \frac{\pi}{2} \right| \cos(m\omega_c t + n\omega_0 t) \right]. \tag{29}$$

It can be seen that all odd carrier and associated sideband harmonics as well as even sideband harmonics are cancelled out from the  $l$ - $l$  output voltage. A further cancellation can be obtained by appropriately phase shifting the remaining harmonics of several series-connected single-phase H-bridges. This process is called phase-shifted cascaded (PSC) PWM. The major principle is that the phase shift between two phases of each H-bridge

cell is kept  $180^\circ$ , and then, carriers of each H-bridge are shifted with respect to each other. Optimum harmonic cancellation is achieved via phase shifting each carrier by  $(i-1)\pi/N$ , where  $i$  is the  $i$ th converter,  $N$  is the number of series-connected single-phase inverter legs, and  $N = (L-1)/2$  and  $L$  is the number of voltage levels that can be achieved. This modulation is also called phase shift (PS) PWM. The overall cascaded inverter phase leg to dc link midpoint voltage can be obtained by adding up the  $l$ -l output reference voltages of each cell:

$$v(t) = \sum_{i=1}^N v_{ab}^i(t). \tag{30}$$

One can see in **Figures 24–32** that carrier harmonics of odd order and even order sideband harmonics are cancelled out in the three-level CHB inverter for all presented topologies, and increasing the level of the inverter is leading to cancelling out other carrier harmonics of order  $m \neq kN, k = 1, 2, 3, \dots$

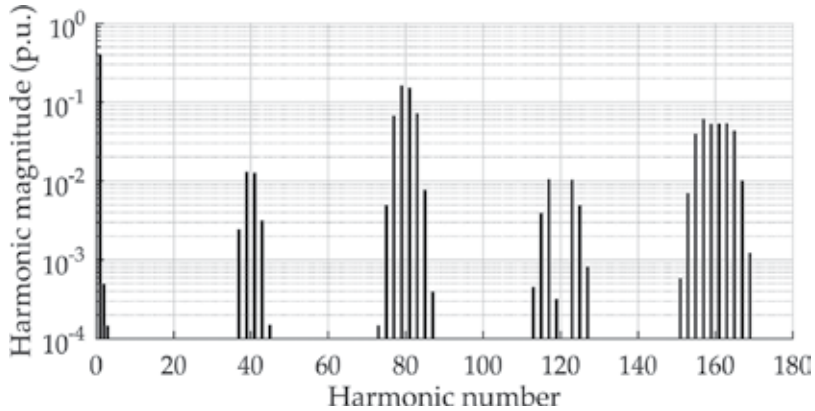


**Figure 24.** Theoretical harmonic spectrum of a single-phase half-bridge inverter modulated using NS PS PWM.

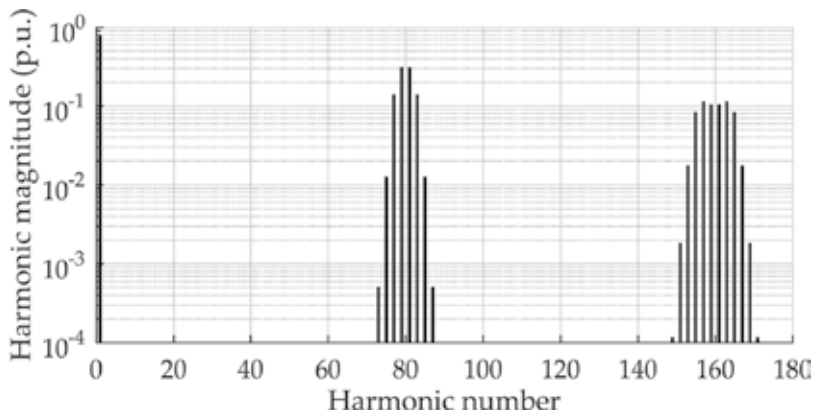


**Figure 25.** Theoretical harmonic spectrum of a single-phase full-bridge inverter modulated using NS PS PWM.

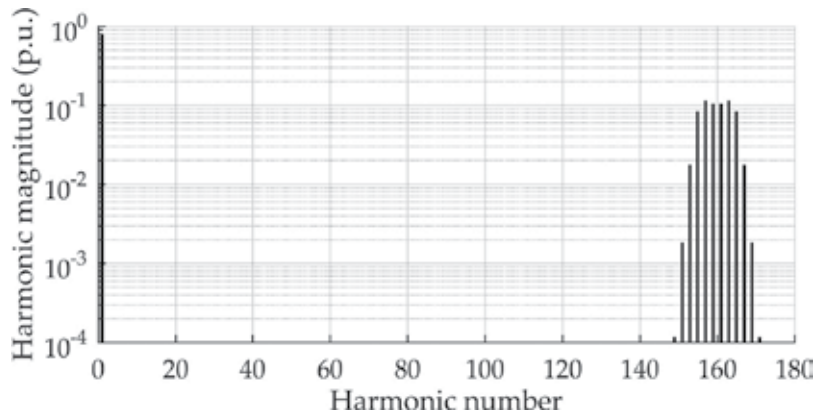


**Figure 26.** Theoretical harmonic spectrum of a single-phase cascaded H-bridge inverter modulated using NS PS PWM.

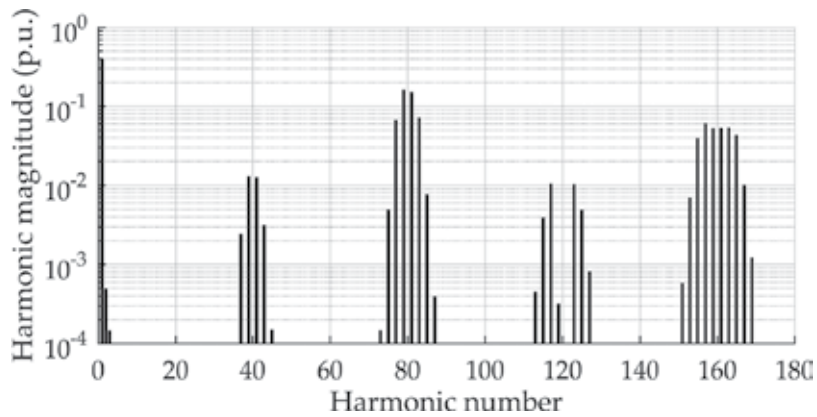


**Figure 27.** Theoretical harmonic spectrum of a single-phase half-bridge inverter modulated using SR PS PWM.

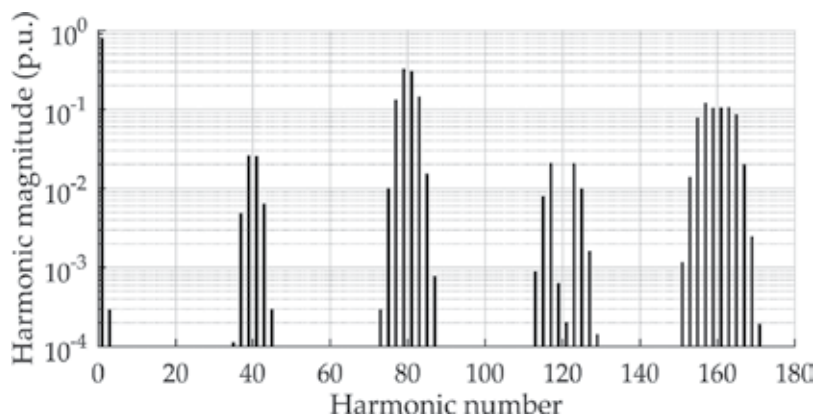


**Figure 28.** Theoretical harmonic spectrum of a single-phase full-bridge inverter modulated using SR PS PWM.

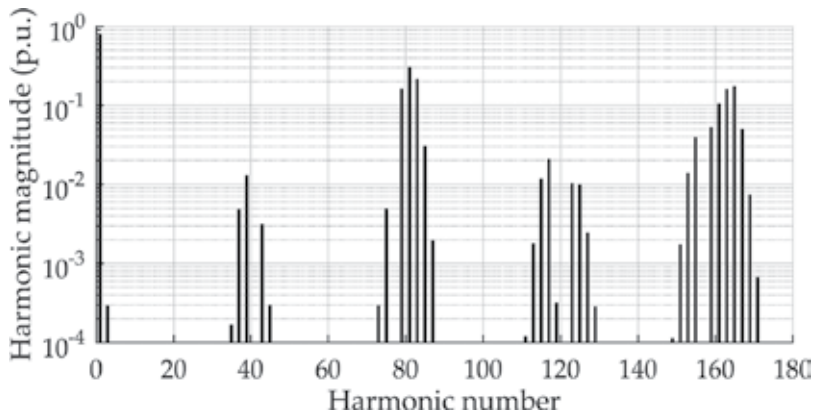


Figure 29. Theoretical harmonic spectrum of a single-phase cascaded H-bridge inverter modulated using SR PS PWM.

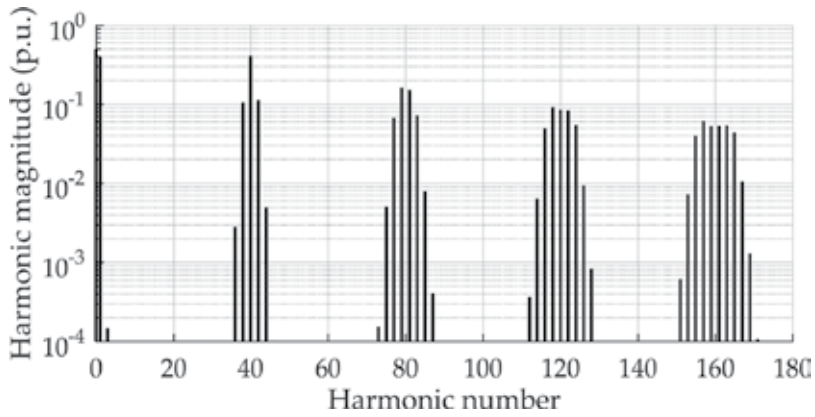


Figure 30. Theoretical harmonic spectrum of a single-phase half-bridge inverter modulated using AR PS PWM.

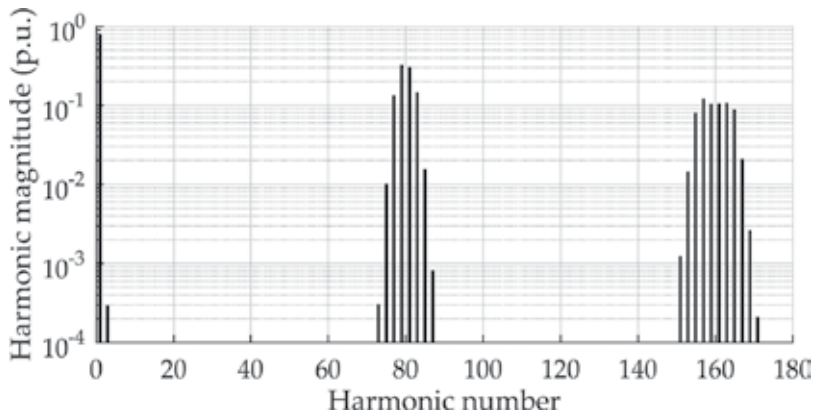
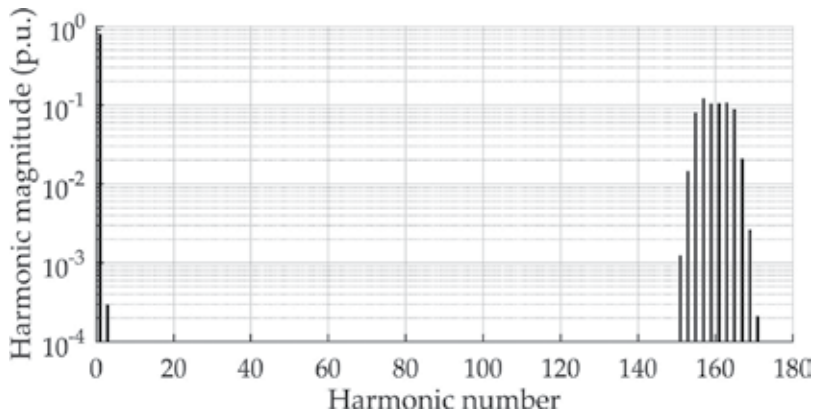


Figure 31. Theoretical harmonic spectrum of a single-phase full-bridge inverter modulated using AR PS PWM.



**Figure 32.** Theoretical harmonic spectrum of a single-phase half-bridge inverter modulated using AR PS PWM.

## 5. Harmonic distortion

Modern power electronic equipment operates in different discrete modes which causes a deviation of the output waveform from the desirable sine waveform due to insertion of undesirable harmonics. The rate of the deviation is presented by a number of basic indices characterizing the harmonic distortion. In particular, these indices enable us to compare the effectiveness of various inverter modulation algorithms. The indices are introduced in this section, and different inverter topologies are compared in their terms.

### 5.1. Harmonic distortion indices

Given that the output voltage  $v(t)$  of a power converter is a periodic function with period  $T$ , the *root-mean-square* (RMS) value of the function is defined by

$$V_{rms} = \sqrt{\frac{1}{T} \int_0^T v(t)^2 dt}. \quad (31)$$

Since  $v(t)$  is periodic with the Fourier series  $v(t) = V_0 + \sum_{n=1}^{\infty} V_n \cos(n\omega t + \varphi_n)$ , the Parseval's theorem can be used to find the RMS voltage of  $v(t)$ :

$$V_{rms} = \sqrt{V_0^2 + \sum_{n=1}^{\infty} \frac{V_n^2}{2}}. \quad (32)$$

In most of the practical cases, the fundamental harmonic  $V_1$  can be considered as the desired output voltage. The remainder of this expression is then considered as a “distortion” to the output. Factoring out  $V_1$  gives us

$$V_{rms} = V_{1,rms} \sqrt{1 + \frac{2V_0^2}{V_1^2} + \sum_{n=2}^{\infty} \left(\frac{V_n}{V_1}\right)^2}, \quad (33)$$

where  $V_{1,rms} = V_1/\sqrt{2}$ . The *total harmonic distortion* (THD) of the voltage is defined as

$$THD = \sqrt{\frac{2V_0^2}{V_1^2} + \sum_{n=2}^{\infty} \left(\frac{V_n}{V_1}\right)^2} \quad (34)$$

and the RMS voltage becomes

$$V_{rms} = V_{1,rms} \sqrt{1 + THD^2}. \quad (35)$$

For the purpose of comparing various switching strategies, the *weighted total harmonic distortion* (WTHD) is used:

$$WTHD = \frac{1}{V_1} \sqrt{\sum_{n=2}^{\infty} \left(\frac{V_n}{n}\right)^2} \quad (36)$$

In the case of pulse-width-modulated inverters, the DC voltage remains constant, while the fundamental component varies. On the other hand, for the same ratio of switching to output frequency, the harmonic components vary relatively little, resulting in a large variation of THD and WTHD. Therefore, a normalized WTHD can be used. For the case of half-bridge inverter, the normalization factor is chosen to be the value of the fundamental ac voltage when the modulation index  $M$  equals 1, that is,  $V_{dc}$ . Thus, the normalized WTHD,  $WTHD_0$ , becomes

$$WTHD_0 = \sqrt{\sum_{n=2}^{\infty} \frac{1}{n^2} \left(\frac{V_n}{V_{dc}}\right)^2} = WTHD \frac{V_1}{V_{dc}} = WTHD \cdot M. \quad (37)$$

## 5.2. Harmonic distortion indices for a DCMLI

Harmonic distortion indices for all presented inverter topologies and PWMs are provided in **Table 1**. Spectra are evaluated for  $M = 0.8$  and  $\omega_c/\omega_0 = 40$ . It can be noted that a half-bridge inverters and full-bridge inverters demonstrate similar waveform quality regardless the PWM strategy applied. Cascaded H-bridge inverters show improvement in performance with increase in number of levels, which appears due to extensive harmonics cancelations up to harmonics of a high order. Performance of diode-clamped inverters also improves with increasing number of levels; however, the improvement is significantly lower than for the cascaded H-bridge inverters.

There is a substantial difference between different modulations used for the same converter. For example, AR PD is showing the worst performance among all other carrier-based

modulations of a three-level DC inverter which can be explained by the fact that very few harmonics are cancelled unlike the other modulations.

	$V_{rms}$ (p.u.)	THD (%)	WTHD (%)	WTHD0 (%)
<i>Three-level diode-clamped inverter phase leg</i>				
NS POD/APOD PWM	0.6959	71.66	1.58	1.27
NS PD PWM	0.6959	71.65	1.58	1.27
SR POD/APOD PWM	0.6959	71.76	1.59	1.27
SR PD PWM	0.7003	73.23	3.70	2.96
AR POD/APOD PWM	0.6956	71.61	1.58	1.26
AR PD PWM	0.6131	42.37	1.82	1.46
<i>Five-level diode-clamped inverter phase leg</i>				
NS POD PWM	0.6790	65.91	1.57	1.26
NS PD PWM	0.6457	55.02	1.30	1.04
NS APOD PWM	0.6007	35.71	0.81	0.65
<i>Five-level cascaded H-bridge inverter phase leg</i>				
AR PS PWM	0.5929	31.44	0.20	0.16
SR PS PWM	0.6638	61.60	0.67	0.53
NS PS PWM	0.5930	31.43	0.20	0.16
<i>Three-level cascaded H-bridge inverter phase leg</i>				
AR PS PWM	0.6856	68.50	0.79	0.63
SR PS PWM	0.6856	68.67	0.79	0.64
NS PS PWM	0.6856	68.47	0.79	0.63
<i>Single phase half-bridge inverter</i>				
AR PWM	0.4796	136.98	2.87	2.30
SR PWM	0.4797	137.15	2.87	2.30
NS PWM	0.4796	136.93	2.87	2.30

**Table 1.** Harmonic distortion factors for MLI.

## 6. Conclusion

In this chapter, an application of double Fourier series to analytical analysis of power width modulation of power electronic converters was presented. The pulse width modulation concept was given, and different pulse width modulation schemes were described. Harmonic spectra and various distortion factors were calculated for various inverter topologies, namely three- and five-level diode-clamped inverters, three- and five-level cascaded H-bridge inverters, and modulated using different PWM schemes. PWM schemes performance varied for different converter topologies; therefore, the preferable PWM strategy is usually determined by a specific converter topology.

Comparing different topologies, the cascaded H-bridge topology contains the least number of sideband harmonics, and they can be further eliminated by increasing the number of levels of the inverter. DCMLIs and CCMLIs are constrained in the number of levels due to diodes physical properties.

## Author details

Irina Dolguntseva

Address all correspondence to: [irina.dolguntseva@angstrom.uu.se](mailto:irina.dolguntseva@angstrom.uu.se)

Uppsala University, Uppsala, Sweden

## References

- [1] Bowes SR, Bullough R. PWM strategies for current-fed inverter drives. IEE Proceedings B - Electric Power Applications. September 1994;**131**(5):195–202. doi:10.1049/ip-b:19840026
- [2] Boost MA, Ziogas PD. State-of-the-art carrier PWM techniques: a critical evaluation. IEEE Transactions on Industry Applications. March 1988;**24**(2):271–280. doi:10.1109/28.2867
- [3] van der Broeck HW, Skudelny HC. Analytical analysis of the harmonic effects of a PWM ac drive. IEEE Transactions on Power Electronics. March/April 1988;**3**(2):216–223. doi:10.1109/63.4352
- [4] Holmes DG, Lipo TA. Pulse Width Modulation for Power Converters: Principles and Practice. 1st ed. Piscataway, NJ: John Wiley & Sons; 2003. 445 p.
- [5] Watson GN. A Treatise on the Theory of Bessel Functions. 1st ed. Cambridge: University Press; 1922. 804 p.
- [6] Bennett WR. New results in the calculation of modulation products. Bell System Technical Journal. April 1933;**12**:228–243. doi:10.1002/j.1538-7305.1933.tb03224.x
- [7] Black HS. Modulation Theory. New York, NY: Van Nostrand Reinhold; 1953. 363 p.
- [8] Nabae A, Takahashi I, Akagi H. A new neutral-point-clamped PWM inverter. IEEE Transactions on Industry Applications. Sept./Oct. 1981;**IA-17**:518–523.
- [9] Bhagwat P, Stefanovic VR. Generalized structure of a multilevel PWM inverter. IEEE Transactions on Industry Applications. Nov./Dec. 1983;**19**(6):1057–1069.
- [10] Marchesoni M, Mazzucchelli M, Tenconi S. A non-conventional power converter for plasma stabilization. In: Power Electronics Specialists Conference, 1988. PESC '88 Record., 19th Annual IEEE; Kyoto, Japan. 1988. pp. 122–129. doi:10.1109/PESC.1988.18125

- [11] Meynard TA, Foch H. Multi-level conversion: high voltage choppers and voltage-source inverters. In: Power Electronics Specialists Conference, 1992. PESC '92 Record., 23rd Annual IEEE; Toledo, Spain. 1992. pp. 397–403. doi:10.1109/PESC.1992.254717
- [12] Rodrigues J, Lai J-S, Peng FZ. Multilevel inverters: a survey of topologies, controls, and applications. IEEE Transactions on Industrial Electronics. August 2002;49(4):724–738. doi:10.1109/TIE.2002.801052



---

# New Spectral Application of the Fourier Transforms

---



---

# **Study of Green Nanoparticles and Biocomplexes Based on Exopolysaccharide by Modern Fourier Transform Spectroscopy**

---

Goran S. Nikolić, Milorad D. Cakić, Slobodan Glišić,  
Dragan J. Cvetković, Žarko J. Mitić and  
Dragana Z. Marković

Additional information is available at the end of the chapter

<http://dx.doi.org/10.5772/64611>

---

## **Abstract**

The intention of this chapter is to contribute in clarification of nanoparticle synthesis and biocomplexes based on exopolysaccharide, green synthetic method development, their physico-chemical characterization by modern spectroscopy, as well as testing of their antimicrobial activity. Silver nanoparticles of polysaccharide type have scientific interest, but practical importance too, because of their application in pharmaceutical and cosmetic product development due to proven antimicrobial and antioxidant activities. On the other hand, the biocomplexes based on exopolysaccharides are important in treatment of biometal deficiency in human and veterinary medicine, as well as in metal ion transporting in organism. Despite a number of studies of this kind of complexes, the investigations of effect of their structure to pharmaco-biological activity are still interesting. It is important that question of interaction between reducing and stabilizing agents with metal ions is still opened. In this respect, the presented chapter offers further progress in the examination of silver nanoparticles and cobalt biocomplex synthesis with dextran oligosaccharides and its derivatives (such as dextran sulfate and carboxymethyl dextran). The complex structure, spectroscopic characterization, and the spectra-structure correlation have been analyzed by different Fourier transform infrared (FTIR) spectroscopic techniques combined with energy-dispersive X-ray (EDX), X-ray diffraction (XRD), scanning electron microscopy (SEM), and surface plasmon resonance UV-Vis methods.

**Keywords:** nanoparticles, biocomplexes, polysaccharides, silver, cobalt, FTIR spectroscopy

---

## 1. Introduction

Investigation of nanoparticles by different methods, especially by Fourier transform infrared (FTIR) spectroscopy, is very interesting in last years since they have a wide potential application in different industries [1–5]. Thus, silver nanoparticles (AgNP) of polysaccharide type and other natural products have scientific interest, but practical importance too, because of their application in pharmaceutical and cosmetic products development due to proven antimicrobial and antioxidant activities [6–9]. The nanoparticles are commonly synthesized by silver (or other metals) ions reduction to elementary state. But, reducing agents should also possess stabilizing properties in order to prevent aggregation [1]. Bankura and coworkers described a simple method of AgNP synthesis at room temperature from dextran, as well as their characterization and microbiological activity [6]. Pullulan-mediated Ag nanoparticles, their synthesis, characterization, and microbiological activities are also reported [4]. Soluble starch, starch-like polysaccharides, and chitosan are used in AgNP synthesis [5–9]. AgNP chitosan/gelatin bionanocomposites have also been studied [5]. Compounds containing carbonyl group are relatively easy complexed with different metals [10–12]. This functional group contains some polysaccharide derivatives like carboxymethyl cellulose (CMC) or carboxymethyl dextran (CMD), which are obtained by different chemical reactions of proton exchange between OH groups of glucoside moiety and carboxymethyl groups. AgNP-CMC nanoparticles were prepared in weak alkaline solution by reaction of  $\text{AgNO}_3$  with CMC as a reducing and capping agent. It has been established that size distribution and morphology of mentioned nanoparticles are depended on Ag: CMC weight ratio, reaction time, temperature, and pH value of the reaction system. FTIR spectrophotometric analysis has shown that interactions between AgNP and polysaccharide have steric character [13]. Studies of composite hydrazine-CMD and CMD magnetic Fe-based nanoparticles [14, 15] have shown that solubility of these nanoparticles depends on pH value (NaOH), not on CMD content. This fact indicates on strong interactions of carbonyl group with magnetic nanoparticles on the surface.

Hence, there are indications that carboxymethyl dextran form nanoparticles with Ag ions. CMD possess COOH group which can react with positively charged Ag ions to form complex compounds, but, it can also reduce Ag ions and stabilize the formed nanoparticles as in the case of hyaluronic acid with AgNP [16]. Since CMD has the ability to form nanoparticles, the intention of this chapter is to contribute in clarification of AgNP synthesis, physico-chemical characterization by FTIR spectroscopic, diffraction and chromatographic methods, as well as testing of their antimicrobial activity. On the other hand, the biocomplexes based on exopolysaccharides are important in treatment of biometals deficiency in human and veterinary medicine [1, 17]. Polysaccharides, oligosaccharides and their derivatives, as well as simple sugars, may be used as ligands for the synthesis of biocomplexes with different metal ions (Cu, Fe, and Zn). These biocomplexes have an important role in metal ions transporting in organism [18]. Despite a number of studies of this kind of complexes, the investigations of effect of their structure to pharmaco-biological activity are still interesting [19]. In this respect, the presented chapter offers further progress in the investigation of cobalt complex synthesis with dextran oligosaccharide, spectroscopic characterization, and the spectra-structure correlation by various FTIR techniques.

## 2. Green nanoparticles of silver

Recent investigations of nanoparticles synthesis are mostly directed to green synthetic methods development. These methods include nontoxic reagents, synthesis procedures without problematic side products, and especially usage of biodegradable materials. Thus, chemical reduction in silver ions is the most frequently used besides photochemical or electrochemical methods [1]. In order to reduce and stabilize the Ag nanoparticles, the polysaccharides (dextran, starch, pullulan, cellulose) and their derivatives (dextran sulfate-DS, carboxymethyl cellulose, carboxymethyl dextran, chitosan, hyaluronic acid, heparin), and biocomposites AgNP chitosan/gelatin, are developed and improved [2–6, 13, 14, 16, 20–25]. Characterization of these particles has been carried out by UV-Vis, FTIR spectroscopy, X-ray diffraction (XRD), and energy-dispersive X-ray (EDX) methods. Electronic microscopy techniques [scanning electron microscopy (SEM) and TEM] are used for particle size determination and distribution, as well as shape defining. It is interesting that question of interaction nature between reducing and stabilizing agents with AgNP is still opened. Some authors [13] consider that steric physical interactions are relevant, while others [2, 16] give an explanation via coordination complex of Ag ions with reducing and stabilizing agents which contain suitable functional groups (COOH, NH<sub>2</sub>, OH, OSO<sub>3</sub>H), as in the case of Cu(II) ions complexes with carboxymethyl dextran or dextran sulfate (**Figure 1**).

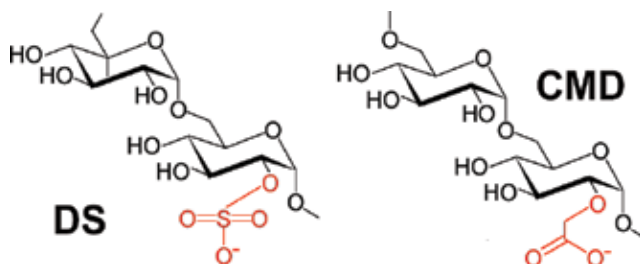


**Figure 1.** Structural fragment of dextran sulfate sodium salt (DS) and carboxymethyl dextran (CMD) molecule.

Having in mind these facts, it can be assumed that dextran sulfate, which contains one or more sulfo groups in its structure, can be used as reducing and stabilizing agent for the AgNP synthesis. Also, it may be assumed that dextran sulfate forms complexes similar to CMD about what there are no literature data. Therefore, investigations in this chapter are related to the AgNP-DS and AgNP-CMD synthesis, their characterization by different methods and antimicrobial activity determination.

### 2.1. Synthesis procedure

The synthesis of AgNP-DS has been performed in a reactor at temperature of 100°C, during 240 min, at constant pH of 7.5 and continuously stirring. Dextran sulfate has been used as a ligand in the synthesis. The synthesis is performed by DS solution (100 cm<sup>3</sup>, 0.002 M)

adding in 100 cm<sup>3</sup> of AgNO<sub>3</sub> solution (0.001 M). The complex formation has been monitored via changing of reaction solution color, from white to yellow. The AgNP-DS complex was precipitated with 96% ethanol after cooling down the reaction mixture to the room temperature. The obtained product has been dried at 105°C under vacuum during 180 min. On the other hand, the carboxymethyl dextran has been used in the case of the AgNP-CMD complex synthesis. The synthesis has been performed by 100 cm<sup>3</sup> of AgNO<sub>3</sub> (0.001 M) solution adding in 200 cm<sup>3</sup> of CMD ligand solution (0.002 M) at constant pH of 7.0 (adjusted by NaOH). The synthesis is performed to the defined M:L ratio (from 1:1 to 1:2) by changing of reagents volume. The complexation has been performed at 100°C and continuously stirring during 120 min. A successful outcome of the AgNP-CMD complex synthesis has been identified by changing of reaction solution color, from white to yellow. The reaction mixture has kept under reflux 24 h more, after that it has cooled to room temperature, and the complex AgNP-CMD has precipitated by 96% ethanol. Final product has been dried at 105°C under vacuum during 180 min. The prepared AgNP-DS and AgNP-CMD complexes were characterized by different methods (FTIR, UV-Vis, SEM, XRD, EDX) and by antimicrobial activity.

## 2.2. FTIR study

The FTIR spectra were recorded by BOMEM MB-100 (Hartmann & Braun, Canada) FTIR spectroscope and by KBr technique, at room temperature with 2 cm<sup>-1</sup> resolution. Spectra-structure correlation has been performed on empirical manner [2, 22], by comparing the spectra of ligands (DS and CMD) with the spectra of their complexes (AgNP-DS and AgNP-CMD). The appropriate FTIR spectra are shown in **Figures 2** and **3**.

The results of the complex AgNP-DS spectral analysis are shown in **Table 1**. They show the position and assignments of bands that come from vibrations of all types of sulfo groups in DS and AgPN-DS, as well as bands of deformation CH vibrations outside of the plane of glucopyranose unit which are characteristic for its conformation determining. As it can be seen in **Table 1**, there is a difference in the position of the  $\nu_{as}(S-O)$  band which is shifted ~22 cm<sup>-1</sup> toward lower frequencies in the AgPN-DS spectrum (**Figure 2**), as well as the band from  $\nu_{as}(O-S-O)$  which is shifted ~8 cm<sup>-1</sup> toward higher frequencies. This difference in the bands position indicates the formation of coordination complexes between Ag ions and DS, where there is a change in conformation of sulfo groups from Eq to Ax position. The appearance of the spectrum in the area of C-CH out-of-plane deformational vibrations surface coupled with C-C-O, O-C-O and C-O-C vibrations depends on glucopyranose unit conformation [25–27]. When it is <sup>4</sup>C<sub>1</sub> conformation, the bands at ~915 cm<sup>-1</sup> (weak), 850 cm<sup>-1</sup> (shoulder), and 752 cm<sup>-1</sup> are expected in the spectrum. The results from **Table 1** show that starting DS retains the same conformation of glucopyranose unit during complex with Ag ions formation. There is a sharp intensive band at 1384 cm<sup>-1</sup> in the FTIR spectrum of AgNP-DS (**Figure 2**) observed by other authors who have investigated similar complexes and given the explanation of its origin [4, 5, 13, 22]. So, in the case of AgNP-CMD complex (**Figure 3c**), some authors consider that this band is a result of  $\nu_s(O-N-O)$  at O=NO<sub>2</sub><sup>-</sup> radicals which are formed from AgNO<sub>3</sub> agents participating in the formation of nanoparticles through the surface interactions [13].

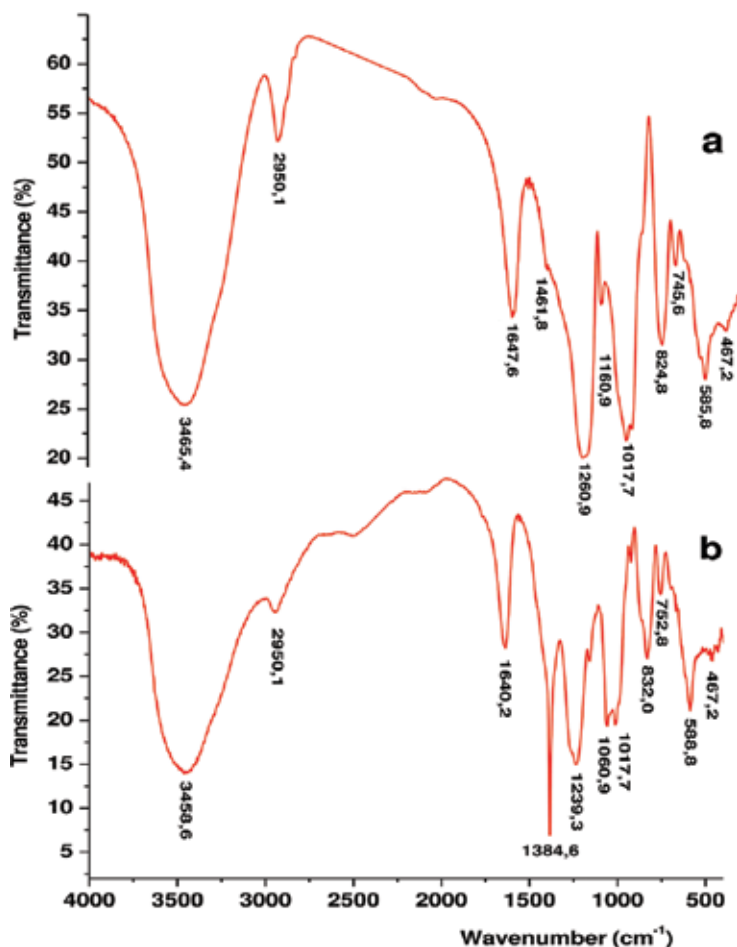


**Figure 2.** FTIR spectra of dextran sulfate sodium salt (a) and AgNP-DS complex (b).

The infrared spectra of AgNP-CMD products and starting CMD agent are compared with literature data and dextran spectrum because of the major bands assignment (**Figure 3**). In the CMD spectrum, vibrations of carboxymethyl groups:  $\nu(\text{C-O})$  around  $1740\text{ cm}^{-1}$ ; deformation vibration  $\delta(\text{C-OH})$  which appears around  $1250\text{ cm}^{-1}$ ;  $\nu(\text{C-O})$  vibration around  $1150\text{ cm}^{-1}$ ; and deformation  $\delta(\text{C-O})$  vibration around  $680\text{ cm}^{-1}$  are expected to oppose starting dextran for CMD synthesis. Stretching  $\nu(\text{C-O})$  vibration has been found in similar carboxymethyl polysaccharides; after carboxymethylation of the k-carrageenan,  $\nu(\text{C-O})$  has found at  $1737\text{ cm}^{-1}$  [28], for carboxymethylated glucan at  $1736\text{ cm}^{-1}$  [29], as well as at  $1750\text{ cm}^{-1}$  in the spectrum of CMD [14]. As it can be seen from **Figure 3b**, the CMD spectra possess bands at  $1740$ ,  $1244$ ,  $1139$ , and  $682\text{ cm}^{-1}$  (which are marked by arrows) from CO carboxymethyl vibration of all types. The aforementioned bands are not in the range of dextran (**Figure 3a**) as it is expected. Changes in the position of the above-mentioned bands can be a good indicator of bonds type that is eventually formed by interaction with  $\text{Ag}^+$  ions [16]. Also, the changes in the area of deformation vibration of C-OH are expected. In the case of AgNP-CMD coordination com-

plexes formation, the frequency  $\nu(\text{C-O})$  band should be lower, or, if both O atoms of COOH groups participate in the coordination, the frequency of  $\nu(\text{C-O})$  vibration should be higher because of electron delocalization, as well as the absence of  $\delta(\text{C-OH})$  bands.

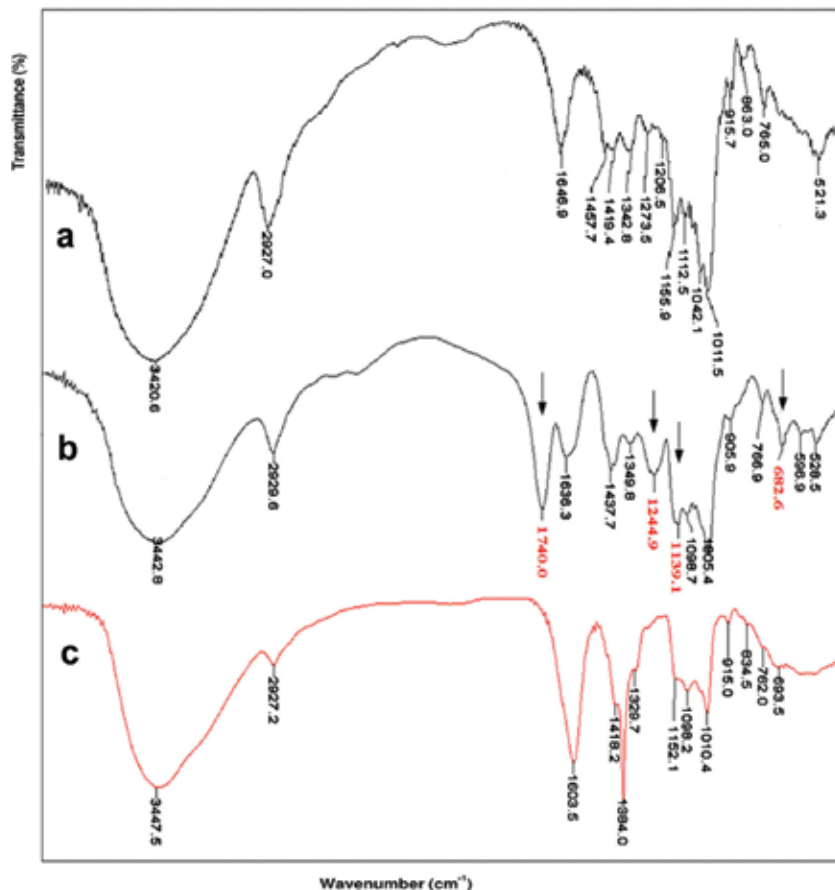


Figure 3. FTIR spectra of dextran (a), CMD (b), and AgNP-CMD (c).

Assignment	DS ( $\text{cm}^{-1}$ )	AgNP-DS ( $\text{cm}^{-1}$ )	$\Delta\nu$ ( $\text{cm}^{-1}$ )
$\nu_{\text{as}}(\text{S-O})$	1261	1239	22
$\nu_{\text{s}}(\text{S-O})$	988	1060	72
$\nu_{\text{as}}(\text{O-S-O})$	824	832	8
$\nu_{\text{s}}(\text{O-S-O})$	585	588	3
${}^4\text{C}_1$ conformation of the $\alpha$ -D-glucopyranose ring	915	915	–
	850	850	–
	745	752	7

Table 1. FTIR analysis data showing various functional groups present in dextran sulfate (DS) and AgNP-DS complex.

Speaking about carboxylate anion, delocalization of electrons causes the order of two CO bonds to be the same, so two bands (at 1600 and 1400  $\text{cm}^{-1}$ ) are expected in CO stretching vibration region, which are ascribed to asymmetric and symmetric C–O vibration, as it is indicated in the literature [13, 16, 28]. The similar situation is in AgNP-CMD complex (Figure 3c) in the CO groups vibration area. In fact, in this area of the spectrum, there are two intensive bands (at 1603 and 1420  $\text{cm}^{-1}$ ) which, according to its position and intensity should be attributed,  $\nu_{\text{as}}(\text{C}-\text{O})$  and  $\nu_{\text{s}}(\text{C}-\text{O})$  vibration, indicating coordination of  $\text{Ag}^+$  ions with a COOH group. In support of this is the absence of  $\nu(\text{C}-\text{O})$  and  $\delta(\text{C}-\text{OH})$  vibration bands. The appearance of spectrum in the area of 1000–700  $\text{cm}^{-1}$ , in all three tested compounds (Figure 3), is very similar and according to the literature data [30, 31] suggests  ${}^4\text{C}_1$  conformation of the glucopyranose unit.

### 2.3. UV-Vis study

Absorption spectra of starting ligand compounds (DSi CMD) as well as of final complexes (AgNP-DS and AgNP-CMD) are obtained by UV-Vis spectrophotometer (Varian Cary-100 Conc.). Spectrophotometric analysis was carried out in the range of 200–800 nm using original Cary UV-Conc. (Varian) software. The obtained UV-Vis spectra are presented in Figures 4 and 5.

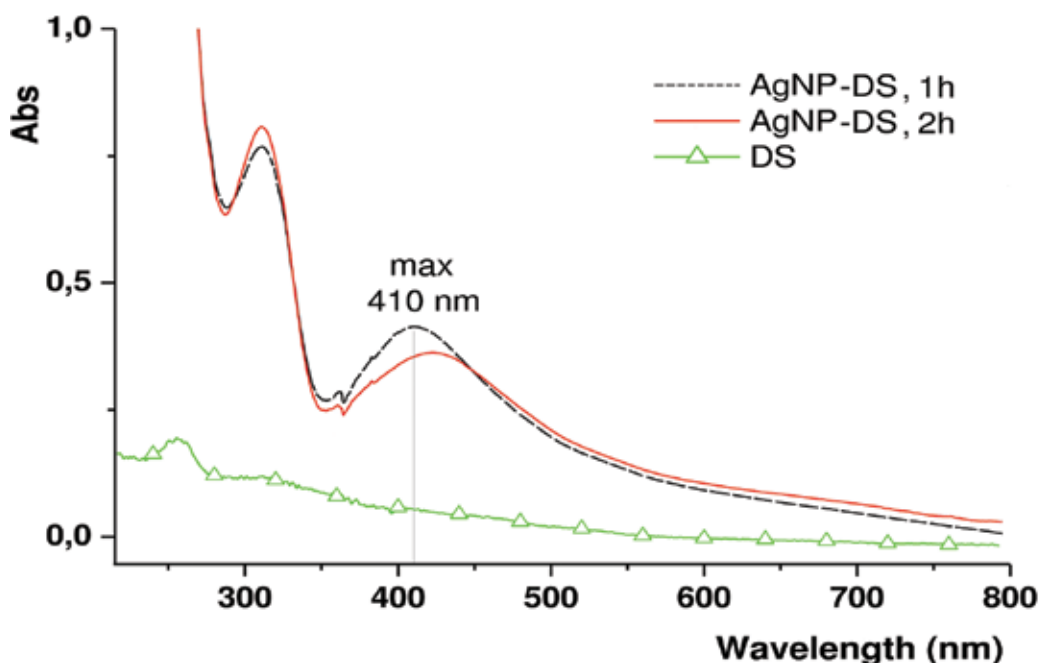
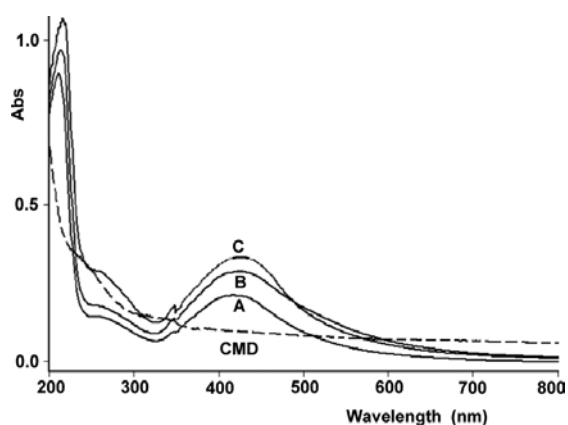


Figure 4. UV-Vis spectra of dextran sulfate (DS) and AgNP-DS complex in function of the synthesis time.

Change in color from yellowish to brown, as well as careful interpretation of UV-Vis spectra, is used for estimating of AgNP synthesis [2–10]. A strong absorption band, called SPR band (surface plasmon resonance), is expected in 370–450 nm region in the UV-Vis spectrum of AgNP [32]. Its exact position depends on numerous factors (the most on AgNP size), while

intensity depends on their concentration [4, 21, 33]. Changes in this band position are used as a criterion of the AgNP stability, that is, aggregation of the nanoparticles during the time. As it can be seen from **Figure 4**, the existence of SPR band at 410 nm indicates the AgNP formation. However, its position is changed during synthesis with time, but after 2 h remains constant at 420 nm. The estimated particle size of AgNP-DS based on the UV data [34] is approximately 40 nm. A change in color from yellowish to brown during the synthesis has been observed in the case of AgNP-CMD formation. SPR band for this complex (**Figure 5**), synthesized at different molar ratio, is located at 420 nm, which is not present in the starting CMD. It is characteristic that intensity of this band is proportional to the amount of AgPN-CMD particles; it increases with increasing amounts of CMD, or during staying of the reaction mixture for 3 months (**Figure 5C**), which is similar to other studies [21]. Unchanged position of SPR band speaks in favor of good aggregation stability of synthesized particles. UV area below 300 nm was not investigated in the literature. However, in the UV spectra of tested compounds (**Figure 5**), there is an intense band of the formed complex at 215 nm ( $\pi \rightarrow \pi^*$  transition of the carboxyl group [35]) indicating red shift effect compared to CMD. This phenomenon is an indicator of Ag ions interaction with CMD and AgNP-CMD complex formation.



**Figure 5.** UV-Vis spectra of CMD ligand, AgNP-CMD = 1:1 complex (A), AgNP-CMD = 1:2 complex (B), and AgNP-CMD complex after 3 months (C).

## 2.4. XRD study

Crystal structure of AgNP-DS and AgNP-CMD nanoparticles was determined and confirmed by X-ray diffraction (XRD) technique. The samples were prepared by press and pull method in top-loading specimen plate [36]. The diffractogram was measured in Bragg-Brentano  $\theta$ :  $2\theta$  geometry by a conventional powder diffractometer, Seifert V-14, using Cu  $K\alpha$  radiation ( $\lambda_{Cu K\alpha_1} = 1.5406 \text{ \AA}$ , Ni filter, generator settings: 30 kV, 30 mA). As an external standard for peak position calibration and instrumental peak broadening determination,  $LaB_6$  was used. XRD data were collected over the  $2\theta$  range of  $5\text{--}90^\circ$  with a step size of  $0.02^\circ$ , and an exposition time of 2 s per step. The obtained diffractograms are shown in **Figures 6** and **7**.

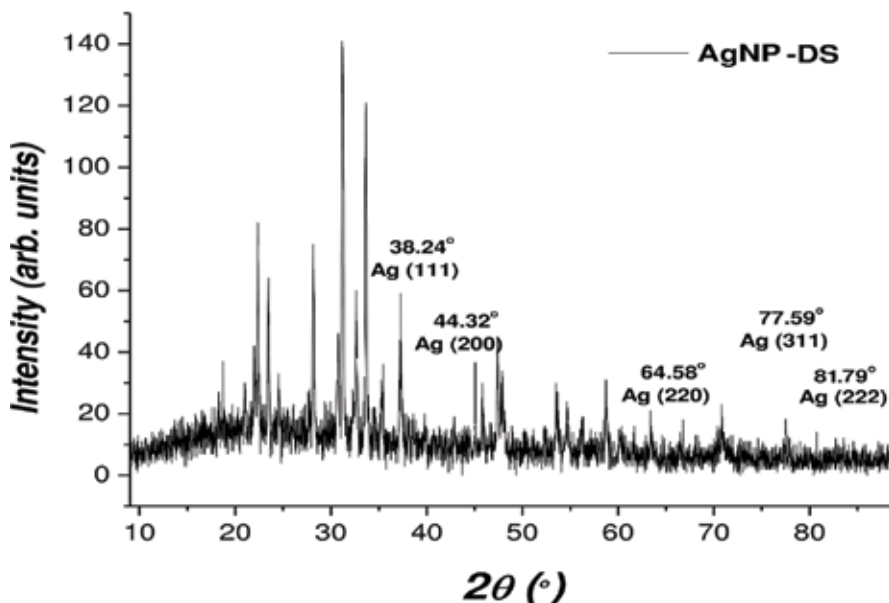


Figure 6. XRD diffraction patterns of AgNP-DS complex.

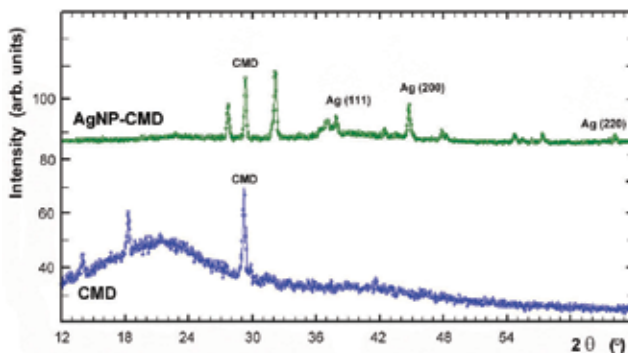


Figure 7. XRD diffraction patterns of CMD and AgNP-CMD complex.

From the presented X-ray diffraction patterns of AgNP-DS (Figure 6) can be noticed the XRD peaks at 38.24, 44.32, 64.58, 77.59, and 81.79°. Based on literature data [4, 6], the characteristic XRD peaks could be determined as next crystallographic planes: 111, 200, 220, 311, and 222. These planes are specific for the face-centered cubic silver crystals. This statement, along with the specified values, indicates the presence of silver nanoparticles in the synthesized AgNP-DS complex. Similar to the previous study, the crystal structure of Ag nanoparticles was determined with complex AgNP-CMD. Based on X-ray diffraction patterns (Figure 7) and the presence of XRD peaks at 38.02, 44.50, and 64.51°, a particular crystallographic planes are as follows: 111, 200, and 220, which are specific for the cubic silver crystals. According to literature [4, 6], the XRD peak at 29.01° is characteristic of the CMD ligand.

The calculation of average AgNP size has been done from the width of reflection in the X-ray diffraction pattern according to the Scherrer's equation (1):

$$D(2\theta) = K\lambda / FW_s \cos\theta \quad (1)$$

where  $D$  is the mean size of metal nanoparticles (nm);  $K$  is Scherrer constant (it's chosen 0.9—roughly spherical particles);  $\lambda$  is wavelength of X-ray radiation (nm);  $\theta$  is angle of diffraction ( $^\circ$ ); and  $FW_s$  is specimen broadening of single peak (in radians).  $FW_s$  is obtained according to the Eq. (2):

$$FW_s^d = FWHM^d - FW_1^d \quad (2)$$

where  $FWHM$  is full width at half maximum of the peak;  $FW_1$  is instrumental broadening gained from  $LaB_6$  diffractogram at the similar  $2\theta$  angles; and  $d$  is parameter of deconvolution (here  $d$  is chosen as 1.5 which means that shape is partly Gaussian and partly Lorentzian). According to Scherrer's equation (1) and XRD peak at  $38.24^\circ$   $2\theta$  from diffraction patterns (**Figure 7**), it is concluded that AgNP have mean crystallite size of  $40 \pm 4$  nm.

## 2.5. SEM and EDX study

The size and shape of AgNP-DS and AgNP-CMD complexes were further characterized by scanning electron microscopy (SEM) on JEOL JSM 5300 scanning electron microscope. Scanning micrographs were transformed into a PC format in order to further analyze the particles morphology. The samples for SEM analysis have been prepared by thin layer of the complex suspension overnight air drying at room temperature. Dried samples have been coated with 10-nm-thick film of gold in JPC JEOL-1100 apparatus. Electron beam of 30 keV has been used. The SEM micrographs of AgNP-DS (**Figure 8A**) showed both individual particles, but a number of aggregates, too. Size of 10–60 nm is predominant for individual spherical particles. Images have also indicated that obtained nanoparticles are stable, and they are not in a mutual contact. This can be ascribed to stabilization of the nanoparticles by DS as a capping agent. Aggregates of nanoparticles with poorly defined morphology and irregular structure have also been found (**Figure 8A**).

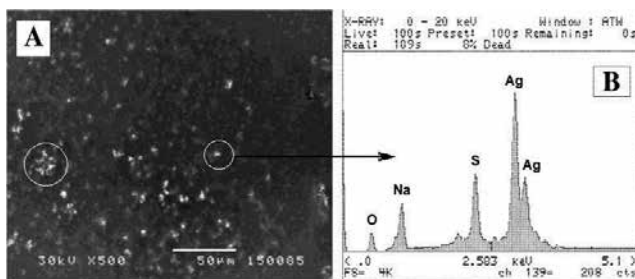


**Figure 8.** SEM images of AgNP-DS showing the existence of individual nanoparticle and large aggregates (A) and EDX spectrum of individual AgNP-DS (B.)

Energy-dispersive X-ray (EDX) spectral analysis has been performed by LINK Analytical 2000 QX microprobe assembled on a JEOL JSM 5300 scanning electron microscope. Samples prepared for SEM analyses have been used for EDX spectra measuring. EDX spectroscopy can be used for qualitative as well as quantitative assessment of silver used for the AgNP production [36]. EDX spectrum of AgNP-DS is shown in **Figure 8B**. Strong signal comes from elemental silver, while weaker signals come from S, O, and Na (from Na salt of DS), confirming that AgNP are formed as a part of AgNP-DS. This is consistent with an optical absorption peak appearance at approximately 3 eV (410 nm), which originates from SPR, and it is characteristic for metallic silver nanocrystals [6].

Similar to the previous complex, the SEM micrographs of AgNP-CMD (**Figure 9A**) show single particles, but a number of aggregates as well. Particle size of 10–60 nm is dominant for individual spherical particles. SEM images showed that obtained nanoparticles are stable and not in direct contact with each other. This can be explained as stabilization effect of CMD, as a capping agent, on produced nanoparticles. But, aggregated nanoparticles with larger irregular structure and no well-defined morphology were also found (**Figure 9B**).

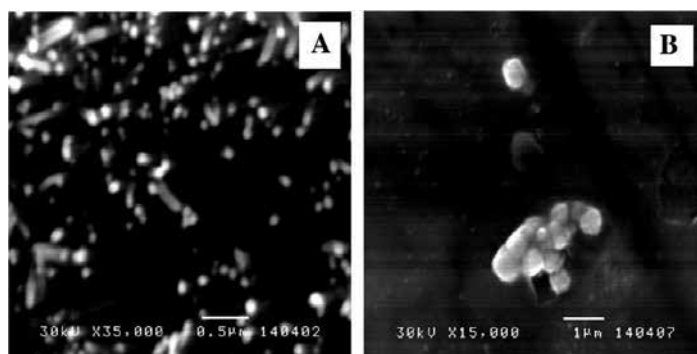


**Figure 9.** SEM images of individual spherical particles (A) and aggregated nanoparticles of AgNP-CMD (B).

## 2.6. Antimicrobial study

Agar disk diffusion method has been used for measuring of antibacterial and antifungal activity of AgNP stabilized by DS. One fungal strain (*Candida albicans* ATCC 2091) and nine bacterial strains such as Gram-positive (*Staphylococcus aureus* ATCC 25923, *Bacillus cereus* ATCC 11778, *Bacillus luteus* haus strain, *Bacillus subtilis* ATCC 6633, and *Listeria monocytogenes* ATCC 15313) and Gram-negative (*Escherichia coli* ATCC 25922, *Pseudomonas aeruginosa* ATCC 27853, *Klebsiella pneumoniae* ATCC 700603, and *Proteus vulgaris* ATCC 8427) were used as an indicator strain for this analysis. Preparation of suspension was performed by already described method [37]. Direct colony method has been used for bacterial and yeast suspensions preparation, and the colonies have been taken directly from the plate and suspended in 5 cm<sup>3</sup> of sterile 0.85% saline. Turbidity of the initial suspension has been adjusted comparing with 0.5 McFarland's [38]. After this adjustment, the bacterium and yeast suspensions contained close to 10<sup>8</sup> and 10<sup>6</sup> colony-forming units (CFU)/cm<sup>3</sup>, respec-

tively. Initial suspension has been additionally prepared by tenfold dilution into sterile 0.85% saline. Inoculation of bacterial cell suspensions has been done to the trypton soya agar plates, while the yeast suspension to the Sabouraud maltose agar plates. Standard sterile cellulose disks of 9 mm diameter have been impregnated with different AgNP-DS concentrations (0.25, 0.5, 1.0 mg cm<sup>-3</sup>) and putted on surface of the inoculated plates. The plates have been incubated at 37°C for 24 h. Inhibition zones were evaluated by measuring the diameter of the zones growth (**Table 2**).

Microbes		AgNP-DS concentration		
		0.25 mg cm <sup>-3</sup>	0.5 mg cm <sup>-3</sup>	1.0 mg cm <sup>-3</sup>
Fungi	<i>C. albicans</i>	–	16	–
Bacteria G <sup>+</sup>	<i>L. monocytogenes</i>	16	17	18
	<i>B. cereus</i>	16	18	19
	<i>B. subtilis</i>	16	17	19
	<i>S. aureus</i>	17	18	19
	<i>B. luteus haus strain</i>	20	21	24
Bacteria G <sup>-</sup>	<i>P. vulgaris</i>	13	14	15
	<i>K. pneumoniae</i>	16	18	19
	<i>E. coli</i>	17	18	21
	<i>P. aeruginosa</i>	23	24	26

**Table 2.** Antimicrobial activity of AgNP-DS, radial diameter of inhibition zones (mm) for tested bacterial and fungal strains.

The investigated AgNP-DS solution has shown antibacterial activity against *S. aureus*, *B. cereus*, *B. luteus in haus strain*, *B. subtilis*, *L. monocytogenes*, *E. coli*, *P. aeruginosa*, *K. pneumoniae*, and *P. vulgaris* bacteria, which is proved by clear inhibition zones of the bacteria growth around the disks (**Table 2**). Inhibition has been observed for all analyzed bacterial strains in the 0.25 mg cm<sup>-3</sup> concentration of AgNP-DS, indicating relatively low minimal inhibitory concentration against these microorganisms. For example, Dhand and coworkers [39] stated that minimal inhibitory concentrations for *E. coli* and *S. aureus* were around 0.26 mg cm<sup>-3</sup>. The highest inhibition zones were observed against *P. aeruginosa* and *B. luteus in haus strain*, and inhibition zones of AgNP-DS against these microorganisms in 1.0 mg cm<sup>-3</sup> concentration were 26 and 24 mm, respectively. *P. vulgaris* was the least sensitive to the AgNP-DS (1.0 mg cm<sup>-3</sup>) activity with zone of 15 mm. Investigation of AgNP-DS activity in different concentrations against other bacterial strains has shown similar results with inhibition zones of 16–17 mm, 18–19 mm, and 18–21 mm for the AgNP-DS concentration of 0.25, 0.5, and 1.0 mg cm<sup>-3</sup>, respectively. The results for *K. pneumoniae*, *B. luteus in haus strain*, and *P. aeruginosa* are higher compared to data for AgNP-CMD (**Table 3**). Antifungal activity against *C. albicans* was observed only in the concentration of 0.5 mg cm<sup>-3</sup> AgNP-DS. Low

antimicrobial activity of AgNP against *C. albicans* has been estimated for AgNP stabilized with CMD. The mechanism of AgNP antimicrobial activity can be related to silver accumulation in the membranes of bacteria, which cause cell death [40]. Silver cation can react with thiol groups and proteins in the cells; nonetheless, it can inactivate enzymes essential for the normal cell metabolism [41]. The investigated AgNP-DS particles, in the concentration of 1.0 mg cm<sup>-3</sup>, have shown a number of specificity concerning its antimicrobial activity. It is important that higher concentration of silver is harmful for consumer and for microbes as well, so the lower concentrations are much more applicable. The effective concentrations of AgNP, which have effect in organisms different from the control, are in the range from a few ng dm<sup>-3</sup> to 10 mg dm<sup>-3</sup>; this effective concentration is depended on the organism itself as well as many other factors [42]. Having in mind these results, it can be concluded that this design of silver nanoparticles synthesis has a great potential because of their antimicrobial activity.

Microbes		AgNP-CMD concentration		
		0.25 mg cm <sup>-3</sup>	0.5 mg cm <sup>-3</sup>	1.0 mg cm <sup>-3</sup>
Bacteria G <sup>+</sup>	<i>B. lutea</i>	11	13	20
	<i>B. cereus</i>	11	12	14
	<i>B. aureus</i>	12	18	21
Bacteria G <sup>-</sup>	<i>E. fecalis</i>	–	–	11
	<i>P. aeruginosa</i>	–	–	12
	<i>K. pneumoniae</i>	13	14	15
Fungi	<i>Aspergillus</i> spp.	–	–	12
	<i>Penicillium</i> spp.	13	20	20
	<i>C. albicans</i>	–	–	11

**Table 3.** Antimicrobial activity of AgNP-CMD, radial diameter of inhibition zones (mm) for tested bacterial and fungal strains.

In order to compare antimicrobial activity of similar complexes, the results of AgNP-CMD antimicrobial activity (radial diameter of inhibition zones) are presented in **Table 3**. The AgNP-CMD solution exhibited antibacterial activity against bacteria *B. lutea*, *B. aureus*, *B. cereus*, *E. fecalis*, *P. aeruginosa*, and *K. pneumoniae* showing clear inhibition zones of the bacteria growth around the disk. AgNP-CMD in the concentration of 1.0 mg cm<sup>-3</sup> have shown a number of specificity concerning its antimicrobial activity. The antifungal activity of the AgNP-CMD has been analyzed by agar disk diffusion method. *Aspergillus* spp., *Penicillium* spp., and *C. albicans* were inhibited in a concentration-dependent manner. The radial growth inhibition zones increased with the AgNP-CMD concentration increasing from 0.25 to 1.0 mg cm<sup>-3</sup>. The fungus *Penicillium* spp. was more sensitive to the AgNP-CMD comparing to the other two fungal strains.

### 3. Cobalt(II)-dextran biocomplexes

A lot of investigations in the field of coordination chemistry are based on synthesis and characterizations of different biocomplexes present in the biological systems. Synthetic ligands, which can serve as model molecules for complex biomolecular structures, are also investigated [19]. Bioligands or synthetic ligands are mostly natural macromolecular compounds. These products of special importance mostly represent complexes of different metals (Fe, Co, Cu, Zn) with ligands of polysaccharide type (such as pullulan, inulin, dextran) [43–45]. However, the native polysaccharide possessing antigen characteristics wherefore is not of pharmaceutical importance [18]. Depolymerization of raw polysaccharides, trying to get products with adequate molar masses distribution for commercial purposes, has been done. Dextran, is a well-known, extracellular, water-soluble neutral polysaccharide with  $\alpha$ -(1–6)-linked D-glucopyranose unit chain, with a wide range of applications. Dextran gained from *Leuconostoc mesenteroides* B-512(F) is composed of  $\alpha$ -(1–6)-linked glucan with side chains attached to C3-positions of backbone glucopyranose units. Various biometal ions (Fe, Co, Cu, Ca, Zn, Mg, etc.) are included in the complexation with dextran in alkaline solutions. Complexes of iron [17, 46] and copper [47–49] with polysaccharides have a great significance, and they have been described in detail. The content of metals and solution composition is pH dependent [17, 48]. Cobalt preparations, based on carbohydrates and its derivatives, are used in both human and veterinary medicine [50, 51]. The different FTIR spectroscopic methods (such as microspectroscopy, attenuated total reflection) are commonly used for the characterization of these complexes [52, 53]. This section applies to some spectroscopic examination of dextran complexes with cobalt ions.

#### 3.1. Complex synthesis

The cobalt complexes with reduced low-molar dextran as ligand (Co(II)-RLMD) were synthesized in water solutions, at different pH values (7.5–13.5) and different temperatures (298–373 K), using  $\text{CoCl}_2 \times 6\text{H}_2\text{O}$  and RLMD (5000 g/mol). The details of synthesis have been described [54, 55]. The complexes were isolated in the solid state. For further structural examination, the samples of Co(II)-RLMD were deuterated ( $\text{D}_2\text{O}$ , Merck) for 2 h, at room temperature, in vacuum.

#### 3.2. FTIR study

KBr pastille method has been used for sample preparation. The FTIR spectra have been recorded at room temperature, as an average value of 40 scans (resolution of  $2\text{ cm}^{-1}$ ) on a Bomem MB-100 FTIR spectrometer (Hartmann & Braun, Canada) coupled with a DTGS/KBr detector. Spectrostructural correlation of dextran by FTIR spectroscopy has been the subject of attention of many researchers [30, 31, 56–58]. It was shown that by studying the individual spectral areas, the information on linearity [content of  $\alpha$ -(1–6) bond], crystallinity, conformation, conformational transitions, and changes in the structure of differently treated dextrans can be obtained. The FTIR spectrum of reduced low-molar dextran is shown in **Figure 11a**. Bands at  $765$  and  $916\text{ cm}^{-1}$  are indicating the presence of the  $\alpha$ -(1–6) glycosidic bonds, and the estimated content of these bonds is greater than 96% that indicates a high linearity of polysaccharide. The presence of these bands as those at the  $845\text{ cm}^{-1}$  indicates a  $\text{C}_1$  conformation of glucopyranose units

(eq-ax-ax-ax-ax arrangement of adjacent C–H groups). There is an intense broad band whose centroid is at about  $3400\text{ cm}^{-1}$ , in the area of stretching OH vibrations. Summary intensity of this band comes from the  $\nu(\text{O-H})$  vibrations of hydroxyl groups involved in the formation of several by the strength of hydrogen bonds, but also from the  $\text{H}_2\text{O}$  molecule whose presence is confirmed by the band at  $1640\text{ cm}^{-1}$ , which is result of  $\delta(\text{HOH})$  vibrations [54].

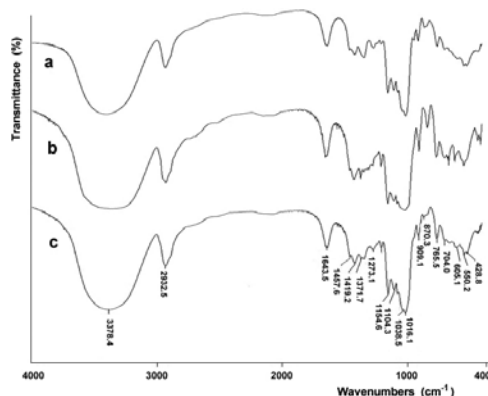


**Figure 10.** The FTIR spectra of RLMD (a) and Co(II)-RLMD complexes synthesized on the boiling temperature and different pH: 7.5 (b) and 13.0 (c).

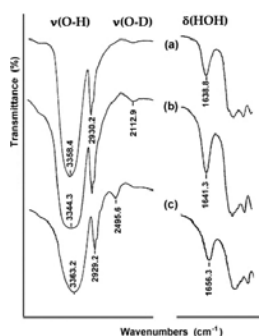


**Figure 11.** FTIR spectral segments of dextran (a), partially deuterated (b), and fully deuterated (c) RLMD analogs in  $\nu(\text{O-H})$ ,  $\nu(\text{O-D})$ , and  $\delta(\text{HOH})$  vibrations.

The FTIR spectra of synthesized Co(II)-RLMD complex, which were obtained under various reaction conditions, are presented in **Figure 10**. The FTIR spectra of RLMD and its Co(II)-RLMD complex are basically similar. In the FTIR spectra of synthesized complex, there are the differences in the area of O–H vibrations. In this area, there is a large, complex band approximately  $3390\text{ cm}^{-1}$  of  $\nu(\text{O-H})$ , which is likely due to the stretching vibrations of polysaccharide OH groups. The characteristic IR band of  $\delta(\text{HOH})$  at about  $1645\text{ cm}^{-1}$  in the spectra of synthesized complexes, as well as in the spectrum of RLMD, as noted above, indicates the presence of crystal water in the structure [54, 55]. By analyzing the low-frequency part of the RLMD spectrum ( $\gamma(\text{C-H})$  vibrations, **Figure 10a**), the FTIR spectra of Co(II)-RLMD complex

(**Figure 10b** and **c**), and the presence of bands at about  $915$  and  $845\text{ cm}^{-1}$ ,  ${}^4C_1$  conformation of glucopyranose units, which indicates that the complexation with Co(II) ions does not lead to conformational changes in glucopyranose units, can be determined. In accordance with this is the change in the intensity of IR band in the area approximately  $1350\text{ cm}^{-1}$  that originates from  $\delta(\text{C-H})$  and  $\delta(\text{O-H})$  vibrations. With an increase in the pH synthesis (from 7.5 to 13.5), the band intensity of  $\nu(\text{O-H})$  vibration increases, and the frequency of  $\nu(\text{O-H})$  vibration band at lower pH (7.5–8.5) stays almost unchanged and then increases with increasing pH (11–13.5). If the complexation with Co(II) ions takes place via OH groups at the C-2, C-3, or C-4 carbon atoms of dextran glucopyranose units (involved in the formation of various by the strength of hydrogen bonds in dextran), hydrogen bonds disappear by complexation, so the bands are expected at the higher frequencies. In complexes with the highest metal content (10.07% Co), which were synthesized at pH 12, a set of IR bands in this area is close to that at starting RLMD. In the complex which was synthesized at pH 13 with a minimum cobalt content of 1.89% in the IR spectrum (**Figure 10c**), there are intense bands at  $3400\text{ cm}^{-1}$  to the binder of low-frequency side in this region. This could indicate that the structure of this complex differs slightly from the structure of other Co(II)-RLMD complex, which were synthesized under different reaction conditions. In the low-frequency area ( $<800\text{ cm}^{-1}$ ) of the FTIR spectra of RLMD and Co(II)-RLMD complex, there are some differences. In this region of the IR spectrum, in addition to the band of  $\nu(\text{Co-O})$ , the bands of deformation  $\gamma(\text{O-H})$  vibrations of polysaccharide as well as the deformation vibrations of glucopyranose ring are expected (**Figure 10**). Wide band of medium intensity in the FTIR spectra of Co(II)-RLMD complex at about  $450\text{ cm}^{-1}$  shows a fine structure.

### 3.3. Isotopic $\text{D}_2\text{O}$ exchange study

Isotopic substitution of hydrogen atoms by deuterium, connected with FTIR spectroscopy, has an important role in determining the structure of dextran. Isotopic exchange results indicate that dextran and its Co(II)-RLMD complex are crystal hydrates (probably one type of water molecules) [59]. Structural changes in the process have been detected by absorption bands in the area of  $3600\text{--}3000\text{ cm}^{-1}$ , caused by  $\nu(\text{O-H})$  vibrations. In the case of isotopic exchanges of O-H to O-D group, the frequency of stretching vibration is reduced to  $\sqrt{2}$ , and it is located in the area of  $2700\text{--}2300\text{ cm}^{-1}$ . Deuteration is a very sensitive method to assess the environment of OH groups, which is associated with the intensity generated by hydrogen bonds. The degree of crystallinity of the polysaccharide can be determined by FTIR spectroscopy method with deuteration. Crystallinity is a part of the regulated saccharide area in which the macromolecules are connected with parallel hydrogen bonds. In processing the sample with  $\text{D}_2\text{O}$ , usually OH groups in less regulated or amorphous regions were rapidly converted into OD groups. Conversion of OH groups in the crystal areas is very slow. Thus, the degree of crystallinity has been determined by the change in intensity of asymmetrical  $\nu(\text{O-H})$  band vibrations and by the appearance of new bands of  $\nu(\text{O-D})$  vibration. The relations of band intensity at  $1429$  and  $893\text{ cm}^{-1}$  were taken as empirical indicators of the degree of crystallinity of samples. With decrease in the crystallinity, the band at about  $1430\text{ cm}^{-1}$  disappears and comes to an increase in the intensity of the band at approximately  $900\text{ cm}^{-1}$ , typical for the amorphousness. Even better relationship can be seen at the band at approximately  $1370$  and  $2900\text{ cm}^{-1}$ . Namely, in the spectrum of partially deuterated analogs of dextran (**Figure 11**) in

the  $\nu(\text{O-D})$  area of the vibration of HDO molecules, there is a single band at about  $2495\text{ cm}^{-1}$ . Partners of these vibrations would be expected at about  $3400\text{ cm}^{-1}$  in the  $\nu(\text{O-H})$  areas (taking into account the displacement factor of 1.35).

The FTIR spectra of Co(II)-RLMD complex (a) and its deuterated analog (b), which was synthesized at pH 13, are shown in **Figure 12**. In the FTIR spectrum of Co(II)-RLMD complex (**Figure 12b**), in the area of  $\nu(\text{O-D})$  vibrations of HDO molecules, there is a single band at about  $2483\text{ cm}^{-1}$  in the corresponding complexes with crossfold on the high-frequency side. Partners of these vibrations would be expected at about  $3400\text{ cm}^{-1}$  in  $\nu(\text{O-H})$  area. Results of partial deuteration indicate that the band at about  $3400\text{ cm}^{-1}$  is sensitive to isotopic substitution, in both cases (RLMD and Co(II)-RLMD complexes). Reducing the intensity of this band by deuteration demonstrates that the  $\nu(\text{O-H})$  vibrations of water molecules are its part. This fact indicates that both compounds contain crystal water in their structure. Confirmation of this conclusion is that in the spectra of deuterated analogs of both compounds (**Figures 11 and 12**), an intense band near  $1645\text{ cm}^{-1}$  is also highly sensitive to isotopic substitution and is to be attributed to the HOH deformation vibration of the crystal water.

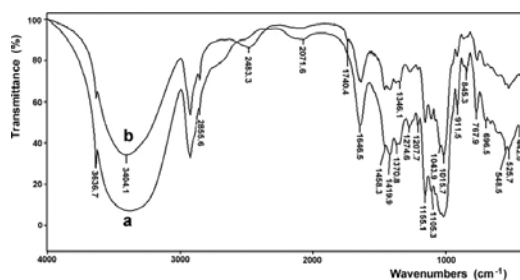


**Figure 12.** FTIR spectra of Co(II)-RLMD complex (a) and its deuterated analog (b) synthesized at pH 13.

As known, Seidl et al. [60] proposed criteria according to which, based on the study of spectra of protonated, partially and fully deuterated hydrate, it is possible to determine the number of types of  $\text{H}_2\text{O}$  molecules ( $n$ ) and the number of nonequivalent OH groups ( $m$ ). By the spectra appearances, in the stretching OD area of HDO molecules, and the appearance of a band, whose intensity increases monotonically with increasing degree of deuteration when the frequency does not change, it can be concluded from the above criteria [60] that in the structure of dextran and its complexes with Co(II) ions is present one crystallographic type of water molecule ( $n = 1$ ). On the basis of Berglund correlation [61], from equation (3), Ow...O distances are estimated at 283.1 pm for dextran and 281.8 pm for Co(II)-RLMD complex:

$$\nu(\text{OD}) = 2727 - 8.97 \times 10^6 \times e^{-3.73 \times R(\text{Ow} \times \times \times \text{O})}. \quad (3)$$

Water protons are involved in the formation of relatively weak hydrogen bonds ( $m = 1$ ). In bending area of HDO and  $\text{D}_2\text{O}$ , in the spectrum of deuterated analogs of the complex, there are bands around  $1315$  and  $1070\text{ cm}^{-1}$ , which confirm the previously disclosed consideration

of the water binding. From FTIR spectrum shown in **Figure 12b**, decrease in the intensity of the band around  $1430\text{ cm}^{-1}$  and an increase in the band intensity at approximately  $910\text{ cm}^{-1}$  can be observed, which is a characteristic for amorphous character. An even better relationship can be observed in the FTIR spectrum of **Figure 12**, with the band of about  $1370$  and  $2900\text{ cm}^{-1}$ . Based on the results of FTIR spectroscopy, an amorphous structure of the synthesized Co(II)-RLMD complex can be assumed.

### 3.4. ATR-FTIR microscopy study

The ATR-FTIR spectral analysis has been performed by microspectroscopy ATR-FTIR system (Bruker, Tensor-27). Within this system, FTIR spectroscope is connected to a microscope ( $15\times$  objective) (Bruker, Hyperion-1000/2000) and a computer system capable of microanalysis by using a liquid-nitrogen-cooled ( $250\text{ }\mu\text{m}$ ) MCT detector (GMBH, Germany). The ATR-FTIR spectra (Kubelka-Munk option) have been recorded in the range of  $4000\text{--}400\text{ cm}^{-1}$ , with  $4\text{ cm}^{-1}$  resolution and 260 scans. The newly formed FTIR vibrational microspectroscopy can provide information on the sample at the molecular level, with high spatial resolution at the microscopic level. Small sample can be analyzed by both nondestructive vibrational spectroscopic techniques (Raman, IR) [62–67]. Spectra can be recorded continuously in different parts of the microsample in order to obtain appropriate databases. **Figures 13** and **14** show the absorption ATR-FTIR spectra of Co(II)-RLMD complex, which were obtained under various reaction conditions.

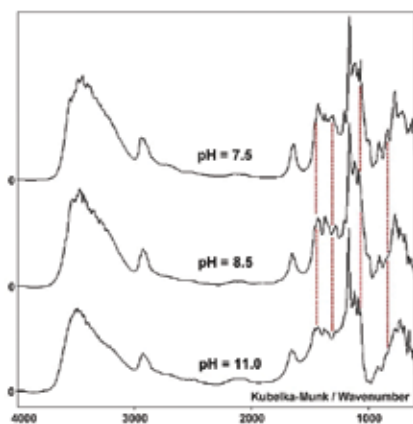


**Figure 13.** ATR-FTIR spectra of Co(II)-RLMD complex synthesized at the boiling temperature and pH values in the range of 7–11.

The wavenumber values of characteristic IR bands in the ATR-FTIR spectra of Co(II)-RLMD complex are given in **Table 4**.

Absorption bands corresponding to the specific chemical components can be represented as a map. ATR-FTIR spectra, presented in **Figures 13** and **14**, correspond to the different

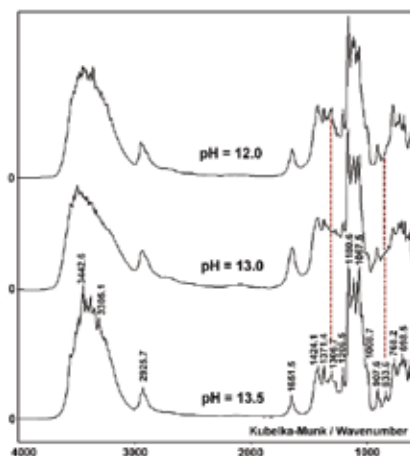


**Figure 14.** ATR-FTIR spectra of Co(II)-RLMD complex synthesized at the boiling temperature and pH values in the range of 12–14.

Wavenumber (cm <sup>-1</sup> )	Band assignment	Intensity	Comment
3400	$\nu(\text{O-H})$	Very strong, complex	CH-OH glucopyranose, H <sub>2</sub> O
2930	$\nu_{\text{as}}(\text{C-H})$ i $\nu_{\text{sy}}(\text{C-H})$	Medium	CH
1640	$\delta(\text{HOH})$	Medium	H <sub>2</sub> O
1450–1345	$\delta(\text{C-H})$	Medium	CH
1420	$\delta(\text{O-H})$	Medium	OH
1150, 1110, 1070, 1040, and 1010	$\nu_{\text{as}}(\text{C-O}), (\text{C-O-C}),$ $\nu_{\text{as}}(\text{C-C-C})$ i $(\text{C-C-O})$	Very strong, strong	Glucopyranose
1000–700	$\gamma(\text{C-H})$	Medium	Configuration

**Table 4.** Assignment of characteristic IR bands of RLMD and the synthesized Co(II)-RLMD complexes.

parts of the sample of Co(II)-RLMD complex, which show a homogeneity of the samples. A new way of visualization shows the capability of visualization not only of heterogeneous region of the samples, but also at the same time provides microspectroscopic spatial information. The visualization of different concentrations of components and presentation as 3D maps is also enabled. Application of ATR-FTIR microscopy to Co(II)-RLMD complex, which were synthesized under different reaction conditions, is shown in **Figure 15**. The changes in color contours at certain parts of the image indicate the content and distribution of cobalt and polysaccharides in Co(II)-RLMD samples. ATR-FTIR microspectroscopic data show a high homogeneity of the samples, and the presence of Co(II) ions (the results obtained by other spectroscopic techniques) has been confirmed by the color of Co(II)-RLMD complex.

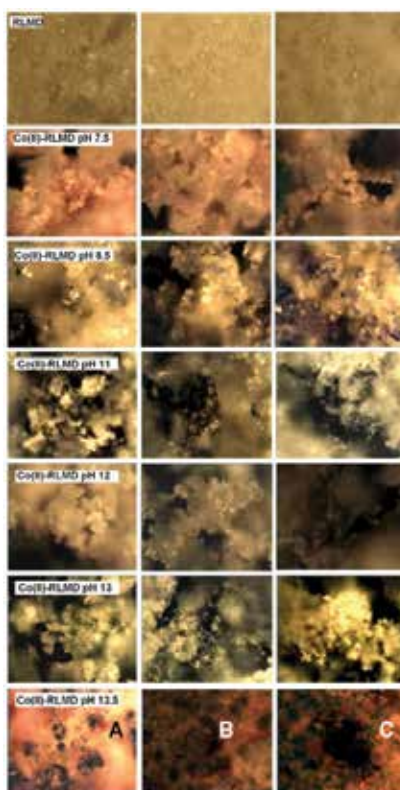


**Figure 15.** Different FTIR microscopic profiles (A–C) ( $300\ \mu\text{m} \times 250\ \mu\text{m}$ ) for ligand (RLMD) and Co(II)-RLMD complexes at different pH values.

#### 4. Conclusion

The modern Fourier transform infrared spectroscopic techniques (linear scan, reflection, transmission, mapping, video analysis) in combination with diffraction (XRD), energy-dispersive X-ray (EDX), spectrophotometric (UV-Vis), and electronic microscopy (SEM) methods are applied in the structure analysis of synthesized green nanoparticles and polysaccharide complexes, as well as for the confirmation of suggested types of complexes structure and for the testing of samples homogeneity. In this respect, silver nanoparticles were prepared with dextran sulfate or carboxymethyl dextran as a reducing and capping agent, while cobalt biocomplexes were synthesized with reduced low-molar dextran as ligand. Comparison of FTIR spectra of initial exopolysaccharide compounds (DS, CMD, RLMD) and final products (AgNP-DS, AgNP-CMD, Co(II)-RLMD complexes), in the specific region of characteristic functional group vibrations, has indicated on coordination complexes forming as a part of complex structure. FTIR spectroscopic analysis has shown that interactions between metal ions and specific polysaccharide functional groups have steric character and suggest  ${}^4C_1$  conformation of the glucopyranose unit. The existence of nanoparticles (in range of 10–60 nm) has been confirmed by SPR band in the UV-Vis spectra, by SEM microscopy, and XRD meth-

ods. AgNP size was determined on the Bragg reflection at  $38.24^\circ 2\theta$ , yielding mean crystallite size of  $40 \pm 4$  nm. It has been found that crystalline structures of silver complexes are face-centered cubic type by XRD method. Morphological SEM analysis has been shown that formed nanoparticles are spherical and inclined to aggregation. It has been established that size distribution and morphology of mentioned nanoparticles (by SEM and FTIR microspectroscopy methods), as well as the structural form of the complexes (by FTIR, UV-Vis, XRD), are depended on ligand properties (such as constitution, degree of amorphousness or crystallinity, molar mass, units conformation, chain linearity) and on the reaction conditions (such as metal-ligand weight ratio, reaction time, temperature, and pH values). Also, antimicrobial and antifungal activities of synthesized AgNP have been determined. The highest inhibition zones were observed against *P. aeruginosa* and *B. luteus* *haus strain*, while *P. vulgaris* was the least sensitive to the nanoparticles. The fungus *Penicillium* spp. was more sensitive to the AgNP comparing to the other two fungal strains. Having in mind these results, it can be concluded that this design of silver nanoparticles synthesis has a great potential because of their antimicrobial activity.

## Acknowledgements

This study is the result of the project TR-34012, funded by the Ministry of Education, Science and Technological Development, of the Republic of Serbia.

## Author details

Goran S. Nikolić<sup>1\*</sup>, Milorad D. Cakić<sup>1</sup>, Slobodan Glišić<sup>1</sup>, Dragan J. Cvetković<sup>1</sup>, Žarko J. Mitić<sup>2</sup> and Dragana Z. Marković<sup>3</sup>

\*Address all correspondence to: [goranchem\\_yu@yahoo.com](mailto:goranchem_yu@yahoo.com)

1 Department of Chemical Technology, Faculty of Technology, University of Niš, Leskovac, Serbia

2 Department of Chemistry, Faculty of Medicine, University of Niš, Niš, Serbia

3 High Technologically Artistic Professional School, Leskovac, Serbia

## References

- [1] A.L. Daniel-da-Silva, T. Trinidad, Biofuncional composites of polysaccharides containing inorganic nanoparticles, *Adv. Nanotechnol.* 98(7) (2011) 953–955. ISBN 978-953-308-55-0
- [2] P.V. Quelemes, F.B. Araruna, B.E.F. de Faria, S.A.S. Kuckelhaus, D.A. da Silva, R.Z. Mendonça, C. Eiras, M.S. Soares, J.S.A. Leite, Development and antibacterial activity of cashew gum-based silver nanoparticles, *Int. J. Mol. Sci.* 14 (2013) 4969–4981.

- [3] H.V. Tran, L.D. Tran, T.B. Cham, H.D. Vu, T.N. Nguyen, D.G. Pham, P.X. Nguyen, Synthesis, characterization, antibacterial and antiproliferative activities of monodisperse chitosan-based silver nanoparticles, *Colloids Surf. A* 360 (2010) 32–40.
- [4] P. Kanmani, S.T. Lim, Synthesis and characterization of pullulan-mediated silver nanoparticles and its antimicrobial activities, *Carbohydr. Polym.* 97 (2013) 421–428.
- [5] M.B. Ahmad, J.J. Lim, K. Shameli, N.A. Ibrahim, M.Y. Tay, Synthesis of silver nanoparticles in chitosan, gelatin and chitosan/gelatin bionanocomposites by a chemical reducing agent and their characterization, *Molecules* 16 (2011) 7237–7248.
- [6] K.P. Bankura, D. Maity, M.M.R. Mollick, D. Mondal, B. Bhowmick, M.K. Bain, A. Chakraborty, J. Sarkar, K. Acharya, D. Chattopadhyay, Synthesis, characterization and antimicrobial activity of dextran stabilized silver nanoparticles in aqueous medium, *Carbohydr. Polym.* 89 (2012) 1159–1165.
- [7] D. Chudobova, K. Cihalova, B. Ruttkey-Nedecky, P. Kopel, M. Zurek, K. Bastl, V. Adam, R. Kizek, Use of the silver phosphate nanoparticles (SPNPs) for their antimicrobial effect on bacterial strains, *Nanocon 16–18.10.2013, Brno, Czech Republic, EU* (2013).
- [8] D. Chudobova, L. Nejdil, J. Gumulec, O. Krystofova, M.A.M. Rodrigo, J. Kynicky, B. Ruttkey–Nedecky, P. Kopel, P. Babula, V. Adam, R. Kizek, Complexes of silver(I) ions and silver phosphate nanoparticles with hyaluronic acid and/or chitosan as promising antimicrobial agents for vascular grafts, *Int. J. Mol. Sci.* 14 (2013) 13592–13614.
- [9] S.M. Ghaseminezhad, S. Hamedi, S.A. Shojaosadati, Green synthesis of silver nanoparticles by a novel method: comparative study of their properties, *Carbohydr. Polym.* 89 (2012) 467–472.
- [10] M.N. Nadagouda, R.S. Varma, Synthesis of thermally stable carboxymethyl cellulose/metal biodegradable nanocomposites for potential biological applications, *Biomacromolecules* 8(9) (2007) 2762–2767.
- [11] J. Liu, F. He, T.M. Gunn, D. Zhao, C.B. Roberts, Precise seed-mediated growth and size-controlled synthesis of palladium nanoparticles using a green chemistry approach, *Langmuir* 25(12) (2009) 7116–7128.
- [12] F. He, D. Zhao, J. Liu, C.B. Roberts, Stabilization of Fe-Pd nanoparticles with sodium carboxymethyl cellulose for enhanced transport and dechlorination of trichloroethylene in soil and groundwater, *Ind. Eng. Chem. Res.* 46(1) (2007) 29–34.
- [13] M.A. Garza-Navarro, J.A. Aguirre-Rosales, E.E. Llanas-Vazquez, I.E. Moreno-Cortez, A. Torres-Castro, V. Gonzalez-Gonzalez, Totally ecofriendly synthesis of silver nanoparticles from aqueous dissolutions of polysaccharides, *Int. J. Polym. Sci.* 2013 (2013) 436201. 8 pages. doi:10.1155/2013/436021
- [14] E.M. Prinz, R. Eggers, H.H. Lee, U. Steinfeld, R. Hempelmann, Synthesis of drug loaded magnetic nanoparticles and their uptake into immune cells, *J. Phys. Conf. Ser.* 200 (2010) 122009. doi:10.1088/1742-6596/200/12/122009

- [15] K. Tao, S. Song, J. Ding, H. Dou, K. Sun, Carbonyl groups anchoring for the water dispersibility of magnetite nanoparticles, *Colloid Polym. Sci.* 289 (2011) 361–369.
- [16] A.M. Abdel-Mohsen, R. Hrdina, L. Burgert, G. Krylova, R.M. Abdel-Rahman, A. Krejcová, M. Steinhart, L. Benes, Green synthesis of hyaluronan fibers with silver nanoparticles, *Carbohydr. Polym.* 89 (2012) 411–422.
- [17] G.S. Nikolić, M. Cakić, Lj. Ilić, S. Ristić, Ž. Cakić, Synthesis of some new antianemics I. Iron pullulan complexes of pharmaceutical interest, *Pharmazie* 57(3) (2002) 155–158.
- [18] O. Elmalak, M.A. Lovich, E. Edelman, Correlation of transarterial transport of various dextrans with their physicochemical properties, *Biomaterials* 21 (2000) 2263–2272.
- [19] B. Gyurcsik, L. Nagy, Carbohydrates as ligands: coordination equilibria and structure of the metal complexes, *Coord. Chem. Rev.* 203 (2000) 81–149.
- [20] D. Wei, W. Sun, W. Qian, Y. Ye, X. Ma, The synthesis of chitosan-based silver nanoparticles and their antibacterial activity, *Carbohydr. Res.* 344 (2009) 2375–2382.
- [21] S. Hamed, S.M. Ghaseminezhad, S.A. Shojaosadati, S. Shokrollahzadeh, Comparative study on silver nanoparticles properties produced by green methods, *Iran. J. Biotechnol.* 10 (2012) 191–197.
- [22] S. Glišić, M. Cakić, G.S. Nikolić, B. Danilović, Synthesis, characterization and antimicrobial activity of carboxymethyl dextrane stabilized silver nanoparticles, *J. Mol. Str.* 1084 (2015) 345–351.
- [23] S. Tripathi, G.K. Mehrotra, P.K. Dutta, Chitosan/silver oxide nanocomposite film: preparation and antimicrobial activity, *Bull. Mater. Sci.* 34(1) (2011) 29–35.
- [24] M. Guzman, J. Dille, S. Godet, Synthesis and antibacterial activity of silver nanoparticles against gram-positive and gram-negative bacteria, *Nanomedicine* 8(1) (2012) 37–45.
- [25] S. Glišić, G.S. Nikolić, M. Cakić, N. Trutić, Spectroscopic study of copper(II) complexes with carboxymethyl dextran and dextran sulphate, *Russ. J. Phys. Chem. A* 89(7) (2015) 1254–1262.
- [26] M. Cakić, G.S. Nikolić, Lj. Ilić, S. Stanković, Synthesis and FTIR characterization of some dextran sulphates, *Chem. Ind. Chem. Eng. Q* 11(2) (2005) 74–78.
- [27] V.A. Litvin, B.F. Minaev, Spectroscopy study of silver nanoparticles fabrication using synthetic humic substances and their antimicrobial activity, *Spectrochim. Acta Part A Mol. Biomol. Spectrosc.* 108 (2013) 115–122.
- [28] A.L. Daniel-da-Silva, S. Fateixa, A.J. Guiomar, B.F.O. Costa, N.J.O. Silva, T. Trindade, B.J. Goodfellow, A.M. Gil, Biofunctionalized magnetic hydrogel nanospheres of magnetite and  $\kappa$ -carrageenan, *Nanotechnology* 20(35) (2009) 355602. doi:10.1088/0957-4484/20/35/355602
- [29] X.F. Bao, Y. Zhen, L. Ruan, J.N. Fang, Purification, characterization, and modification of T lymphocyte-stimulating polysaccharide from spores of *Ganoderma lucidum*, *Chem. Pharm. Bull. (Tokyo)* 50 (2002) 623–629.

- [30] R.G. Zhbakov, *Infrared spectra and structure of carbohydrates*, Nauka i Tekhnika, Minsk, Belarus, 1972.
- [31] V.P. Panov, R.G. Zhbakov, *Intra- and intermolecular interactions in carbohydrates*, Nauka i Tekhnika, Minsk, Belarus, 1988.
- [32] M.R. Bindhu, M. Umadevi, Synthesis of monodispersed silver nanoparticles using *Hibiscus cannabinus* leaf extract and its antimicrobial activity, *Spectrochim. Acta Part A Mol. Biomol. Spectrosc.* 101 (2013) 184–190.
- [33] P.P. Gan, S.H. Ng, Y. Huang, S.F. Li, Green synthesis of gold nanoparticles using palm oil mill effluent (POME): a low-cost and eco-friendly viable approach, *Bioresour. Technol.* 113 (2012) 132–135.
- [34] G. Magudapatty, P. Gangopaghyayrans, B.K. Panigrahi, K.G.M. Nair, S. Dhara, Electrical transport studies of Ag nanoparticles embedded in glass matrix, *Phys. B Condens. Matter* 299 (2001) 142–146.
- [35] S.A. Hapse, P.T. Kadaskar, A.S. Shirsath, Difference spectrophotometric estimation and validation of ibuprofen from bulk and tablet dosage form, *Der Pharm. Lett.* 3(6) (2011) 18–23.
- [36] A. Clearfield, J. Reibenspies, N. Bhuvanesh, *Principles and applications of powder diffraction*, Wiley, 2008.
- [37] M.V. Nikolić, M.Ž. Mijajlović, V.V. Jevtić, Z.R. Ratković, I.D. Radojević, Lj.R. Čomić, S.B. Novaković, G.A. Bogdanović, S.R. Trifunović, G.P. Radić, Synthesis, characterization and antimicrobial activity of copper(II) complexes with some S-alkyl derivatives of thiosalicylic acid. Crystal structure of the binuclear copper(II) complex with S-methyl derivative of thiosalicylic acid, *Polyhedron* 79 (2014) 80–87.
- [38] J.M. Andrews, BSAC standardized disc susceptibility testing method, *J. Antimicrob. Chemother.* 56 (2005) 60–76.
- [39] V. Dhand, L. Soumya, S. Bharadwaj, S. Chakra, B. Deepika, B. Sreedhar, Green synthesis of silver nanoparticles using *Coffea arabica* seed extract and its antibacterial activity, *Mater. Sci. Eng. C* 58 (2016) 36–43.
- [40] A.B.A. Boxall, Q. Chaudhry, C. Sinclair, A. Jones, R. Aitken, B. Jefferson, C. Watts, *Current and future predicted environmental exposure to engineered nanoparticles*, Central Science Laboratory Publications, York, UK, 2007, p. 89.
- [41] S.J. Klaine, P.J.J. Alvarez, G.E. Batley, T.F. Fernandes, R.D. Handy, D.Y. Lyon, S.Y. Mahendra, M.J. Mclaughlin, J.R. Lead, *Nanomaterials in the environment: behavior, fate, bioavailability, and effects*, *Environ. Toxicol. Chem.* 27(9) (2008) 1825–1851.
- [42] I. Moreno-Garrido, S. Perez, J. Blasco, Toxicity of silver and gold nanoparticles on marine microalgae, *Mar. Environ. Res.* 111 (2015) 60–73.
- [43] Ž. Mitić, M. Cakić, G.S. Nikolić, FTIR spectroscopic investigations of Co(II)–dextran complexes by using D<sub>2</sub>O isotopic exchange. In: XIII European Conference on the Spectroscopy of Biological Molecules, Palermo, Italy, 2009, p. 83.

- [44] Lj. Ilić, S. Ristić, M. Cakić, G.S. Nikolić, S. Stanković, Polynuclear complex Fe(III) with pullulan oligomers, process of its obtaining, and pharmaceutical preparations on the basis of the complex, WO Patent 2002046241A2, 2002.
- [45] G.S. Nikolić, M.D. Cakić, Physical investigation of the colloidal iron–inulin complex, *Colloid J.* 69(4) (2007), 464–473.
- [46] E. London, The molecular formula and proposed structure of the iron–dextran complex, imferon, *J. Pharm. Sci.* 93(7) (2004) 1838–1846.
- [47] W.F. Leech, D.G. McLaren, K.D. McSporran, Administration of copper to an animal, US Patent 2009/0029942 A1, 2009.
- [48] Ž. Mitić, G.S. Nikolić, M. Cakić, R. Nikolić, Lj. Ilić, Synthesis and spectroscopic characterization of copper(II) dextran complexes, *Russ. J. Phys. Chem.* 81(9) (2007), 1433–1437.
- [49] G.S. Nikolić, M.D. Cakić, Analysis of bioactive oligosaccharide-metal complexes by modern FTIR spectroscopy: Copper complexes, Chapter 2, pp. 15–44, In book: “Fourier transforms—New analytical approaches and FTIR strategies”, Ed. Goran Nikolic, ISBN: 978-953-307-232-6, Publisher: InTech, April 2011. Available from: <http://www.intechopen.com>
- [50] R. Bandwar, M. Sastry, R. Kadam and C. Rao, Transition-metal saccharide chemistry: synthesis and characterization of D-glucose, D-fructose, D-galactose, D-xylose, D-ribose, and maltose complexes of Co(II), *Carbohydr. Res.* 297 (1997) 333–339.
- [51] Expert Group on Vitamins and Minerals, Review of cobalt, EVM/99/19, Secretariat, UK Government, London, May 2002.
- [52] M. Cakić, Ž. Mitić, G.S. Nikolić, Lj. Ilić, G.M. Nikolić, The investigations of bioactive copper(II) complexes with reduced low-molar dextran, *Spectroscopy* 22(2, 3) (2008) 177–185.
- [53] G.S. Nikolić, M. Cakić, Ž. Mitić, Lj. Ilić, P. Premović, Attenuated total reflectance-Fourier transform infrared microspectroscopy of Cu(II) complexes with reduced dextran derivatives, *Russ. J. Phys. Chem.* 83(9) (2009) 1520–1525.
- [54] Ž. Mitić, M. Cakić, G. Nikolić, Fourier-Transform IR spectroscopic investigations of Cobalt(II)-dextran complexes by using D<sub>2</sub>O isotopic exchange, *Spectroscopy Int. J.* 24(3, 4) (2010) 269–275.
- [55] Ž.J. Mitić, G.S. Nikolić, M.D. Cakić, R.S. Nikolić, Lj.A. Ilić, The investigation of Co(II)–dextran complexes, *Chem. Ind. (Serbia)* 61(5) (2007) 257–262.
- [56] Ž. Mitić, M. Cakić, Pharmaceutically important complex compounds of some microbial exopolysaccharides, *Acta Medica Medianae* 53(4) (2014) 54–63.
- [57] M. Cakić, G. Nikolić, Lj. Ilić, FTIR spectra of iron(III) complexes with dextran, pullulan and inulin oligomers, *Bull. Chem. Technol. Macedonia* 21(2) (2002) 135–146.
- [58] M. Cakić, D. Cvetković, K. Stojanovski, P. Premović and M. Ristova, Spectroscopic study of polynuclear complex of iron(III) with hydrogenated dextran, *Spectrosc. Lett.* 9(7) (1994) 1437–1448.

- [59] V.P. Kiselev, V.P. Komar, I.V. Skornyakov, S.P. Firsov, A.D. Virnik, R.G. Zhbakov, Spektroskopicheskoe issledovanie razlichnih strukturnih modifikacij dekstrana, *Vysokomolek. Soedin. Serie A* 19(8) (1977) 1867–1872.
- [60] V. Seidl, O. Knop, M. Falk, Infrared studies of water in crystalline hydrates, *Canad. J. Chem.* 47 (1969) 1361–1368.
- [61] B. Berglund, J. Lindgren, J. Tegenfeldt, On the correlation between deuteron quadrupole coupling constants, O-H and O-D stretching frequencies and hydrogen bond distances in solid hydrates, *J. Mol. Struct.* 43 (1978) 179–191.
- [62] M. Kačurakova, R.H. Wilson, Developments in mid-infrared FT-IR spectroscopy of selected carbohydrates, *Carbohydr. Polym.* 44 (2001) 291–303.
- [63] S.Y. Lin, M.J. Li, W.T. Cheng, FT-IR and Raman vibrational microspectroscopies used for spectral biodiagnosis of human tissues, *Spectroscopy* 21 (2007) 1–30.
- [64] Z. Mousia, I.A. Farhat, M. Pearson, M.A. Chesters, J.R. Mitchell, FTIR microspectroscopy study of composition fluctuations in extruded amylopectin–gelatin blends, *Biopolymers (Biospectroscopy)* 62(4) (2001) 208–218.
- [65] W. Yu, L. Xiong, Effect of various morphology and testing conditions on fiber infrared spectrum, *J. Appl. Polym. Sci.* 96(4) (2005) 1003–1010.
- [66] N. Gierlinger, M. Schwanninger, The potential of Raman microscopy and Raman imaging in plant research, *Spectroscopy* 21(2) (2007) 69–89.
- [67] D. Chenery, H. Bowring, Infrared and Raman spectroscopic imaging in bioscience, *Spectrosc. Europe* 15(4) (2003) 8–14.

---

# Fourier Transform Infrared and Two-Dimensional Correlation Spectroscopy for Substance Analysis

---

Yew-Keong Choong

Additional information is available at the end of the chapter

<http://dx.doi.org/10.5772/66584>

---

## Abstract

The development of Fourier transform infrared (FTIR) has had widened its scope of perspective application on different types of substances in terms of technique of material analysis and identification. The tri-step infrared analysis has shown its powerful application in the analysis and interpretation of spectra from pure compound, fraction, raw material, natural product and complex mixture.

**Keywords:** Fourier transform infrared, pure compound, fraction, raw material, natural product, complex mixture

---

## 1. Introduction

### 1.1. Types of infrared spectrometer: dispersive and Fourier transform

Dispersive spectrometer has been described as a traditional way in the transformation of Fourier transform infrared (FTIR) spectrometer [1]. The basic function of dispersive spectrometer using diffraction gratings or prisms is to disperse the radiations with wave numbers at several positions. The moving of the gratings is the key that allows the radiations with wave numbers over a short interval of irradiation into the detector. Normally, the spectrum of a sample is created by the ratio between the beam passing through the sample and the reference or background. In comparison, Fourier transform infrared (FTIR) spectrometer is more sensitive and accurate in detecting and determining the higher signal-to-noise ratio within a short period of time. The principle of FTIR is generation of interferogram from the interferometer of the radiation produced by the source. Detecting the signal of radiations with different wave numbers by the Fourier transform to determine frequency domain instead of time domain will enhance the spectrum. In this way, the performance of modern

---

FTIR is advantageous compared with dispersive spectrometer. FTIR also simplifies the complex algorithm into presentable data and is user-friendly.

The development of numerous sampling accessories, such as attenuated total reflection (ATR), sample cell with different window material for liquid sample, 2DIR sample cell etc., widens the utility of FTIR for multi-sample type analysis. Therefore, the origin of the sample material has no barrier for FTIR, albeit the different objectives of the investigation. In fact, FTIR has been recognised as a rapid, direct and non-destructive analytical method. The challenge confronting FTIR is the interpretation of the qualitative or quantitative spectral data from different direction of view.

Factors that influence the frequency vibration mode of a polyatoms molecule included concentration, thermal, time and chemical reaction. This so-called perturbation is an additional input manipulating the vibration mode of the functional group. Typically dominating the motion of the molecules in the normal mode are only one or few groups which vibrate relatively. The establishment of two dimensional correlation spectroscopy via appropriate perturbation on mid-infrared could be used to enhance the detail of infrared spectrum interpretation.

## 2. Fourier transform infrared spectrum and 2DIR correlation spectroscopy for pure compound analysis

This is the conventional and most widely used spectroscopy in functional group determination. For a known pure compound, each peak of spectrum will identify the main functional group within the specific range of wave number. The matching of peaks in spectrum of unknown and known compound is commonly used as a complimentary analytical method besides LCMS and NMR. Hence, such evidences of compound structure configuration are reliable. Software library incorporated into the system plays a main role in authentication of the compounds. **Figure 1** showed the one dimensional Fourier transform infrared spectrum of delphinidin-3-*O*-sambubioside in the range of 4000–400  $\text{cm}^{-1}$ .

The 2DIR correlation spectroscopy on pure compound needs to be presented in the form of synchronous and asynchronous spectra [2]. Synchronous spectrum is developed by combination and accumulation of two spectra of the same substance scanned under perturbation. The most commonly used perturbation is the thermal perturbation which supplies the heat at a range of temperature such as 50–120°C, and this supposedly provokes the vibration mode of the relevant bonds. The 2DIR spectra of pure compound, which represents the active sites of different bonding in the molecule, reacts to the heat simultaneously. The region of peak detected on the diagonal positively formed is named as autopeak. It is possible for the autopeak to increase or decrease during the thermal supply phase. The abundance part of 2DIR spectrum is the crosspeaks that are not scattered on the diagonal. They are either positive or negative, depending on the combination of increased or decreased spectral peak from both axes. In term of correlation, the correlation square

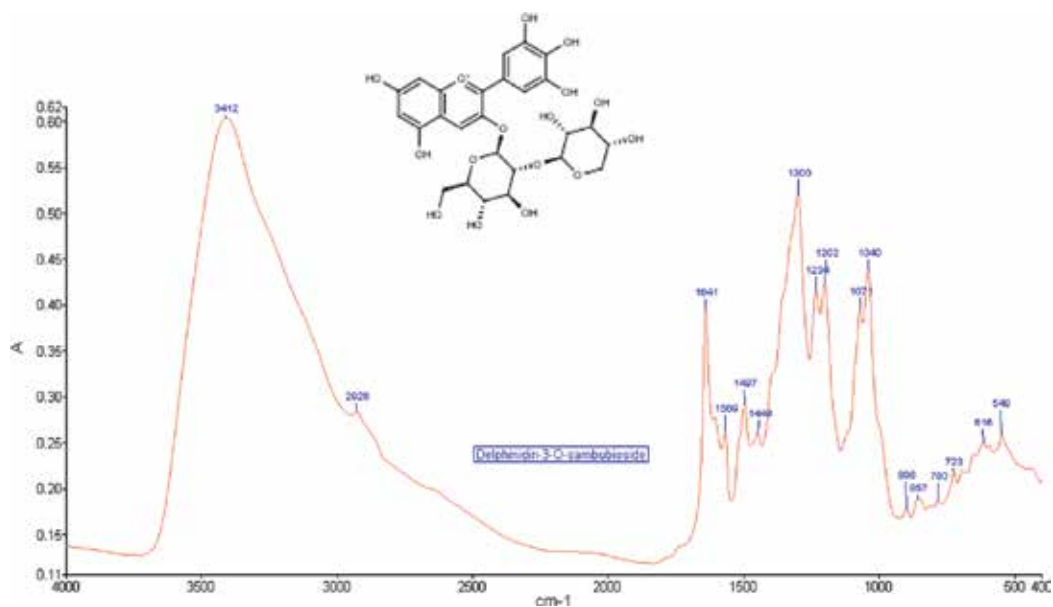


**Figure 1.** The 1D FTIR spectrum of the pure compound delphinidin-3-O-sambubioside in the range of 4000–400  $\text{cm}^{-1}$ . The appearance of Absorbance is transferred from 51.2% of transmission with the threshold of one. Most of the peaks are sharp and in various intensities depending on the absorption of each functional group under the wave number in the range of mid-infrared. The peak at 3412  $\text{cm}^{-1}$  is assigned to –OH group. Methyl group could be determined by peak 2928  $\text{cm}^{-1}$ . These two peaks are common and normally appear in all the organic material. The range from 1700  $\text{cm}^{-1}$  downward is the specific and important range for different characteristic of each compound., e.g. peak 1641  $\text{cm}^{-1}$  refers to amide I for bonding C-O, etc.

existing on certain autopeaks and crosspeaks is the best way to interpret the correlation circumstances during the perturbation. The asynchronous spectrum was created on region not related to synchronous spectrum. The Noda's rules [3] are abided during the interpretation data process.

**Figure 2** showed the synchronous and asynchronous spectra of delphinidin-3-O-sambubioside in the range of 1700–700  $\text{cm}^{-1}$ .

## 2.1. Important usage of FTIR and 2DIR correlation spectroscopy in pure compound

### 2.1.1. Qualification analysis for special functional group in the compound

Pure compound has the capacity to show the whole corresponded bond taking part in the infrared transmission. The vibration mode of the whole molecule will be determined under the specific assignment. Pure compound normally shows many sharp peaks compared to compound with low purity. This concept is ideal for qualification and the respective peaks are used to identify each component in the molecule itself. In some way, the selective range of particular peak could be used in quantification under the Beer's Law using the spectrum Quant software [4].

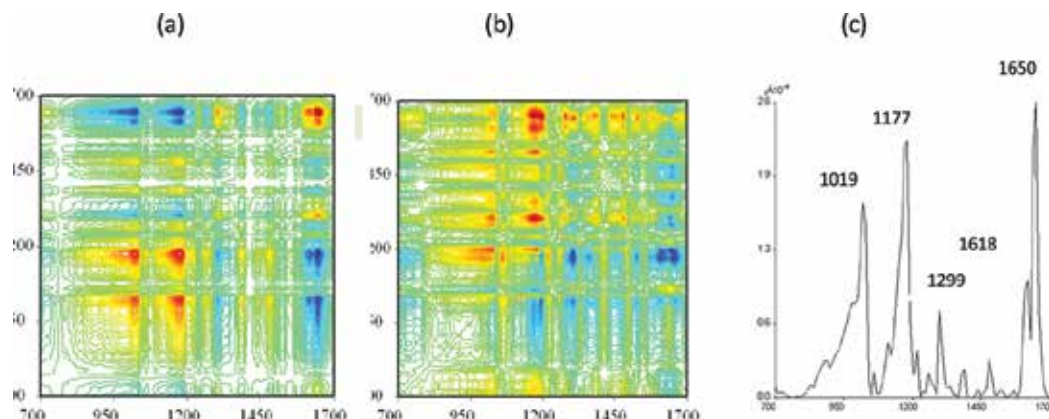


**Figure 2.** The 2DIR spectra of delphinidin-3-O-sambubioside in the range of 1700–700  $\text{cm}^{-1}$ . (a) Synchronous spectrum. The correlation square is created from negative crosspeak at (1177, 1650), autopeak 1650  $\text{cm}^{-1}$ , negative crosspeak (1650, 1177) and autopeak 1177  $\text{cm}^{-1}$ . There is another bigger correlation square which is created from negative crosspeak (1019, 1650), autopeak 1649  $\text{cm}^{-1}$ , negative crosspeak (1650, 1019) and autopeak 1019  $\text{cm}^{-1}$ . A smaller correlation square is created from four red areas. They are positive crosspeak (1019, 1177), autopeak 1177  $\text{cm}^{-1}$ , positive crosspeak (1177, 1019) and autopeak 1019  $\text{cm}^{-1}$ . (b) Asynchronous spectrum. The positive crosspeak at (1177, 1650) determines the sequence action against perturbation of the area at 1650  $\text{cm}^{-1}$  first reacted than area at 1177  $\text{cm}^{-1}$ . The similar scenario for the bigger correlation square where the peak area at 1650  $\text{cm}^{-1}$  reacted first than area at 1019  $\text{cm}^{-1}$ . When compared with the area at 1019  $\text{cm}^{-1}$  and 1177  $\text{cm}^{-1}$ , 1019  $\text{cm}^{-1}$  is reacted first than 1177  $\text{cm}^{-1}$ . The sequence of decrease reacted to the thermal perturbation in The series is 1650  $\text{cm}^{-1}$ , 1019  $\text{cm}^{-1}$ , 1177  $\text{cm}^{-1}$ . (c) The autopeak spectrum of the 2DIR.

### 2.1.2. Identification of the functional groups present in unknown pure compound

In identification of new compound by micro-fingerprinting via spectroscopy, this robust technique can be used to obtain useful information in chemical analysis.

### 2.1.3. Correlation of main functioning group

Determination of correlation of main functioning group under autopeaks at diagonal line indicates another important interpretation that the bondings in the molecule react positively with mid-infrared. In addition, creating the correlation square among the autopeaks and the crosspeaks for pure compound is advantageous using 2DIR correlation spectroscopy interpretation of inter-molecule.

### 2.1.4. Quantification study for the sample

The innovative Quant software specific for quantification under mid-infrared is another scope of investigation. The standard compound with different concentration is the conventional method for plotting the standard graph. The new version of Quant software has either the single peak or the range of wave number chosen for the quantification compatible under the standard graph. The single peak is chosen for crude extract spectrum as the way to eliminate the interruption of enormous overlapping vibration mode from uncertain components, while the range of wave number is the best tool for purified compound.

### 3. Fourier transform infrared spectrum and 2DIR correlation spectroscopy for fractions analysis

Fraction is the intermediate stage of extraction and is situated between crude extract and pure compound. This level eliminates most of the debris, fibre and primary metabolites, and exportation of secondary metabolomics of therapeutic value.

The FTIR spectroscopy analyses with fractions are dependent on the condition of the material. There are two methods on the solid form of fraction, i.e. making a disc with powder KBr, or directly scan with ATR. However, the consideration must be taken on the coverage of wave number using different method. The first method will cover the whole range of wave number, while ATR only scans until  $650\text{ cm}^{-1}$ . The KBr method is able to detect more peaks compared to ATR method. Although ATR has its limitations, it is the best choice since in forming the original spectrum, and it is devoid of any problem in transmission percentage.

Liquid fraction is analysed using sample cell with different window material. The exploration of aqueous solution is restricted to any KBr matrix since the O-H bond affects the range around  $3600\text{ cm}^{-1}$ . The  $\text{CaF}_2$  matrix is appropriate for solution containing water, though the transmission is limited to below  $900\text{ cm}^{-1}$ .  $\text{BaF}_2$  has clearer transmission for acidic solution from  $800$  to  $400\text{ cm}^{-1}$ .

The differentiation spectra by another calculation in second derivative has been recognised and proven to be the most proper derivative to correct nonlinear baseline anomalies. The

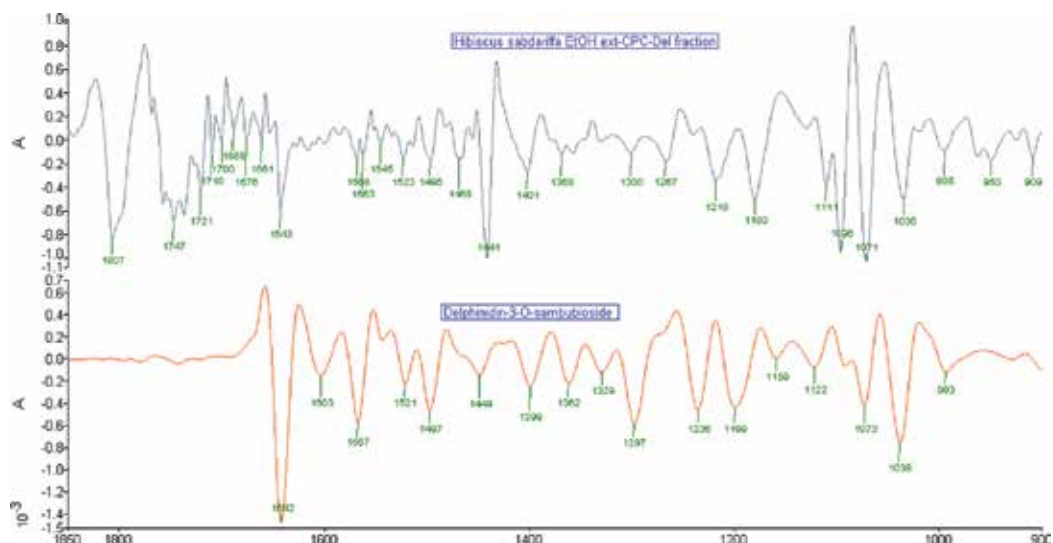


**Figure 3.** Second derivative spectra of CPC delphinidin fraction of *H. sabdariffa* ethanol extract in the range of  $1850\text{--}900\text{ cm}^{-1}$ . There are 10 base peaks which are compatible when matching the peaks from fraction and the pure compound. The correlation between the fraction and the compound is 0.52. The base peak of the fraction within  $1807$  and  $1643\text{ cm}^{-1}$  does not appear in the spectrum of delphinidin-3-O-sambubioside, since these could be the natural substances of *H. sabdariffa*.

compression of peaks at a single point could be expressed in wider wave number with second derivative. This is crucial as a fraction may consist of more than one compound. The problem of overlapping in 1D FTIR spectrum is caused by similar stretching of vibration mode from different compounds or numerous identical peaks from isomers. It is possible that peak forming in 1D FTIR is due to the combination of closer transmission and clumping together as one. Therefore, the reading on second derivative spectrum is indicative of several aspects initially based on the condition of the fraction.

**Figure 3** showed the second derivative spectrum of *Hibiscus sabdariffa* L ethanol fraction purified by HPLC preparative in the range of 1850–900  $\text{cm}^{-1}$ .

### 3.1. Important usage of FTIR and 2DIR correlation spectroscopy in fractions

#### 3.1.1. Investigation of the quality of extraction and isolation

The spectrum of a fraction could be different when compared with the pure compound. A fraction is actually the specific range of peaks chosen from the crude extract chromatogram. Technical experience of the operator will help to determine the nature of the fraction as a single or mixed compound. The pattern of the fraction can be authenticated as macro-fingerprint of the identified material. In fact, each fraction has a specific spectral pattern depending on the quality of extraction. A sample may exhibit different pattern of spectrum when different method of extraction is implemented. For example (**Figure 4**), the pattern of *H. sabdariffa* raw material spectrum showed 20% dissimilarity with *H. sabdariffa* ethanol crude extract when both spectral relatively correlated with spectrum of residue. The fraction of *H. sabdariffa* spectrum showed content of anthocyanins at the peak 1071  $\text{cm}^{-1}$  and the pattern is completely different from the anthocyanin pure compound. Hence, the spectrum of material can be used to estimate the quality of extraction and purification. Assignment of peak in spectrum is an alternative method for identification of the main compounds in the fraction isolated from HPLC preparative. The spectrum of fraction has the higher percentage of similarity with pure compound compared with extract. The quality of extraction from the raw material and compound can be clearly discerned monitored by spectroscopy.

#### 3.1.2. Detection of enriched compound

Most of the herbal medicinal products in the market are in the form of fraction. The possibility of the presence of enrich compound added in these products can be detected by FTIR and 2DIR. The concentration of certain active compounds in standard extract is the guide to the formula. Examining this kind of distinctive criteria could be carried out by quantification using spectrum Quant. The plotting of the straight line with various dosage of standard compound is typically prophetic on the targeted compound concentration in the fraction. Normally, the specific spectrum peak has to be determined accordingly because there are procedures for peak selection instead of using the whole spectrum.

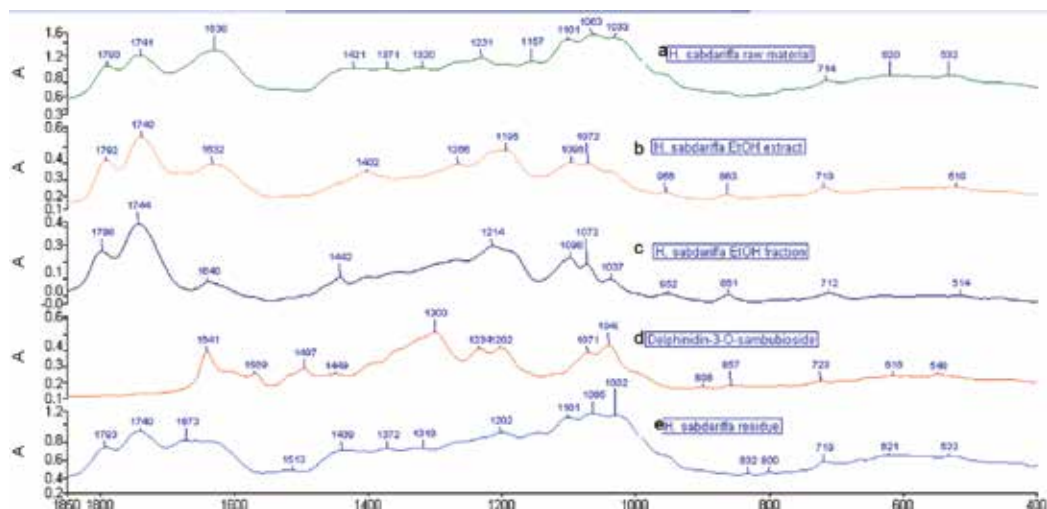


**Figure 4.** FTIR spectra of *H. sabdariffa* sample material in the range of 1850–400  $\text{cm}^{-1}$  from different level of extraction (a) *H. sabdariffa* raw material. The whole spectrum is divided into three areas and represented most of the primary metabolism. The first three peaks started from peak 1790  $\text{cm}^{-1}$  and is unique for this plant. Peak 1741  $\text{cm}^{-1}$ , assigned for C–O bonding, normally refers to ester components, while peak 1630  $\text{cm}^{-1}$  refers to amide I. There is no amide II bonding, since the range from 1500 to 400  $\text{cm}^{-1}$  consisted of the bonding for fatty acid and carbohydrate. (b) *H. sabdariffa* ethanol extract. The first three peaks are still maintained except peaks in the range of 1500–1000  $\text{cm}^{-1}$  are replaced by few new peaks. Intensity of peak 1632  $\text{cm}^{-1}$  is reduced and peak 956  $\text{cm}^{-1}$  and 863  $\text{cm}^{-1}$  appear and are not found in raw material spectrum. (c) *H. sabdariffa* Centrifugal Partition Chromatography (CPC) delphinidin fraction. The curve between the peak 1214  $\text{cm}^{-1}$  and 1098  $\text{cm}^{-1}$  is getting wider. The intensity of peak 1640  $\text{cm}^{-1}$  and 1037  $\text{cm}^{-1}$  is getting lower compared to the raw. But the peak 1073  $\text{cm}^{-1}$  and 1037  $\text{cm}^{-1}$  which matched with delphenidin-3-*O*-sambubioside are sharp in appearance. (d) Delphenidin-3-*O*-sambubioside pure compound. There are only three peaks that matched with *H. sabdariffa* fraction and two with *H. sabdariffa* ethanol extract. (e) The *H. sabdariffa* residue. The peak 1640  $\text{cm}^{-1}$  is lost and 89% of the spectrum correlated with raw, 69% correlated with extract, and 47% correlated with fraction. Only 11% of the content is extracted from the raw material.

### 3.1.3. Investigation of adulterant in commercial products with similar molecular weight but different structural configuration

The differences could be the pattern of spectrum or the absence or the presence of strangle peak in 1D FTIR. Second derivative is an alternative to detail the differences, but the most powerful is the 2DIR correlation spectroscopy. Tri-step macro-fingerprint infrared method is also able to enhance the discrimination and distinguish the real product.

### 3.1.4. Determination of halal and non-halal food

Since in the fraction or extract, the main components can be easily mixed up with other ingredients in food, the challenge to separate halal and non-halal food through spectroscopy is choosing the proper range of wave number for comparison. **Figure 5** showed the example of determination of halal food with 2DIR.

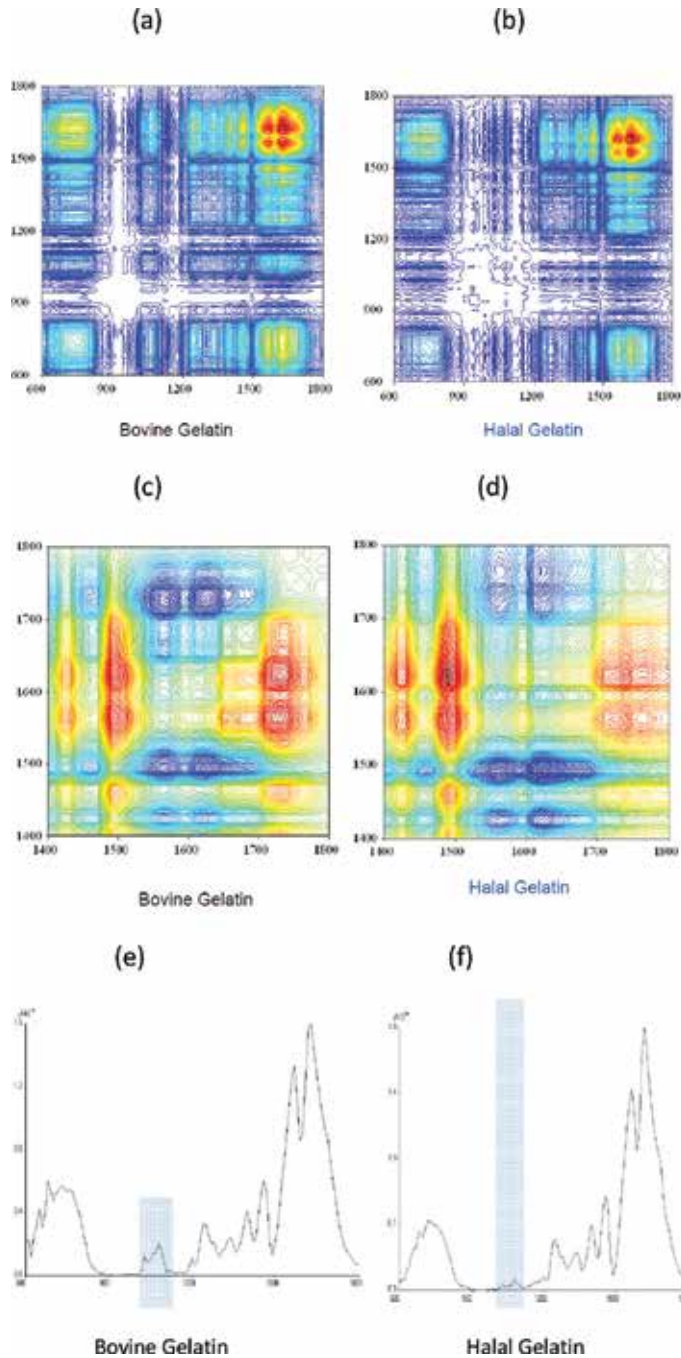


**Figure 5.** Comparison of bovine gelatin and halal gelatin using 2DIR. (a) Synchronous spectrum of bovine gelatin in the range of 1800–600  $\text{cm}^{-1}$ . The higher intensity in the area of 1100–1000  $\text{cm}^{-1}$  compared to spectrum of halal gelatin. (b) Synchronous spectrum of halal gelatin in the range of 1800–600  $\text{cm}^{-1}$ . (c) Asynchronous spectrum of bovine gelatin in the range 1800–1400  $\text{cm}^{-1}$ . The differences with halal spectrum are the intensity of the crosspeaks at (1480, 1625), (1572, 1733) and (1620, 1733) is more intense. (d) Asynchronous spectrum of halal gelatin in the range of 1800–1400  $\text{cm}^{-1}$ . (e) The autopeak spectrum of bovine gelatin in the range of 1800–600  $\text{cm}^{-1}$ . (f) The autopeak spectrum of halal gelatin in the range of 1800–600  $\text{cm}^{-1}$ .

### *3.1.5. Elaborate the correlation of the main compounds with 2DIR in the fraction*

The fraction spectrum profile of the pure compound usually shows the quality of extraction. The majority of the debris, precipitate and high fibre content has been discarded. The elaboration on the main compound that reacted and correlated in the overall profile of the spectrum could be clearly shown by 2DIR correlation spectroscopy. The exploration of the main compounds in the fraction increases the degree of the correlation and less problematic compared with crude extract.

## **4. Fourier transform infrared spectrum and 2DIR correlation spectroscopy for raw material analysis**

Application of the new method of FTIR and 2DIR on raw material is still raising doubt due to the severely overlapping of peak making interpretation difficult. The detected peak could be due to more than one compound with similar assignment. Methods must be developed to ensure the assignment is interpreted correctly. In real life, raw material can be analysed using FTIR and 2DIR which will indirectly reduce the time for sample preparation. It is convenient in term of preparation and conserves the majority of the raw content.

Traditional Chinese medicines are the primer study model as raw material in the dried form using FTIR and 2DIR [5]. The difficulties, besides the problem of overlapping assignment, also include searching the main compounds which may coincide with the raw material spectrum. This kind of matching is reliable if the sufficient literature background on the raw material exists. Despite interruption of the 1D FTIR spectrum on raw material by mixture of compounds, the spectrum can be confirmed when 60% or more transmission is achieved with KBr. The second derivative is mandatory for the raw material spectrum. Modification on the derivative of spectrum shows that second derivative is the most appropriate for exploring the spectrum since the diagram is easily interpreted. In addition, the 2DIR correlation spectroscopy is another step to enhance the detail of the spectrum for detailed interpretation. Therefore, the tri-step analysis combine method, which involves stepwise progression from the superficial to high level of analysis, is advantageous for raw material using the mid-infrared spectroscopy analysis.

### **4.1. The advantages of FTIR and 2DIR for raw material**

#### *4.1.1. Reduction in sample preparation steps*

Raw material from natural product has to be dried completely and pulverised before making disc with KBr. In FTIR and 2DIR analysis, the sample preparation process is simple. Since the presence of moisture in the environment affects the FTIR processing method, it is necessary to use dehumidifier to maintain the dryness of the environment.

#### *4.1.2. Rapid*

By simplifying complicated preparation steps, analysis of raw material is rapid and direct. The analysis of the spectrum with air as background could be performed immediately after the infrared scanning. The pattern of each raw material will possess footage for the identifica-

tion. Each raw material will be able to show the first image of its content under the scanning. The fingerprint of the original raw material will further confirm the material profile.

#### 4.1.3. No-destructive method and conserve the material information

A raw material conserves most of the natural contents except when contaminated with pollutants. The vulnerable step in the raw material processing is grinding, sufficiently drying and sieving with at least 200 mesh of sieve. However, these are considered less destructive when compared with further extraction on the raw material. In fact, the raw material can be tested under ATR which does not require a disc. The interferon beam has a glimpse of refraction on the sample with diamond platform and produce spectrum in the range of 4000–650  $\text{cm}^{-1}$ . Comparison of the *H. sabdariffa* raw material spectrum performed with KBr and ATR, respectively, is shown in **Figure 6**.

#### 4.1.4. Interpretation of poly-nutrient in crude

When the whole profile of the raw material is presented with spectra especially in 2DIR, the correlation square generated under the perturbation is based on the active compounds responding concurrently. Such response is associated with a variety of compounds found in the raw extract. Information derived from such interpretation is vital as it provides a holistic picture of the reaction. **Figure 7** showed the correlation square formed between flavonoids peak and carbohydrate peak in *H. sabdariffa* raw material 2DIR synchronous spectrum.

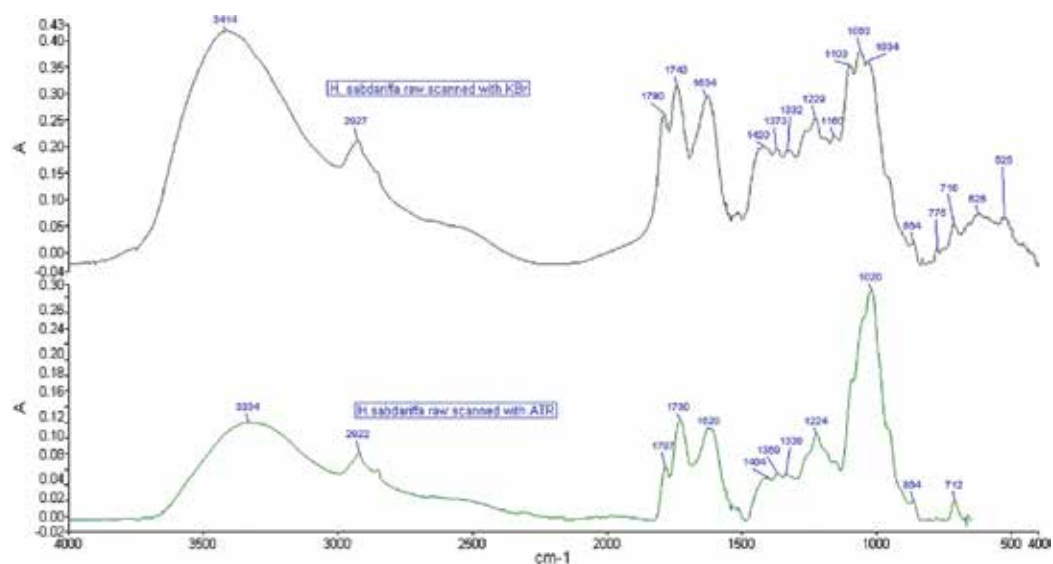


**Figure 6.** 1D FTIR spectra of *H. sabdariffa* raw material scanned by two analysis methods. First spectrum is produced by mixing the Kbr powder with *H. sabdariffa* raw powder dried sample in the ratio 200:1. The range of the spectrum is maximised from 4000 to 400  $\text{cm}^{-1}$ . Second spectrum is background with air and the raw material was placed on a diamond platform under ATR method. The range of spectrum is achieved till 650  $\text{cm}^{-1}$ , while the spectrum from 650  $\text{cm}^{-1}$  to 400  $\text{cm}^{-1}$  is lost. More number of peaks is observed under KBr method. However, ATR method is simpler since no disc is needed.

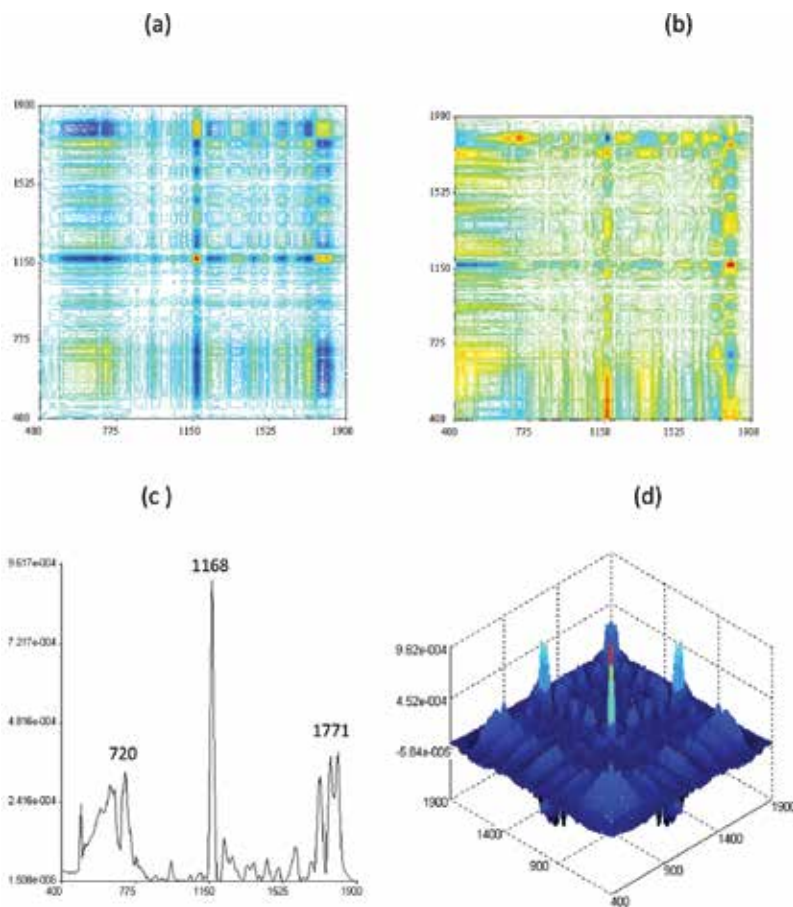


**Figure 7.** 2DIR spectra of *H. sabdariffa* water extract with Trifluoroacetic acid (TFA) in the range of 1900–400  $\text{cm}^{-1}$  from Selangor, Malaysia. (a) Synchronous spectrum. Three correlation squares are formed which are correlated with the C-O bond from ester group with carbohydrate group. They are negative crosspeak (720, 1771), 1771  $\text{cm}^{-1}$ , negative crosspeak (1771, 720) and 720  $\text{cm}^{-1}$ ; positive crosspeak (1168, 1771), 1771  $\text{cm}^{-1}$ , positive crosspeak (1771, 1168) and 1168  $\text{cm}^{-1}$ ; negative crosspeak (720, 1168), 1168  $\text{cm}^{-1}$ , negative crosspeak (1168, 720) and 720  $\text{cm}^{-1}$ . The spectrum indicates the holistic view of perturbation reaction of the different types of compound in the water crude extract. (b) Asynchronous spectrum. The sequence of reacted decrease as determined by Noda's rules under the thermal perturbation between 30 and 120°C with 10°C interval degree, i.e. 1171  $\text{cm}^{-1}$ , 1168  $\text{cm}^{-1}$ , 720  $\text{cm}^{-1}$ . (c) Autopeak graph. (d) 3D spectrum. The colour in dark blue illustrates the negative peak facing downward from plane.

#### 4.1.5. Standardised method for authentication of a raw material derived from natural product

The origin of the raw material in certain commercial medicinal products is difficult to be authenticated especially when they are presented as powder. Such products could be a portion of plant or other types of organism. Screening of the powder using KBr or ATR method will elucidate its chemical profile as the spectrum will confirm the origin as well as the purity. The compendium and monograph of herbal plants should include the spectrum as one of the methods in the authentication of medicinal products.

## 5. Fourier transform infrared spectrum and 2DIR correlation spectroscopy for natural product analysis

Analysis of natural product with FTIR and 2DIR have to confront with the obstacles coming from the natural texture of the subjects, since their contents consist of water in living cells found leaf, fruit, stem, flower, seed or fruiting body, stalk and sclerotium from medicinal mushroom. The spectroscopy analysis of natural product needs to avoid the interrupting H<sub>2</sub>O background and preserve the nature of the features. Therefore, the analysis must apply the correct method chosen as well as appropriate spectrum interpretation on natural product.

There are three choices of FTIR spectrum scanning for natural product. Firstly, mixture with KBr if the natural product is completely dried and without the need for further drying process, such as seed, some rhizome or hash portion of fruiting body. Secondly, ATR is the best choice if the sample is sensitive to the environment conditions when they are being removed or still contain water and mucous secretions. Even though there is a slight reflection on the sample surface through the diamond platform, the spectrum created is still sufficient to represent the actual profile when using air as a background. In comparison, the juice of the natural product containing water can be analysed using liquid sample cell with calcium fluoride window. The third method is the FTIR imaging attached to a microscope with a spectroscopy system. The combination enriches the scope of analysis and is more powerful and user-friendly.

No doubt that human error is unavoidable when dealing with natural product analysis. The content(s) may have been lost during the sample processing, poor quality of extraction, physical deterioration and extended period of storage. The more the natural content of the subject model is preserved, the more accurate it can be analysed. These kinds of natural product are found in Malay, Chinese [6] and Ayurvedic medicine such as medicinal mushroom. Many remedies in these communities contain ready to use formulae of the natural products for therapy, e.g. use of turmeric product [7] for blood clotting. FTIR is one of the methods to study the key chemical contents in such treatment.

### 5.1. Analysis of natural product and raw material

#### 5.1.1. *Appropriate for quantification of chemical marker analysis*

In order to determine the exact quantity of the chemical(s) involved in the treatment, the Spectrum Quant is especially effective for this purpose, using different concentrations of standards that will generate the range of spectra for the targeted compound. The other algorithms such as PCR+, PLS and Quant C can also be chosen depending on the respective objectives of the study. The results of analysing an unknown sample can be used to predict its concentration by comparing with the range of standards.

#### 5.1.2. *Exposure to various factors*

The original natural product is the best type of sample for chemical fingerprint profiling, maturity or storage period determination. Time factors such as oxidation, exposure to air, etc., could affect the whole experiment. The sample of natural product analysed using FTIR and 2DIR is prevented from the detrimental effects of these factors.

### 5.1.3. Determination of different geographical origin of natural product using principal component analysis or SIMCA

Natural product especially the medicinal plants and mushroom of different geographical origin would have a variety of chemical contents with respect to the quality and the quantity. Mean spectral data from randomly chosen plants from a plantation and those from individual plants can be compared. This kind of statistical value could be plotted using a software such as Assured ID which will provide overall comparison of the similar type of natural product collected from different geographical locations. The differences are due to factors such as different types of soil, water, weather, pH of the soil, water, etc. These factors will influence the distance and the percentage of rejection of SIMCA created by three principle components. **Figure 8** showed the example of SIMCA result of *H. sabdariffa* [8, 9] sample from two different locations in Malaysia.

#### Generate Model Summary

Number of problem materials with extreme samples : 2  
 Number of overlapped materials : 0

#### Diagnostic Report

##### Inter Material Distances

Material	JHR (J1-J35)	P,P (S1-S35)
JHR (J1-J35)	-	3.06

##### Classification Performance Report

Material	% Recognition rate	% Rejection rate
JHR (J1-J35)	97(101/104)	100(105/105)
P,P (S1-S35)	100(105/105)	100(104/104)

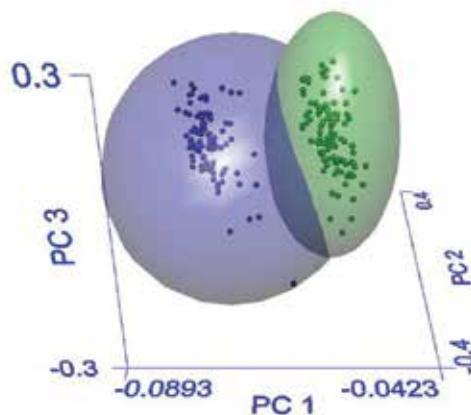


**Figure 8.** Statistic result checking with SIMCA on *H. sabdariffa* collected from two different locations in Malaysia. Thirty five plants were randomly selected from a plantation in Johor (JHR) and Penang (P.P) where there are separately 340 km away. The fruits from each plant were collected in different net bag. Thirty-five net bags of *H. sabdariffa* fruits from two locations were processed and produced the pulverised dry powder for the ATR spectroscopy method. Two locations of samples spectrum were grouped in the software Assure ID with triplicates. The result showed that there are some factors caused the samples from two locations was successfully discriminated with the inter-material distance 3.06. Two spheres sharp of diagrams created ever combined at a portion that joined them together under Principal Component (PC) 1, 2 and 3. The conclusion is the samples from two different locations are different in term of some factors such as water, weather, air, soil, but they still contain certain factors that they are having the same. The data produced can be used for further prediction for geographical origin of the unknown sample.

## 6. Fourier transform infrared spectrum and 2DIR correlation spectroscopy for complex mixture analysis

Today, use of combo medicinal contents has been reported to be more efficient compared to single compound when treating viral diseases. Research on the effects of combination of different substances has been reported *in vitro* and *in vivo*. This method is claimed to be

effective against mutating virus. Several medicinal products are known to kill selectively and prevent the spread of the infection virus. Many possibility of combination of medicinal products exist [10], e.g. raw and the fractions, fractions from different plants, fractions plus compound and raw with compounds. Identification of this kind of the contents in this type of combination is not a priority as long as the efficacy is enhanced and patient acceptance is good. On the other hand, analysis of the interaction of components in the combination is crucial to generate information for the design of new medicinal product in future. The 2DIR correlation spectroscopy plays a vital role in the combo medicine interpretation.

### **6.1. Difficulty in interpretation**

Analysis of the complex mixture of samples required pre-knowledge of the main compounds involved. The addition of different types of standards is needed to determine the assignment of bond in 1D FTIR. There could be no actual matching of standards peak with the complex mixture because of the overlapping and interruption of the bonds from each other. Consequently, more standards or fractions need to be used for different scope of comparison. The additional library in the software could be helpful in this aspect. When the peaks have been confirmed, then the next step will be carried out as usual. The 2DIR with synchronous spectrum is the best option to investigate the interaction of mixture under the appropriate perturbation.

### **6.2. Level of sensitivity**

It is often difficult to address the interaction of a mixture as it may contain totally dissimilar types of compounds. However, they can react concurrently when perturbation is applied. The degree of sensitivity, either from the user or the system is very much relied on the experience and practice, e.g. two possible interpretations based on the similar spectrum. Therefore, the analysis on the mixture with FTIR and 2DIR must be accurate and detailed initially to prevent subsequent misinterpretation.

### **6.3. Strengthening of data**

It is not advisable to use the asynchronous spectrum in 2DIR for the mixture due to the tremendous overlapping of assignment which is confusing. Other types of data generated from HPTLC, HPLC, GCMS, LCMS and NMR could be additional evidences for mixture complex analysis.

## **7. Limitations of FTIR and 2DIR**

FTIR and 2DIR technique used in analysis has their limitations that could reduce the degree of efficiency. Fractions in solution form are not eligible for 2DIR analysis except using liquid sample cell, since special sample cell is needed to create high temperature changes and the rate of evaporation of the natural product solution is unknown. However, liquid sample cell is expensive. Besides, there is no appropriate FTIR equipment to capture the changes of spectrum within a few seconds, such as oxidation from the natural product. The thermal perturbation is commonly utilised for analysis of different substances and difficult to interpret compound with more than

one isomers structure. However, no standardise method exist to determine the degree of peak differences. Some researchers agree that the range 2–3  $\text{cm}^{-1}$  is for detecting the pure compound and the fraction, while the range 5–8  $\text{cm}^{-1}$  is for the raw material and other materials. However, the acceptance of these ranges is still debatable. Lastly, there will be confusion on spectra for comparison when the quality of extraction is not the same especially the fractions.

## 8. Conclusion

In conclusion, much research on FTIR and 2DIR is still ongoing in order to overcome the various limitations confronting their widespread use. With accumulated experience and sophisticated innovation such as imaging microscope connect to FTIR, the techniques will be improved and enhanced in the near future.

## Acknowledgements

We would like to thank the Director General of Health of Malaysia for his permission to publish this article and the Director of Institute for Medical Research (IMR), Kuala Lumpur for the support of this project. This work was financially supported by the NKEA AGRICULTURE (EPP#1), NKEA Research Grant Scheme (NRGS) (Grant No: NH1014D060). The author also thanks Dr. Aswir (IMR), Dr. Hussin (IMR) and Dr. Lee Han Lim (IMR) for critically reviewing this paper and technical support from Perkin Elmer Sdn Bhd. (Malaysia). The previous support of Islam Development Bank (IDB) for training in FTIR and 2DIR under the Merit Fellowship is gratefully acknowledged.

## Author details

Yew-Keong Choong

Address all correspondence to: [yewkeong@imr.gov.my](mailto:yewkeong@imr.gov.my)

Phytochemistry Unit, Herbal Medicine Research Centre, Institute for Medical Research, Jalan Pahang, Kuala Lumpur, Malaysia

## References

- [1] Nakanishi K., Solomon P.H. *Infrared Absorption Spectroscopy*. 2nd ed. Holden-day, San Francisco. 1977.
- [2] Noda I, Ozaki Y. *Two-Dimensional Correlation Spectroscopy Application in Vibrational Optical Spectroscopy*, Hohn-Wiley and Sons Ltd. Chichester, West Sussex. 2004.
- [3] Noda I. 2DCOS and I. Three decades of two-dimensional correlation spectroscopy. *Journal of Molecular Structure*. 2016;1124: 3–7.

- [4] Product Note, Spectrum Quant Quantitative Analysis Software. PerkinElmer, Inc. Waltham, MA, USA. (2014) [www.perkinelmer.com](http://www.perkinelmer.com).
- [5] Sun S.Q., Zhou Q. Atlas of Two-dimensional correlational Infrared Spectroscopy for Traditional Chinese Medicine Identification, Chemical Industry Press, Beijing, 2003.
- [6] Wu Y.W., Sun S.Q., Zhou Q., Tao J.X., Noda I. Volatility-dependent 2DIR correlation analysis of traditional Chinese medicine "Red Flower Oil" preparation from different manufacturers. *Journal of Molecular Structure*. 2008;882;107–115.
- [7] Aggarwal B.B. Curcumin-free tumeric exhibits anti-inflammatory and anticancer activities: Identification of novel components of tumeric. *Molecular Nutrition & Food Research*. 2013;57:1529–1542.
- [8] Norhaizan M.-E., Fong S.H., Amin I., Chew L.Y. Antioxidant activity in different parts of roselle (*Hibiscus sabdariffa* L.) extracts and potential exploitation on the seeds. *Food chemistry*. 2010;122:1055–1060.
- [9] Salem M.Z.M., Olivares-Perez J., Salem A.Z.M. Studies on biological activities and phytochemicals composition of *Hibiscus* species-A review. *Life Science Journal*. 2014;11(5):1–8. (ISSN:1097-8135). <http://www.lifesciencesite.com>.
- [10] Sun S.Q., Chen J.B., Zhou Q. Infrared Spectroscopy for Complex Mixtures, Chemical Industry Press, Beijing, 2011.

---

# Fourier Transform Infrared Spectroscopy in the Study of Hydrated Biological Macromolecules

---

Maria Grazia Bridelli

Additional information is available at the end of the chapter

<http://dx.doi.org/10.5772/66576>

---

## Abstract

The interaction between biological macromolecules (proteins, nucleic acids, lipids and other biomolecules in the cell) and environmental water is an important determining factor in their conformational properties, stability and function. The hydration processes of biopolymers have been extensively studied in the past 20 years with reference to a considerable variety of models and concepts. In all recent works, a distinction is made between intracellular water that maintains the ordinary liquid state (bulk water) and water ordered in extended hydrogen-bonded lattices at the surface and structured in the internal grooves of macromolecules (hydration water) in dependence on the chemical properties of the macromolecule surface. FTIR spectroscopy has been implemented in this field both for the sensitivity in the conformational analysis of biological macromolecules and the reliability in the investigation of the water network. A perturbation technique such as dehydration-rehydration treatment modifies the macromolecule structure and water distribution. It was applied to two structurally different proteins: lysozyme, a globular ( $\alpha + \beta$ ) protein and collagen, a fibrous protein characterized by the triple helix structure. Submitted to the treatment both of them display irreversible conformational changes.

**Keywords:** FTIR spectroscopy, biological macromolecules, hydration, adsorption isotherms, lysozyme, collagen

---

## 1. Introduction

Water controls and affects in large extent structure and function of biological macromolecules [1]. This unique molecule has had an essential role in the evolution of living systems, and its functions are manifold. At macromolecular level, very small water amount or small aggregates are fundamental both in the determination and maintenance of the biologically active

---

structure of proteins, nucleotides, carbohydrates and other biopolymers. The solvent organization around the solute macromolecule structures allows folding to the native and functional conformation and the development of many biological functions such as for example, substrate recognition and binding to an enzyme, protein subunits assembling and to originate and stabilize higher order structures such as membranes. A lot of biochemical reactions fundamental in metabolism and synthesis are involving water as universal reagent, such as hydrolysis, condensation, reduction and oxidation. Despite the great interest in the problem, the relationship between the biopolymer conformation and the structure of the water network cannot still be described with confidence. In the case of proteins, it is well-known that polypeptide molecules are surrounded in the cell by a hydration shell which can be described as formed by differently interacting water molecules organized in layers surrounding macromolecule. The simplified description of the hydration shells formed by a uniform layering of water molecules around the macromolecule is not realistic: most proteins, for example, offer a surface where binding sites, cleft or crevices provide favorable environments for solvent molecules. Such water molecules are organized in clusters or patches decorating the macromolecule surface and are called "bound" water due to the restricted mobility with respect to the water molecules in bulk. Orientation changes may be related to structural or conformational differences among macromolecules. The bond strength variety of bound water affects mobility, reorientation and vibrational properties [2–7].

A variety of experimental techniques were introduced and applied to study the hydration properties of biological macromolecules: DSC (differential scanning calorimetry), NMR (nuclear magnetic resonance), neutron and X-ray diffraction, gravimetric techniques, as well as UV-vis and CD spectroscopies have been employed to characterize the extent of water-biomolecules interaction. In addition, the problem of water interactions was object of theoretical analysis and structure prediction as well as molecular dynamics simulations.

Fourier transform IR absorption spectroscopy represents a powerful method to gain structural information on hydrated biological macromolecules, alternative to other well-established techniques whose application presents severe limitation to dry compounds or in the first hydration events. It requires a minimal sample amount and preparation, and it can be used in a wide variety of conditions and geometries. It enables to study (1) the amplitude and position changes of the main absorption bands associated with characteristic functional macromolecule groups, as a function of water content; (2) the properties of water structured around the biomolecules, using H<sub>2</sub>O molecules as probes to detect conformational changes in the macromolecule structure induced by water interactions [8].

H<sub>2</sub>O displays a strong IR spectrum with three main bands corresponding to the OH stretching, bending and libration modes. Their contribution can be identified in the spectrum of macromolecules and changes in the hydration conditions significantly influence the infrared spectral pattern. The spectral changes observed as a function of water removal may be monitored, correlated to the changes in macromolecule conformation and used to identify the sites of water sorption. The OH stretching band, in particular, by appropriate mathematic manipulation, can be used to build the water adsorption-desorption isotherms describing the hydration processes governing each water population.

The technique and the related experimental procedures were successfully applied in the past on two macromolecular systems very different in chemical composition and structure. Melanin and lipid array have been object of past publications [9, 10]. The present work is concerning two proteins, collagen and lysozyme, and their interaction with water.

## 2. Infrared spectroscopy of water

Water has a strong absorbance in the infrared [11–13]. The characteristic normal modes of the H<sub>2</sub>O molecule are due to vibrating O–H bond whose frequencies are critically dependent on the aggregation state of water: gas, liquid and solid. In the medium infrared wave number region (MIR), the isolated water molecule (gas phase) has three main normal modes of vibration. The symmetric and asymmetric OH stretching vibrations ( $\nu_1$ ,  $\nu_3$ ) have band maximum at 3656 and 3755 cm<sup>-1</sup> and the bending mode,  $\delta(\text{OH})$ , has the band center at 1594 cm<sup>-1</sup>. Upon formation of hydrogen bonds in the liquid phase and because of the broadening of the spectral features,  $\nu_1$  and  $\nu_3$  features are collapsing to a diffuse absorption band that appears 200–400 cm<sup>-1</sup> shifted towards high wave number region with respect to the gas phase values. In addition,  $\nu(\text{OH})$  band width at half-maximum (FWHM) will broaden as a consequence of the H bond pattern formation. In general, the more heterogeneous are the molecular environments of hydrogen-bonded molecules, the broader the band. For this reason, the liquid water spectrum is broader than that found for ice spectrum reflecting the vibrations of more selected hydrogen bond energies and configurations. The bending mode shifts towards high wave number region as a consequence of formation of hydrogen bonds: liquid water and ice display bending absorption bands at 1645 and 1670 cm<sup>-1</sup>, respectively. Libration modes  $\nu_L$  are other vibrational modes of condensed phase water. They appear at 685 cm<sup>-1</sup> for liquid water and shifts at 830 cm<sup>-1</sup> for ice. Moreover, an absorption band is observed around 2200 cm<sup>-1</sup>, centered at 2100 cm<sup>-1</sup> for liquid water and around 2255 cm<sup>-1</sup> for different phases of ice. It represents a combination band, due to the association of the bending  $\delta$  and libration  $\nu_L$  features.

### 2.1. OH stretching band ( $\nu(\text{OH})$ )

The IR OH stretching band has been widely studied to investigate the properties of water structured around biomolecules. The first pioneering work concerning the study of hydration water of globular proteins was performed by Buontempo, Careri and Fasella in 1972 by analyzing the differential Infrared band near 3300 cm<sup>-1</sup> in the spectrum of Lysozyme and Bovine Serum Albumin before and after dehydration under various conditions [14]. The study evidenced the presence of water molecules differently mutually interacting and with the protein surface, being possible to distinguish a contribution due to liquid water and a component corresponding to the so-called tightly bound water. In the following years, thanks to the implementation of the interferometric spectrophotometers instead of the dispersive one, measurements were performed with a much better sensitivity and reliability. The enhancement in the peak fitting procedures with help of second derivative operation and iteration procedures allowed to improve the qualitative picture by fitting the band into component sub-bands

related to different local H bonding structure. In the paper of Onori and Santucci [15] and Mallamace et al. [16], the best fit deconvolution of the band was performed in the study of, respectively, AOT hydrated micelles and lysozyme at different temperatures to investigate structural dynamical transitions.

Pure water  $\nu(\text{OH})$  band ( $3800\text{--}2800\text{ cm}^{-1}$ ) cannot be fitted by a single Gaussian line, but can be deconvoluted into components, usually assigned to different sets of molecules. Following the central limit theorem stating that the distribution of the sum (or average) of a large number of independent, identically distributed variables will be approximately normal, regardless of the underlying distribution, the component number could be enormously large. However, the structural constraints settled on the basis of the number and strength of hydrogen bonds in different arrangements avoids effects of overfitting, allowing the breakdown of the band up to a maximum of six sub-bands in dependence on the model assumed to describe water system. The structure of  $\nu(\text{OH})$  band is described in details by Schmidt and Miki [17] and directly related to the O-H bond lengths: variations in the bond lengths are caused by the influence of the surrounding hydrogen-bonded network of water molecules and affect position and width of the components bands. According to this view, from the higher wave number region towards the lower one, the first peak ( $3680\text{ cm}^{-1}$ ) can be attributed to monomer-like vibration, due to free O-H vibration of  $\text{H}_2\text{O}$  molecules behaving as in the vapor state. The three intermediate components contribute 85% to the total signal, indicating that the majority of water molecules have a local hydrogen-bonded network which includes 3–7  $\text{H}_2\text{O}$  molecules as confirmed by theoretical calculations. Solid clusters (6–10  $\text{H}_2\text{O}$ ) is responsible for the envelope of the two low wave number bands. The peak position of each band was related to O-H bond length. The values were calculated by transforming the frequency and full-width half-maximum values of the  $\nu(\text{OH})$  band components using Badger's rule [18].

In recent times, we have developed a technique operating the removal from the spectrum of the features due to the spurious vibrational bands unrelated to water by means of the operation of subtraction of the “dry sample” spectrum, i.e., the spectrum of the sample gently dehydrated to expel as much solvent as possible without affecting the molecule structure [9, 10, 19]. The cleaned band obtained by such procedure can be treated as a water  $\nu(\text{OH})$  band and therefore compared with the corresponding band of pure water and analyzed by deconvolution in component bands, each one related to different hydrogen bond engagements and lengths.

### 3. Experimental section

Infrared spectroscopy is an experimental technique able to detect the absorption of infrared radiation by the matter [20]. Characteristic vibrational states may be attained by the molecule at the frequencies characteristic for each component molecular group. They can be measured as an absorption spectrum, i.e., a plot of the absorbed intensity of the applied radiation, expressed as absorbance, as a function of its frequency, measured in terms of wave number ( $\text{cm}^{-1}$ ). The infrared spectrum is characteristic for any molecule to such an extent that it may

be considered the molecule fingerprint. For a molecule that consists of  $N$  atoms, there are  $(3N-6)$  ways in which the molecule can vibrate, or  $(3N-5)$ , if it is linear, therefore, it is reasonable to expect that complex molecules or mixture of substances could originate complex IR spectra, difficult to analyze and to interpret. Nevertheless, some moieties of the molecules, the so-called functional groups, display one or more absorption infrared bands at specific frequencies, slightly influenced by the surrounding parts of the molecule. In such a way, it is possible to identify the chemical groups responsible for such features even though the molecule is not known.

FTIR spectrophotometers use the technique of Michelson interferometry to simultaneously sample a range of frequencies. The IR beam emitted by the source is collected by a beam splitter and divided into two beams each one of half intensity with respect to the original beam. One is falling on the moving mirror and the other one on the fixed mirror. The light beams reflected by the moving and the fixed mirrors are combined generating a complex interferogram, as a function of the position of the moving mirror. The resulting interferogram is subjected to Fourier analysis to generate a spectrum, i.e., a plot of intensity versus frequency. Absorption spectra are obtained by measuring the interferograms with a sample and with the empty sample cell (blank) in the beam, being the interferogram intensity

$$I_{interferogram}(t) = k \int_{-\infty}^{+\infty} I_{beam}(\nu) e^{i2\pi\nu t} d\nu \quad (1)$$

where  $k$  is a constant,  $I_{beam}$  the intensity of the beams and  $\nu$  the wave number. From the interferogram, the intensity of the beams can be calculated by inverse Fourier transforming the resulting interferograms

$$I_{beam}(\nu) = k \int_{-\infty}^{+\infty} I_{int}(t) e^{-i2\pi\nu t} dt \quad (2)$$

The IR absorption spectrum is calculated as the logarithm of the intensity quotient of blank to sample.

### 3.1. Equipment and materials

Any standard commercial Fourier transform infrared spectrophotometer can be used to perform the experiments described in the present paper. We have used two kinds of equipment: BOMEM DA8 and Jasco 420 FTIR spectrophotometers operating in the  $4000-400 \text{ cm}^{-1}$  range, at temperature close to ambient ( $290-300 \text{ K}$ ). Each spectrum was measured by acquiring 128 scans at  $2 \text{ cm}^{-1}$  spectral resolution.

The samples were thin films obtained by depositing aqueous solutions ( $c = 10-40 \text{ mg/ml}$ ) on  $\text{CaF}_2$  windows and allowing them to dry in air under ambient conditions. The film smeared on the calcium fluoride platelets was assembled in a sealed sample cell consisting in a dry box equipped with IR transparent  $\text{CaF}_2$  windows. In the box were inserted (1) a vessel containing a saturated salt solution suitable to assess the opportune relative humidity (RH) to which the sample has to be equilibrated; (2) the sample prepared as a film smeared on a  $\text{CaF}_2$  platelet, vertically positioned in such a way as to allow for transmission measurements (**Figure 1**). The box, avoiding any contact of the sample with the external atmosphere, was inserted in the sample chamber of the FTIR spectrophotometer.

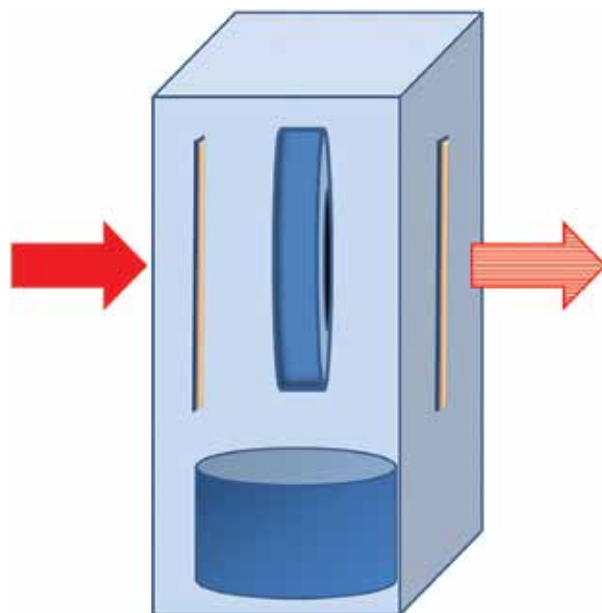


**Figure 1.** Sketch of the sample holder employed to attain the desired hydration degree in the samples. The samples were obtained as films of macromolecule solution smeared on the vertical  $\text{CaF}_2$  platelet, allowed to dry in air before to expose them to the moist ambient in the box. Different relative humidity was achieved in the inner ambient of the box by saturated salt solutions put in the vessel placed on the box base and assembled together with the sample.

Blank measurements were recorded on the sample holder in order to subtract the contribution of the  $\text{CaF}_2$  platelet on which the sample was deposited and the spectrum of the dry box  $\text{CaF}_2$  windows.

### 3.2. Experimental procedures and analysis of water sorption

The protein film together with the salt solution suitable to keep it at the desired humidity level was assembled in the sample holder for 1–2 days before to submit it to the measurements. **Table 1** lists the salts employed for preparing salt solutions able to provide in the desiccator water activities  $a_w$  ranging between 0.06 and 0.97.

The change in the hydrating solution was performed in a dry box under a controlled  $\text{N}_2$  atmosphere. The lowest hydration value was reached by maintaining the sample in an oven at about  $80^\circ\text{C}$  for 2 h. This sample was called the “dry” sample.

Fitting operation of the OH stretching and Amide bands was performed according to Gaussian curves starting from a second derivative analysis [21]. In particular, the OH-stretching mode band ( $\nu \sim 3400 \text{ cm}^{-1}$ ) was analyzed following the approach, adopted in the literature to describe the solvent role of water and deconvoluted into components, which, in principle, might be related to different hydrogen-bond distances [17]. A twofold analysis was performed on the  $\nu(\text{OH})$  band. First, the spectra of the samples collected by decreasing (desorption run) and increasing (adsorption run) the ambient relative humidity were compared and analyzed with

Salt	$a_w$
NaOH	0.06
KOH	0.09
CaBr <sub>2</sub>	0.16
CaCl <sub>2</sub>	0.29
NaI	0.38
Ca(NO <sub>3</sub> ) <sub>2</sub>	0.51
NaBr	0.58
KI	0.69
NaNO <sub>3</sub>	0.74
NaCl	0.75
NH <sub>4</sub> Cl	0.79
KBr	0.81
KCl	0.84
BaCl <sub>2</sub>	0.90
KNO <sub>3</sub>	0.92
K <sub>2</sub> SO <sub>4</sub>	0.97

**Table 1.** Salts employed for saturated salt solutions necessary to accomplish the controlled activities  $a_w$  in the box where the macromolecule films were equilibrated before FTIR measurements.

respect to the other spectral features (Amide bands). Second, the OH stretching band was resolved, by a curve fitting approach, in Gaussian components. The goal in the method is to decompose the feature into three component bands which can be assigned to three different sets of hydrogen bond strength. The Gaussian component amplitude, converted into water amounts, can be used to plot sorption isotherm curves [22]. The relative amounts of water in the three different structural forms were expressed in terms of the area of each peak by assuming that the sum of the areas of the peaks is proportional to the total amount of water in the protein. The corresponding H bond lengths were evaluated by employing Nakamoto plots [23].

Water sorption isotherms were obtained as the sorbed water vapor amount versus water vapor activity  $a_w$  at fixed temperature [22]. The water content of the sample was spectrophotometrically determined from the  $\nu(\text{OH})$  band amplitude subtraction of the spectrum of the same sample fully dehydrated (“dry” sample). In this way, any contribution to the band of N–H and C–H stretching vibrations, occurring in the same wave number range, was systematically eliminated. Due to the thin thickness of the samples, layered as film and the very low water content ( $0.97\text{--}0.06 \text{ g}_{\text{water}}/\text{g}_{\text{dry sample}}$ ), the very small change in the optical path produced by dehydrating the sample does not affect significantly the spectra intensity. Adaptation of Beer's law was successively used to rescale the intensity of the “cleaned”  $\nu(\text{OH})$  bands, in

accordance with the approach proposed in the literature to study various hydrated biomaterials [24]. To quantify the integrated absorbance in terms of water surface coverage, we can assume a modified form of Beer-Lambert' law

$$\tilde{A} = \int_{band} A dv = \varepsilon(v_{MAX}) \bar{c}d \quad (3)$$

where  $\tilde{A}$  is the integrated absorbance of the component band,  $\varepsilon(v_{MAX})$  is the molar absorptivity at wave number  $v_{MAX}$  corresponding to the peak of the band ( $L mol^{-1} cm^{-1}$ ),  $\bar{c}$  is the concentration of the absorbing species ( $mmol/cm^3$  or, equivalent  $mol/L$ ) and  $d$  is the average thickness of the absorbing species film, that is, adsorbed water, in centimeters [9].

For water, it is possible to evaluate the molar absorptivity  $\varepsilon(v)$  at fixed wave number [24]: for example, one can evaluate  $\varepsilon(3600 cm^{-1}) = 1.647 L mol^{-1} cm^{-1}$ . By assuming the path length  $d$  as the thickness of a film of water, the corresponding amount of the water content can be converted in concentration  $\bar{c}$  of water, assumed as only absorbing species. The concentration  $\bar{c}$  in each sample prepared at each hydration degree can be evaluated and employed to normalize the amplitude of the subcomponents in the  $\nu(OH)$  band. The desorption-adsorption branches of the isotherm curves were therefore obtained for each Gaussian component. As a rule, the desorption experiments were performed by starting from the highest  $a_w$  value ( $a_w = 0.97$ ) and accomplished before the adsorption one, to avoid possible damages in the samples produced by dehydration treatments.

## 4. Collagen

Collagens are a large protein family forming a characteristic triple helix of three polypeptide chains giving rise to supramolecular structures in the extracellular matrix: their size, function and tissue distribution vary considerably [25]. So far, 26 genetically distinct collagen types have been described. It is the main fibrous component of skin, bone, tendon and cartilage, accounting in particular for three-quarters of the dry weight of skin, and representing the most prevalent component of the extracellular matrix. The collagen molecule is a rigid rod-like structure able to resist stretching. It is composed of three polypeptide left-handed  $\alpha$  chains coiled around each other to form a typical right-handed rope-like triple helical rod (approximately, 1.5 nm in diameter, 300 nm in length). The triple helical sequences are composed of Gly-X-Y repeats, X and Y being frequently proline and hydroxy-proline, respectively [26]. Stabilization of the triple helix is assured by a lot of structural conditions as the presence of glycine as every third residue, a high content of imino acids with a rigid cyclical structure (proline and hydroxy-proline) and electrostatic interactions involving lysine and aspartate [27]. Both in the structural and functional properties, a key role is undoubtedly played by water, which provides inter-chain hydrogen bonds and water bridges and coats triple helix by a cylinder-like of hydration [28, 29]. Moreover, water critically regulates chain flexibility and assures the water mediated H-bonds favoring fiber recognition and alignment. Water lacking is a very dangerous process for the protein, damaging the structure in irreversible way. Water depletion, caused by tissue maturation, exposition to UV light and/or some pathological processes, such as diabetes, triggers detrimental conformational rearrangements

due by nonenzymatic glycation reactions between the protein and the complex carbohydrates present in the matrix, leading to the formation of oxidation products, known as Advanced Glycation End-products (AGE) [30, 31] having the effect to modify the collagen fibers physical properties, inducing an increase in stiffness and breaking load, denaturation temperature, solubility and a decrease in resistance to degradative enzymes [32].

Despite the great amount of studies [33], the explicit relationship between protein and hydration water structure is still an open question and the detailed dehydration scheme of collagen and the structural implications are not yet completely elucidated.

#### 4.1. Hydration structure of collagen: FTIR spectroscopy and water sorption isotherms

Complementary FTIR measurements on collagen prepared at very low hydration level ( $a_w$  in the range 0.06–0.97) and adsorption isotherm technique have put in evidence the critical hydration level which induces an irreversible conformational change in the protein, responsible for the first ageing step.

In **Figure 2**, the spectra of collagen extracted from rat tail tendon (type I collagen) are shown during the dehydration run.

In order to study the role of water interacting with collagen, FTIR spectrum was analyzed in the OH stretching region by changing the hydration content of the sample following the method described above (Section 3.2).

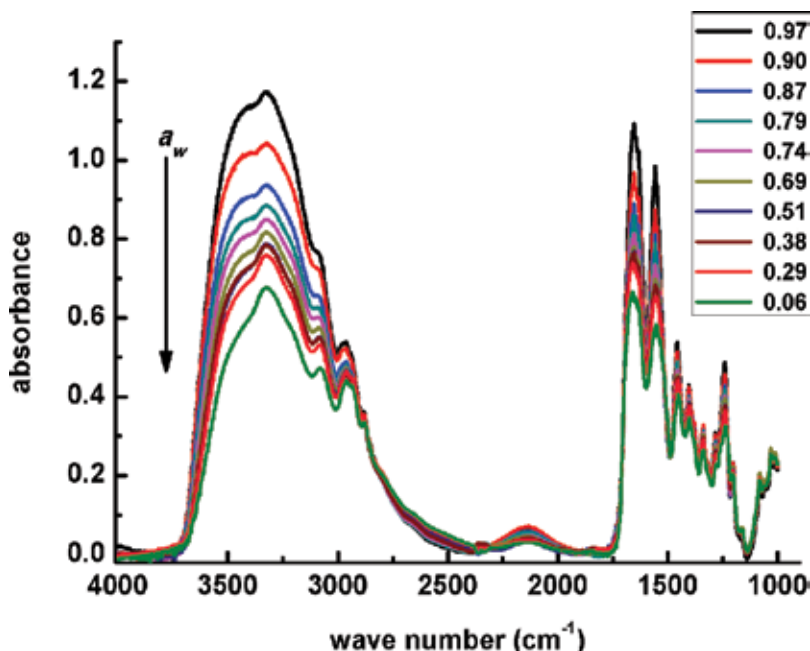


**Figure 2.** FTIR spectra of rat tail tendon collagen, recorded at different water activities during dehydration treatment from  $a_w = 0.97$  to  $a_w = 0.06$ .

OH stretching band (wave number range 4000–3000  $\text{cm}^{-1}$ ) was analyzed after subtraction of the “dry” spectrum and decomposed into four components (**Figure 3**) whose frequencies were related to different O-H bond lengths as listed in **Table 2**.

The  $\nu(\text{OH})$  feature composition in Gaussian sub-bands in such a way can be correlated to the hydrogen bond network around the protein and provides information about the structural modifications induced by changing the hydration level. The four Gaussian components are peaking, for the sample at the maximum hydration, at 3598, 3467, 3295 and 3115  $\text{cm}^{-1}$ , following the procedure of the second derivative analysis. They are corresponding to four classes of water molecules bound to the protein, different in vibrational energies and each one characterized by a single average H-bond distance ( $\text{H}\cdots\text{OH}$  length): 0.31, 0.29, 0.28 and 0.25 nm, respectively [18, 23].

The sub-band peaking at the highest wave number region is corresponding to H-bond distances characteristic of vapor-like state. Similar features, detected for different biological macromolecules [9, 10, 16], were assigned to the non-H-bonded or weakly H-bonded O-H groups. It is reasonable to suppose that in collagen prepared at very low hydration levels, as in our case, they could be originated by the dangling most external water molecules sitting on the outer hydration layer coating the macromolecule. The inability for these molecules to establish active H-bonds with surrounding water molecules, accounts for the high mobility and the large vibrational energy comparable with those of free water molecules in the vapor state. They represent about the 5% of the total amount of water hydrating collagen at the relative humidity settled for the experiment, being the percentages calculated as the

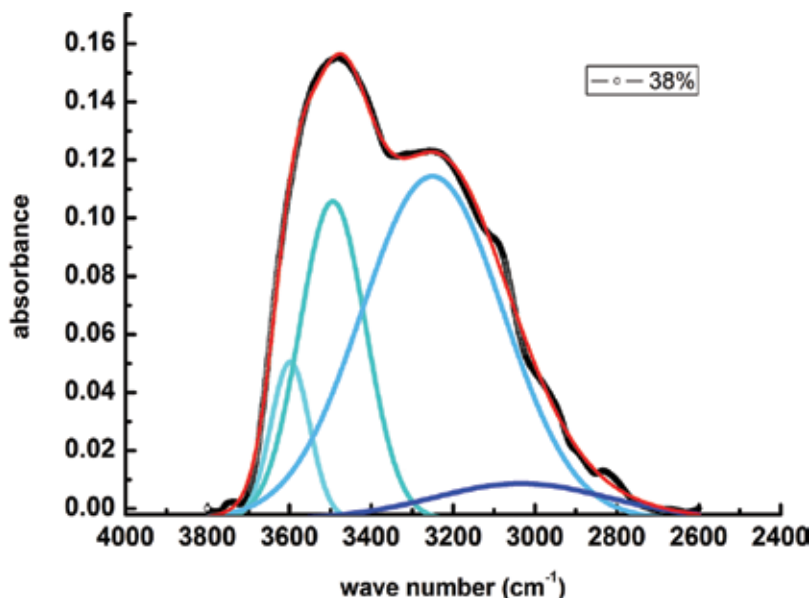


**Figure 3.** Gaussian deconvolution of FTIR spectrum of collagen ( $a_w=0.38$ ) in the  $\nu(\text{OH})$  region, by means of four component bands, as obtained by means of second derivative method. The sum of the fitted curves is shown as the red line, closely overlapping the experimental data trace, which is shown as a full black line.

Molecule	Stretching frequency (cm <sup>-1</sup> )				H-bond distances (nm)			
	$\nu_1$	$\nu_2$	$\nu_3$	$\nu_4$	$d_1$	$d_2$	$d_3$	$d_4$
Pure water	3570	3434	3322		0.30	0.29	0.28	
Collagen	3598	3467	3295	3115	0.31	0.29	0.28	0.25
Lysozyme	3539	3315	3008		0.29	0.28	0.24	

**Table 2.** Hydrogen bond distances estimated from the vibrational frequencies following Nakamoto et al. [23].

ratio  $A_i/A_{\text{tot}}$  of the single component area ( $A_i$ ) with respect to the total band area ( $A_{\text{tot}}$ ). The two component bands peaking at the intermediate wave numbers may be related to H<sub>2</sub>O molecules coordinated by two or three, more or less distorted or strained, H bonds. They may be identified with H<sub>2</sub>O molecules deeply located inside the protein helix, acting as water bridges within a single peptide chain and/or interconnecting the different  $\alpha$ -chains in the triple helix. They constitute the 19% and the 31%, respectively, of the total water amount. The corresponding H-bond distances suggest that they could represent the solvation molecules involving C=O groups belonging to glycine ( $d(\text{C}=\text{O}\cdots\text{W}) = 0.295$  nm) and hydroxyproline (Hyp) ( $d(\text{C}=\text{O}\cdots\text{W}) = 0.284$  nm) hydroxyl moieties [29]. The component at 3180 cm<sup>-1</sup> may be attributed to water molecules located near to the protein surface and hydrogen bonded to polar and charged groups exposed to the macromolecule surface: they originate some ice-like tetrahedral structures more or less distorted. The corresponding average H bond length is in fact characteristic for arrangement of H<sub>2</sub>O molecules as in small solid water clusters, assuming the length O $\cdots$ O of hydrogen bonds in ice as 0.276 nm [34]. The broad profile of such a band, extending on a wide wave number range, testifies for the large distribution of water vibrational states in a configuration variety, concurring to the feature. Such a sub-band represents the main hydration fraction at the highest settled humidity, corresponding to the 45% of the total amount of hydration water.

The dehydration treatment at  $a_w = 0.06$  followed by a subsequent rehydration up to the original relative humidity ( $a_w = 0.92$ ) reveals a pronounced hysteresis effect in the  $\nu(\text{OH})$  band amplitude and a remarkable modification of the profile, as shown in **Figure 4**.

The difference spectrum is peaking at  $\nu \sim 3400$  cm<sup>-1</sup>; therefore, it is roughly filling the position of the third component of the overall  $\nu(\text{OH})$  band. Moreover, it exhibits a shoulder on the low wave number side ( $\nu \sim 3000$  cm<sup>-1</sup>). This finding suggests that dehydration treatment causes in collagen the loss of a considerable amount of H<sub>2</sub>O molecules truly involved in the internal water bridges, probably coordinated by glycine C=O, and a fraction of molecules coating the polypeptide surface, bound to the Hyp hydroxyls. This water portion once desorbed, only partially can be re-adsorbed. It accounts for the 21% of the total water amount initially hydrating the sample.

With the aim to better investigate this topic, the peak areas of the two intermediate sub-bands, peaking at  $\nu = 3467$  cm<sup>-1</sup> and  $\nu = 3295$  cm<sup>-1</sup>, detected in the spectrum of the sample at the highest hydration level, were plotted as a function of the activity  $a_w$  during the desorption and the subsequent adsorption processes to build the corresponding isotherm curves. **Figure 5** summarizes the isotherm curves related to the two component bands highlighting the large differences occurring in sorption mechanisms of the two related water sets.

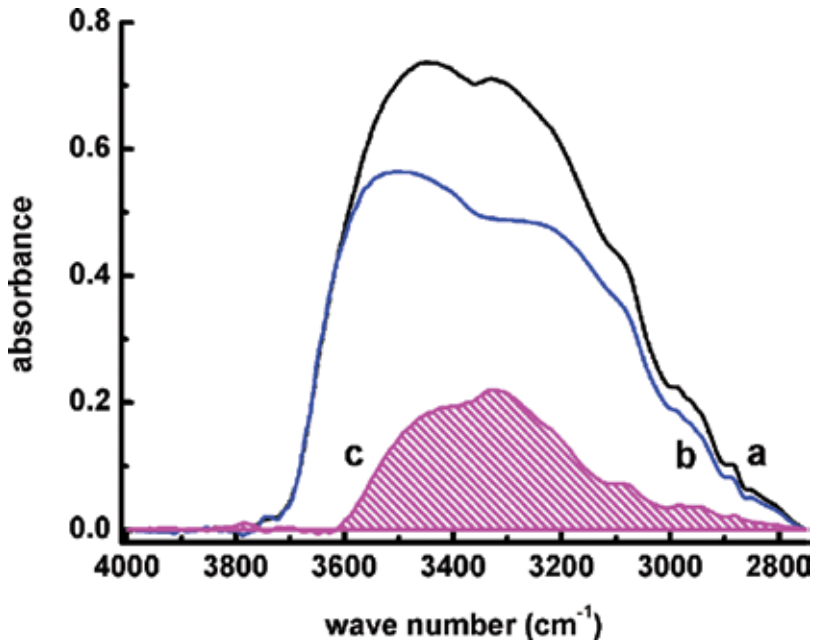


**Figure 4.** OH stretching bands measured for collagen at  $a_w = 0.97$ , before (curve a) and after (curve b) dehydration at  $a_w = 0.06$ . Curve c represents the difference between a and b bands and the subtended area (pink dashed area) can be related to the water amount desorbed by the sample during dehydration and no more recovered along rehydration.

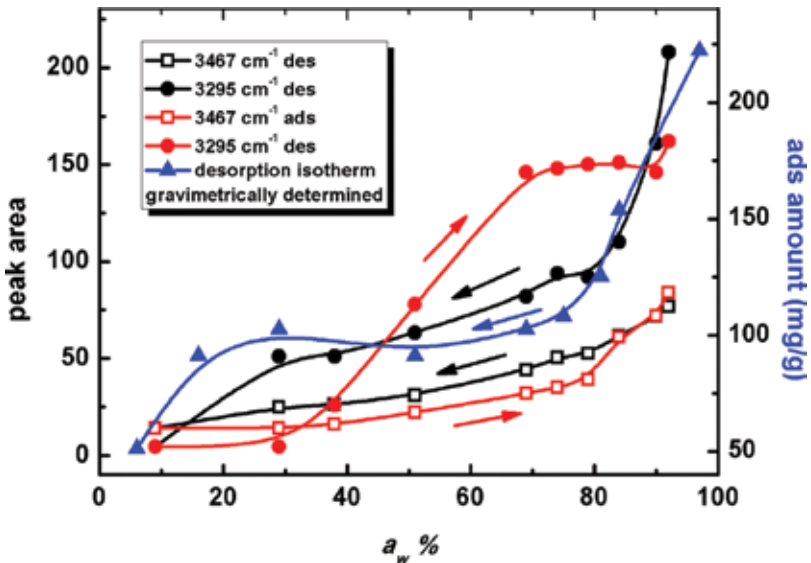


**Figure 5.** Desorption and adsorption curves for two sub-bands ( $\nu = 3467 \text{ cm}^{-1}$  and  $\nu = 3295 \text{ cm}^{-1}$ ) of OH stretching band measured for collagen, during dehydration (black symbols) and re-hydration (red symbols) treatments. Blue triangles represent the desorption data obtained by means of the gravimetric experiment. The lines are a guide for the eye.

The band at  $3295\text{ cm}^{-1}$  displays a type II-like desorption and adsorption behavior [22]. The band amplitude completely recovers at the end of the process; therefore, such component only partially participates to the lacking of recover in amplitude of the total  $\nu(\text{OH})$  band, the weak hysteresis effect being probably due to the reassessment of the interchain water bridges as a consequence of the perturbation induced by water subtraction. Concerning the band at  $3467\text{ cm}^{-1}$ , the mechanism of dehydration is very different than that of rehydration. The desorption branch correlates well with the curve gravimetrically measured by weighing the sample after equilibration at each different humidity level, as shown in **Figure 5** (blue full triangles): the two desorption curves show the same trend. They are as type II curve, where three phases can be distinguished: a starting rapid dehydration step from  $a_w = 0.92$  to about  $a_w = 0.80$ , a second one in the  $a_w$  range  $0.80\text{--}0.40$ , where water desorption occurs more slowly with the decrease in ambient relative humidity and a third phase at low water activities, extending from  $a_w = 0.40$  to  $a_w = 0.06$ , describing a characteristic “knee” [2]. The first phase may be assigned to the removal of water molecules forming hydrogen-bonded clusters, the second one to subtraction of  $\text{H}_2\text{O}$  molecules from weakly interacting surface regions and the third branch to the dehydration of strongly bound water molecules by Hyp hydroxyl moieties exposed at the surface. The result suggests that the whole protein desorption process is mainly concerning the dehydration of the external water layer.

Water uptake exhibits a very different behavior with respect to the dehydration, resulting in a large hysteresis loop, extending over the whole activity range. Adsorption isotherm displays features not conform to any isotherm type in the Brunauer classification [22]. From  $a_w = 0.06$  to  $a_w = 0.40$ , the amount of water adsorbed is rather negligible. The activity  $a_w = 0.40$  represents a threshold activity above which a sudden water uptake occurs attaining a saturation hydration value, lower than the moisture content of the freshly prepared sample.

Water deprivation and restitution has considerable consequences on the macromolecule structure. The changes in the high wave number region of the IR spectrum can be correlated with the secondary structure analysis carried out on Amide I band which was resolved in Gaussian components. Qualitative and quantitative information about the conformational composition of the protein prepared in the different hydration states were obtained. Amide I band in fact was decomposed in sub-bands whose position and area were related, respectively, to the different types and to the amount of secondary structures (**Figure 6**). The sum of the areas of the peaks represents the total amount of secondary structure in the protein.

The curve fitting procedure [8, 21] allowed determining the secondary structure composition in the freshly prepared sample ( $a_w = 0.97$ ), as displayed in **Figure 6A**:  $\beta$ -turn ( $1695\text{ cm}^{-1}$ ),  $\beta$ -sheet ( $1680\text{ cm}^{-1}$ ),  $\alpha$ -like helix ( $1660\text{ cm}^{-1}$ ), unordered structure ( $1644\text{ cm}^{-1}$ ), triple helix ( $1628\text{ cm}^{-1}$ ),  $\beta$ -sheet ( $1615\text{ cm}^{-1}$ ), side chains ( $1607\text{ cm}^{-1}$ ). The multippeak decomposition of the band measured in the sample rehydrated at the original activity, after dehydration at  $a_w = 0.06$  (**Figure 6B**), revealed the modification occurred in the secondary structure, the most significant change concerning the increase in the broad sub-band peaking at  $\nu \sim 1670\text{ cm}^{-1}$  largely spanning the high wave number region of the Amide I band and the parallel decrease in the component bands at  $1695$  and  $1660\text{ cm}^{-1}$ . The formation of such structures may be related to the relative increase in  $\beta$  components (antiparallel  $\beta$ -sheet and aggregated strands) with

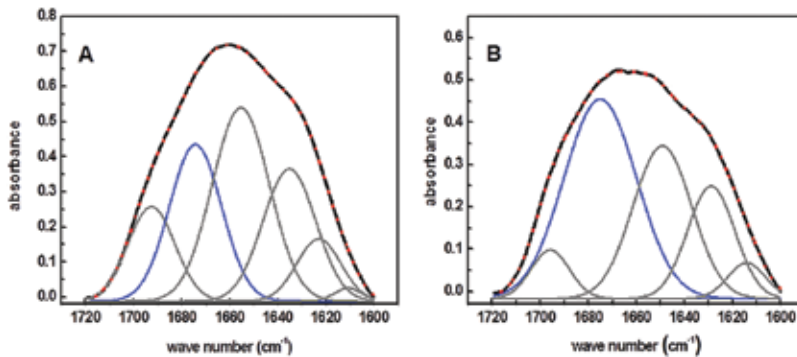


**Figure 6.** Amide I band deconvolution for collagen at  $a_w = 0.97$  before (A) and after (B) dehydration at  $a_w = 0.06$ . The set of Gaussian components can be related to the secondary structure composition of the protein. The full blue lines highlight the component bands related to the antiparallel  $\beta$ -sheet/aggregated strand motif. The dotted red lines represent the sum of the components.

respect to the  $\alpha$ -helix contribution in the Amide I envelope. Such effect may be explained by assuming the formation of bridges among near collagen molecules laterally associating by forming chain structures side by side interacting, involving Hyp residues [35], spectroscopically mimicking  $\beta$ -sheet structures [36].

These results would be consistent with the physiologic behavior of collagen and may be correlated to the changes in the structural properties of collagen fiber assembly as a consequence of dehydration. The spectroscopic data are consistent with specific binding of water molecules to collagen chains stabilizing the collagen triple helix by Hyp residues through intramolecular water bridges. The difference in interfacial surface water may be the physical reason for the hysteresis phenomena observed in water adsorption isotherms. As a consequence of the removal of water down to water activity  $a_w < 0.40$ , the association of the collagen molecules takes place and once water is restituted, the assembled fibers are no more able to re-adsorb all the water available during the rehydration phase. This arrangement, responsible for the lacking in the hydration recover of protein, may be considered one of the main causes of collagen maturation and ageing.

## 5. Lysozyme

Lysozyme is a small globular protein shaped as an approximate ellipsoid of dimension  $45 \times 30 \times 30 \text{ \AA}$  composed of 129 residues, acting as an enzyme causing lysis of Gram positive bacteria by hydrolyzing the  $\beta$ -(1-4) glycosidic links in the cell wall peptidoglycan [37]. Lysozymes have been isolated from a great variety of sources. Lysozyme from hen egg white (HEWL, MW 14600) is an  $\alpha + \beta$  protein with 30% helical residues and 13%  $\beta$ -sheet content. As for the majority of protein molecules, lysozyme structure and stability are largely determined by the interaction between the protein and the aqueous surroundings [38-40]. Investigation of the structural changes occurring during the change in the activity of water was important for understanding the mechanism of this interaction. In particular, Careri et al. [41] suggested a connection between the water-induced onset of enzymatic activity and some water triggered

physical properties of the protein system, i.e., heat capacity, diamagnetic susceptibility, IR absorption, percolation threshold for proton conduction, recognizing that the hydration threshold for lysozyme, occurred at 0.22 g of water/g of protein.

### 5.1. Hydration structure of lysozyme: FTIR spectroscopy and water sorption isotherms

Lysozyme from hen egg white was used without further chemical purification and submitted to FTIR investigation following the experimental method above described (Section 3.2). The solvent architecture around the protein was correlated to the macromolecule conformation by means of two different procedures:

By monitoring secondary structure from the inspection of the changes occurring both in Amide I and Amide III features by changing the protein hydration level. Amide I band analysis in fact suffers from the extensive overlap of the underlying water H–O–H bending band, lying in close proximity ( $\sim 1645\text{ cm}^{-1}$ ), the line broadening making quantitation arduous. The secondary structure assignments can be reinforced by taking into account Amide III, attributed to N–H deformation coupled with the C–N stretching motion and ranging in the wave number region  $1220\text{--}1340\text{ cm}^{-1}$ . It occurs out of any water absorption region and its behavior, monitored along secondary structure changes of the protein, may be correlated with the changes suffered by the enzyme structure to provide a consistent picture of the hydrated protein conformational properties [8].

By studying the evolution of the broad  $\nu(\text{OH})$  feature along the protein hydration and dehydration processes. The OH stretching bands, recorded at each activity value, were decomposed into three Gaussian components, corresponding to the three main water fractions hydrating lysozyme, different in structure and clustering order. By appropriate analysis of the data, sorption isotherm curves were built, able to provide information on relationship between the water content and the different protein structural features. The water amount bound to Lysozyme was deduced from the  $\nu(\text{OH})$  band area after subtraction of the spectrum of the “dry” sample.

Figure 7A and B shows  $\nu(\text{OH})$  bands recorded for the protein prepared at different hydration degree along the dehydration and the rehydration runs.

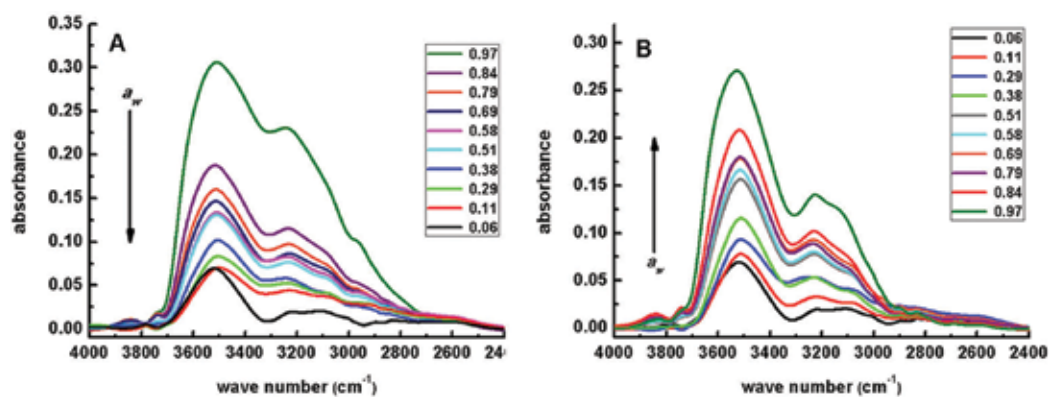
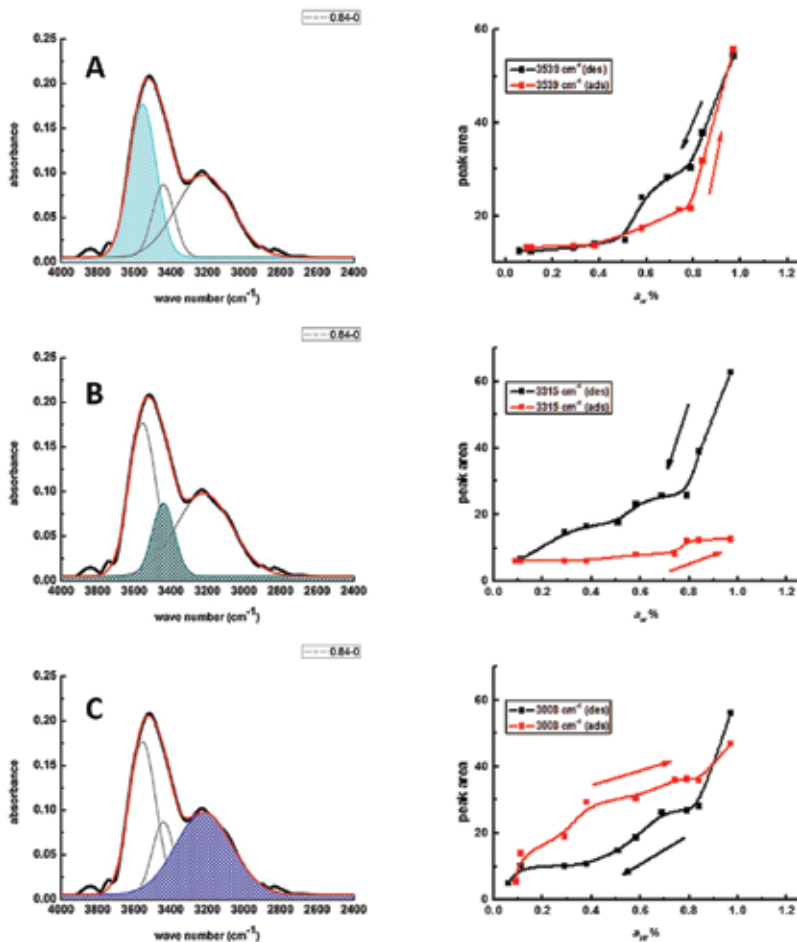


Figure 7. OH stretching bands measured for lysozyme along dehydration (A) and rehydration (B) treatments between  $a_w = 0.97$  and  $a_w = 0.06$ .

Following the decomposition of the band in Gaussian components, three sub-bands were detected (**Figure 8**, left side): their positions and the corresponding OH $\cdots$ O distances, measured for the sample at the highest hydration degree, are listed in **Table 2**. First component band (I) (**Figure 8A**) peaking at the higher wave number (3539 cm $^{-1}$ ) may be attributed to surface water molecules easily adsorbed on the most external hydration layer. They show the dangling OH vibrational frequency typical for free-like H $_2$ O molecules at the interfaces water-air. The sub-band at  $\nu = 3315$  cm $^{-1}$  (II) (**Figure 8B**) may be related to water molecules directly interacting with protein backbone, particularly engaged in hydrogen bonding with peptide carbonyl moieties (C=O $\cdots$ W). The broadband at  $\nu = 3008$  cm $^{-1}$  (III) (**Figure 8C**), representing the most prevalent component, corresponds to water molecules forming the hydration shells around the protein, interacting with neighboring adsorbed water molecules. The position of the feature is indicative of the intermolecular hydrogen bond distances matching the average



**Figure 8.** Gaussian deconvolution of FTIR spectrum of lysozyme ( $a_w = 0.84$ ) in the  $\nu(\text{OH})$  region, by means of three component bands (dashed areas). For each component band, the isotherm curves were plotted: black symbols represent the desorption data and red symbols represent the adsorption data. The lines are a guide for the eye.

characteristic lengths typical for tetrahedral ice structure but the large bandwidth reveals that it is suffering lengthening and distortions in the distances and orientation.

**Figure 8**, right side, displays the isotherm curves obtained by monitoring the areas of the three component bands as a function of the moisture of the sample, both during the sequential decrease in the water content of the sample and during the opposite treatment, rehydration at RT. Sub-band I gives rise to a desorption isotherm classified as Type IV, characteristic for the evaporation process of water at the interface water-air. In the converse process of condensation, the underlying liquid surface acts as to nucleate the adsorption, therefore, the isotherm is quite different, showing the shape of a Type III curve, characteristic for cooperative interactions. The loop desorption-adsorption gives rise to a hysteresis because evaporation and condensation do not take place as exact reverse of each other. The hysteresis effect indicates that between  $a_w = 0.40$  and  $a_w = 0.80$ , the amount of water desorbed is greater than that adsorbed, suggesting a change or an assessment of the condensation surface, as a consequence of dehydration, until the highest moisture degree is achieved. Sub-band III originates a hysteresis loop as well, although the isotherm curves are not easy to be classified according to the literature [22]. The intermediate component (sub-band II) reveals an anomalous behavior reflecting an irreversible structural modification of the protein. Water desorption describes a Type IV-like isotherm but the adsorption branch is a flat line up to  $a_w = 0.80$ , showing a small increase for the highest hydration values attained, but unable to completely recover the original amplitude. It notifies the inability of the macromolecule to re-adsorb in a reversible manner the water phase originally coordinated by the polypeptide backbone, once desorbed.

The process can be explained by assuming that water subtraction modifies the structural properties of the macromolecule which would tend to narrow down the crevices where water molecules were inserted, by establishing intrachain bonds difficult to reverse. As discussed in the literature, in the absence of water, the protein molecule tends to fill the voids left by water by adopting structures that can continuously fill the space [38]. The hysteresis effect is confirmed by the difference in amplitude between the  $\nu(\text{OH})$  band of the native sample and the rehydrated one after dehydration, as shown in **Figure 9**. The difference band centered at  $\nu \approx 3300 \text{ cm}^{-1}$  corresponds to the water fraction desorbed during the dehydration run and no more re-adsorbed during the subsequent hydration process.

In **Figures 10** and **11**, the spectral windows related to the two polypeptide secondary structures, i.e.,  $1700\text{--}1550 \text{ cm}^{-1}$  and  $1300\text{--}1230 \text{ cm}^{-1}$  corresponding to the Amide I and III ranges are shown for the two samples prepared at the highest hydration degree. The Gaussian decomposition of the native lysozyme Amide I band (**Figure 10**) was carried out in four major components, in agreement with previous studies performed on lysozyme and other kinds of proteins [42, 43]. The band fairly asymmetric and peaking at  $\sim 1656 \text{ cm}^{-1}$ , is mainly due to the contribution of  $\alpha$ -helical structure (75%), in agreement with the literature [44]. The  $\beta$ -sheet content is lower and can be measured from the two components around  $1618$  and  $1684 \text{ cm}^{-1}$ . The component centered at  $1635 \text{ cm}^{-1}$  can be attributed to unordered structures.

**Figure 11** displays Amide III bands for the sample at  $a_w = 0.97$  and after dehydration down to  $a_w = 0.06$ . The curve fitting analysis for lysozyme in the native hydrated form reveals three

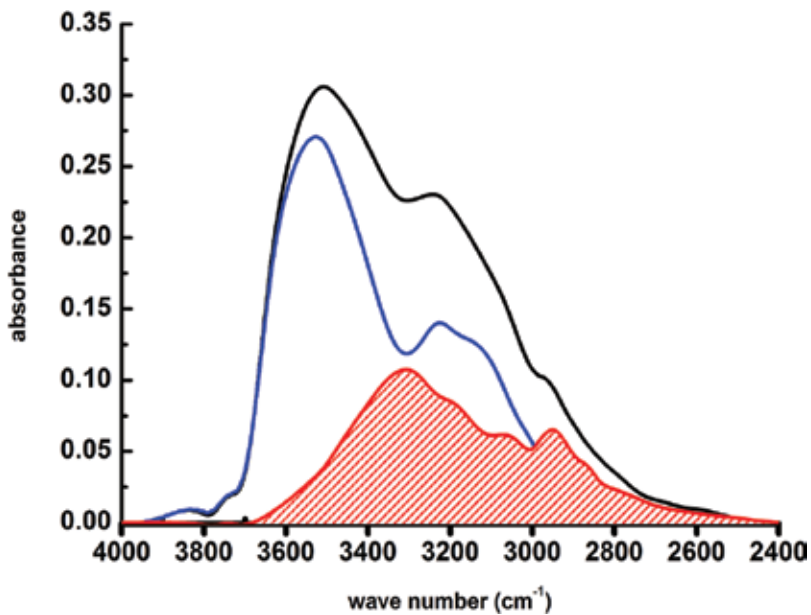


**Figure 9.** OH stretching bands measured for lysozyme at  $a_w = 0.97$ , before (black curve) and after (blue curve) dehydration at  $a_w = 0.06$ . The red curve represents the difference of the two curves and the subtended area (red dashed area) can be related to the water amount desorbed by the sample during dehydration and no more recovered along rehydration.

main sub-bands peaked at 1338, 1320 and 1300  $\text{cm}^{-1}$ , which can be categorized as being  $\alpha$ -helical with a total relative band strength of 40%. The relatively sharp band at 1230  $\text{cm}^{-1}$  is assigned to  $\beta$  sheet structure for 21% and two broadbands at 1260 and 1285  $\text{cm}^{-1}$  indicate the presence of unordered structures for 35%. Dehydration induces modifications of the bands with respect to the spectrum of the native hydrated sample: they can be related to changes in the secondary structure composition.

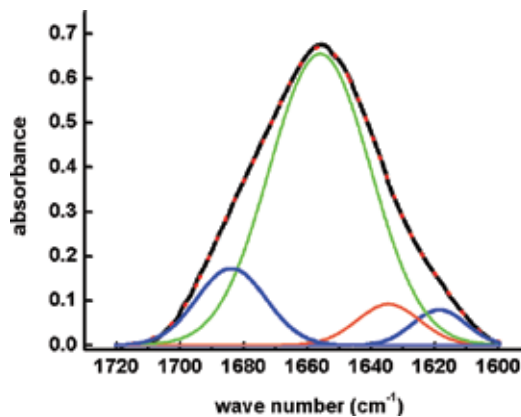


**Figure 10.** Amide I band deconvolution for lysozyme at  $a_w = 0.97$ . The component bands can be related to the structural contribution of  $\alpha$ -helix (green line),  $\beta$ -sheet (blue line) and unordered (orange line) structures.

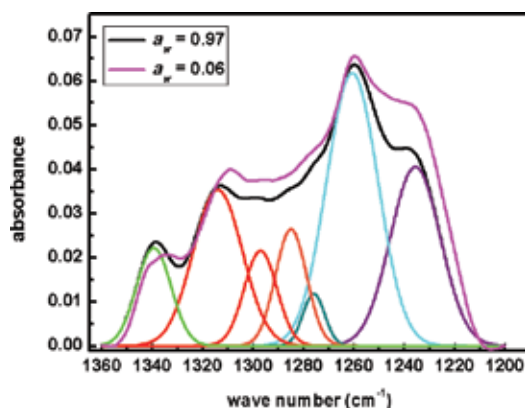


**Figure 11.** Amide III band measured for lysozyme at  $a_w = 0.97$  (black line) and  $a_w = 0.06$  (pink line). The deconvolution in Gaussian components is related to the spectrum of the sample at the higher hydration degree. The main components band are as follows:  $\alpha$ -helix at 1338, 1320 and 1300  $\text{cm}^{-1}$ ,  $\beta$  sheet at 1230  $\text{cm}^{-1}$  and unordered structures at 1260  $\text{cm}^{-1}$  and 1285  $\text{cm}^{-1}$ .

In **Figure 12**, the percentage amount of each component band corresponding to each secondary structure element was plotted as a function of the increasing water activity  $a_w$ , settled in the dry box.

It appears that dehydration treatment induces small but significant conformational changes involving the increase in the  $\beta$  structure fraction. Interestingly, the plot points out as the  $\alpha$ -helix

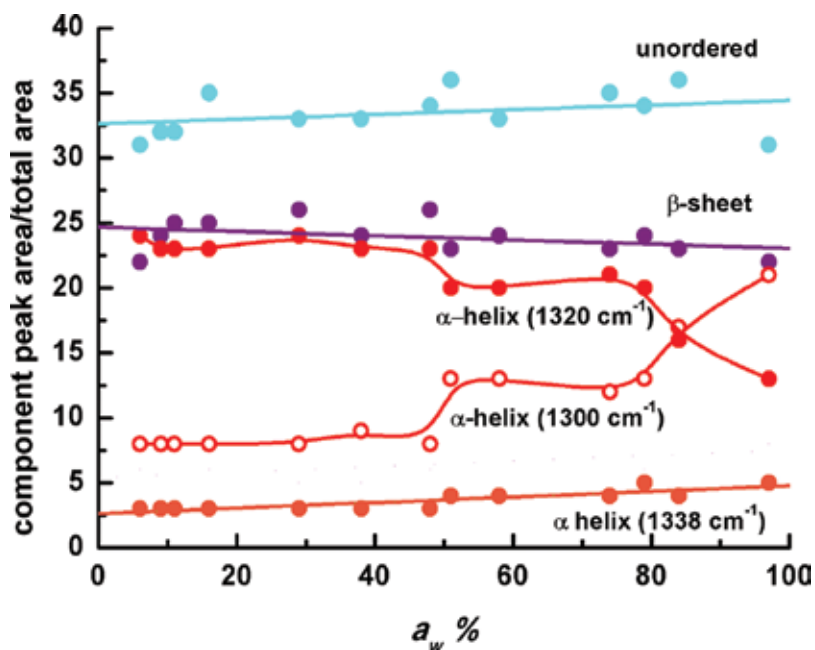


**Figure 12.** Evolution of the amount of secondary structures in lysozyme, monitored by the deconvolution of Amide III band, along the dehydration treatment, plotted as the relative area peak  $A_i/A_{tot}$  as a function of the activity  $a_w$ . The color code is related to component bands in **Figure 11**.

portion of the protein is heavily affected by water subtraction. The two bands peaking at 1320 and 1300  $\text{cm}^{-1}$ , related to this conformational motif, reveal a mutual amplitude interconversion following a stepped trend, similar but specular, as a function of water content changes. The observed effect could be related to small conformational changes, as a result of hydration changes, involving different fractions of  $\alpha$ -helices which could be affected by mutual conformational fluctuations. The observed conformational modification may be due to the change in the orientation of two  $\alpha$  domains monitored by the Amide III component bands. Water deprivation could affect intermolecular distances making different helix structure more or less consistent with hydrogen bond. Although this result could not be considered as definitive proof, however, it is important in the understanding the dynamical equilibrium of protein structure, crucial for many biological processes involving the enzyme.

The different response to hydration change of the different polypeptide regions at different secondary structure may be interpreted on the light of the crystallographic studies revealing relatively rigid and flexible regions in the macromolecule [45]. The interdomain dynamics modulated by water interaction could be related to the mechanisms involving the active-site cleft dynamics of the protein needed for the enzymatic activity, whose onset appears over a threshold hydration level and causing the irreversibility of functionality if a critical dehydration threshold is exceeded [41].

## 6. Concluding remarks

The present study amply demonstrated the sensitivity of FTIR technique in the association of biomacromolecule vibrational frequencies to relatively small conformational changes induced by hydration. The critical dependence of the structural properties on the water content may be related to the shape of isotherm curves obtained for  $\nu(\text{OH})$  component bands and in particular to the isteretic behavior of sub-bands. Water molecules set up very intimate interactions with biological macromolecules. Their structural rearrangement induced by water deprivation would provide local restructuring of the molecule and modification in the exposition of the side chain groups. The first effect, portrayed by  $\nu(\text{OH})$  stretching band, affects the second one, monitored by changes in fingerprint characteristic features. The critical interrelations between the hydration shell and the relative mobility of different regions of the molecule allows considerable progresses in this field accounting for the loss of enzymatic activity and functionality for proteins [41], phase transition in lipid assembly [10] and change in physical properties for melanins [9], in conditions of extreme dehydration.

## Author details

Maria Grazia Bridelli

Address all correspondence to: [mariagrazia.bridelli@unipr.it](mailto:mariagrazia.bridelli@unipr.it)

Department of Physics and Earth Sciences "Macedonio Melloni," University of Parma, Parma, Italy

## References

- [1] Franks F, *Water: 2nd Edition. A Matrix of Life*. RSC Paperbacks, Cambridge, UK; 2000.
- [2] Gregory R B, editor. *Protein–Solvent Interactions*. New York: Dekker; 1995.
- [3] Levy Y and Onuchic J N: Water mediation in protein folding and molecular recognition. *Annu. Rev. Biophys. Biomol. Struct.* 2006;35:389–415.
- [4] Rupley J A, Gratton E and Careri G: Water and globular proteins. *Trends Biochem. Sci.* 1983;8:18–22.
- [5] Rupley J A and Careri G: Protein hydration and function. *Adv. Protein Chem.* 1991;41:37–172.
- [6] Raschke T M: Water structure and interactions with protein surfaces, *Curr. Opin. Struct. Biol.* 2006;16:152–159.
- [7] Wernet Ph et al: The structure of the first coordination shell in liquid water, *Science* 2004;304:995–999.
- [8] Mantsch H H, Chapman D. editors. *Infrared Spectroscopy of Biomolecules*. Wiley-Liss, Inc, New York; 1996.
- [9] Bridelli M G, Crippa P R: Infrared and water sorption studies of the hydration structure and mechanism in natural and synthetic melanin. *J. Phys. Chem. B.* 2010;114:9381–9390.
- [10] Bridelli M G, Capelletti R, Mora C: Structural features and functional properties of water in model DMPC membranes: thermally stimulated depolarization currents (TSDCs) and Fourier transform infrared (FTIR) studies. *J. Phys. D: Appl. Phys.* 2013;46:485401
- [11] Falk M and Ford T A: Infrared spectrum and structure of liquid water. *Can. J. Chem.* 1966;44:1699–1707.
- [12] Auer B M, Skinner J L: IR and Raman spectra of liquid water: theory and interpretation. *J. Chem. Phys.* 2008;128:224511.
- [13] Brubach J B et al.: Signatures of the hydrogen bonding in the infrared bands of water. *J. Chem. Phys.* 2001;122:184509.
- [14] Buontempo U, Careri G, Fasella P: Hydration water of globular proteins: the infrared band near 3300 cm<sup>-1</sup>. *Biopolymers* 1972;11:519–521.
- [15] Onori G, Santucci A, IR investigations of water structure in aerosol OT reverse micellar aggregates. *J. Phys. Chem.* 1993;97:5430–5434.
- [16] Mallamace F et al.: Role of the solvent in the dynamical transitions of proteins: the case of the lysozyme-water system. *J. Chem. Phys.* 2007;127:045104.
- [17] Schmidt D A and Miki K: Structural correlations in liquid water: a new interpretation of IR spectroscopy. *J. Phys. Chem. A.* 2007;111:10119–10122.

- [18] Badger R M: A relation between internuclear distances and bond force constants. *Chem. J. Phys.* 1934;2:128–131.
- [19] Bridelli M G, Capelletti R, Maraia F, Mora C, Pirola L: Initial hydration steps in lipase studied by means of water sorption isotherms, FTIR spectroscopy and thermally stimulated depolarization currents. *J. Phys. D: Appl. Phys.* 2002;35:1039–1048.
- [20] Atkins P and de Paula J, *Physical Chemistry*. 7th Edition. Oxford University Press, Oxford, UK; 2002.
- [21] Byler D M and Susi H: Examination of the secondary structure of proteins by deconvolved FTIR spectra. *Biopolymers*. 1986;25:469–487.
- [22] Gregg S J, Sing K S W, *Adsorption, Surface Area, and Porosity*. Academic Press: New York; 1982.
- [23] Nakamoto K, Margoshes M, Rundle RE: Stretching frequencies as a function of distances in hydrogen bonds. *J. Am. Chem. Soc.* 1955;77:6480–6486.
- [24] Venyaminov S Yu, Prendergast F G: Water (H<sub>2</sub>O and D<sub>2</sub>O) molar absorptivity in the 1000–4000 cm<sup>-1</sup> range and quantitative infrared spectroscopy of aqueous solutions. *Anal. Biochem.* 1997;248:234.
- [25] Perumal S, Antipova O, Orgel J P R O: Collagen fibril architecture, domain organization, and triple-helical conformation govern its proteolysis. *Proc. Natl. Acad. Sci. U S A* 2008;105(8):2824–2829.
- [26] Shoulders M D, Raines R T: Collagen structure and stability. *Annu. Rev. Biochem.* 2009;78:929–958.
- [27] Kotch F W, Raines R T P: Self-assembly of synthetic collagen triple helices. *Proc. Natl. Acad. Sci. U S A*. 2006;103(9):3028–3033.
- [28] Kawahara K, Nishi Y, Nakamura S, Uchiyama S, Nishiuchi Y, Nakazawa T, Ohkubo T, and Kobayashi Y: Effect of hydration on the stability of the collagen-like triple-helical structure of [4(R)-Hydroxyprolyl-4(R)-hydroxyprolyl]glycine]. *Biochemistry*. 2005;44:15812–1522.
- [29] Bella J, Brodsky B and Berman H M: Hydration structure of a collagen peptide. *Structure*. 1995;3:893–906.
- [30] Bailey A J, Sims T J, Avery N C, Halligan E P: Non-enzymic glycation of fibrous collagen: reaction products of glucose and ribose. *Biochem. J.* 1995;305(Pt 2):385–390.
- [31] Bailey A J, Paul R G, Knott L: Mechanisms of maturation and ageing of collagen. *Mech. Ageing Develop.* 1998;106:1–56.
- [32] Bai P, Phua K, Hardt T, Cernadas M, and Brodsky B: Glycation alters collagen fibril organization. *Connect. Tissue Res.* 1992;28:1–12.
- [33] Hoeve C A J and Tata A S: The structure of water absorbed in collagen. *J. Phys. Chem.* 1978;82:1660–1663.

- [34] Ben-Naim A. *Molecular Theory of water and aqueous solutions. Part I: Understanding water.* World Scientific Publishing Co. Pte. Ltd., Singapore; 2010.
- [35] Cameron I L, Lanctot A C and Fullerton G D: The molecular stoichiometric hydration model (SHM) as applied to tendon/collagen, globular proteins and cells. *Cell. Biol. Int.* 2011;35:1205–1215.
- [36] Rath A, Davidson A R, Deber C M: The Structure of “Unstructured” Regions in peptides and proteins: role of the polyproline II Helix in protein folding and recognition. *Biopolymers (Peptide Science)*. 2005;80:179–185.
- [37] Matthews B W. In *The Proteins*, Neurath H & Hill R L, editors. 3rd Edition. Vol. 3: 403–590; Academic Press, New York: 1977.
- [38] Kocherbitov V, Arnebrant, and Söderman O: Lysozyme-water interactions studied by sorption calorimetry. *J. Phys. Chem. B.* 2004;108(49):19036–19042.
- [39] Shah N K and Ludescher R: Influence of hydration on the internal dynamics of hen egg white lysozyme in the dry state. *Photochem. Photobiol.* 1993;58(2):169–174.
- [40] Bridelli M G, Capelletti R, and Vecli A: Sequential hydration-dehydration studies of lysozyme by the thermally stimulated depolarization currents (TSDC) technique. *J. Biochem. Biophys. Methods.* 1992;24:135–146.
- [41] Careri G, Gratton E, Yang P H and Rupley J A: Correlation of IR spectroscopic, heat capacity, diamagnetic susceptibility and enzymatic measurements on lysozyme powder. *Nature.* 1980;284:572–573.
- [42] Barth A and Zscherp C: What vibrations tell us about proteins. *Q. Rev. Biophys.* 2002;35(4):369–430.
- [43] Bridelli M G, Capelletti R: Hydration structure analysis of lysozyme amyloid fibrils by thermally stimulated depolarization currents (TSDC) technique. *Spectroscopy.* 2008;22:165–176.
- [44] Bramanti E, Benedetti E: Determination of the secondary structure of isomeric forms of serum Albumin by a particular frequency deconvolution procedure applied to Fourier transform analysis. *Biopolymers.* 1996;38:639–653.
- [45] Madhusudan, and Vijayan M: Rigid and flexible region in lysozyme and the invariant features in its hydration shell. *Current Science (Bangalore)* 1991;60(3):165–170.



---

# Fourier Transform Hyperspectral Imaging for Cultural Heritage

---

Massimo Zucco, Marco Pisani and Tiziana Cavaleri

Additional information is available at the end of the chapter

<http://dx.doi.org/10.5772/66107>

---

## Abstract

Hyperspectral imaging is a technique of analysis that associates to each pixel of the image the spectral content of the radiation coming from the scene. This content can be helpful to recognize the chemical nature of the materials within the scene or to calculate their colours under particular conditions. Different solutions of hyperspectral imager have been realized with different spatial resolution, spectral resolution and range in the electromagnetic spectrum. In particular, improving the spectral resolution allows discriminating smaller features in the spectrum and the unambiguous detection of the absorption bands characteristic of superficial materials. Hyperspectral imagers based on interferometers have the advantage of having a spectral resolution that can be varied according to the needs by changing the optical path delay of the interferometer. A spectrum for each pixel is obtained with an algorithm based on the Fourier transform of the calibrated interferogram. We present the results of the application of a hyperspectral imager based on Fabry-Perot interferometers to the field of cultural heritage. On different artworks, the hyperspectral imager has been used for pigment recognition, for colour rendering elaborations of the image with different light sources or standard illuminants and for calculating the chromatic coordinates useful for specific purposes.

**Keywords:** hyperspectral imaging (HSI), fibre optics reflectance spectroscopy (FORS), cultural heritage, conservation, colour rendering, Fourier transform

---

## 1. Introduction

Hyperspectral imaging (HSI) is a powerful technique of analysis where each pixel of the image is associated with the spectral content of the radiation coming from the scene in the spectral band of interest. Different solutions with different spectral resolutions have been

---

adopted to separate the spectral content of the radiation impinging on the pixel: starting from the three bands of the Bayer filter camera [1], to the tens of bands with fixed bandpass filters like in the OSIRIS camera on Rosetta spacecraft [2] or hundreds or even thousands of bands of imagers based on dispersive means with gratings or prism like on the VIRTIS camera on Rosetta spacecraft [3]. In this work, we are interested in hyperspectral imagers based on interferometers: an interferometer is placed in the optical system in front of the camera, and while the optical path delay (OPD) of the interferometer is varied, the interferogram for each pixel is acquired by the camera and the spectrum is calculated with an algorithm based on the Fourier transform. The final attainable resolution in principle is only limited by the maximal optical path delay of the interferometer. HSI based on Michelson interferometers have been implemented with success in commercial instruments by Bruker [4] and Telops [5] ensuring more than 500 bands in the infrared region and reaching a resolution of less than  $1 \text{ cm}^{-1}$ . At INRIM, we have realized a different concept of HSI based on Fabry-Perot interferometer (FPI) and we have validated it in different regions of the spectrum: in the UV [6], in the visible [7] and in the near infrared [8] and in different applications [9].

In paragraph 2 of this chapter, we will describe the principle of the reflectance spectra calculation based on the Fourier transform. In paragraph 3, we will show the application of this technique to the field of cultural heritage in collaboration with Centre for Conservation and Restoration *La Venaria Reale* (CCR). Reflectance spectra indeed contain information useful for identifying pigments and dyes and thus for discriminating original and possibly superimposed materials (e.g. pictorial retouching) that is one of the main aims of a diagnostic campaign intended at preserving artworks and guiding the conservation treatment. Moreover, reflectance spectra can be used for rendering the artworks' colour appearance under different lights in order to choose the light source most suitable for enhancing some aesthetical aspects of the objects, for increasing the visitors' satisfaction, in the meantime taking into account the preventive conservation principles and the standard recommendations for lighting in museums. On the other hand, the possibility of studying the pigments' colour appearance can be of some help when choosing materials for the conservation treatment. Finally, spectra can be converted in colorimetric values for different light sources or standard illuminants useful for calculating chromatic differences for specific purposes. Results here presented concern some real artworks of different art periods (e.g. coffins from Ancient Egypt, Italian Renaissance polychrome artworks) and some mockups used as references made with known pigments and binders.

## 2. Fabry-Perot hyperspectral imager

Our hyperspectral imager (HSI) is based on a Fabry-Perot interferometer (FPI), the optical system is represented in **Figure 1** where the scene is firstly imaged in the FPI so that the transmitted intensity is modulated by the interference, and the second image is then formed on the camera sensor by means of the relay lens.

A sequence of frames carrying the interference fringe information is acquired synchronized with the scan of the optical path delay (OPD) between the mirrors of the FPI, from contact to the maximal distance of the mirror. For each pixel of the image, the interferogram is extracted from

the acquired video: as an example, we present the interferogram of a light-emitting diode (LED) at about 635 nm in **Figure 2** where it is evident the non-linearity of the actuators used to vary the OPD near the contact of the mirrors. The  $x$  axis of the interferogram is calibrated by using a laser in the optical setup. More details of the calibration technique are described in the previous work [10]. In **Figure 3**, we present the calibrated, resampled and rescaled interferogram.

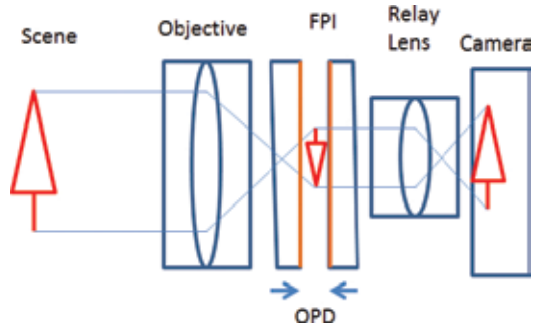


**Figure 1.** The scheme of the HSI: the FPI is inserted in an optical setup and the first image of the scene is formed in the FPI, where it is modulated by the interference and the second image with the interference is formed on the camera sensor. The optical path delay is changed while the image is acquired by the camera.

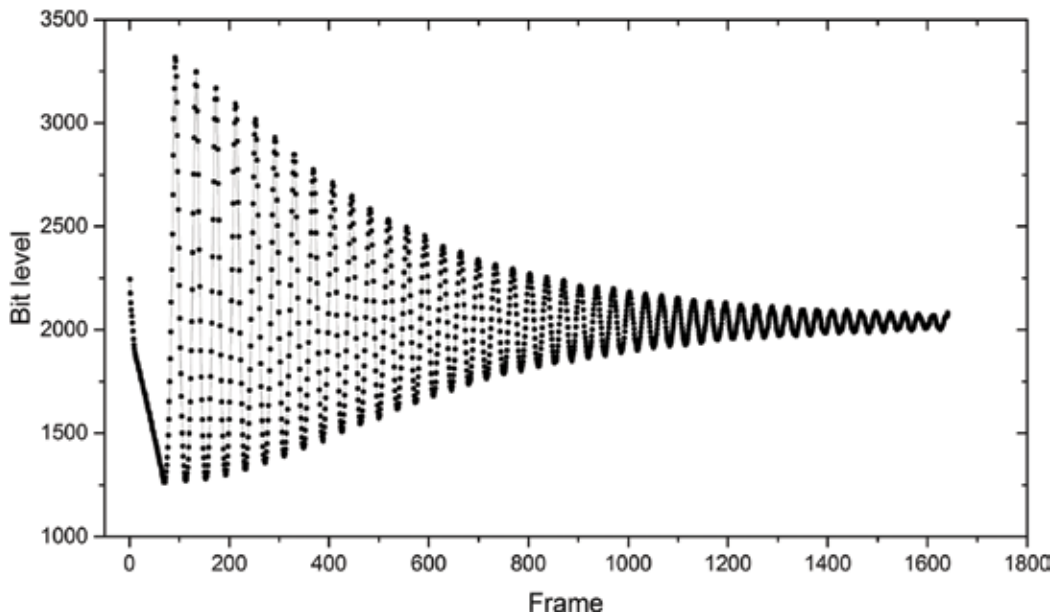


**Figure 2.** The interferogram extracted from the succession of frames of a LED at 635 nm. The  $x$  axis is the frame number. The first points of the interferogram are missing due to the penetration depth of the mirror coating.

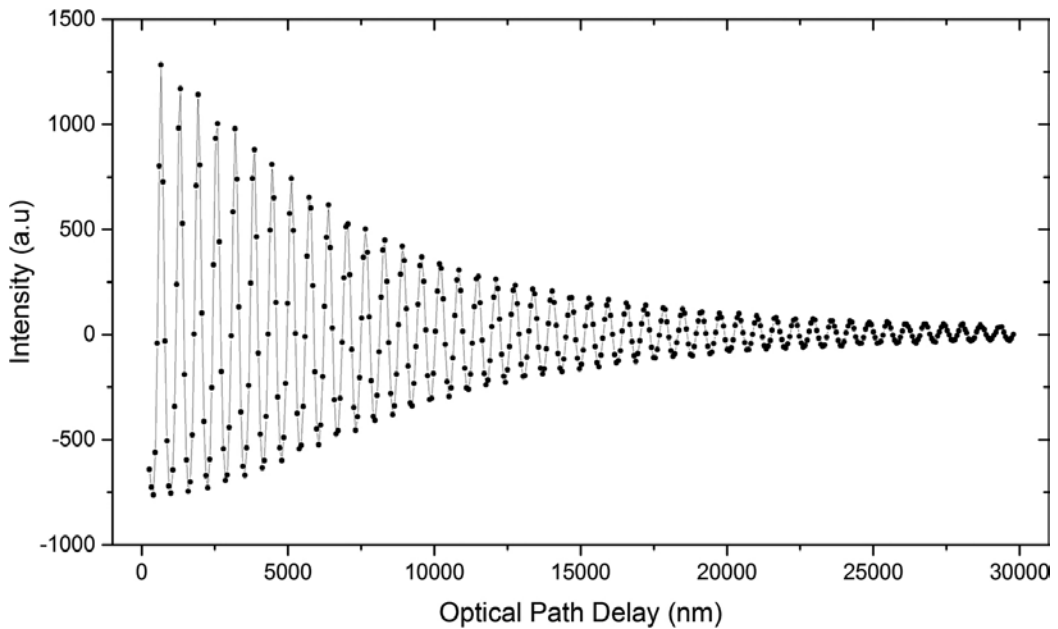


**Figure 3.** The calibrated, resampled and rescaled interferogram from **Figure 2**.

The first points of the interferograms are missing due to the penetration depth of mirror coatings, and according to Fourier transform theory, they correspond to the cosine contributions having the longest period in the spectra calculation. By inserting a bandpass filter in the optical setup and using the information that the spectrum has to be zero in certain regions of the electromagnetic spectrum, it is possible to find the amplitude of the missing points of the interferogram and reconstitute the original spectrum by applying the discrete Fourier transform (DFT) [10]. In **Figure 4**, we present the spectrum obtained from the DFT applied to the calibrated interferogram in **Figure 3** using the Hanning apodization function. The DFT spectrum is expressed in the frequency domain, and the spectrum of interest is in the band 400–720 nm (416–750 THz) according to the bandpass filter. The peak of the LED is at about 472 THz, corresponding to 635 nm, and since the base of the FPI is the Airy function, and not the cosine as in the Michelson interferometer, DFT creates the harmonics of the peak at 472 THz that decrease as  $R^n/n$ , where  $R$  is the reflectance of the mirrors and  $n$  is the order of the harmonic [11]. The interferogram in **Figure 3** is obtained with a maximal OPD of about 30  $\mu\text{m}$  that corresponds to a spectral resolution of about 10 THz. The frequency interval in the spectrum, as visible in the inset of **Figure 4**, is decreased below the spectral resolution by using the zero padding method [10]. A phase correction has been applied to the spectrum calculation in order to take into account the phase dispersion of the mirror coatings [11]. In the right side of spectrum are evident the aliases of the LED peak, artefacts of the DFT. The effect of aliases on the original spectrum is decreased by increasing the number of points per fringe and decreasing the reflectivity of the mirrors. Since the aliases of the LED peak have a phase dispersion that is not corrected they have deformed peaks.

Once a spectrum for each pixel is calculated, all the spectral information are stored in a hyper-spectral cube, a three dimensional array with the spatial information of the scene on the  $x$

and  $y$  axis, and the spectral content on the third axis. The hyperspectral cube contains all the spectral information that can be used for the applications of the next sections.

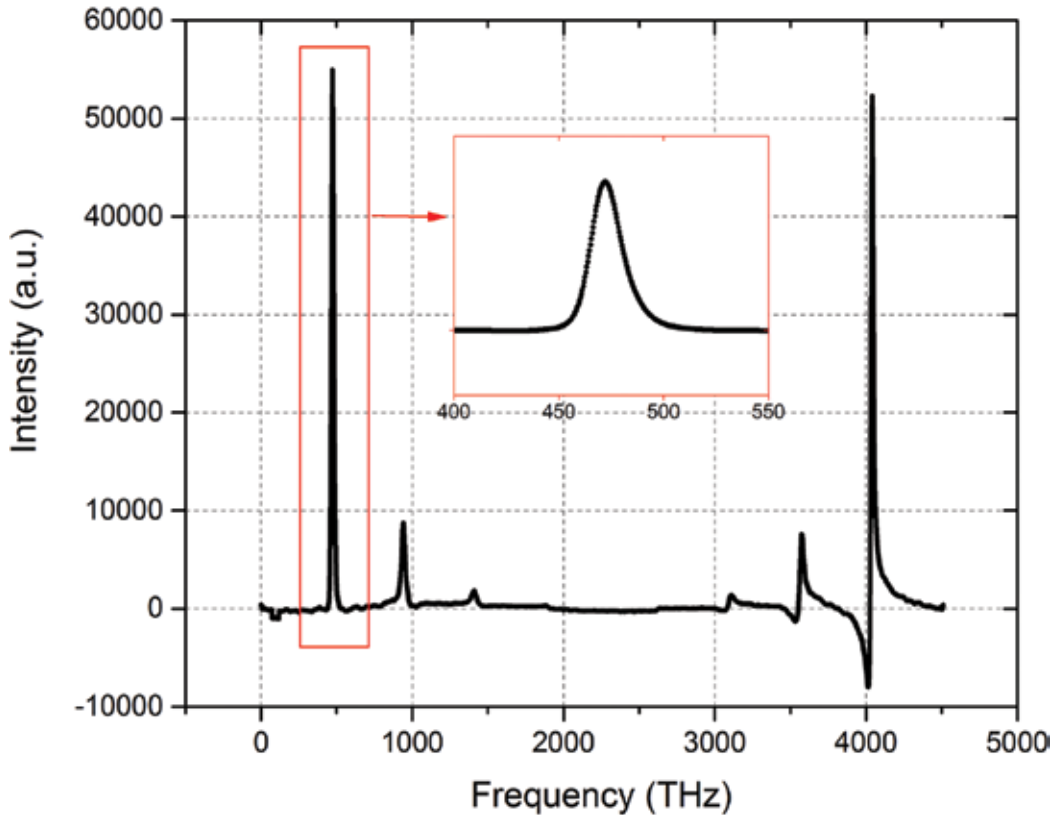


**Figure 4.** The spectrum in frequency of the LED from the interferogram of **Figure 3** by applying the DFT. Harmonics of the fundamental peak with decreasing amplitude are present. In the inset the spectrum of the LED of interest at 472 THz (635 nm).

### 3. Applications in cultural heritage

In the field of cultural heritage, the study of the artwork intended as physical object is very important for knowing constitutive materials, state of preservation and degradation phenomena. It is surely helpful for taking measurements suitable for the artwork conservation during the exposition, that is, in museums or art galleries, but also during possible conservation treatment. Moreover, it may provide precious information about the object's history and provenience, sometimes affecting its economic value.

This study normally implies the development of a diagnostic campaign through different analytical techniques, from the so-called *imaging* techniques to the *punctual*—noninvasive or micro-invasive, destructive or not destructive—chemical analyses. The main aims are to map

and chemically identify in the artwork both the original materials, with connected alteration and degradation phenomena, and the substances possibly superimposed during past interventions, such as pictorial retouching or inpainting.

Since the artwork is a unique piece, it has to be fully preserved and therefore the use of non-invasive diagnostic techniques is always preferred: on the contrary, the sample taken for analysis has to be limited because it is inevitably an irreversible operation. Luckily, from the interaction between artwork and radiation, many data about materials can be collected in a completely noninvasive manner.

Going beyond the traditional multispectral analyses, where few radiation bands are used for investigating materials, the HSI techniques represent the innovation so that they are making inroads as diagnostic tools [12, 13]: the possibility of combining the painting's image with the spectral information of each pixel has evident advantages in comparison with punctual analyses. The punctual analysis corresponding to the HSI is the fibre optic reflectance spectroscopy (FORS) [14–18]: for this reason, in the next case studies and applications, we will report the comparison between the spectra extracted from the hyperspectral cube to the ones coming from the spectrophotometer. In both kinds of spectra, it is possible to reveal characteristic peaks, shoulders or absorption bands [19]; the performance of the two instruments in material identification deeply varies depending on the wavelength range used [20, 21].

In the examples below, concerning artworks studied at CCR, FORS analyses were carried out in the 350–1000 nm band with 0.5 nm spectral resolution by means of an Ocean Optics HR2000+ES spectrophotometer, bounded by optical fibres of 400  $\mu\text{m}$  in diameter to an Ocean Optics HL2000 halogen lamp. Spectralon<sup>®</sup> 99% was used as white reference. Measures were acquired with a probe in  $45^\circ\text{x}/0^\circ$  geometry, so following the standard illuminating/viewing geometry defined by CIE (*Commission Internationale de l'Éclairage*) [22], on areas of fixed dimension (approximately 3 mm in diameter).

### 3.1. Study of the spatial resolution of HSI

As for other imaging techniques, the application of the HSI requires to choose the right distance between the camera and the object, an important parameter that inevitably determines the quality of the result.

In order to evaluate the spatial resolution performance of the HSI device here discussed [23], a small Flemish painting on copper (34 cm wide and 49 cm high, **Figure 5a**: “Passaggio del Mar Rosso”, inv. 299, *Musei Reali di Torino: Galleria Sabauda*), characterized by crowded and analytic composition with brilliant colours and very subtle brushes typical of the Flemish School was chosen for the test.

Interesting points/pixel areas of the painting were thus selected from the HSI cube, even in correspondence of very small paintbrushes, for extracting the interferogram and calculating the reflectance spectra; FORS analyses on the same points were carried out and used as comparison means for validating the results.

Placing the painting 120 cm distant from the HSI camera and illuminating the scene at  $45^\circ$  angle on the right by means of a halogen lamp, as for the FORS analyses, we acquired videos

framing about 10 cm x 10 cm painting areas. The image size is about 1000 pixel x 1000 pixel due to the aperture of the FPI.

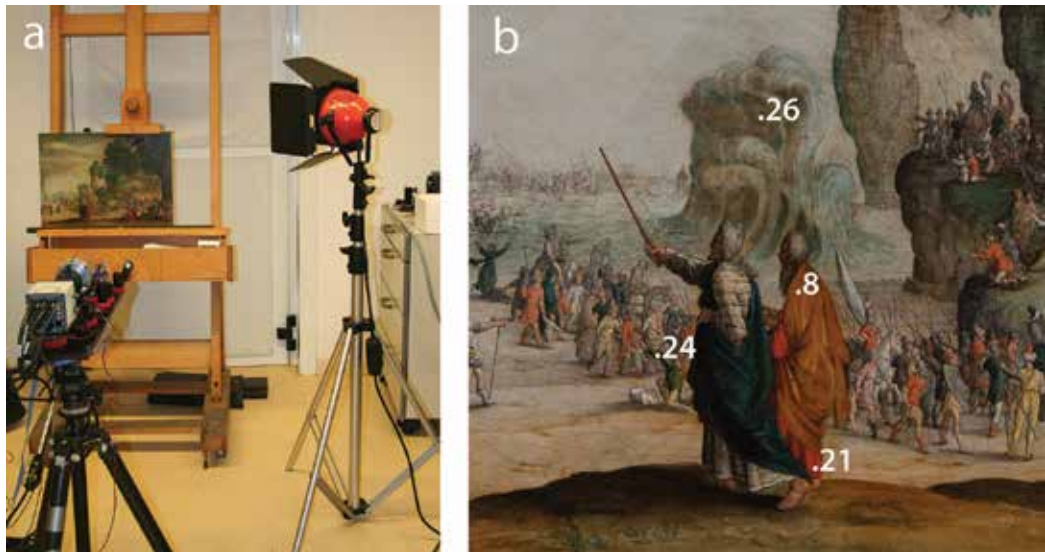


**Figure 5.** (a) Picture of the set during a hyperspectral video acquisition. (b) Main scene (numbers refer to the FORS analyses' measurement points); details of the painting "Passaggio del Mar Rosso" (inv. 299), *Musei Reali di Torino: Galleria Sabauda*.

Without changing the camera-object distance, we chose various scenes of the painting portrayed in different views in order to analyse paintbrushes of different size: for example, the main central scene displaying Moses (**Figure 5b**) has bigger homogeneous areas of paint. The crowded scene on the left is portrayed in the background and so it presents very small brushes (**Figure 6a**); the lateral scene on the right, portrayed in the foreground, has medium or small size details (**Figure 6b**). Reflectance spectra were extracted from the hyperspectral cube, attempting to select as most as possible homogeneous coloured pixel areas or paintbrushes. The examples in **Table 1**, reported as blue, green, yellow, orange, red and purple, called p1, p2, etc., are from 25 to 279 pixel areas. The smallest pixel area corresponds to a paintbrush that is about 0.5 mm x 0.5 mm. These videos took 180 s each, spatial resolution is about 100  $\mu\text{m}$  corresponding to about 250 ppi, spectral resolution is 10 THz.

FORS analyses were performed on the same selected areas (p1, p2, etc.) to verify the reliability of the results of the Fabry-Perot hyperspectral device when used as diagnostic tool. **Figures 7–9** report some examples: the correspondence among calculated HSI and FORS spectra is evident. In red areas of paint (p1 and p32), it is possible to recognize the flex at around 585 nm ascribable to the red pigment *cinnabar* (**Figure 7**). In the green area (p24), spectra suggest the presence of a green *copper-based* pigment (**Figure 8**); in purple area (p34), spectra show the double absorption band at around 530 and 560 nm ascribable to the use of *red lake* (**Figure 8**), probably coming from *cochineal* [24, 25]. In blue areas (**Figure 9**), spectra acquired in two

bands report the double absorption band at around 595 and 650 nm (p26) suggesting the presence of the smalt pigment [26, 27].

Actually, the spectrum of the green area p24 comes from the smallest pixel area, a paintbrush that on the painting is 0.5 mm × 0.5 mm, and so it defines the spatial resolution performance of the HSI system: it was possible to use this HSI instrument as diagnostic tool for pigment identification selecting areas of just 25 pixels.



**Figure 6.** (a) Lateral scene on the left; (b) lateral scene on the right (numbers refer to the FORS analyses' measurement points); details of the painting "Passaggio del Mar Rosso" (inv. 299), Musei Reali di Torino: Galleria Sabauda.

Painting detail	Selected areas	Image coordinates		Area size [pixel]	Area size [mm x mm]
		X	Y		
Main central scene ( <b>Figure 5b</b> )	Red (p1)	325–335	775–790	176	1.1 x 1.6
	Blue (p2)	122–130	990–1020	279	0.9 x 3.1
	Yellow (p10)	574–580	999–1006	56	0.7 x 0.8
Lateral scene on the left ( <b>Figure 6a</b> )	Red (p32)	1131–1139	715–719	45	0.9 x 0.5
	Purple (p34)	1245–1249	835–870	180	0.5 x 3.6
	Green (p35)	1065–1080	588–591	64	1.6 x 0.4
Lateral scene on the right ( <b>Figure 6b</b> )	Orange (p8)	317–321	288–297	50	0.5 x 1
	Red (p21)	294–301	406–415	80	0.8 x 1
	Green (p24)	156–160	314–318	25	0.5 x 0.5
	Graysh blue (p26)	258–264	94–103	70	0.7 x 1

**Table 1.** Description of the areas of paint selected in the details of **Figures 5a, 6a** and **6b**.

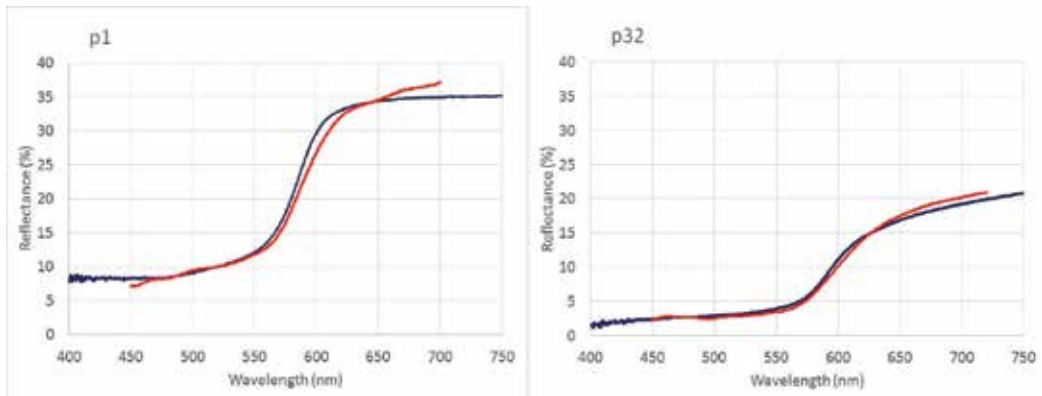


**Figure 7.** Spectral reflectance factor of the areas p1, p32 acquired by FORS (blue curves) compared to the ones calculated from the hyperspectral cube (red curves).

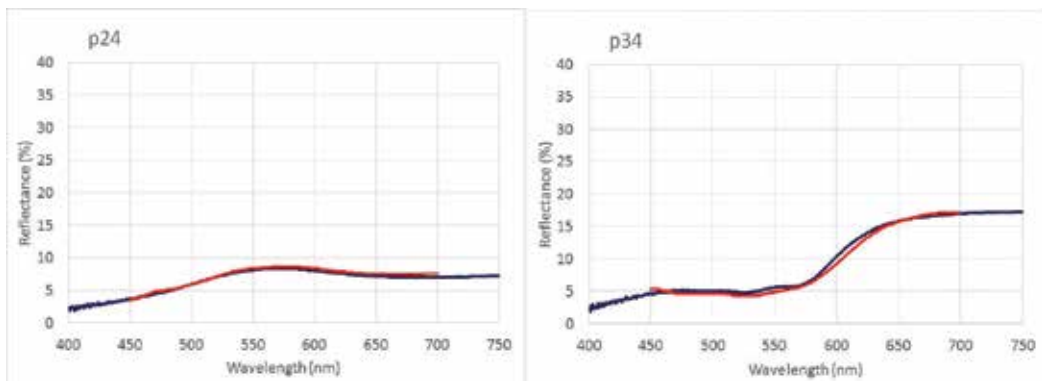


**Figure 8.** Spectral reflectance factor of the areas p24, p34 acquired by FORS (blue curves) compared to the ones calculated from the hyperspectral cube (red curves).

This feature will be helpful in the diagnostic investigation on Flemish, Divisionist or Pointillist paintings that present very small paintbrushes or glazing, but also on three-dimensional surfaces that may be difficult to reach with punctual contact instruments.

### 3.2. Study of the pigment recognition

Here we report two important case studies where the use of HSI for the comprehension about materials was fundamental. The first one refers to the noninvasive study of the “Croce astile” (*Museo Poldi Pezzoli*, Milan), attributed to Raffaello Sanzio (1483–1520). The second one refers to some Egyptian wooden coffins (*Museo Egizio*, Turin), dating back to the Third Intermediate Period (1070–712 BC approximately).

Concerning the wooden cross, it presents polychrome areas and gold leaf gilding. Figures of the saints are portrayed within rounded medals, one per each extreme of the cross on the front

and on the back; mouldings of the wooden support are along the perimeter and all around the medals (**Figure 10**).

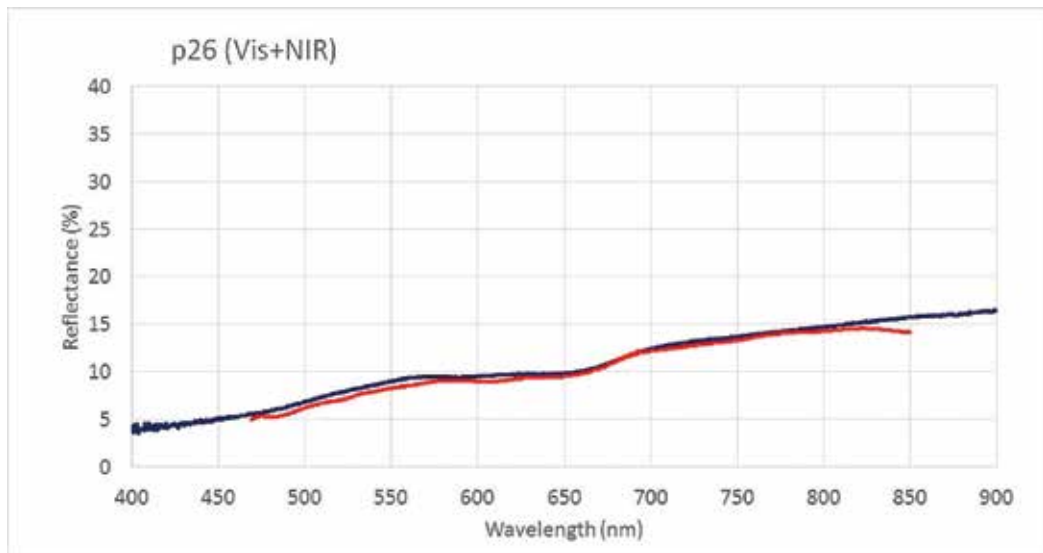


**Figure 9.** Spectral reflectance factor of the area p26 acquired by FORS (blue curve) compared to the ones calculated from the HS cube (red curve) in two bands (400–720 nm and 600–1000 nm) then combined together.

Because of the discontinuities of the support, the pigment identification by FORS, in particular on some lateral details nearby the moulding, would have been complicated since this technique normally requires putting the probe (usually of few centimetres in diameter) in contact with the artwork surface. Therefore, the hyperspectral imaging investigation was decisive.

Reflectance spectra extracted and calculated from the HSI cubes showed to be very helpful for pigment identification. The comparison and the integration with other complementary analyses, as required by an efficient diagnostic investigation, allowed the identification of the pictorial palette used for the cross. **Figure 11** reports the example showing the use of azurite in the blue backgrounds (blue curves), red lake in the pink stoles (red curves), Sienna earth in the brown hair (orange curves), green copper-based pigments in the green gowns (green curves), and ochre-based mixtures in the representation of the skin (grey curve).

Concerning the Egyptian coffins, the hyperspectral investigation allowed the rapid identification of the palette and the total pigment mapping over the surface thanks to the implementation of an algorithm built for recognizing similar reflectance spectra within the hyperspectral cube.

As known, paints of the same hue can have different saturation levels due to various factors, such as different amount of white pigment in the mixture or differences in the state of preservation. Therefore, the resulting reflectance spectra may change even if the main “coloured” pigment is the same. In fact, the possibility of identifying the pigment lies in the fact that the trend of the reflectance curve is recognizable, since it maintains the position of the absorption bands

fixed in the spectrum, while the percent reflectance values over the spectrum can vary more or less uniformly. **Figure 12** shows the example of two red ochre-based mixtures containing 50% and 90% in weight of white pigment. Converted in colorimetric coordinates expressed in the CIELAB 1976 colour space [22],  $L^*$  (lightness) increases when the paint is clearer, whereas  $a^*$  and  $b^*$  (hue) components maintain approximately constant values. From 50% to 90% of white,  $L^*$  passes from 33.6 to 38.9,  $a^*$  from 34.4 to 34.1 and  $b^*$  from 32.7 to 31.3 (measures obtained by a Konica Minolta CM700d colorimeter in D65, SCE and  $d/8^\circ$  condition).



**Figure 10.** Hyperspectral imaging session on the wooden cross “Crocce astile” attributed to Raffaello Sanzio (*Museo Poldi Pezzoli, Milan*).

In imaging acquisition as in HSI, moreover, the intensity of the light source may be not so uniform over the artwork, so that the reflectance spectra have a vertical scaling. Aiming at obtaining the pigment clustering and recognition from the spectrum analysis, independently of the light intensity, a metric has to be defined in order to measure the similarity of two spectra, represented as vectors in the vector space formed by the spectral components. A vertical scaling of the spectrum would change the length of the vectors without changing the direction in the vector space. We consider the metric, and the closeness of two vectors, as the angle between the two vectors using the spectral angle mapper (SAM) technique [28]. **Figure 13** shows the

false colours elaboration coming from hyperspectral cube acquired on the lid of an anthropoid coffin (Museo Egizio, S. 05239): red and yellow ochres/earths, Egyptian blue and copper green, commonly used in Ancient Egypt, have been identified and their distribution over the coffin surface is highlighted by the false colours. The lower part of the figure shows the red, green, blue (RGB) image composed of two HSI cubes and rendered for a standard illuminant (D65).

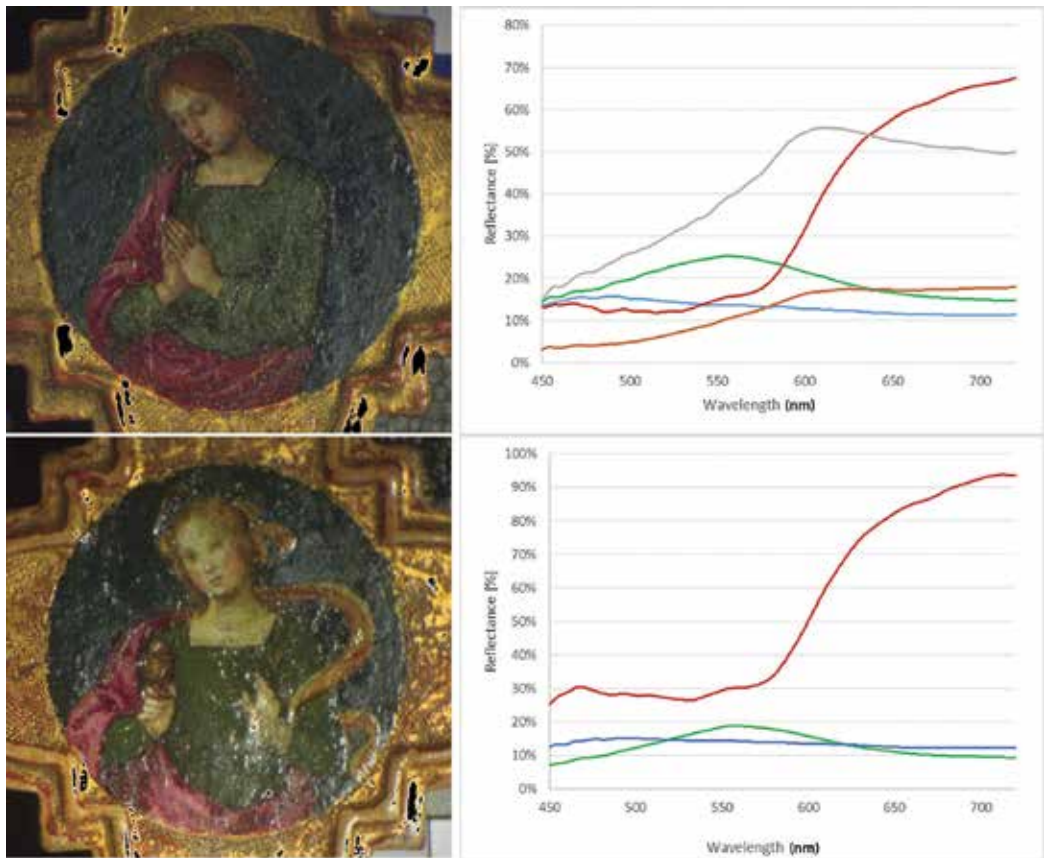


**Figure 11.** Details of the wooden cross “Croce astile” attributed to Raffaello Sanzio (*Museo Poldi Pezzoli, Milan*). Hyperspectral images calculated for D65 illuminant and 10° standard observer, with reflectance spectrum extracted from the HS cubes.

### 3.3. Study of the colour rendering

Another important advantage of the hyperspectral imaging is the possibility of using the HSI data for colour rendering operations. This means that the RGB image of the artwork may be calculated starting from the reflectance spectrum of each pixel, as shown previously.

If necessary, by correcting the spatial non-uniformity (in intensity) of the illumination, it is possible to obtain “hyperspectral images” of the artworks where each spectrum depends only

on the pictorial material's characteristics, and it is not affected by the light source (neither the quality, nor the intensity) used during the acquisition.

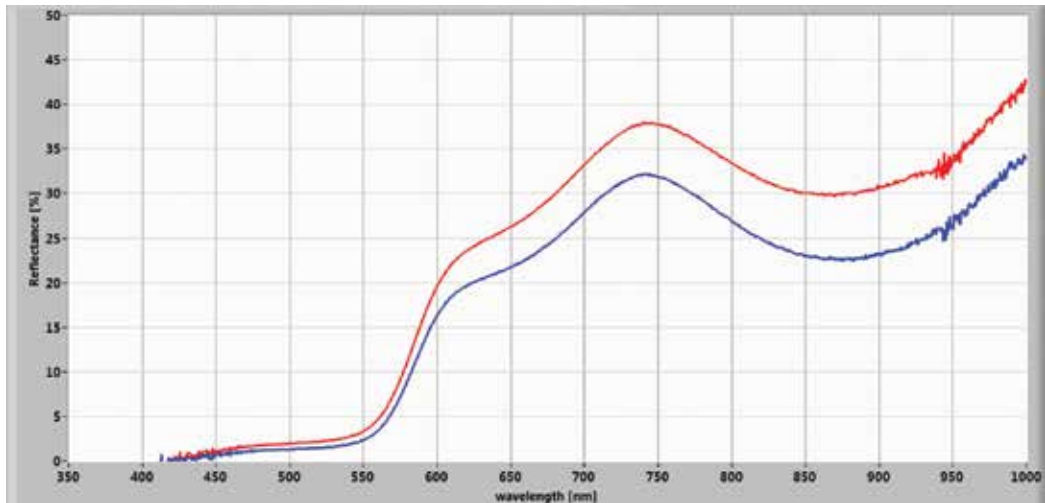


**Figure 12.** Reflectance spectra of red ochre-based mixtures acquired by FORS, containing 50% in weight (blue line) and 90% in weight (red line) of white pigment (calcium carbonate).

In this way, it is possible to calculate and render the hyperspectral (HS) image for the lamp you prefer, simply by choosing the emission spectrum for the illumination you want to simulate (i.e. CIE standard illuminants, or commercial light sources, depending on the purpose).

In the conservation field, the possibility of studying how the artwork—or more generally, a pictorial material—would appear under different illumination conditions represents a real advantage not only for the aspects linked to the exhibition lightening but also for the choice of pigments for conservation. In fact, the pictorial retouching and the inpainting made in laboratory shall appear different outside it, losing their harmony with the original painting.

The case study of the painting “Gesù tra i dottori” attributed to Giovanni Battista Beinaschi (1636–1688), belonging to the *Castle of Racconigi* (province of Cuneo, Italy), is particularly significant for this aspect. The surface presents many lacunae, at present filled with stucco, that have to be inpainted at CCR. In **Figure 14**, we present two different details from the painting calculated from the HSI cube, the detail on the left is acquired using a xenon lamp and rendered with a D65 illuminant, with standard CIE 10° observer, on the right a particular acquired using a halogen lamp and rendered with an LED4000K illuminant, with standard CIE 10° observer.

It is not so easy to find pigments “suitable” for the inpainting treatment. Light plays an important role, obviously, also on the in-painting’s colour appearance, and often we know very few about the lighting system of the museum.

Based on some selected pigments and light sources, we exploited the HSI data for giving an evaluation of the colour appearance variability. Just to make an example, **Figure 15** shows

the HSI images of two mockups, the one on the left made of copper blue (Kremer Pigmente GmbH & Co. KG, n° 45364), the one on the right made of Zirconium Cerulean Blue (n° 45400). Images are rendered with one halogen lamp (3000 K) and with some different, from “warm” to “neutral” white, LED sources (LED 3000K, typical light source in art galleries or museums simulating halogen lamp; LED 2700 K and LED 4000 K).



**Figure 13.** False colours hyperspectral image, portion of lid of an anthropoid coffin (*Museo Egizio*, Turin, inv. S. 05239), picture of the lid (up); combination of two portions of the lid, HS image rendered for a standard illuminant (D65).

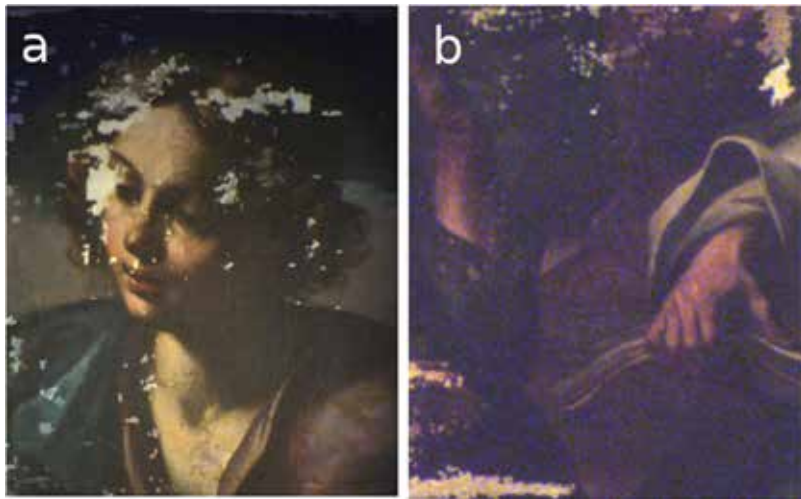


**Figure 14.** Detail of the painting “Gesù tra i dottori” attributed to Giovanni Battista Beinaschi (1636–1688), belonging to the *Castle of Racconigi* (province of Cuneo, Italy). (a) Image acquired using a xenon lamp and rendered with a D65 illuminant, with standard CIE 10° observer, (b) image acquired using a halogen lamp and rendered with a LED 4000K illuminant, with standard CIE 10° observer.

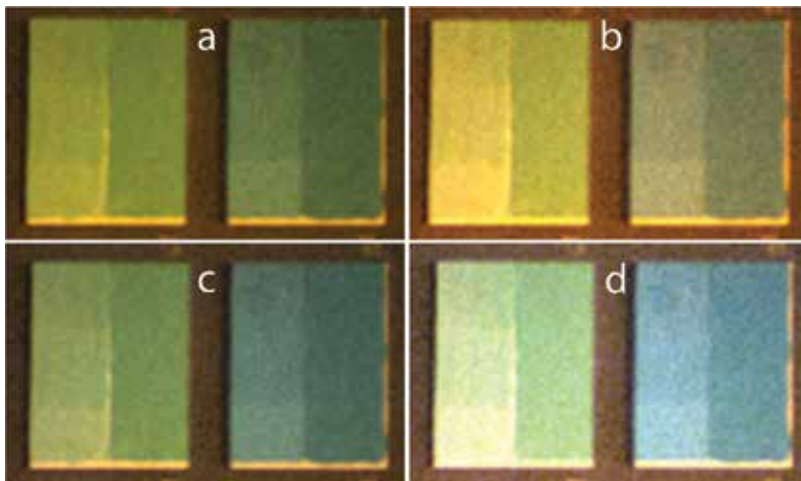


**Figure 15.** Hyperspectral image of two mockups: copper blue in polyvinyl acetate (PVAc, left column) and in linseed oil (right column); zirconium cerulean blue in PVAc (left column) and in linseed oil (right column). (a) Images are rendered for the halogen 3000 K lamp, (b) the 3000K LED, (c) the 2700K LED, and (d) the 4000 K LED..

Beyond the visual comparison that would be surely affected by many factors (first of all by the computer screen), the HSI images allows to extract the colorimetric values of the mockups for each lamp and to find which one has the minimum chromatic variability. In this case, the zirconium cerulean blue presents a slightly lower variability with respect to the copper blue and relatively to the four lamps tested (**Table 2**).

MOCKUPS D65/10°	Copper blue in PVAc		Copper blue in oil		Zirconium blue in PVAc		Zirconium blue in oil					
	L*	a*	b*	L*	a*	b*	L*	a*	b*			
halogen 3000 K	52.1	-23.3	-29.0	44.6	-23.7	-26.1	67.3	-20.6	-6.3	56.7	-23.5	-5.4
LED 3000 K	53.2	-22.0	-27.8	45.6	-22.6	-24.8	67.7	-20.2	-5.3	57.1	-23.3	-4.4
LED 2700 K	51.3	-21.8	-30.7	43.8	-22.4	-27.6	66.5	-20.8	-7.5	55.8	-23.8	-6.8
LED 4000 K	53.5	-19.2	-27.2	45.9	-20.1	-24.1	67.9	-19.0	-4.9	57.3	-22.0	-3.9
Average	52.5	-21.6	-28.7	45.0	-22.2	-25.6	67.4	-20.2	-6.0	56.7	-23.2	-5.1
Standard deviation	1.0	1.7	1.5	1.0	1.5	1.5	0.6	0.8	1.1	0.7	0.8	1.3

**Table 2.** Colorimetric coordinates (CIELAB 1976 colour space) of mockups reported in **Figure 15**.

Obviously, only the precise knowledge of the museum lighting system, that will host the artwork, would be the key for the right consideration about materials, to prefer in the conservation treatment. We think this example may show the system potentiality and its precious contribution in the choice of pigments and binders for restoration and in promoting interventions that might consider not only the chemical properties of the materials but also the colour appearance.

#### **4. Future work**

The opportunity of collecting, in very little time and in noninvasive and contactless modality, the spectral information of the entire artwork is undoubtedly an advantage of the HSI technique with respect to punctual analyses. When the aim is the material identification, the wavelength range used for the investigation surely affects the system performance. In this case, we worked in two bands, covering the range from 420 to 1000 nm, but the use of wider ranges can surely improve the performance of the HSI for identifying also organic materials, such as consolidating materials [29], natural polymers and resins [30], or to map paint binders in situ [31].

Moreover, HSI offers the possibility of calculating the colours of the artwork in a more controlled way: some attempts have been made for applying this technique to the digital documentation of the artworks through the production of high-quality images [32], maybe comparable to professional photographs.

Probably the future, natural development of the hyperspectral imaging may be the integration of the HSI in 3D acquisition systems that will solve the problem of not flat surfaces.

#### **5. Conclusion**

Hyperspectral imaging (HSI) based on a Fabry-Perot interferometer showed to be a powerful technique of analysis in the field of cultural heritage, providing at the same time the artwork's image and the spectral behaviour of each pixel. This has evident advantage with respect to punctual analysis as fibre optics reflectance spectroscopy (FORS) in terms of time spending for pigment recognition. Nevertheless, the system performance in the identification of materials strictly depends on the wavelength range used for the analysis: aware of that, the most recent research is intended to enlarge the investigation range in order to study in imaging modality specific features in particular of organic materials. Further HSI applications were tested on the artworks at CCR for elaborating the images rendered with different light sources or illuminants, in order to enhance particular aspects of the materials, such as for highlighting the areas with pictorial retouching. The hyperspectral data were shown to be useful also for calculating colorimetric coordinates for different light sources permitting a better evaluation of the pictorial materials to use in the conservation treatment.

## Acknowledgements

The authors like to thank the *Museo Poldi Pezzoli* (Milan), *Museo Egizio* (Turin), *Ministero dei Beni e delle Attività Culturali e del Turismo - Musei Reali di Torino*, *Castle of Racconigi* (province of Cuneo) and *Polo Museale del Piemonte* which promoted the diagnostic campaign on their artworks. The authors want to acknowledge Dr Gabriele Piccablotto, LAMSA, Department of Architecture and Design, Polytechnic of Turin for sharing the emission spectra of the light sources used for the colour rendering elaborations. A special thanks to the conservators that took care of the artworks and all the staff of CCR La Venaria Reale for availability and useful discussions.

## Author details

Massimo Zucco<sup>1\*</sup>, Marco Pisani<sup>1</sup> and Tiziana Cavaleri<sup>2</sup>

\*Address all correspondence to: m.zucco@inrim.it

1 National Institute of Metrological Research, Strada delle Cacce, Turin, Italy

2 Centre for Conservation and Restoration La Venaria Reale, Venaria Reale, Province of Turin, Italy

## References

- [1] Dillon P L, Lewis D W, Kaspar F G: Color imaging system using a single CCD area array. *IEEE Transactions on Electron Devices*. 1978;**25**:102–107.
- [2] Keller HU et al.: OSIRIS–The scientific camera system onboard Rosetta. *Space Science Reviews*. 2007;**128**:433–506.
- [3] Coradini A et al: VIRTIS: An imaging spectrometer for the Rosetta mission. *Space Science Reviews*. 2007;**128**:529–559.
- [4] Braun R, Harig R. Identification and mapping of spilled liquids by passive hyperspectral imaging. *Proc. SPIE 8546, Optics and Photonics for Counterterrorism, Crime Fighting, and Defence VIII*, 85460F (October 30, 2012); doi:10.1117/12.974496.
- [5] Kastek M et al. Method of gas detection applied to an infrared hyperspectral sensor. *Photonics Letters of Poland*. 2012;**4**(4):146–148.
- [6] Zucco M, Caricato V, Egidi A, Pisani M. A hyperspectral camera in the UVA band. *IEEE Transactions on Instrumentation and Measurement*. 2015;**64**(6):1425–1430.
- [7] Pisani M, Zucco M. Compact imaging spectrometer combining Fourier transform spectroscopy with a Fabry-Perot interferometer. *Optics Express*. 2009;**17**(10):8319–8331.
- [8] Pisani M, Bianco P, Zucco M. Hyperspectral imaging for thermal analysis and remote gas sensing in the short wave infrared. *Applied Physics B*. 2012;**108**(1):231–236.

- [9] INRIM. [http://www.inrim.it/res/hyperspectral\\_imaging](http://www.inrim.it/res/hyperspectral_imaging), accessed date 28/11/2016.
- [10] Pisani M, Zucco M: Fourier transform based hyperspectral imaging, in *Fourier Transforms - Approach to Scientific Principles*, Prof. Goran Nikolic (Ed.), InTech, 2011, DOI: 10.5772/15464.
- [11] Zucco M, Pisani M, Caricato V, Egidi A. A hyperspectral imager based on a Fabry-Perot interferometer with dielectric mirrors. *Optics Express*. 2014;**22**(2):1824–1834.
- [12] Liang H. Advances in multispectral and hyperspectral imaging for archeology and art conservation. *Applied Physics A*. 2012;**106**(2):309–323.
- [13] Legrand S et al. Examination of historical paintings by state-of-the-art hyperspectral imaging methods: from scanning infra-red spectroscopy to computed X-ray laminography. *Heritage Science*. 2014;**2**(1):2–13.
- [14] Bacci M et al. Non-invasive spectroscopic measurements on the *Il ritratto della figliastra* by Giovanni Fattori: identification of pigments and colourimetric analysis. *Journal of Cultural Heritage*. 2003;**4**:329–33.
- [15] Casini A et al. Fiber optic reflectance spectroscopy and hyper-spectral image spectroscopy: two integrated techniques for the study of the *Madonna dei Fusi*. *Proc. SPIE 5857, Optical Methods for Arts and Archaeology*, ed Salimbeni and Pezzati, Munich, Germany, 58570M (August 12, 2005); doi:10.1117/12.611500.
- [16] Poldi G. Ricostruire la tavolozza di Pellizza da Volpedo mediante spettrometria in riflettanza. In: *Il colore dei Divisionisti. Tecnica e teoria, analisi e prospettive di ricerca*; ed A. Scotti, Tortona (It), 30 Sept. 2005, 2007. p. 113–128.
- [17] Montagner C et al. Library of UV-Vis-NIR reflectance spectra of modern organic dyes from historic pattern-card coloured papers. *Spectrochimica Acta Part A: Molecular and Biomolecular Spectroscopy*. 2011;**79**(5):1669–1680.
- [18] Depuis G, Menu M. Quantitative characterization of pigment mixtures used in art by fiber-optics diffuse-reflectance spectroscopy. *Applied physics A*. 2006;**83**:469–474.
- [19] Johnston-Feller R. *Color science in the examination of museum objects: nondestructive procedures*. The Getty Conservation Institute, Los Angeles, Publications ed. 2001.
- [20] Berns R, Imai F. The use of multi-channel visible spectrum imaging for pigment identification. In: *ICOM Committee for Conservation, editor. 13th Triennial Meeting Rio de Janeiro, Vol 1*; 2002. p. 217–222.
- [21] Kubik M. Hyperspectral Imaging: a new technique for the non-invasive study of artworks. *Physical Techniques in the Study of Art, Archeology and Cultural Heritage*. 2007;**2**:199–259.
- [22] Oleari C. *Misurare il colore*, pp 53–60, Hoepli, Florence Italy. 2008.
- [23] Caricato V, Egidi A, Pisani M, Zucco M. A device for efficient hyperspectral imaging for color analysis. In: *Rossi, Maggioli, editors. Colour and Colorimetry: Multidisciplinary Contribution, 10th Conferenza del Colore, Vol. X B*; 2014. p. 13–18.

- [24] Bisulca C et al. UV-VIS-NIR reflectance spectroscopy of red lakes in paintings. In: 9th international conference on NTD of Art, Jerusalem Israel. 2008.
- [25] Gulmini M et al. Identification of dyestuffs in historical textiles: strong and weak points of a non-invasive approach. *Dyes and Pigments*. 2013;**98**(1):136–145.
- [26] Gil M et al. Blue pigments colors from wall paintings churches in danger (Portugal 15th to 18th century): identification, diagnosis and color evaluation. *Applied Spectroscopy*. 2011;**65**(7):782–789.
- [27] Dik J. Scientific analysis of historical paint and the implications for art history and art conservation: the case studies of naples yellow and discoloured smalt, Thesis of Van 't Hoff Institute for Molecular Sciences, Amsterdam Holland; 2003.
- [28] Kruse FA et al. The spectral image processing system (SIPS) - interactive visualization and analysis of imaging spectrometer data. *Remote Sensing of Environment*. 1993;**44**(1):145–163.
- [29] Bonifazi et al. Study of consolidant materials applied on wood by hyperspectral Imaging. In: International Society for Optics and Photonics, editors. *SPIE Commercial+ Scientific Sensing and Imaging*; 2016. pp. 98620I–98620L.
- [30] Vagnini M et al. FT-NIR spectroscopy for non-invasive identification of natural polymers and resins in easel paintings. *Analytical and bioanalytical chemistry*. 2009;**395**(7):2107–2118.
- [31] Ricciardi P et al. Near infrared reflectance imaging spectroscopy to map paint binders in situ on illuminated manuscripts. *Angewandte Chemie International Edition*. 2012;**51**(23):5607–5610.
- [32] Cucci C et al. A hyper-spectral scanner for high quality image spectroscopy: Digital documentation and spectroscopic characterization of polychrome surfaces. In: ART11-10th International Conference on Non-destructive Investigations and Microanalysis for the Diagnostics and Conservation of Cultural and Environmental Heritage; 2011.

---

# New Spectral Applications of the Fourier Transforms in Medicine, Biological and Biomedical Fields

---

Anca Armășelu

Additional information is available at the end of the chapter

<http://dx.doi.org/10.5772/66577>

---

## Abstract

This chapter reviews some recent spectral applications of the Fourier transform techniques as they are applied in spectroscopy. An overview about Fourier transform spectroscopy (FTS) used like a powerful and sensitive tool in medical, biological, and biomedical analysis is provided. The advanced spectroscopic techniques of FTS, such as Fourier transform visible spectroscopy (FTVS), Fourier transform infrared-attenuated total reflectance (FTIR-ATR), Fourier transform infrared-photoacoustic spectroscopy (FTIR-PAS), Fourier transform infrared imaging spectroscopy (FTIR imaging), and their biomedical applications are described. A special attention has been paid to the description of the FTVS method of commercial quantum dots like an innovative and reliable technique used in the field of nanobiotechnology.

**Keywords:** Fourier transform, Fourier transform visible spectroscopy, Fourier transform infrared spectroscopy, biological and biomedical applications, nanobiotechnology

---

## 1. Introduction

Fourier transform (FT) represents one of the oldest and the most powerful analytical tools in many fields such as applied mathematics, physical sciences, and engineering. Because FT helps to describe the physical mechanism of collecting and reconstructing data, it also becomes a priceless image-processing instrument in other areas which are related to biomedicine. The development of FT techniques pushed the utilization of the spectroscopic methods dramatically. So, FT methods have long been proved to be extremely useful in all fields of science and technology, such as radio-astronomy, seismology, spectroscopy crystallography, medical image processing, and signal analysis techniques.

---

Particularly, Fourier transform spectroscopy (FTS) has become an innovative, powerful, and extra sensitive method to study biologically important systems, varying from simple molecules to highly complex samples such as living cells and tissues. These enhanced spectroscopic methods in their modern form represent an important area of research with various applications in diverse fields of science and industry.

The main purpose of this chapter is to provide a modern review about the recent advances on FTS technique with a wide range of medical, biological, and biomedical applications. This chapter begins with a short history about FTS, followed by a description of the theoretical background of FTS with emphasis of some remarkable new results of the research of the quantum dots (QDs) based on Fourier transform visible spectroscopy (FTVS).

After a short historical presentation of the evolution of the important discoveries in the field of the Fourier transforms, the basic ideas of the FT theory are briefly reviewed. In what follows, the power of the Fourier transforms is illustrated through new spectral applications in medicine, biological, and biomedical areas.

In this present chapter, the Fourier transform spectroscopic techniques discussed in the chapter and their important physical principles will be described, that is, Fourier transform spectroscopy, such as Fourier transform visible spectroscopy, Fourier transform infrared-attenuated total reflectance (FTIR-ATR), Fourier transform infrared-photoacoustic spectroscopy (FTIR-PAS), Fourier transform infrared imaging spectroscopy (FTIR imaging), and Fourier transform ion cyclotron resonance mass spectrometry (FTICR-MS).

This review is focused on presenting new developments in FTS technique sample preparation methods, experimental conditions used in these investigations, and its useful applications in various fields of biomedical and biological research, including examples of recent advances in the area of nanobiotechnology. Among many other various products of nanotechnology, semiconductor nanocrystals or quantum dots are useful for biomedical research and applications.

Nanobiology, as an area of study, represents the fusion of the biological research with the nanotechnologies such as nanodevices and nanoparticles. This combination of nanotechnology with biology has resulted in the development of diagnostic tools, contrast agents, physical therapy applications, and targeted drug delivery vehicles [1].

Nanomedicine is the medical application of nanotechnology and involves the programs for the application of newly emerging nanotechnologies to molecular processes at the cellular level. The applications of this area of nanoscience include drug delivery, both *in vitro* and *in vivo* diagnostics, nutraceuticals, and production of biocompatible materials. An important device to achieve a series of applications is the engineered nanoparticles [2].

By grouping the study into these areas of research, the general modalities in which the nanotechnology, biology, medicine, and FTS methods are brought together for common research purposes can be noticed.

In this sense, an FTS system able to evaluate optical properties of the CdSe/ZnS core-shell QDs, produced by Evident Technologies, is presented. So, by the use of ARCSpectroHT-HR

Fourier transform spectrometer (ARCOPTIX S.A. Switzerland), the fluorescence spectra of QDs for two excitation sources (a UV laser and a blue LED) are discussed [3]. This study reveals that the FTVS of commercial quantum dots is used to show that CdSe/ZnS core-shell QDs are an example of nanomaterial that is useful such as an alternative to classical fluorochromes in order to label microbial cells.

In another research work, the FTVS is presented like a novel, rapid, and efficient technique to provide quantitative information about the QDs, including their sizes. The use of FTVS methodology for the size determination of CdSe/ZnS core-shell QDs can be easily extended to other types of QDs. Some relationships between the QD size and its corresponding fluorescence average wavelength, calculated from each emission peak of the Fourier transform spectrum, are discussed in this study [4]. The characterization of QD dimension with the help of the FTVS is important in their preparation procedures and their applications.

The reference list contains both historical and extensive analysis works together with the articles that describe several key breakthroughs in the mentioned areas of interest.

## **2. Advanced applications of Fourier transform methods in spectroscopy**

### **2.1. Historical background**

Integral transforms history begins in the eighteenth century, when Jean Le Rond D'Alembert used the overlapping of some sine functions in order to describe the oscillations of the violin strings. In 1822, Joseph Fourier published the book entitled "Théorie analytique de la chaleur" ("The analytical theory of heat") [5]. After James Clerk Maxwell found the equations of the electromagnetic field in 1873, the use of Fourier analysis became crucial for the study of the electromagnetic waves and their harmonic components [6].

In 1954, the French mathematician Laurent Schwartz introduced a new theory of generalized functions named distributions, using the extension of Fourier transform in the study of the tempered distributions [7].

The FT shows a powerful time-frequency duality. This property was used in 1983 by the American mathematician Charles Louis Fefferman in the paper entitled "The uncertainty principle." In his work, Fefferman deduces important results of quantum mechanics using multidimensional Fourier approach [8].

The FT has long been proved to be extremely useful as applied to spectroscopy in all research fields which require high resolution and high wavelength accuracy and broad tunability. These spectroscopic methods that use the FT are considered FTS. FTS is a well-known spectroscopic method where interferograms are collected based on measurements of the coherence of an electromagnetic radiation source in time domain or space domain and converted into the frequency domain through FT.

A Fourier transform spectrometer is a Michelson interferometer invented by Albert A. Michelson in 1880 [9] with a moving mirror at one arm. Using this instrument, Michelson

elaborated the fundamental techniques of FTS [10, 11]. The advantages of the FT spectrometers that are superior to the prism and grating ones are well known. These are the advantages of Fellgett (an increase in a signal value of signal-to-noise ratio due to the simultaneous registration of all the spectral elements [12]), Jacquinot (a greater light efficiency at a given resolution [13]), and Connes (the accuracy of the frequency determination obtained by the control of mirror displacements in the interferometer with a helium-neon laser [14, 15]).

Drs. J.E. Chamberlain, J.E. Gibbs, and H.A. Gebbie improved the Michelson interferometer equipment for molecular spectroscopy used to study the experiments on ozone and in the upper atmosphere. Their group developed the asymmetric Fourier transform spectroscopy technique for the measurement of the refractive indices of gases, liquids, and solids [16].

In 1964, Dr. Paul L. Richards constructed a lamellar grating interferometer which is a Michelson interferometer and proved that this instrument is a highly effective tool at low wave numbers [17]. In 1965, the invention of the fast Fourier transform (FFT) algorithm by J.W. Cooley and J.W. Tukey represented an important date for Fourier spectroscopy. The Cooley-Tukey algorithm reduces the calculation time by several orders of magnitude when compared to the classical Fourier transform [18]. In 1966, D.L. Forman published a paper that treats the implementation of the FFT algorithm in Fourier spectroscopy [19].

Only the significant historical data for the development of the FTS technique were presented here. The history of the field of the FTS shows the great utility of this promising and strongly developed instrument. The FTS method rapidly developed in the last decades. FTS is an analytic spectroscopic method with applications in astronomy, physics, physical chemistry, chemistry, chemical engineering, optics, biology, medicine, and nanotechnology.

FTS can be applied to a broad diversity of kinds of spectroscopy such as Fourier transform visible spectroscopy, Fourier transform infrared-attenuated total reflectance, Fourier transform infrared-photoacoustic spectroscopy, Fourier transform infrared imaging spectroscopy, and Fourier transform ion cyclotron resonance mass spectrometry.

## 2.2. New applications of Fourier transform visible spectroscopy in nanobiotechnology

In this part of the chapter, the Fourier transform visible spectroscopy of commercial quantum dots is briefly presented [3]. The fluorescence spectra of QDs produced by Evident Technologies were studied in the case of the existence of two excitation sources (a UV laser and a blue LED) with the help of ARCspectro HT-HR Fourier transform spectrometer. Due to the quantum confinement effect, QDs are semiconductor nanocrystals which exhibit significant optical characteristics such as high photostability, fluorescence properties with broad absorption spectra, size-dependent narrow emission spectra, and slow excited-state decay rates, thus leading to major breakthroughs in microbiology, molecular and cell biology, and medical diagnostics [20–22]. Among many other various products of nanotechnology, QDs are suitable to be used in various biological and biomedical researches as the next-generation fluorescent probes for detection and imaging applications.

In addition to the research results mentioned above, a relevant biological application of CdSe/ZnS core-shell QDs as microbial labeling both for pure cultures of cyanobacteria (*Synechocystis*

PCC 6803) and for mixed cultures of phototrophic and heterotrophic microorganism was presented in the same paper [3]. Different semiconductor nanocrystals, such as CdSe/ZnS core-shell QDs dispersed in toluene with long-chain amine-capping agent, that were used in some studies, which analyze the Fourier transform spectra of these QDs [3, 4], were acquired from Evident Technologies. The QDs have the dimensions in the domain of (3–5) nm and the emission in the range (490–600) nm.

The Fourier transform spectra of QDs were studied using the experimental device shown in **Figure 1**. The experimental setup comprised the sources of excitation (a blue or a UV source), the sample (QD) containing quantum dots, the optical fiber (OF) that transmits the fluorescence signal, and the Fourier transform spectrometer which is acted by a computer [3].

ARCspectro HT-HR (ARCOPTIX S.A. Switzerland) is a Fourier transform spectrometer which is used to record the fluorescence spectra. This static Fourier transform spectrometer is based on the operating principle of the so-called common path polarization interferometer which measures the coherence function of the light. The interference image, which is formed at the output of the device, is recorded with the help of a charge-coupled device (CCD) detector array. The light spectrum is calculated using the computer with a Fourier transform algorithm and calibration tables. The ARCSpectro HT-HR shows the extraordinary advantage which is given by the fact that the high luminosity of the system is (50–100) times greater than

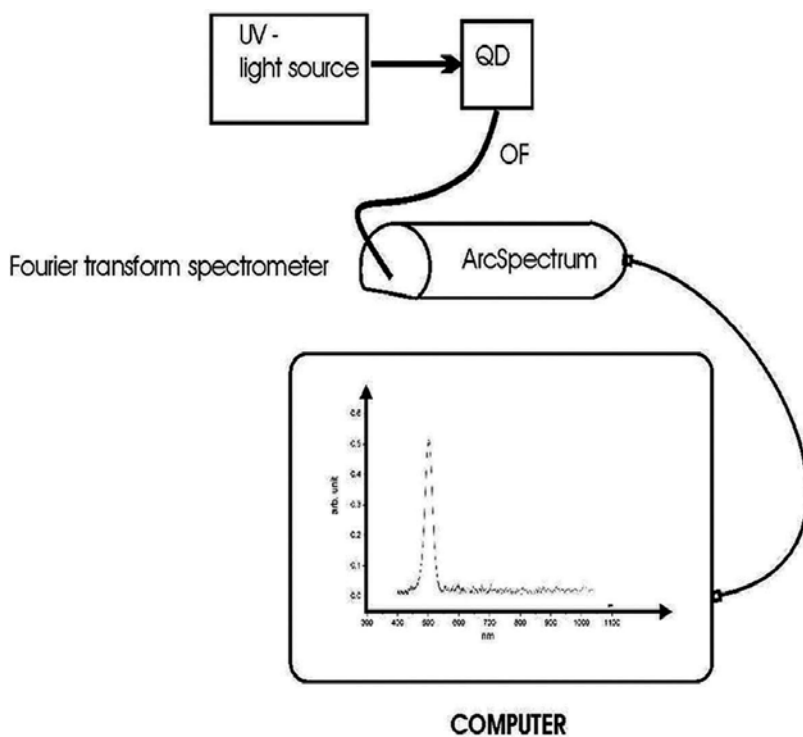


**Figure 1.** The schematic diagram of the fluorescent emission spectroscopy system [3].

a grating one. An advantage of this Fourier transform spectrometer, which is useful for certain applications, is the fact that fiber and collimation optics are not absolutely necessary.

Using FTVS, the emission properties of four kinds of CdSe/ZnS core-shell QDs (0490, 0520, 0560, and 0600 Evidot fluids) were analyzed and were evaluated [3, 4]. Each of **Figures 2–4** displays a Fourier transform spectrum which shows the manner in which the QDs are irradiated by the light from a NdYAG@355 nm laser or from a luminescent diode ( $\lambda = 480$  nm). The calculation of the average wavelengths from each emission peak of the spectra of QDs for two excitation sources was reported [3, 4].

**Figure 2** shows the Fourier transform spectra of the 0490 Evidot fluid, for two situations. First situation treats the case of the enlightenment the probe with the laser light from an NdYAG@355 nm, obtaining the fact that the maximum of the peak intensity corresponds to an average wavelength calculated at 500 nm. The second situation presents the case where the fluorescence wavelength, which corresponds to a maximal value of the intensity, has the value of 511 nm, when the sample is illuminated with a luminescent diode ( $\lambda = 480$  nm) [3].

For the Fourier transform spectra of the 0520 Evidot, it was observed that for UV laser excitation, the average fluorescence wavelength was 510 nm, while for the excitation with blue LED light, the corresponding average wavelength of fluorescence was calculated at 525 nm [4].

The Fourier transform spectra of the 0560 Evidot in **Figure 3** illustrate that for the illumination with laser light, the average fluorescence wavelength was 572 nm and for the excitation with blue LED light, the corresponding average wavelength of fluorescence was the 588 nm [3].

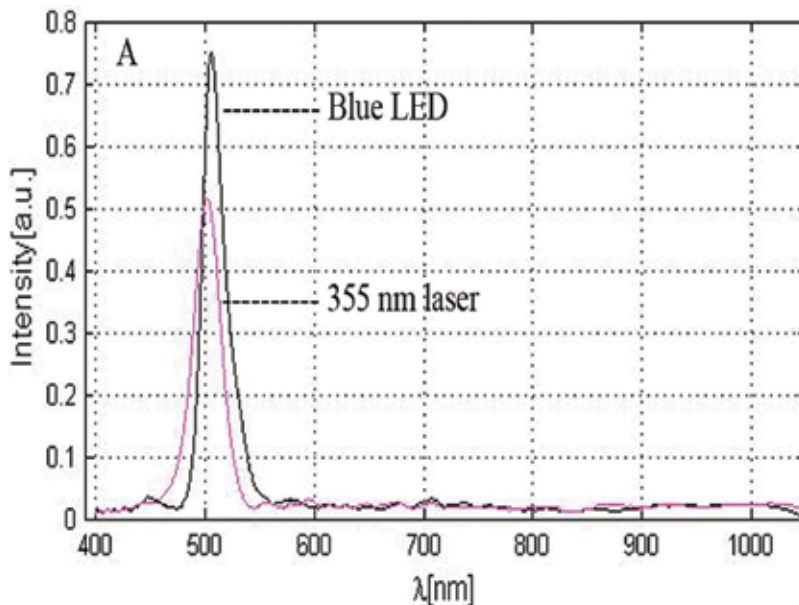


**Figure 2.** The Fourier transform spectra of CdSe/ZnS core-shell QDs of the 0490 Evidot fluid type in the case of two excitation sources: a laser (NdYAG@355 nm) and a luminescent diode ( $\lambda = 480$  nm) [3].

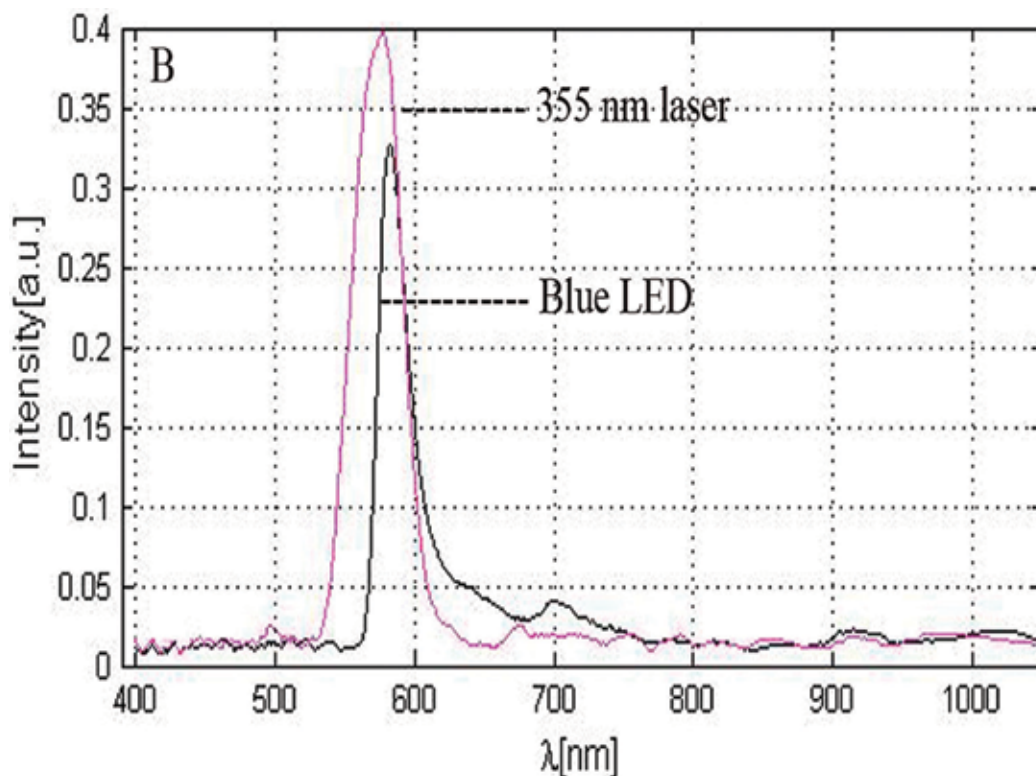


**Figure 3.** The Fourier transform spectra of the 0560 QDs fluid in the situation of two excitation sources: a laser (NdYAG@355 nm) and a blue LED [3].

In **Figure 4**, the Fourier transform spectra of the 0600 Evidot are shown. When the probe was irradiated with the laser light, the average value of the emitted light was 614 nm and in the case of the blue LED the average wavelength was 634 nm [3].

**Figure 5** presents five Fourier transform spectra obtained in the case of a probe of 0520 Evidot suspension with the concentration 23 ml QDs in 3 ml toluene in a quartz container for the following values of the energy emitted by the laser: 1, 3, 8, 18, and 25 mJ, respectively [3].

In this section, several important aspects of previous research studies of the author of this chapter regarding the investigation of the optical properties of QDs and their role as fluorescent probes for different biological and medical applications using an FTVS system that helps to study the spectral characteristics of the fluorescence emission have been revised.

Another significant research direction in this review, which must be mentioned in this study, is the discovery of some fast and reliable methods for the determination of the QD size. Such a method, which assists at the evaluation of the diameter of commercial CdSe/ZnS core-shell QDs, is FTVS technique. Due to the high sensitivity and simplicity, FTVS has numerous performance advantages over conventional methods, in providing qualitative and quantitative information about QDs, including their sizes.

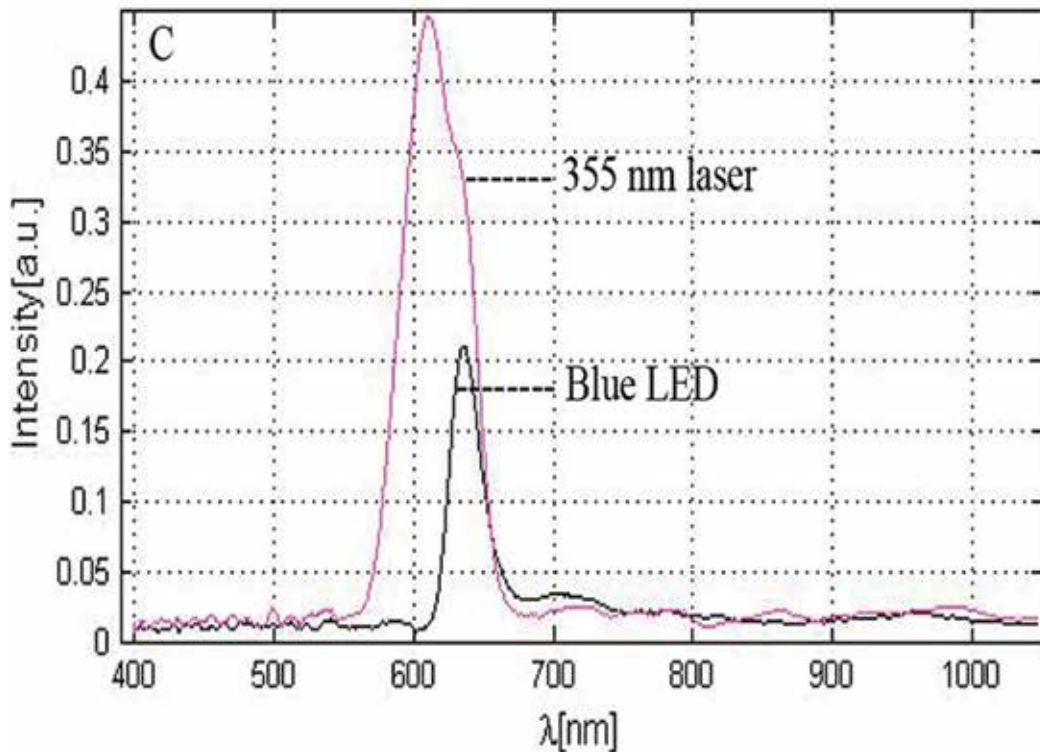


**Figure 4.** The Fourier transform spectra of the 0600 QDs fluid for two excitations sources that were used in the research paper [3].

In Ref. [4], the relationship between the QD size and its calculated fluorescence average wavelength of corresponding Fourier transform spectrum is discussed. So, the dependence of the dimension of the QDs and excitation conditions of the maxima of the fluorescence emission were analyzed with the help of FTVS. In this research, the empirical equations that fit these dependences aiming to elaborate a simple and trustworthy technique for the determination of the dimension of QDs, besides conventional techniques, were obtained.

The measurements required for FTVS method were made by means of the ARCSpectro HT-HR (ARCOPTIX S.A. Switzerland) Fourier transform spectrometer. The major components of the experimental system were elaborately presented in [3, 4]. This investigation method proposed in [4] helps to estimate the dimensions of core-shell CdSe/ZnS QDs of a certain type and their fluorescence features which are determined by the wavelength of each peak of fluorescence.

In **Figure 6**, a triplet of the fitting curves of the QD size with their emission wavelength is represented. The fitting functions of the curves (a)–(c) from **Figure 6** were built by utilization of the interpolating polynomials from Mathematica software.

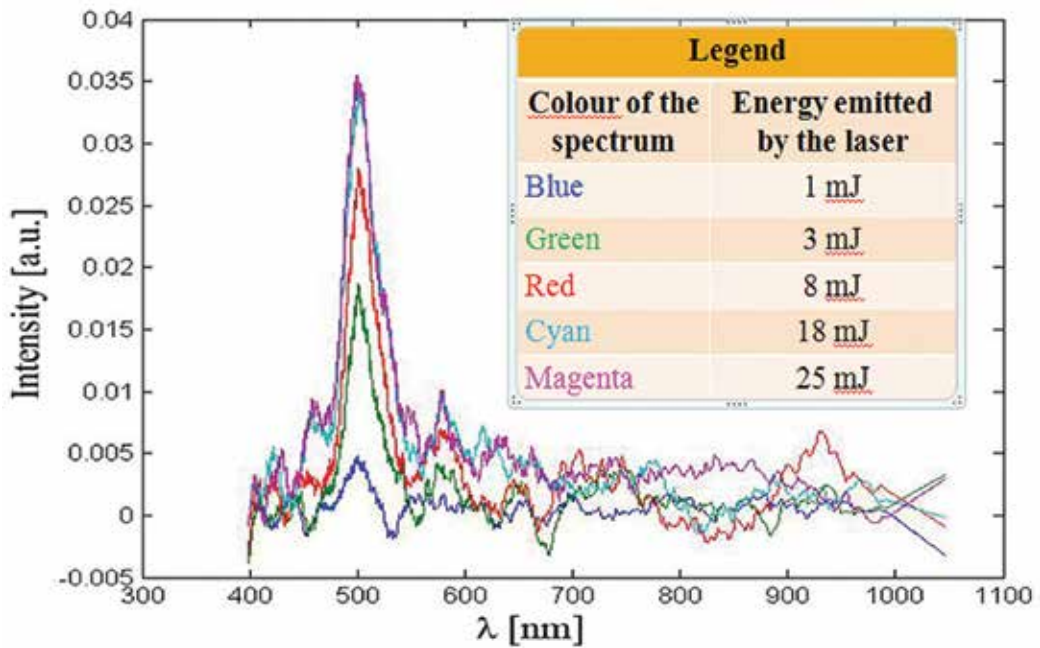


**Figure 5.** Five presented smoothed Fourier transform spectra for the case of increasing values of the laser energy. The height of the main peaks grows and the main fluorescence band considerably broadens with the increasing of the values of the laser energy [3].

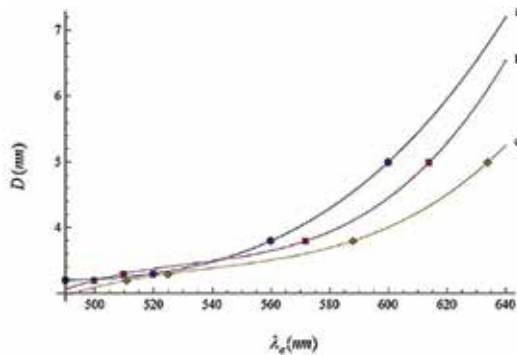


**Figure 6.** Sizing curves for CdSe/ZnS core-shell QDs. Solid lines (a–c) represent the fitting curves illustrated by Eqs. (1)–(3), while the symbols used for points (circles, squares, and rhombs) on curves refer to the catalog data (curve a) and experimental data (curves b and c) [4].

Eq. (1), which represents the fitting function of curve (a) from **Figure 6** and was constructed by fitting the known diameters,  $D$ , of CdSe/ZnS QDs versus the values of the emission wavelengths,  $\lambda_e$ , from the Evident Technologies catalog specifications, is given by

$$D_{CdSe/ZnS} = (7.9816 \times 10^{-7})\lambda_e^3 - (1.12216 \times 10^{-3})\lambda_e^2 + (5.25882 \times 10^{-1})\lambda_e - 78.9545 \quad (1)$$

By fitting the known sizes of different CdSe/ZnS core-shell QDs versus the experimental data of the emission wavelengths found in [3, 4] with the help of FTVS method for QDs enlightened by the laser light from a NdYAG@355 nm (curve b) or by the blue LED (curve c), the empirical fitting functions of curves (b) and (c) were obtained as can be seen in **Figure 6**.

$$D_{CdSe/ZnS} = (1.96547 \times 10^{-6})\lambda_{e_b}^3 - (3.13626 \times 10^{-3})\lambda_{e_b}^2 + (1.67384)\lambda_{e_b} - (295.338) \quad (2)$$

$$D_{CdSe/ZnS} = (1.27001 \times 10^{-6})\lambda_{e_c}^3 - (2.05218 \times 10^{-3})\lambda_{e_c}^2 + (1.11082)\lambda_{e_c} - (198.023) \quad (3)$$

In Eqs. (2) and (3),  $D_{CdSe/ZnS}$  (nm) denotes the diameter of the core-shell QDs and  $\lambda_{e_b}$ ,  $\lambda_{e_c}$  (nm) represent the values of the fluorescence average wavelengths, calculated from each emission peak of the Fourier transform spectra for those two excitation sources that were used [3, 4].

It should be pointed that unlike other studies the obtained empirical formulae refer to the whole core-shell QD diameter and comprise both the thickness of CdSe hard-core and the thickness of ZnS shell. In Ref. [4], it has been proved that FTVS is a simple, rapid, and efficacious technique for the size evaluation of the core-shell QDs. The procedure analyzed could be developed for the dimension determination of other fluorescent nanoparticles.

### 2.3. Recent applications of Fourier transform infrared spectroscopy in medical, biological, and biomedical sphere

Fourier transform infrared spectroscopy represents a fundamental and a reliable technique, with many potential useful applications in the area of biology and medicine, thanks to its nonperturbative and highly sensitive features.

FTIR spectroscopic method analyzes the wavelength of the light absorbed by the probe at certain vibrational frequencies. The spectrum produced in this way, which is peculiar for the biological material exposed to radiation in this method, represents a "molecular fingerprint." More exactly, the biological materials such as carbohydrates, proteins, lipids, nucleic acids, biomembranes, animal tissues, microbial cells, plants, and clinical samples possess unique structures leading to the obtaining spectral fingerprints according to their functional groups, bends, and molecular structure [22]. So, FTIR can be used to detect structural changes of individual amino acid residues, backbone peptides, binding ligands, chromophores, and internal water molecules [23]. The application of FTIR to biological problems is continuously extending, thus evolving from the study of isolated biological molecules to the study of more sophisticated and complex systems, such as diseased tissues.

Also, FTIR is a suitable and a well-established standard technique utilized to study nanoparticles coupled with molecules in order to use them for drug delivery systems, for targeting strategy, or for bioimaging scopes [24].

Recent methods of FTIR are Fourier transform infrared-attenuated total reflectance, Fourier transform infrared-photoacoustic spectroscopy, Fourier transform infrared imaging spectroscopy, and Fourier transform infrared microspectrometry (FTIR microspectrometry).

In the late 1980s and 1990s, Nauman and his collaborators [25, 26] reinsert the FTIR techniques in order to analyze *in situ* the bacterial cells and to identify, differentiate, and classify bacteria [27]. Since then, FTIR spectroscopy has been proved to be a preferred and a valuable tool for characterization and for differentiation of microorganisms. The FTIR spectra furnish highly accurate spectroscopic fingerprints of microbial strains permitting a rapid and reliable identification at both species and subspecies level [28].

The identification of microorganisms in a rapid and simple way is a vital task for the food safety and quality in a processing retail, or production environment. Conventional plating, biochemical, and serological tests represent traditional techniques that have several stages and that can last a long period of time until the obtaining of the confirmatory results. Because of the fact that FTIR techniques produce biochemical fingerprints of bacteria in a short period of time, there is therefore an encouragingly large goal for study on the use of FTIR spectroscopy in the area of food microbiology.

FTIR methods combined with various chemometric analyses procedures [28–30] can be applied to the field of medical applications, pharmaceutical industry, and food microbiology, comprising the detection of bacteria from culture and food, discrimination between various microbial species and strains, classification of a diversity of microorganisms at genus, species, and subspecies levels, bacteria viability analysis, characterization growth-dependent phenomena and cell-drug interactions, investigation *in situ* intracellular components or structures such as inclusion bodies (IBs), storage materials, or endospores [31]. Because in biological and in medical field, protein aggregation represents an important issue encountered in the expression of recombinant proteins in bacterial cells in the form of IBs and in some diseases, the monitoring *in vivo* of the kinetics of protein aggregation in *Escherichia coli* within intact cells using the FTIR spectroscopy methods constitutes a fast and a facile technique used to acquire structural information on proteins within IBs [32].

Due to its rapidity, simplicity, and high sensitivity, FTIR spectroscopy technique can also be utilized for the identification and differentiation of the most frequent yeast species isolated from infected human mouth/vagina, chronic disease cows, crop mycosis in chicken, and soil contaminated with pigeon droppings [33]. Based on the research results published by some authors, the feasibility of FTIR for identification of *Candida*, *Cryptococcus*, *Trichosporon*, *Rhodotorula*, and *Geotrichum* isolated from humans and animals [33–35] has been proved.

The FTIR-attenuated total reflection technique is based on the interaction between IR light and an absorbing sample at its interface. ATR is a specialized sampling technique where the sample is situated in contact with an ATR crystal which has a high refractive index material. As a result of the phenomenon of total intern reflection of light produced at the interface between the ATR crystal and a sample of lower refracting index, an evanescent wave is formed which extends into the sample. The sample absorbs at discrete IR frequencies which leads to the attenuation of the incident IR light. Therefore, the infrared spectra of solid or liquid samples in their native state are obtained by combining ATR with FTIR [36, 37].

The release of the drugs in semisolid and solid formulations, the penetration of the drug into artificial and biological membranes, and the influence of penetration modifiers *in vivo* studies are investigated with the FTIR-ATR method [36, 38]. FTIR-ATR is utilized for the examination

of the structure of the stratum corneum (SC) at the molecular level for the estimation of the penetration enhancers which grow the permeation of the drugs through the human SC and for the analysis of its lipids, proteins, and water content [36, 39].

Genistein (GEN; 4, 5, 7-trihydroxyisoflavone), which is also known as phytoestrogen because it has similar structure with the human hormone  $17\beta$ -oestradiol, represents a powerful tyrosine kinase inhibitor that has been widely utilized in order to prevent and to cure many diseases and disorders such as cardiovascular disease, osteoporosis, and cancer [39, 40]. Recent results [40, 41] have shown that using FTIR-ATR technique helps to discover new ways for the improvement of the transdermal transport of a lyotropic liquid crystal genistein-based formulation (LLC-GEN). In order to increase the transdermal drug transport, LLC-GEN was coupled with electroporation (EP). So, in Ref. [40] the synergistic effect of EP in the case of the hairless mouse skin with the help of FTIR-ATR has been proved.

The FTIR-ATR method is among characterization techniques of surfaces used to investigate new properties of the nanomaterials for various biomedical applications including the implant applications. In this sense, in order to investigate the interactions of nanomaterials with biological systems such as proteins, FTIR-ATR is used to provide information about the changes in the surface chemistry after certain nanotechnology-based chemical or physical after treatments are applied with the aim of the contribution to the regeneration of the different tissues (such as those of bone, cartilage, vascular, and neural systems) [42, 43].

The potential of the FTIR method combined with photoacoustic spectroscopy and diffuse reflectance spectroscopy (DRS) was exploited for the applications in the detection of the fungi and the mycotoxins which represent a severe cause of food poisoning in humans and animals. More exactly, there are some recent studies that show the usefulness of FTIR-PAS technique for the identification of corn kernels infected with fungi *Fusarium moniliforme* and *Aspergillus flavus* [44].

FTIR-PAS also provides the possibility to obtain information about the drug mechanism and the barrier function of SC in order to implement them to the biomedical and cosmetic applications [36, 45].

Recently, by coupling the FTIR techniques with imaging methods, a correlation of the biochemical information such as protein misfolding and metal homeostasis was reached, which has resulted in understanding of the mechanism of the neurodegenerative protein misfolding disease including Alzheimer's disease, Parkinson's disease, Huntington's disease, and multiple sclerosis [46, 38].

Fourier transform ion cyclotron resonance mass spectrometry (FTICR-MS) represents one of the most advanced and complex techniques of mass analysis and detection. FTICR-MS is a powerful tool which can be utilized to find masses with high accuracy. Many applications of FTICR-MS utilize the mass accuracy like a very important parameter in order to find the composition of the molecules based on accurate mass. FTICR-MS has been shown to provide important clues regarding the nontargeted metabolic profiling and functional characterization of novel genes [47, 48]. The compilation of the high mass accuracy and the ultra-high-resolving power of FTICR-MS is ideal for the resolving of the analytical problems of the complex-mixed analyses encountered in proteomics [49, 50] and petroleomics [50, 51].

Electrospray ionization Fourier transform ion cyclotron resonance mass spectrometry (ESI FTICR-MS) represents an emerging method which helps to analyze the biological macromolecules, like in the case of the investigation of non-covalent interactions of proteins [52].

Electron capture dissociation (ECD) represents a relatively new technique used for the analysis of peptides and proteins and is a method utilized for inducing fragmentation in FTIR-MS [50]. ECD combined with FTIR-MS represents a powerful and useful technique in proteomic studies.

In some successful advanced works [51, 53], new techniques are described for the deployment of the improved electron injection methods. So, in Ref. [53, 54] the improvement of the overlap of ion, photon, and electron beams in the ICR ion trap is reported, using the compressed hollow electron beam injection technique.

Collision-induced dissociation (CID) and infrared multiphoton dissociation (IRMPD) are traditional methods that are used to induce fragment spectra in tandem mass spectrometry analyses. CID and IRMPD generate the dissociation of the peptides by breaking the backbone amide linkages [55]. When applying ECD fragmentation technique, co- and post-translational modifications within the peptide and protein sequence are maintained, as opposed to the using of those two methods, namely CID and IRMPD, which may provoke dissociation of post-translational modifications [55]. This fact is important for the application of ECD to glycosylation [56, 57], sulfation [56, 57], and phosphorylation analysis [56, 58].

### 3. Conclusions

This chapter represents a reference review for Fourier transform methods as they are applied in spectroscopy. More exactly, the work concerns an overview of the current status, of the recent achievements in FTS spectroscopy, and some selected new applications of FTS in the medical, biological, and biomedical fields, with the emphasis on the own work done by the author of this chapter.

The confluence of Fourier transform spectroscopy methods with nanotechnology, biology, and medicine opens new opportunities for the detection and handling of the atoms and molecules using nanodevices, with potential for a large variety of biological and medical applications at the cellular level.

### Author details

Anca Armășelu

Address all correspondence to: [anca\\_armaselu@yahoo.com](mailto:anca_armaselu@yahoo.com)

Faculty of Electrical Engineering and Computer Science, Department of Electrical Engineering and Applied Physics, Transilvania University of Brasov, Brasov, Romania

## References

- [1] Alharbi KK, Al-Sheikh YA. Role and implications of nanodiagnostics in the changing trends of clinical diagnosis. *Saudi J. Biol. Sci.* 2014; 21(2): 109–117. DOI: 10.1016/j.sjbs.2013.11.001
- [2] Tibbals HF. *Medical Nanotechnology and Nanomedicine*. Ed. CRC Press: Taylor & Francis Group; 2010. 528 p. DOI: 10.1201/b10151
- [3] Damian V, Ardelean I, Armășelu A, Apostol D. Fourier transform spectra of quantum dots. *Proc. SPIE*, 2010; 7469. DOI: 10.1117/12.862053
- [4] Armășelu A. Determination of quantum dot size by Fourier transform visible spectroscopy. *Optoelectr. Adv. Mater. Rapid Commun.* 2015; 9(3): 531–536.
- [5] Fourier JBJ. *The analytical theory of heat*. Paris: Chez Firmin Didot, Père et Fils; 1822. 638 p.
- [6] Maxwell JC. *A Treatise on Electricity and Magnetism*, vol. 1, Clarendon Press, Oxford; 1873, 534 p.
- [7] Schwartz L. On the impossibility of the multiplication of distributions. *C. R. Acad. Sci. Paris* 1954; 239: 847–848.
- [8] Fefferman CL. The uncertainty principle. *Bull. Amer. Math. Soc.* 1983; 9(2): 129–206. Available from: <http://projecteuclid.org/euclid.bams/1183551116>
- [9] Michelson AA. On the application of interference methods to astronomical measurements. *Philos. Mag.* 1890; 30(182): 1–21.
- [10] Fowles GR. *Introduction to Modern Optics*. 2nd ed. New York, NY: Dover Publications; 1989. 336 p. ISBN: 9780486659572
- [11] Bell RJ. *Introductory Fourier Transform Spectroscopy*. New York, NY: Academic Press; 1972.
- [12] Fellgett PJ. A contribution to the theory of the multiplex interferometric spectrometer. *J. Phys. Radium*. 1958; 19: 187. DOI: 10.1051/jphysrad:01958001903018700.
- [13] Jacquinot P. New developments in interference spectroscopy. *Rep. Prog. Phys.* 1960; 23: 267–312.
- [14] Connes P, Connes J, Maillard JP. *Atlas of Near Infrared Spectra of Venus, Mars, Jupiter, and Saturn*. Paris: Editions Du Centre National de Recherche Scientifique; 1969.
- [15] Connes J. Spectroscopic studies using Fourier transformations. *Rev. Opt. Theor. Instrum.* 1961; 40: 45, 116, 171, 231.
- [16] Chamberlain JE, Gibbs JE, Gebbie HA. The determination of refractive index spectra by Fourier spectroscopy. *Infrared Phys.* 1969; 9: 185.

- [17] Richards PL. High-resolution Fourier transform spectroscopy in the far infrared. *J. Opt. Soc. Amer.* 1964; 54(12): 1474-1484. Available from: <https://doi.org/10.1364/JOSA.54.001474>
- [18] Cooley JW, Tukey JW. An algorithm for the machine calculation of complex Fourier series. *Math Comput.* 1965; 19: 297.
- [19] Forman ML. Fast Fourier transform technique and its application to Fourier spectroscopy. *J. Opt. Soc. Amer.* 1966; 56: 978.
- [20] Parak WJ, Pellegrino T, Plank C. *Nanotechnology.* 2005; 16: 9.
- [21] Delehanty JB, Mattoussi H, Medintz IL. *Anal. Bioanal. Chem.* 2009; 393: 1091.
- [22] Bhattacharyya S. Fourier transform infrared spectroscopy: applications in medicine. *J. Phys. Chem. Biophys.* 2015; 5: 4. DOI: 10.4172/2161-0398.1000e128
- [23] Kenneth RJ. The early development and application of FTIR difference spectroscopy to membrane proteins. A personal perspective. *Biomed. Spectrosc. Imaging.* 2016; 5: 231–267. DOI: 10.3233/BSI-160148
- [24] Kumar A, Mansour HM, Friedman A, Blough ER, editors. *Nanomedicine in Drug Delivery.* CRC Press: Taylor & Francis Group, LLC; 2013. 469 p. ISBN 13:978-1-4665-0617-6
- [25] Naumann D, Fijala V, Labischinski H. The rapid differentiation and identification of pathogenic bacteria using Fourier Transform spectroscopic and multivariate statistical analysis. *J. Mol. Struct.* 1988; 174: 165–170.
- [26] Naumann D, Helm D, Labischinski H. Microbiological characterizations by FT-IR Spectroscopy. *Nature.* 1991; 35181: 2.
- [27] Gomez MA, Perez MAB, Gil FJM. Identification of species of *Brucella* using Fourier transform infrared spectroscopy. *J. Microbiol. Meth.* 2003; 55: 121–131.
- [28] Maquelin K, Kirschner C. Identification of medically relevant microorganism by vibrational spectroscopy. *J. Microbiol. Meth.* 2002; 51: 255–271.
- [29] Al-Qadiri HM, Al-Holy MA, Lin M, Alami NI, Cavinato AG, Rasco BA. Rapid detection and identification of *Pseudomonas aeruginosa* and *Escherichia coli* as pure and mixed cultures in bottled drinking water using Fourier transform infrared spectroscopy and multivariate analysis. *J. Agric. Food Chem.* 2006; 54(16): 5749–5754.
- [30] Al-Qadiri HM, Lin M, Al-Holy MA, Cavinato AG, Rasco BA. Detection of sublethal thermal injury in *Salmonella enterica* serotype Typhimurium and *Listeria monocytogenes* using Fourier transform infrared (FT-IR) spectroscopy (4000 to 600  $\text{cm}^{-1}$ ). *J. Food Sci.* 2008; 73: M54–M61.
- [31] Davis R, Mauer LJ. Fourier transform infrared (FT-IR) spectroscopy: a rapid tool for detection and analysis of foodborne pathogenic bacteria. In: Méndez-Vilas A, editor.

- Current Research, Technology and Education Topics in Applied Microbiology and Microbial Biotechnology. Formatex Research Center: Badajoz, Spain. 2010; 2:1582-1594.
- [32] Natalello A, Ami D, Gatti-Lafranconi P, Ario de Marco, Lotti M and Doglia SM. Kinetics of aggregation and structural properties of proteins in inclusion bodies studied by Fourier transform infrared spectroscopy. *Microb. Cell Fact.* 2006; 5 (Suppl 1): S10. DOI: 10.1186/1475-2859-5-S1-S10
- [33] Taha M, Hassan M, Essa S, Tartor Y. Use of Fourier transform infrared spectroscopy (FTIR) for rapid and accurate identification of Yeast isolated from human and animals. *Int. J. Vet. Sci. Med.* 2013; 1: 15–20. Available from: <http://dx.doi.org/10.1016/j.ijvsm.2013.03.001>
- [34] Salem EZ, Shahin IM, Yaser FM, Hamed MA, Abdel Hamid MF, Emam H et al. Applicability of Fourier transform infrared spectroscopy for rapid identification of some yeast and dermatophytes isolated from superficial fungal infections. *J. Egypt Women Dermatol. Soc.* 2010; 7: 105–110.
- [35] Allam AA, Salem JM. Evaluation of rapid molecular identification of clinically important *Candida* spp. isolated from immuno-compromised patients using RF-PCR. *J. Am. Sci.* 2012; 8: 463–468.
- [36] Dole MN, Patel PA, Sawant SD, Shedpure PS. Advance applications of Fourier transform infrared spectroscopy. *Int. J. Pharm. Sci. Rev. Res.* 2011; 7(2): 159–166. Article-029. ISSN 0976-044X
- [37] Dougan AJ, Kazarian GS. Fourier transform infrared spectroscopy imaging of live cells. *Spectrosc. Eur.* 2013; 25(5): 6–12.
- [38] Krafft C, Sergo V. Biomedical applications of Raman and infrared spectroscopy to diagnose tissues. *Spectroscopy* 2006; 20: 195–218. DOI: 10.1155/2006/738186
- [39] Balász B, Sipos P, Danciu C, Avram Ș, Soica C, Deheleanu C, Varju G, Erős G, Budai-Szücs M, Berkó S, Csányi E. ATR-FTIR and Raman spectroscopic investigation of the electroporation-mediated transdermal delivery of a nanocarrier system containing an antitumour drug. *Biomed. Opt. Express.* 2016; 7(1): 67–78. Available from: <https://doi.org/10.1364/BOE.7.000067>
- [40] Pawlikowska-Pawlega B, Misiak LE, Zarzyka B, Paduch R, Gawron A, Gruszecki WL. Localization and interaction of genistein with model membranes formed with dipalmitoylphosphatidylcholine (DPPC). *Biochim. Biophys. Acta* 2012; 1818(7): 1785–1793. DOI: 10.1016/j.bbamem.2012.03.020
- [41] Mbah CJ, Uzor PF, Omeje EO. Perspectives on transdermal drug delivery. *J. Chem. Pharm. Res.* 2011; 3(3): 680–700. ISSN No: 0975-7384 CODEN (USA): JCPRC5. Available from: [www.jocpr.com](http://www.jocpr.com)
- [42] Khaizan NA, Wong WT. Microwave: effects and implications in transdermal drug delivery. *Progr. Electromag. Res.* 2013; 141: 619–643.

- [43] Lin PC, Lin S, Wang PC, Sridhar R. Techniques for physicochemical characterization of nanomaterials. *Biotechnol. Adv.* 2014; 32(4): 711–726. DOI:10.1016/j.biotechadv.2013.11.006
- [44] Sarah De Saeger, editor. *Determining Mycotoxins and Mycotoxigenic Fungi in Food and Feed*. Woodhead Publishing Series in Food Science, Technology and Nutrition. Cambridge, UK: Woodhead; 2011. No 203. 427 p. ISBN: 9781845696740
- [45] Chauchan A, FTIR: a novel bio-analytical technique. *J. Anal. Bioanal. Tech.* 2012; 3: e107. DOI: 10.4172/2155-9872.1000e107
- [46] Severcan F, Haris PI, (Eds). *Vibrational Spectroscopy in Diagnosis and Screening*. Amsterdam: IOS Press; 2012. 432 p. DOI: 10.3233/978-1-61499-059-8-118
- [47] Jack C (Ed) (Ewing's) *Analytical Instrumentation Handbook, Third Edition*. Ed. CRC Press Taylor & Francis Group: Taylor & Taylor Group; 2004. 1064 p.
- [48] Ohta D, Kanaya S, Suzuki H. Application of Fourier-transform ion cyclotron resonance mass spectrometry to metabolic profiling and metabolic identification. *Curr. Opin. Biotechnol.* 2010; 21(1): 35–44. DOI: 10.1016/j.copbio.2010.01.012
- [49] Bogdanov B, Smith RD. Proteomics by FTICR mass spectrometry: top down and bottom up. *Mass Spectrum. Rev.* 2005; 24(2): 168–200. DOI: 10.1002/mas.20015
- [50] Nikolaev EN, Kostyukevich YI, Vladimirov GN. Fourier transform ion cyclotron resonance (FTICR) mass spectrometry: theory and simulations. *Mass Spectrum. Rev.* 2016; 35: 219–258. DOI: 10.1002/mas.21422
- [51] Creese AJ, Cooper HJ. Liquid chromatography electron capture dissociation tandem mass spectrometry (LC-ECD-MS/MS) versus liquid chromatography collision-induced dissociation tandem mass spectrometry (LC-CID-MS/MS) for the identification of proteins. *J. Am. Soc. Mass Spectrom.* 2007; 18(5): 891–897. DOI:10.1016/j.jasms.2007.01.008
- [52] Barrow MP, Burkitt WI, Derrick PJ. Principles of Fourier transform ion cyclotron resonance mass spectrometry and its application in structural biology. *Analyst.* 2005; 130: 18–28. DOI: 10.1039/B403880K
- [53] Tsybin YO, Quinn JP, Tsybin OY, Hendrikson CL, Marshall AG. Electron capture dissociation implementation progress in Fourier transform ion cyclotron resonance mass spectrometry. *J. Am. Soc. Mass Spectrom.* 2008; 19(6): 762–771. DOI: 10.1016/j.jasms.2008.02.007
- [54] Marshall AG, Chen T. 40 years of Fourier transform ion cyclotron resonance mass spectrometry. *Int. J. Mass Spectrom.* 2015; 377: 410–420. DOI: 10.1016/j.ijms.2014.06.034
- [55] Scigelova M, Hornshaw M, Giannakopoulos A, Makarov A. Fourier transform mass spectrometry. *Mol. Cell. Proteom.* 2011; 10(7): M111.009431-M111.009431. DOI: 10.1074/mcp.M111.009431
- [56] Leach FE, Wolff JJ, Xiao Z, Ly M, Laremore TN, Arungundram S, Al-Mafraji K, Venot A, Boons G-J, Linhardt RJ and Amster IJ. Negative electron transfer dissociation Fourier

transform mass spectrometry of glycosaminoglycan carbohydrates. *Eur J. Mass Spectrom* (Chichester, Eng.). 2011; 17(2): 167–176. DOI: 10.1255/ejms.1120

- [57] Zhou W and Hakansson K. Electron capture dissociation of divalent metal-adducted sulfated N-glycans released from bovine thyroid stimulating hormone. *J. Am. Soc. Mass Spectrom.* 2013; 24(11): 10.1007/s13361-013-0700-3. DOI: 10.1007/s13361-013-0700-3
- [58] Creese AJ and Cooper HJ. The effect of phosphorylation on the electron capture dissociation of peptide ions. *J. Am. Soc. Mass Spectrom.* 2008; 19(9): 1263–1274. DOI: 10.1016/j.jasm.2008.05.015





*Edited by Goran S. Nikolic,  
Milorad D. Cakic and Dragan J. Cvetkovic*

The main purpose of this book is to provide a modern review about recent advances in Fourier transforms as the most powerful analytical tool for high-tech application in electrical, electronic, and computer engineering, as well as Fourier transform spectral techniques with a wide range of biological, biomedical, biotechnological, pharmaceutical, and nanotechnological applications. The confluence of Fourier transform methods with high tech opens new opportunities for detection and handling of atoms and molecules using nanodevices, with potential for a large variety of scientific and technological applications.

Photo by Helga\_Preiman / iStock

**IntechOpen**

